Coupling Laser with Mass Spectrometry for Biomolecules Characterization : From Peptides towards Protein Fibrils

Mohammad Abdul Halim

To cite this version:

Mohammad Abdul Halim. Coupling Laser with Mass Spectrometry for Biomolecules Characterization : From Peptides towards Protein Fibrils. Chemical Physics [physics.chem-ph]. Université de Lyon, 2017. English. NNT : 2017LYSE1088 . tel-01586180

HAL Id: tel-01586180
https://theses.hal.science/tel-01586180v1

Submitted on 12 Sep 2017

N°d’ordre NNT : 2017LYSE1088

THESE de DOCTORAT DE L’UNIVERSITE DE LYON
opérée au sein de
l’Université Claude Bernard Lyon 1

Ecole Doctorale N° ED52
Ecole Doctorale de Physique et d’Astrophysique

Spécialité de doctorat : Spectrométrie de masse
Discipline : Chimie-Physique

Soutenue publiquement le 14/06/2017, par :

Mohammad Abdul HALIM

Coupling Laser with Mass Spectrometry for Biomolecules Characterization: From Peptides towards Protein Fibrils

---

Devant le jury composé de :

Monsieur MASSELON Christophe	Chercheur CEA Grenoble	Rapporteur
Madame CHAMOT-ROOKE Julia	DR CNRS Institut Pasteur	Rapporteure
Madame ROGNIAUX Hélène	IR INRA	Examinatrice
Monsieur CHIROT Fabien	Maître de Conférences UCBL	Examinateur
Monsieur DUGOURD Philippe	DR CNRS	Directeur de thèse
Madame GIROD Marion	CR CNRS	Co-directrice de thèse

UNIVERSITE CLAUDE BERNARD - LYON 1

Président de l'Université	**M. le Professeur Frédéric FLEURY**
Président du Conseil Académique	M. le Professeur Hamda BEN HADID
Vice-président du Conseil d'Administration	M. le Professeur Didier REVEL
Vice-président du Conseil Formation et Vie Universitaire	M. le Professeur Philippe CHEVALIER
Vice-président de la Commission Recherche	M. Fabrice VALLÉE
Directrice Générale des Services	Mme Dominique MARCHAND

COMPOSANTES SANTE

Faculté de Médecine Lyon Est – Claude Bernard	Directeur : M. le Professeur G.RODE
Faculté de Médecine et de Maïeutique Lyon Sud – Charles Mérieux	Directeur : Mme la Professeure C. BURILLON
Faculté d'Odontologie	Directeur : M. le Professeur D. BOURGEOIS
Institut des Sciences Pharmaceutiques et Biologiques	Directeur : Mme la Professeure C. VINCIGUERRA
Institut des Sciences et Techniques de la Réadaptation	Directeur : M. X. PERROT
Département de formation et Centre de Recherche en Biologie Humaine	Directeur : Mme la Professeure A-M. SCHOTT

COMPOSANTES ET DEPARTEMENTS DE SCIENCES ET TECHNOLOGIE

Faculté des Sciences et Technologies	Directeur : M. F. DE MARCHI
Département Biologie	Directeur : M. le Professeur F. THEVENARD
Département Chimie Biochimie	Directeur : Mme C. FELIX
Département GEP	Directeur : M. Hassan HAMMOURI
Département Informatique	Directeur : M. le Professeur S. AKKOUCHE
Département Mathématiques	Directeur : M. le Professeur G. TOMANOV
Département Mécanique	Directeur : M. le Professeur H. BEN HADID
Département Physique	Directeur : M. le Professeur J-C PLENET
UFR Sciences et Techniques des Activités Physiques et Sportives	Directeur : M. Y.VANPOULLE
Observatoire des Sciences de l'Univers de Lyon	Directeur : M. B. GUIDERDONI
Polytech Lyon	Directeur : M. le Professeur E.PERRIN
Ecole Supérieure de Chimie Physique Electronique	Directeur : M. G. PIGNAULT
Institut Universitaire de Technologie de Lyon 1	Directeur : M. le Professeur C. VITON
Ecole Supérieure du Professorat et de l'Education	Directeur : M. le Professeur A. MOUGNIOTTE
Institut de Science Financière et d'Assurances	Directeur : M. N. LEBOISNE

Acknowledgement

I would like to express my deepest gratitude to my supervisor, Dr. Philippe Dugourd, who inspired and supervised me for my scientific endeavours at CNRS. He always creates a space where my thought can grow, follow and sustain itself. I would also thank Dr. Marion Girod for her continuous supports and care in learning mass spectrometry for top-down peptide and protein characterization. Without her guidance and help, I could not able to list all the fragment ions we detected in the top-down spectra. I greatly acknowledge Dr. Rodolphe Antoine's support and assistance for performing experiments with home-made charge-detection mass spectrometer. I should mention that I am profoundly benefited from his wide-ranging knowledge in instrumentation and scientific literatures. His suggestions and comments significantly improved my work both in proteomics and megadalton mass spectrometry. Thanks also go to Dr. Luke MacAleese for his unconditional supports for laser coupling with mass spectrometer. I like to thank Dr. Franck Bertorelle for many discussions on sample preparation and beyond. Special thanks to Anne-Laure Simon and Antonin Soleilhac for their help with French documents and letters. Many ways I received supports and encouragements from our group members: Steven Daly, Geoffrey Knight, Marin Vojkovic, Driss Rayane, Alexander Kulesza, ChangMin Choi, Fabien Chirot, Clothilde Comby-Zerbino, Mathilde Bouakil and Caroline Bourgeois. For financial supports, I would like to extend my gratitude to the residents of Europe who invested their tax–money for my research through different institutions including European Research Council (ERC) and CNRS. I am also thankful to French Republic providing us a good social security and family supports.

This research could not have been done without the sacrifice and support of my wife, Nahid Naznin. I am also indebted to my daughter, Hafsah, and my two sons: Umar and Musab for shortening their beautiful and enjoyable play time for my research. Finally, I would like to thank my mother and father who always inspired me to excel in learning throughout my life.

“For thought is a bird of space, that in a cage of words may indeed unfold its wings but cannot fly.”

— Kahlil Gibran

ABSTRACT

The structural characterization of proteins often required them to be fragmented into small units containing only few amino acids. In bottom-up approach, proteins are cleaved into small peptides by enzyme then these peptides are subjected to further fragmentation in a collision cell of a tandem mass spectrometer. However, in top-down approach, proteins can directly be dissociated (without enzyme) into small fragments by collision, electron and photon-driven dissociations.

Photon-based activation methods including ultraviolet photodissociation (UVPD) and infrared multiphoton dissociation (IRMPD) have received great attention as an alternative to electron-driven and collision induced dissociation methods. Absorption of the high-energy UV photon is dispersed over the whole peptide or protein and stimulates extensive $C–C_\alpha$ backbone fragmentation while the low-energy IR photons gradually increases the internal energy and thus favorably dissociates the most labile amide (C–N) bonds.

This thesis focuses on the method development and applications for characterizing biomolecules by photon-based activation methods. The interest of combining high-energy UV photons and low-energy IR photons in an Orbitrap mass spectrometer, for protein and post-translationally modified peptide characterization, has been evaluated. Moreover, infrared multiphoton dissociation has been implemented in a gated electrostatic ion trap to push forward the limit of fragmentation methods to large megadalton ions. One of the main breakthroughs in this thesis is the ability to adapt these method developments and applications to biomolecular objects ranging from small peptides (in kilodalton mass range) to entire protein fibrils (in megadalton mass range).

To my parents and teachers who inspired and enlighten me

আমার মা-বাবা ও শিক্ষকের প্রতি যারা আমাকে অনুপ্রাণিত ও আলোকিত করেছেন

Contents

Abstract iii

Dedications v

Abbreviations xi

Chapter One: Background, Instrumentation and Presentation 1

- 1.1 Background: Protein, Post-translational Modifications and Fibrils 3
- 1.2 Mass Spectrometry 9
  - 1.2.1 Electrospray ionization (ESI) 10
  - 1.2.2 Quadrupole 11
  - 1.2.3 Orbitrap 15
  - 1.2.4 Charge Detector 18
- 1.3 Fragmentation Methods 21
  - 1.3.1 Collision Activated Dissociation (CAD) 23
  - 1.3.2 Electron Capture and Transfer Dissociations 25
  - 1.3.3 Ultraviolet Photodissociation (UVPD) 26
    - 1.3.3.1 General Discussion 26
    - 1.3.3.2 Basics of UV Photodissociation 28
    - 1.3.3.3 Light source for UVPD 29
  - 1.3.4 Infrared Multiphoton Dissociation (IRMPD) 32
    - 1.3.4.1 General Discussion 32
    - 1.3.4.2 Basics of Infrared Multiphoton Dissociation 33
    - 1.3.4.3 Light Source for IRMPD 35
- 1.4 Presentation of the Thesis 36

Chapter Two: Photodissociation of Peptide Anions 53

- 2.1 Introduction 55
- 2.2 Material and Methods 56
  - 2.2.1 Coupling UV laser with Mass Spectrometer 56
  - 2.2.2 Photodissociation Mass Spectrometry 56

2.2.3 Computation 58

2.3 Result and Discussion 58

2.3.1 The Photodissociation of Peptide 1 (YTIAALLSPYS) 58

2.3.2 The Photodissociation of Peptide 2 (DYKDDDDK) 65

2.3.3 The Photodissociation of Peptide 3 (RGDSPASSKP) 69

2.3.4 Photo-induced Hydrogen Loss at 213 nm 72

2.4 Summary 74

Chapter Three: Photodissociation of a Protein 81

3.1 Introduction 83

3.2 Materials and Methods 84

3.2.1 Coupling CO_2 and UV lasers with Mass Spectrometer 84

3.2.2 Mass Spectrometry 86

3.2.3 Data Analysis 87

3.3 Results and Discussion 87

3.3.1 Optimization of IRMPD on Intact Protein 87

3.3.2 UVPD, IRMPD and HiLoPD on Ubiquitin 91

3.3.3 Amino Acid Specific Fragmentation 98

3.4 Summary 101

Chapter Four: Photodissociation of PTM peptides 109

4.1 Introduction 111

4.2 Materials and Methods 113

4.2.1 Sample Preparation 113

4.2.2 Mass Spectrometry 113

4.2.3 Photodissociation and Computation 113

4.2.4 Data Analysis 115

4.3 Result and Discussion 115

4.3.1 IRMPD, UVPD and HiLoPD on RRLIEDAEY(H_2PO_4)AARG 115

4.3.2 IRMPD, UVPD and HiLoPD on RDY(SO_3)TGWLDF 119

4.3.3 IRMPD, UVPD and HiLoPD on EAISPPDAAS(GalNAc)AAPLR 122

4.4 Summary 126

Chapter Five: Photodissociation of Polymer Ions: Cation *vs* Anion 137

5.1 Introduction 139

5.2 Materials and Methods 141

5.2.1 Coupling CO_2 laser with Charge-detection Mass Spectrometer 141
5.2.2 Gated Electrostatic Ion Trap: “Benner” Trap 142
5.2.3 Electrospray Instrumentation and Sample Preparation 143
5.2.4 Quantum Calculations 144
5.3 Result and Discussion 145
5.3.1 Fragmentation Signatures at the Single Molecule Level 145
5.3.2 Fragmentation Signatures and Activation Energy 147
5.3.3 Decay Pathways 152
5.4 Summary 154

Chapter Six: Weighing Amyloid Fibrils **159**
6.1 Introduction 161
6.2 Materials and Methods 162
6.2.1 Fibrils Sample Preparation 162
6.2.2 Negative Stain Electron Microscopy 163
6.2.3 Atomic Force Microscopy (AFM) 163
6.2.4 Charge-detection Mass Spectrometry 164
6.2.5 Data processing and analysis 164
6.2.6 ESI Conditions 164
6.3 Result and Discussion 165
6.3.1 $A\beta_{1-42}$ peptide Fibrils 165
6.3.2 Alpha (α)-Synuclein Fibrils 169
6.3.3 Tau fibrils 173
6.4 Summary 176

Chapter Seven: Epilogue and Future Outlook **187**

Appendix **197**

Abbreviations

AD	Alzheimer Disease
AFM	Atomic Force Microscopy
Al-NETD	Activated Ion Negative Electron Transfer Dissociation
AF4	Asymmetrical Flow Field-Flow Fractionation
BDE	Bond Dissociation Energy
B3LYP	Hybrid functional developed by Becke, Lee, Yang, and Parr
CD	Circular Dichroism
CDMS	Charge-detection Mass Spectrometry
CDD	Charge Detection Device
CAD	Collision Activated Dissociation
CID	Collision Induced Dissociation
CW	Continuous Wave
DC	Direct Current
DNA	Deoxyribonucleic Acid
DFT	Density Functional Theory
ESI	Electrospray Ionization
EM	Electron Microscopy
ECD	Electron Capture Dissociation
ETD	Electron Transfer Dissociation
EDD	Electron Detachment Dissociation
EPD	Electron Photo-detachment Dissociation
FTIR	Fourier Transforms Infrared Spectroscopy
FTICR	Fourier Transform Ion Cyclotron Resonance
FFT	Fast Fourier Transform
FET	Field Effect Transistor
GalNAc	N-Acetylgalactosamine
HCD	High-Energy Collision Dissociation
HOMO	Highest Occupied Molecular Orbital
HiLoPD	High-Low Photodissociation
IMPs	Integral Membrane Proteins
IC	Internal Conversion
IRMPD	Infrared Multiphoton dissociation
LC	Liquid Chromatography
LUMO	Lowest Unoccupied Molecular Orbital
LIT	Linear Ion Trap

MS	Mass Spectrometry
MDa	Megadalton
MAD	Metastable Atom-Activated Dissociation
MPL	Mass-Per-Length
NMR	Nuclear Magnetic Resonance
NETD	Negative Electron Transfer Dissociation
PTMs	Post-translational Modifications
PEEK	Polyether Ether Ketone
PCB	Printed Circuit Board
PAMPS	Poly(2-acrylamido-2-methyl-1-propanesulfonic acid)
PEO	Polyethylene Oxide
PHFs	Paired Helical Filaments
RNA	Ribonucleic Acid
RF	Radio Frequency
RD	Repeat Domain
SDS-PAGE	Sodium Dodecyl Sulphate-Polyacrylamide Gel Electrophoresis
TEM	Transmission Electron Microscopy
TDDFT	Time-dependent Density Functional Theory
TOF	Time of Flight
TTL	Transistor–transistor Logic
UVPD	Ultraviolet Photodissociation
VUV	Vacuum Ultraviolet

Chapter One:

Background, Instrumentation and Presentation

“The secret to getting ahead is getting started.”

– Mark Twain

1.1 Background: Protein, Post-translational Modifications and Fibrils

The human genome contains around 20-25K genes, however, they are not dynamic and diverse like proteins [1]. It is estimated that the human proteome comprises over 1 million proteins. Proteins perform very diverse cellular functions including catalysis, transport, defense, energy conversions, and many more [2]. However, synthesis and function of proteins are governed by the "doctrine of triad" as proposed by Francis Crick in 1958 [3]. In brief, our genetic information is preserved in DNA, which is copied by RNA, described as "transcription". The copied information is used by RNA to synthesis protein in ribosome, the process is termed as "translation". During this process, cells utilized double-stranded DNA and single-stranded RNA. Over the years, the hypothesis was formulated as "one gene-one ribosome-one protein" [4]. After the transcription and translational processes, only bare and unfolded proteins are synthesized. In order to enter into the functional and dynamic cellular world, these bare proteins may require several post-translational covalent modifications. To understand the complete description of a biological system occurring in every living cell, knowledge of genomic and transcriptomic information are not adequate [5]. Large-scale investigation and detailed information on the proteome including its structure, function and dynamics are equally important [6]. In proteomics, one can study all proteins obtained from a cell in terms of their abundance, identification, structures, modifications, interactions and networks. For years, the structures and functions of proteins have been studied using different biophysical methods including the gold technique X-ray crystallography [7], popular NMR [8] and emerging Cyro-electron microscopy [9] techniques. However, the structure and function of many proteomes are not fully explored yet. Mass-spectrometry-based approach is now well suited for throughput analysis in terms of composition, structure, function and proteome-wide investigations on complex biological systems.

Proteins are abundant with different masses from relatively small proteins of kilodaltons to giant macromolecules of megadaltons; however, these structures consist an assembly of different 20 amino acids. Protein structure is assembled by primary, secondary, tertiary and quaternary arrangement (**Figure 1.1**). In primary structure, amino acids of polypeptide chain are built by the formation of amide (-CONH-) bond, known as the backbone of a protein. Although, the backbone structure of all proteins is same, the side chain (R groups) shape the chemical properties (acidic, basic, hydrophobic, and hydrophilic), conformation, size, and charge of a protein. Secondary structure refers to local structural arrangements such as α-helices, β-sheets and loops. Tertiary structure of a protein is associated with the secondary structure and the three-dimensional shape of the protein. In protein complexes, quaternary structure governs the overall geometry and organization of individual subunits relative to one another.

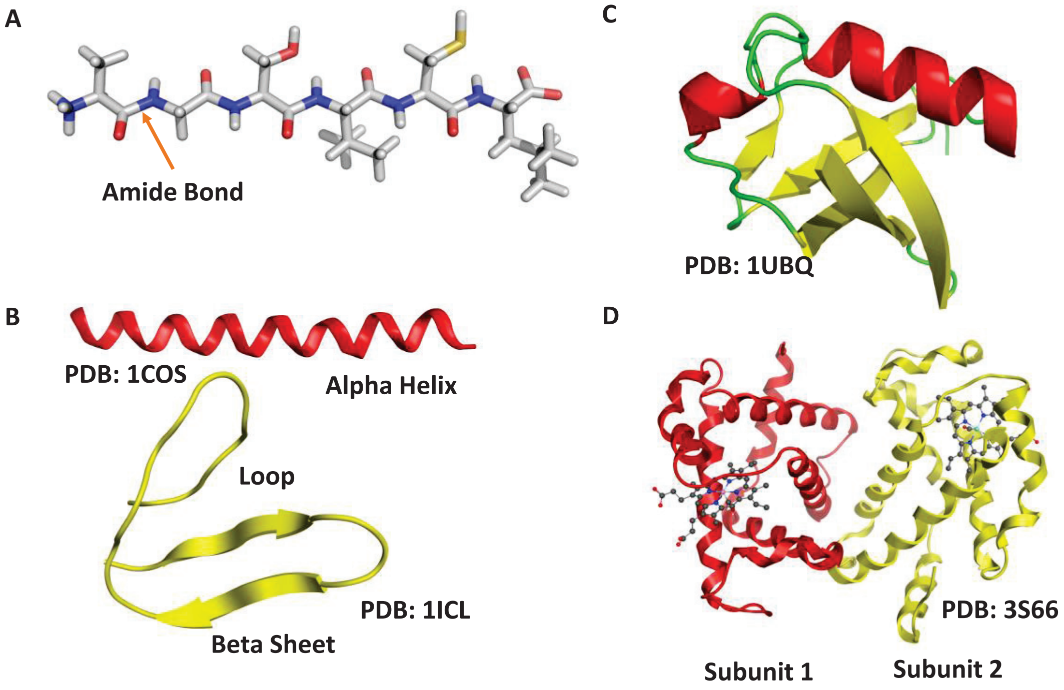

Figure 1.1 A) Primary structure of a peptide B) Secondary structures (helix, sheets and loops) of peptides C) 3D structure of ubiquitin D) Quaternary structure of hemoglobin

Post-translational Modifications

Dynamic molecular processes are mainly mediated by chemically modified functional proteins. In these process, proteins not only interact with each other but also with other biomolecules such as metabolites, phospholipids, carbohydrates and nucleic acids [10]. Post-translational modifications (PTMs) modify the functional and structural characteristics of all type of proteins by regulating activity, localization and interaction with other cellular molecules [11, 12]. Several studies confirmed that post-translationally modified proteins are involved with human diseases such as cancer, neurodegenerative diseases (Alzheimer's and Parkinson's), and diabetes [13, 14] and many others.

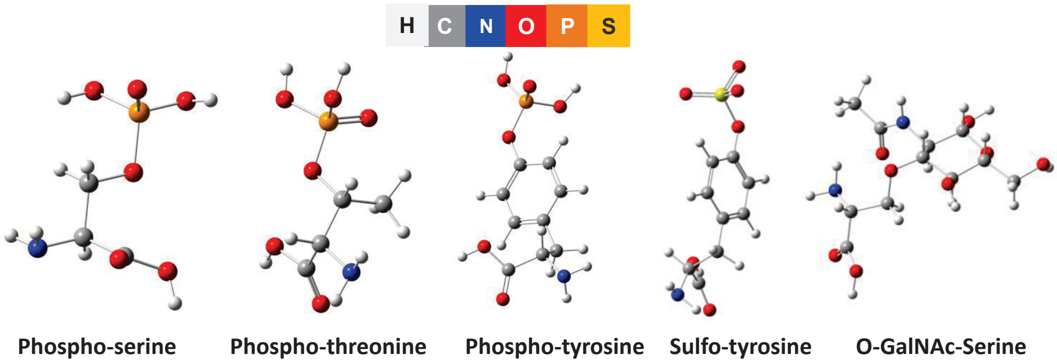

Figure 1.2 Modifications of serine, threonine, and tyrosine amino acids with phospho-, sulfo and GalNAc groups.

The key modification is phosphorylation, which occurs in serine, threonine and tyrosine residues (**Figure 1.2**) [12, 15, 16]. Phosphorylation play pivotal roles in cell cycles, growth, apoptosis and signal transduction pathways [17]. O-sulfation is observed to the tyrosine residue which plays crucial roles in hormonal regulation, protein-protein interactions in the extracellular region, hemostasis, inflammation and viral infections (**Figure 1.2**) [18]. Protein glycosylation is observed in every free-living cell and every cell type [19]. Glycosylation is the prime chemical modifications associated with plasma-membrane and secretory proteins (**Figures 1.2**) [20]. In this modification, oligosaccharides are connected to the protein through hydroxyl group of serine or threonine-linked (O-linked) or amide nitrogen of asparagine-linked (N-linked). These O- and N-linked glycosylation are frequently observed in endoplasmic reticulum (ER) and Golgi apparatus. The post-translational modifications of S-nitrosylation through the sulfur of cysteine residue also regulate the redox sensing, signaling, stability and functions of proteins [21]. Addition of acetyl group to lysine residue of the N-terminal tails of histones changes the biochemical properties of protein by neutralizing the positive charge [22, 23]. This reversible lysine acetylation plays a key role in regulating the gene expression and chromatin biology. Chemical attachments of small protein such as ubiquitin, small ubiquitin-like modifier (SUMO) are also observed as in PTMs [24-27]. Deamidation of glutaminyal and asparaginyal residues, a relatively less frequent but important PTM, is associated with apoptosis and aging [28]. Deamidation of human lens' crystallins, an ideal candidate for studying protein aging, is also a common feature in PTMs [29]. The biological functions of PTMs are very wide-ranging and have great significance. However, identification and characterization of PTMs are hindered due to the dearth of suitable analytical methods [30].

There are various biochemical methods currently available for characterizing PTMs such as antibody based Western blot, radioactive isotope-labeling, peptide/proteins microarrays, 2D gel electrophoresis, and mass spectrometry based proteomics [31-33]. Antibody-based Western blot technique can identify certain PTM such as tyrosine phosphorylation; however, this method is less sensitive for other PTMs such as methylation and acetylation. In isotope-labeling, due to the presence of unlabeled Adenosine triphosphate (ATP), incorporation of phosphate isotope labeling to the tissue sample is very difficult and ineffective in cell culture [34]. Moreover, high level radioactive phosphate labeling can damage the cell and can alter phosphorylation. On the other hand, carbon and hydrogen radio-isotope labeling is not efficient as they are very weak emitters which complicate the identification of methylation and acetylation. Peptide and protein arrays techniques are very rapid and high-throughput, however, these methods are non-specific, have low sensitivity, and require verification by mass spectrometry (MS).

In MS-based proteomic methods, one can detect, identify and mapping of proteome-wide PTMs sites. In the bottom-up approach [35, 36], the protein of interest is enzymatically digested by specific protease (for example, trypsin) to generate peptides. These peptides are then subjected to separate by liquid chromatography. The separated peptides are analyzed by tandem (MS/MS) mass spectrometry in online or offline. MS/MS data are analyzed by manual or automated algorithm to confirm the accuracy of the identification. However, there are several issues remained for the bottom-up approach due to peptide level investigation which may lead to problem associated with poor digestion and separation, protein inference, connectivity, poor fragmentation, incomplete sequence coverage, and missing site-specific modification information. In the top-down approach [37], intact protein are directly infused to the mass spectrometer where masses of protein and fragment ions are measured. Although the top-down approach is very sensitive to the fragmentation methods such as electron capture/transfer dissociation and ultraviolet photodissociation (see later **sections**); this method can provide nearly full sequence coverage and characterization of proteoforms (proteins arising from a single gene) with their diverse molecular complexity [38].

Amyloid Fibrils

Peptide or protein monomers with various amino acids sequence can self-assemble into amyloid fibrils (**Figure 1.3**) [39]. The formation of these amyloid fibrils is associated to biological functions and human diseases [40]. Alzheimer, Parkinson, Diabetes type 2 and the transmissible spongiform encephalopathies are associated with the fibrils formation of peptides and proteins [41]. These fibrils are formed from soluble peptides and proteins, which aggregate to form insoluble fibers [39, 42]. Formation and gradual deposition of these fibrils as amyloid plaques in the neuropil as well as the accumulation of neurofibrillary tangles in neurons are associated with neurodegenerative diseases. Understanding the mechanism of the formation of amyloid fibrils has great importance to develop the therapeutic measures to halting, reversing or avoiding such fibril formation. In particular, amyloid fibrils formation from Aβ peptide, α-synuclein and Tau proteins receives great attention due to their association to Alzheimer's disease (**Figure 1.3**). These fibrils share some common structural features, with variations in internal packing and polymorphism, containing a distinctive cross-β core domain where arrays of β-sheets are formed by parallel or anti-parallel orientations [36]. It is assumed that polymorphism of these fibrils has association with variations in clinical and pathological features of Alzheimer's disease [43].

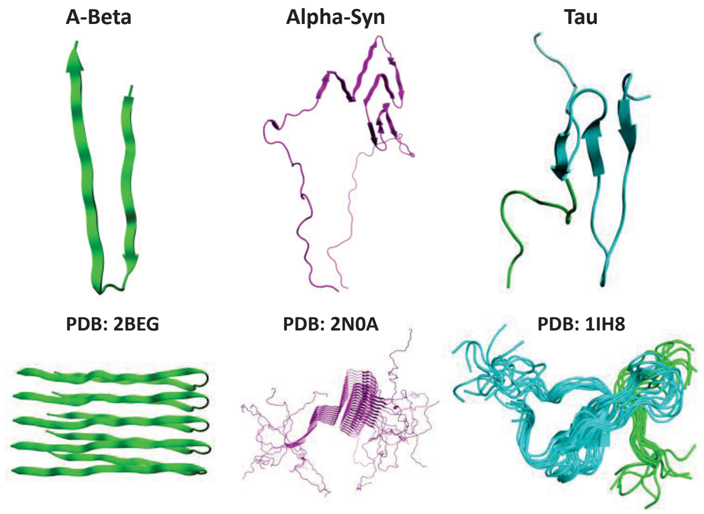

Figure 1.3 Monomer and fibrils structure of Aβ peptide, α-synuclein and Tau proteins

The formation of these fibrils follows three characteristic stages: an initial or lag state, an intermediate growth or elongation phase and terminal-plateau phase (**Figure 1.4A**) [44]. In lag state, monomers start to disappear from solution in which monomers converted to oligomer. The structural features of this conversion are morphologically different from the mature fibrils as evident from electron microscopy (EM) and atomic force microscopy (AFM) studies [45].

The overall nucleation process in which mature fibrils are formed follows two distinctive pathways [46, 47] (**Figure 1.4B**). In primary nucleation pathways, peptide and protein monomers start to aggregate. The rate of this aggregation is associated to the concentration of the monomer only. The primary nucleation process is not influenced by the presence of existing fibril. There is an intermediate step (just after the primary nucleation) known as elongation where monomers are added to the existing fibrils. However, the secondary nucleation process is highly influenced by the existing fibrils concentration [48]. This secondary pathway can be divided into two sub-steps. One is the monomer-dependent step, in which the rate of fibril formation depends on the concentration of existing fibrils as well as the concentration of monomer. In this step,

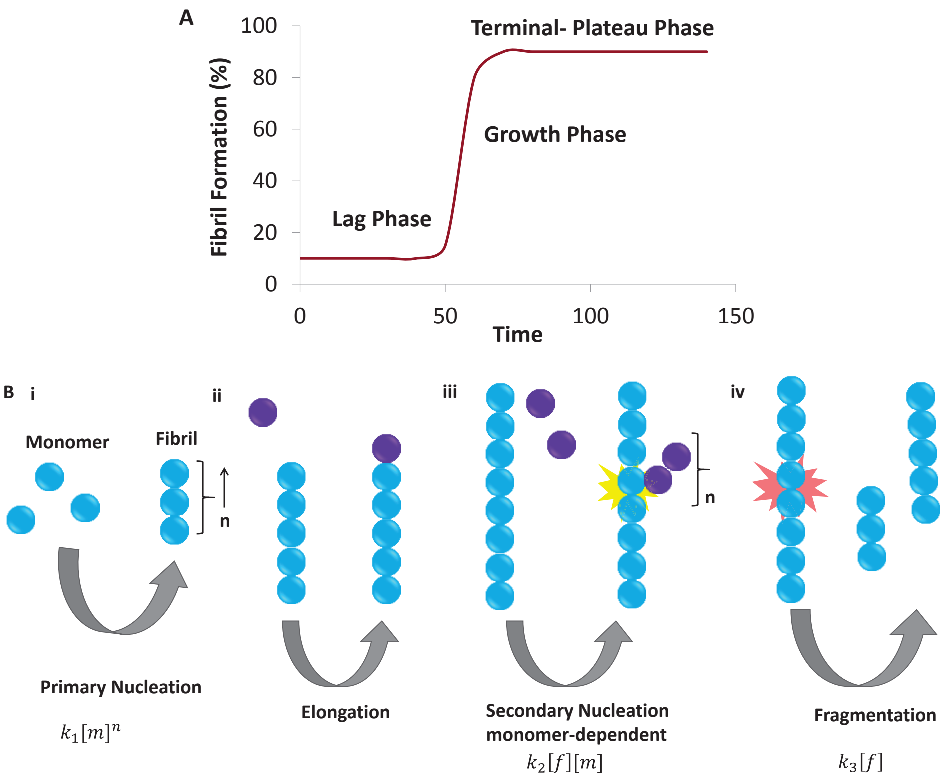

Figure 1.4 A) Fibril formation states B) Nucleation Pathways in which *k* is the rate constant, *f* and *m* are the concentration of fibril and monomer.

some fibrils are observed to continuously form new fibrils from the existing ones by branching and/or breaking [49]. However, in the monomer-independent process, the fibril formation rate is only depended on the concentration of the existing fibrils. This monomer-independent step often leads fibrils into fragmentation [46].

Characterization of fibrils is very challenging by traditional single crystal X-ray crystallography and solution phase nuclear magnetic resonance (NMR) techniques. Others methods such as X-ray fiber diffraction, electron microscopy (EM), solid state NMR, Fourier transform infrared spectroscopy (FTIR) and circular dichroism (CD) can provide considerable information about the morphology of amyloid fibrils and their internal structural conformation [50-53]. Traditional Mass Spectrometry can be employed to disclose the underlying mechanism of the early state of the aggregation but it cannot weigh the mass of megadalton protofibrils and mature fibrils.

1. 2 Mass Spectrometry

The first mass spectrometer was built to weigh the subatomic particles such as electron over a century ago by Sir Joseph Thomson at Cambridge [54]. Up to the late 1980s, with mass spectrometry one can measure the mass of small molecules; however, weighing larger biomolecules such as peptide, proteins and DNA were challenging due to the lack of suitable ionization techniques. The seminal works of the John Fenn group [55, 56] on electrospray ionization (ESI) and Koichi Tanaka [57, 58] on matrix assisted laser desorption/ionization (MALDI) allow researchers to ionize and transfer such giant molecules (proteins and DNA) to gas phase and measuring their masses without fragmenting them. The on-line coupling of solution phase and gas phase detection techniques make ESI-MS a prime choice for many protein experiments. Moreover, combining liquid chromatography with ESI-MS/MS opens a new avenue in proteomics to identify the proteins with a high throughput.

The principle of all mass spectrometric techniques is to analyze the mass-to-charge ratio (*m/z*) of ions in the gas phase. Different types of commercial mass spectrometers are available based on their instrumentations and applications. However, nearly all mass spectrometers consist of three basic components such as: ion source, mass analyzer and detector (**Figure 1.5**). The ion source generates large gas-phased charged ions by ionizing and evaporating of the liquid sample. Mass analyzers separate these charged ions according to their mass-to-charge ratios (*m/z*) based on ion trajectory by applied voltage or electromagnetic field. Separated charged ions are then detected and measured by detector based on their different mass-to-charge ratio. Ions can be produced in many ways. Among them ESI is one of the popular methods of choice in mass spectrometry. As ESI technique has been used in this work, only this method will be discussed herein. There are many mass analyzers are available, however, we will focus our discussion on quadrupole, Orbitrap and charge-detector.

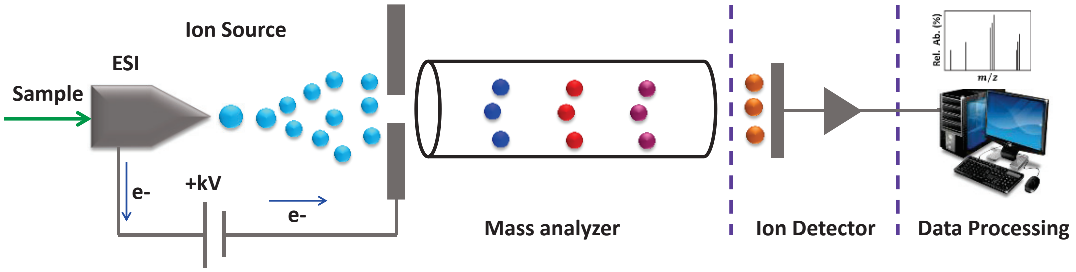

Figure 1.5 Basic components of a Mass Spectrometer

1.2.1 Electrospray ionization (ESI)

The complete ESI process follows three distinctive steps: i) formation of fine micrometer-sized charged droplets ii) evaporation of solvent, iii) ejection and formation of nanometer-sized highly charged droplets. All three steps occurred at atmospheric pressure as ESI operates under this pressure [48]. Formation of charge droplets (positive or negative) happens at the high-voltage capillary *via* electrochemical reaction in presence of solvent molecules [59]. The oxidation of the solvent produces positive ion whereas reduction of the solvent generates negative ion related to the polarity of the emitter electrode. Polar solvents such as water, methanol, and acetonitrile promote the electrochemical reactions.

Analyte solution at the capillary tip, held at an electric potential of several kV, creates a Taylor cone that produces micrometer-sized droplets [60-62]. The initial droplets released from the Taylor cone undergo solvent evaporation, often supported by additional heating. In order to assist on evaporation of solvent and nebulize the liquid, a carrier gas such as nitrogen or helium is introduced. Solvent molecules are emitted from the droplets as neutral species. The process, in turn, increases the charge density at the surface of the droplets. The small droplets show larger surface tension and tend to adopt more spherical shape. The spherical shape of charged droplets is formed by competing two forces. The driving force from surface tension pulls back the liquid into the nozzle whereas electrostatic Coulomb force pushes the liquid to the counter electrode [63]. At a certain point, known as Rayleigh limit, these two forces are counterbalanced for a droplet. At the Rayleigh limit, jet fission occurs leading to a stream of highly charged small droplets. Repetition of these events happened on larger and semi-larger droplets which eventually formed the nanometer-sized small droplets [56]. These gaseous ions can be singly or multiply charged. Since not all ions retain the same number of charges, therefore a number of peaks (charge state distribution) are usually observed in the mass spectrum of a protein.

There are two main mechanisms which were proposed related to the generation of nanometer-sized gaseous ions in ESI [63-64]. Low mass species follow the ion evaporation model (IEM) whereas heavy mass species adopt the charge residue model (CRM). In the IEM, gaseous ions are ejected from the nano-sized droplet surface by field emission; however in the CRM these ions are formed through evaporation of droplets to dryness. A recent mechanistic study disclosed that disordered polymers and unfolded proteins may follow the chain ejection model (CEM) [61].

1.2.2 Quadrupole

A quadrupole mass analyzer consists of four parallel cylindrical rods in which each rod pair opposing each other is joined together electrically (**Figure 1.6**). A radio frequency (RF) and a direct current (DC) are applied to opposing rod pairs [65]. The applied voltages have impact on the ion trajectory travelling through the central path between the four rods. For a given RF and DC voltages, only ions with specific *m/z* value will pass through the quadrupole rods, while, other ions will collide with the rods and become neutral. Choosing RF/DC ratio, quadrupole can act as a mass filter. However, the ions trajectories of the quadrupole mass analyzer are greatly influenced by time-dependent forces which require complex mathematical formulation to understand the stability and instability of gaseous ions.

If we consider an ion having its mass m and charge e at any point within the quadrupole field experienced a force F_x (for simplicity considering x-direction only) can be described by the following equation:

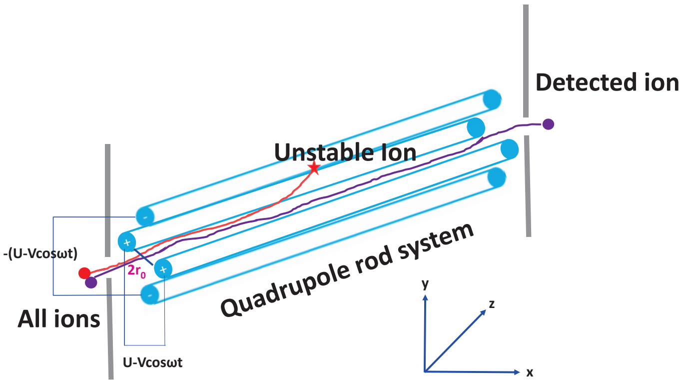

Figure 1.6 Quadrupole mass filter. The ions center and travel in the z-directions while oscillating in the x-y plane. The oscillation is controlled by the DC (U) and RF (V) voltage applied to each pair of rods. Only those ions (purple color) with stable motion at the selected U and V values will pass the quadrupole mass filter and will be detected. Other unstable ions (red) will hit the rod and will be lost.

$$F_x = -e\frac{\partial \varphi_x}{\partial x} \qquad (1)$$

where φ_x is the electrical potential in x-direction. Similar equation can be formulated for F_y and F_z. This equation can be compared with $F_x = ma$ (where a is the acceleration of an ion) and expressed as

$$F_x = ma = m\frac{d^2x}{dt^2} = -e\frac{\partial \varphi_x}{\partial x} \quad (2)$$

In the electric quadrupole field, the potential is quadric in the Cartesian coordinates can be presented by following equation [65]

$$\varphi = \frac{\varphi_0}{2r_0^2}(\lambda x^2 + \sigma y^2 + \gamma z^2) \quad (3)$$

where λ, σ, γ are coefficients or weighing constants, φ_0 is the applied electric potential and $2r_0$ is the distance between two opposite rods.

The Laplace condition $\nabla^2\varphi_0 = 0$ imposes the condition $\lambda+\sigma+\gamma = 0$. There are two ways to satisfy this condition for ion trap or mass filter. For the cylindrically symmetric three dimensional quadrupole ion trap, these constants value should be $\lambda = \sigma = 1$ and $\gamma = -2$, however, for the two-dimensional quadrupole mass filter, they have value of $\lambda = -\sigma = 1$ and $\gamma = 0$.

After substituting the value of $\lambda = \sigma = 1$ and $\gamma = -2$ in equation (3), one obtain

$$\varphi = \frac{\varphi_0}{2r_0^2}(x^2 + y^2 - 2z^2) \qquad (4)$$

Considering cylindrical coordinates and using the transformation $x = r\cos\theta$ and $y = r\sin\theta$, equation (4) becomes

$$\varphi = \frac{\varphi_0}{2r_0^2}(r^2 cos^2\theta + r^2 sin^2\theta - 2z^2) \qquad (5)$$

$$\text{Then, } \varphi = \frac{\varphi_0}{2r_0^2}(r^2 - 2z^2) \qquad (6)$$

$$\text{Since } cos^2 + sin^2 = 1$$

If the applied voltage φ_0 is given by a DC voltage (U) plus an RF voltage (V) with the driving frequency ω, one can write

$$\varphi_0 = U + Vcos\omega t \qquad (7)$$

Substituting the φ_0 value and $\lambda = 1$ into the equation (3) as well as performing differentiation with respect to x, one obtain the following equation

$$\frac{\partial\varphi}{\partial x} = \frac{2x}{r_0^2}(U + V\ cos\omega t) \qquad (8)$$

Substituting equation (8) in equation (2) yields

$$m\frac{d^2x}{dt^2} = \frac{-2e}{r_0^2}(U + Vcos\omega t)x = -\frac{2eU}{r_0^2} - \frac{2eVcos\omega t}{r_0^2} \qquad (9)$$

$$\frac{d^2x}{dt^2} = -\frac{2eU}{mr_0^2}x - \frac{2eVcos\omega t}{mr_0^2}x \qquad (10)$$

The equation obtained at (10), representing the simple form of force = mass x acceleration, requires a mathematical solution which can provide an expression that gives force on an ion in a quadruple field. The motion of ions in quadrupole fields can be described mathematically by a the solution of second-order linear differential equation, known as Mathieu equation, can be written (for x direction) as

$$\frac{d^2x}{d\xi^2} + (a_x - 2q_x\, cos2\xi)x = 0 \qquad (11)$$

where ξ is dimensionless parameter equal to *ωt/2* and a_x and q_x are the dimensionless trapping parameters. After reformatting the equation $\xi = \frac{wt}{2}$ (12) with series of arrangement we can obtain

$$\xi^2 = \frac{\omega^2 t^2}{4} \qquad (12a)$$

$$\frac{d^2x}{dt^2} = \frac{\omega^2}{4} \times \frac{d^2x}{d\xi^2} \qquad (12b)$$

$$\frac{d^2x}{d\xi^2} = \frac{d^2x}{dt^2} \times \frac{4}{\omega^2} \qquad (12c)$$

Substituting the value of equation (12c) into the equation (11) and subsequent rearrangement yields

$$\frac{d^2x}{dt^2} \times \frac{4}{\omega^2} + (a_x - 2q_x \, cos\omega t)x = 0 \qquad (13a)$$

$$\frac{d^2x}{dt^2} = -\frac{w^2 a_x}{4} x + \frac{2\omega^2 q_x \, cos\omega t}{4} x \qquad (13b)$$

Now one can compare the terms in the right hand side of equations (10) and (13b)

$$-\frac{2eU}{mr_0^2} x - \frac{2eVcos\omega t}{mr_0^2} x = -\frac{w^2 a_x}{4} x + \frac{2\omega^2 q_x \, cos\omega t}{4} x \qquad (14)$$

In addition, one can derive the following relationships from the equation (14):

$$a_x = \frac{8eU}{mr_0^2 w^2} = \frac{8U}{r_0^2 w^2} \times \frac{e}{m} \qquad (15a)$$

$$q_x = -\frac{4eVcos\omega t}{mr_0^2 w^2} = -\frac{4Vcos\omega t}{r_0^2 w^2} \times \frac{e}{m} \qquad (15b)$$

Equations (15a) and (15b) can also be written for a_y and q_y; however, $a_y = -a_x$ and $q_y = -q_x$. In stable motion, the ions oscillate in the x-y plane with limited amplitudes and will pass the quadrupole field in z direction without hitting the electrodes. In unstable motion, the amplitude will increase exponentially in x, y or both directions and ions will be lost [66]. The stability of the ions depends on the *a* and *q* parameters and not on the initial motion of the ion. Therefore, in the *a-q* map one can find the regions of stability and instability as shown in **Figure 1.7**. Although, there are infinite numbers of stability regions, herein the **Figure 1.7** only shows three stability regions (dark shaded) [67]. For separating a specific ion from other ions, *U* and *V* values are set in such a way within the stability region of the stability diagram that this particular ion can be transferred through the quadrupole. In this case, the quadrupole acts as a ‘‘mass filter’’. When *U* and *V* values are scanned together with a constant ratio, ions of increasing mass will reach the tip of the stability region according to their mass and will be transmitted sequentially to produce a mass spectrum.

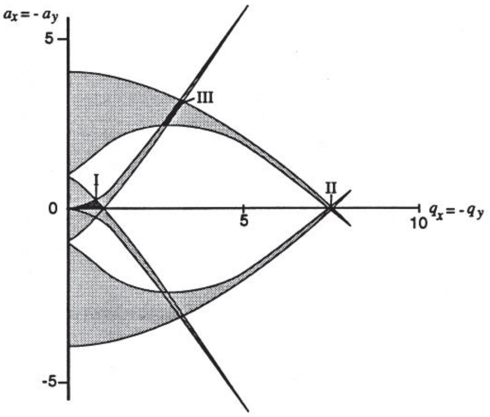

Figure 1.7 Overall stability diagram of quadrupole mass filter are shown by dark shaded region. Image taken from ref. [67].

Along with complicated trapping parameter, quadrupole mass spectrometers have some other issues including low resolution power, low mass range and slow scan rates. However, despite their limited resolution and slow scanning time, quadrupole is very popular instrument in the pharmaceutical and environmental labs. Moreover, recently the performance of the triple-quadrupole instrument has significantly improved in terms of better signal-to-noise, reliable detection using multiple reaction monitoring, better accuracy, reproducibility, low price and high sensitivity [68].

1.2.3 Orbitrap

The working principal of the Orbitrap mass analyzer is different than the conventional trapping instruments such as Paul and Penning Traps. Although the Paul trap in quadrupole mass spectrometers and the Penning trap in Fourier transform ion cyclotron (FT-ICR) are widely used as mass analyzers, they have some limitations. In the Paul trap, the mass resolution and accuracy is fairly low whereas the Penning trap in FT-ICR has low space-charge capacities and also is very costly and not easy to use [69]. In these aspects, Orbitrap can provide excellent mass resolution and accuracy. The working principal is based on simple design and it can also accommodate high space charge. Moreover, it is not too expensive and can be used on benchtop [70].

The Orbitrap mass analyzer is based on the refined model of Knight-style Kingdon trap [71] consisting of three electrodes [67, 72] (**Figure 1.8**). The cup-like two outer electrodes are facing each other and electrically isolated. One spindle-like central electrode connects the trap together and aligns it through the dielectric end-spacers. When a DC voltage is applied to the two axially symmetric electrodes, the electrostatic potential distribution, presented by the sum of quadrupole field (first term) of the ion trap and a logarithmic field (second term) of a cylindrical capacitor, known as quadro-logarithmic field.

$$U(r,z) = \frac{k}{2}\left(z^2 - \frac{r^2}{2}\right) + \frac{k}{2}\,(R_m)^2 \ln[\frac{r}{R_m}] + C \qquad (16)$$

where *r*, *z* are the cylindrical coordinates, *k is* the axial resting force, R_m is the characteristic radius and C is a constant. The geometrical shape of the electrodes can be expressed (where $z = 0$, plane of equatorial plane of symmetry) by the following equation:

$$z_{1,2}(r) = \sqrt{[\left(\frac{r^2}{2}\right) - \frac{R_{1,2}^2}{2} + (R_m)^2 \ln(\frac{R_{1,2}}{2})]} \qquad (17)$$

The subscripts 1 and 2 represent the central and outer electrodes, respectively and R_1 and R_2 are the maximum radii of the central and outer electrodes.

This equation shows that the stable ion motion will be orbiting around the central electrode and oscillation only observed in the z-direction which is independent of *r*, *φ* motion. Only ions with orbital radii lower than R_m will be trapped. In Kingdom trap, the *m/q* ratio is deduced from the frequency of radial oscillation which depends on the rotational frequency, the initial ion velocity and initial radius. However, in Orbitrap, the *m/q* ratio can be derived from the axial frequency which is independent of initial properties of the ions. For this reason, Orbitrap can provide high resolution and mass accuracy. The motion along *z* axis can be described by a simple harmonic oscillator and its exact solution is:

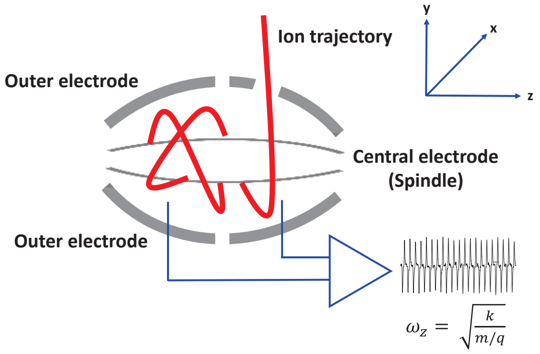

Figure 1.8 The Orbitrap mass analyzer

$$z(t) = z_0 cos\omega t + \sqrt{(\frac{2E_z}{k})}\, sin\omega t \qquad (18)$$

$$\omega = \sqrt{\frac{kq}{m}} \qquad (19a)$$

where z_0 is the axial amplitude, E_z the ion kinetic energy along the z-axis and *ω* is the axial frequency (rad/sec) and *m* and *q* are mass and charge of the ion, respectively. The frequency of the ion oscillations along the z-axis mainly depends on the *m/q* ratio of the ion and the potential (which is held constant) between the electrodes. The image current in the outer electrodes induced by ion axial motion is acquired as time domain transient and fast Fourier-transformed (FFT) to produce frequency spectrum where it is converted to *m/q* ratio by equation (19a). In Orbitrap, the frequency resolution power is twice the mass resolving power. Since the axial frequency is inversely proportional to the square root of *m/q*, unlike the cyclotron frequency in FTICR, which is inversely proportional to *m/q*. The experimental mass resolution can be expressed by following equation:

$$\frac{m}{\Delta m_{50\%}} = \frac{\omega}{2\Delta\omega_{50\%}} = \frac{\sqrt{\frac{kq}{m}}}{2\Delta\omega_{50\%}} \qquad (19b)$$

where subscript 50% presents the full width of a spectral peak at half-maximum peak height (FWHM). The high resolution also takes longer scan time. For 140,000 resolution at *m/z* 200 Th, the transient length will be 512 ms whereas for 17,500 resolution it will be 64 ms, respectively.

The magnitude of the image current produced by a cloud (coherent ion packets) of *N* ions with a frequency *ω*, axial amplitude *Δz* and an average radius *r* with an effective gap *λ* between the detection electrodes can be described by the following equation:

$$I\,(t, r) \approx -qN\omega \frac{\Delta z}{\lambda(r)}\, sin\omega t \qquad (20)$$

As the image current is applied and processed analogous to the FT-ICR, similar sensitivity and signal-to-noise ratios are obtained. Another mass-selective instability in Orbitrap is obtained by addition of RF frequency to the static voltage of the central electrode. The motion of the stable ion along with z-direction is also governed by the Mathieu equation (as described in the previous section 2.3) albeit with more complex nonlinearity. Nonlinearity and axial oscillation allow Orbitrap to operate in a unique region of the stability diagram with several volts (unlike quadrupole) of RF voltage. The detection limit is generally determined by the internal noise of the preamplifier which is 2−4 elementary charges in a 1 s acquisition. The mass accuracies of the Orbitrap mass analyzer is within the range of 2–5 ppm.

1.2.4 Charge Detector

Charge-detection Mass Spectrometry (CDMS) (**Figure 1.9**) is a single ion measurement technique in which mass and charge of each ion can be detected individually. Since this technique is not associated to charge-state resolution, it can be applied to weigh large chemical and biological systems of megadalton or higher species [66]. In addition, this technique can equally be employed for intrinsic and extrinsically heterogeneous systems. The working principal of CDMS is very simple based on the 'image current concept' first implemented by Shelton *et al* in 1960 [73]. From the image-current and fast Fourier Transform (FFT) perspective, CDMS is similar to the Orbitrap mass analyzer; however, the geometrical shape of the detector is quite different. Shelton *et al* employed an electrostatic acceleration method for a charge particle in high vacuum. In this technique, a small 'drift or conductive tube' is used for both detector and time of flight (TOF) mass analyzer (**Figure 1.10**). When a charged ion is passed through the tube, it creates an image current equal to the charge of the ion (*z*). The duration of the induced signal of the charged ion is also equal to the time of flight (TOF) when it moves through the tube. From the oscilloscope trace, one can detect charge (*z*) from the amplitude of the signal and simultaneously able to measure the *m/z* from the time of flight thus can obtain the mass of each ion.

The charge detection device (CDD) consists of a 37.5 mm long and 6 mm bore diameter thin-wall brass charge 'pick-up' tube. This device is built on the design of Walsh *et al* [74]. For electrical shielding, the pick-up tube was supported by a 'polyether ether ketone (PEEK)' insulator inside a second metal cylinder of 30 mm diameter and 50 mm long. The image charge is collected by the 'pick-up' tube and transmitted to a field effect transistor (FET). This transistor is connected to preamplifier which converts the current into the induced voltage. For lowering the link electrical impedances, the JFET transistor, the preamplifier and the first amplification stage are mounted on an integrated circuit to the tube. The transmission between the mechanics of the CDD and the PCB (printed circuit board) is made by a copper rigid connector. In addition to limit

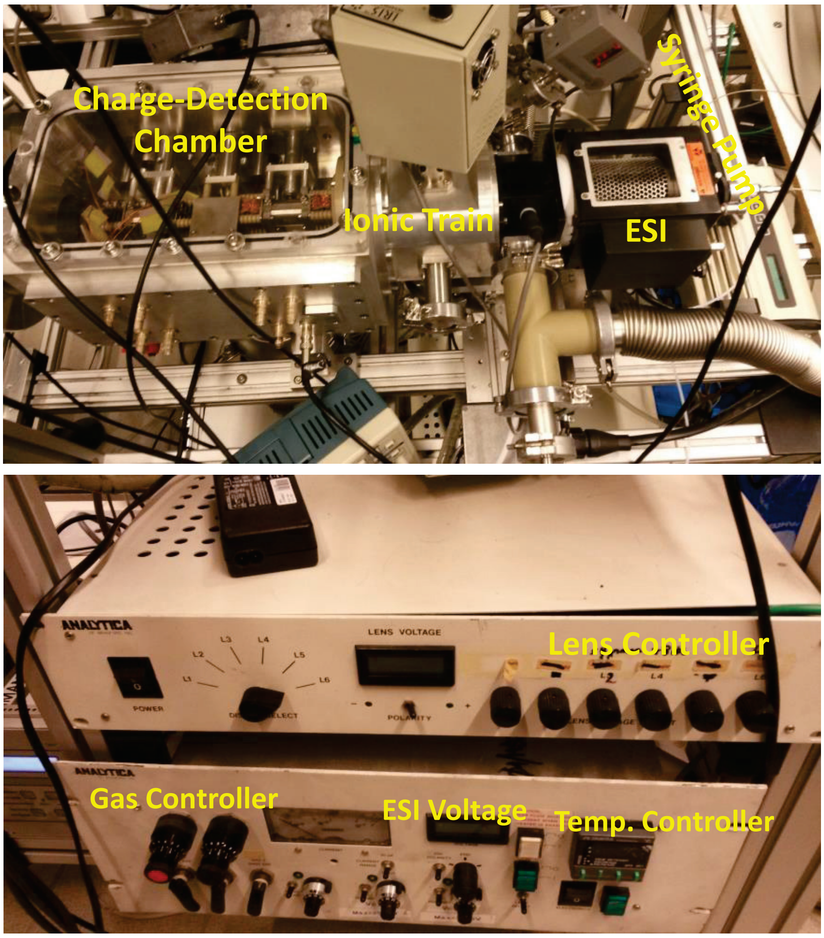

Figure 1.9 Electrospray (ESI) coupled Charge-Detection Mass Spectrometer

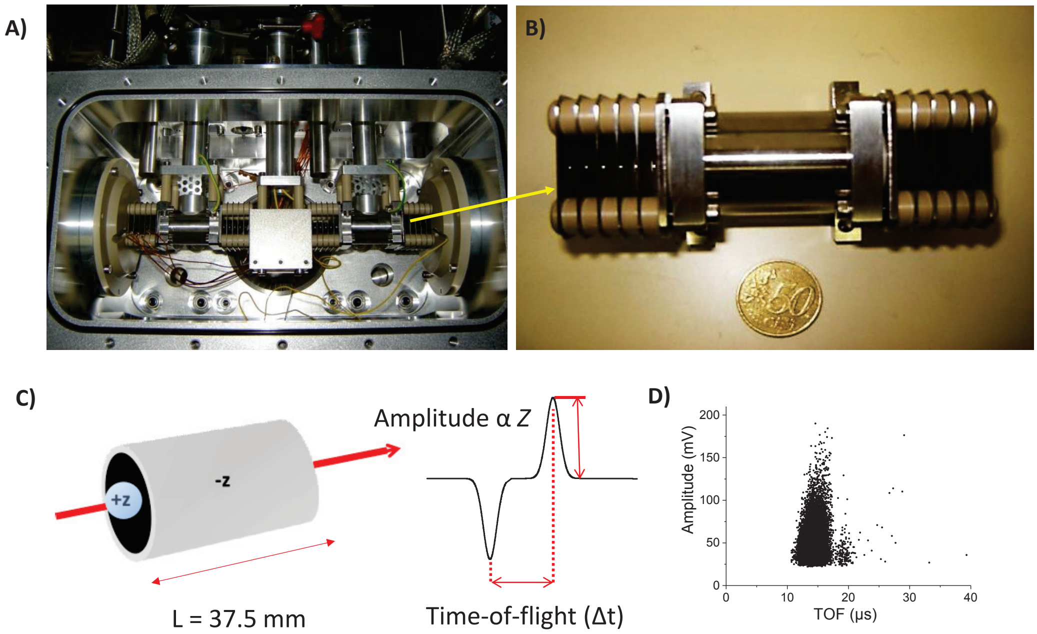

Figure 1.10 A) A set of two charge detective devices in the CDMS B) The detection tube C) A representative oscilloscope trace to measure amplitude and time-of-flight D) A representative spectrum of TOF vs amplitude of a 2 megadalton (MDa) polymer

the ground currents, this rigid link allows to minimize the noise. The equivalent capacity of the link between the pick-up tube and the FET is approximately 1 pF. The entrance and the exit of the pickup tube (stainless tube along 37.5 mm and 6 mm in diameter) are capped by tubes of 8 mm long and the same inner diameter of 6 mm. The gap between the end caps and the pick-up tube is 1 mm and allows a fast rise time for the charge image signal. After the differential amplifier, the resulting output for each ion generated as double pulse signal. The first pulse signal appears when ion enters the detector and the second single observed while ion is leaving the detector.

From the detector tube, two information are generated: i) average signal amplitude ii) average time-of-flight (Δt) of the ions. Average amplitude is converted to a charge number z using a calibration test capacitor, which allowed a known amount of charge to be pulsed onto the pick-up tube. The duration of the signal corresponds to the time-of-flight (TOF) of the ion through the detector. The m/z ratio of an ion can be determine from the time-of-flight Δt (time delay between positive and negative pluses that correspond to the entrance and the exit from the detector tube) shown in **Figure 1.10**. The ion velocity v_m can be measured from the detector tube (where L=37.5 mm):

$$v_m = \frac{L}{\Delta t} \qquad (21)$$

The detector tube worked based on electrostatic acceleration by accelerating a charged particle through a constant potential difference. If an ion, containing charge q and mass m, moves (with a velocity v_m) through a potential difference of V then it will gain kinetic energy of:

$$\frac{1}{2}\,mv_m^2 = qV \qquad (22)$$

$$\frac{m}{q} = \frac{2V}{v_m^2} \qquad (23)$$

However, in this system due to the presence of gas one needs to introduce a correction as the initial kinetic energy is transferred to the ion by the free jet expansion of the gas prior to the acceleration by electric field [75]. If the velocity due to gas expansion is v_g, one can rewrite the equation (23) into:

$$m = \frac{2qV}{v_m^2 - v_g^2} \qquad (24)$$

Using this equation (24), one can measure the mass m in the charge detection mass spectrometry.

1.3 Fragmentation Methods

Tandem Mass Spectrometry (MS/MS) has emerged as an indispensable tool for analyzing proteins as it can provide structural information in single amino acid resolution with high accuracy [76, 77]. Although mass changes in the proteins can be monitored by MS analysis of an intact protein; proteolytic investigation can reveal additional information [78, 79]. In the ‘bottom-up’ approach, proteins are cleaved into peptides by proteolytic enzymes such as trypsin. These peptides are then separated by liquid chromatography before infusing to the mass spectrometer. In this approach, separated peptides are then fragmented in a collision cell in order to deduce sequence information by comparing with databases or spectral libraries. However, this method has some shortcomings. It is quite challenging to recover all peptides from digested proteins or protein complex which leads to limited sequence coverage or loss of site-specific modification [80]. In addition, mass fingerprinting of isomeric peptides generated from complex proteins sample lead to incorrect protein identification [81]. On the other hand, a relatively new technique known as the 'top-down' technique, has emerged as a popular alternative, where intact proteins are injected into the ESI without prior digestion and subsequently fragmented in the MS [82, 83] Both proteins and their fragment ions are then determined in MS. There are different fragmentation methods available for tandem MS/MS in bottom-up and top-down approaches such as collision induced dissociation, electron capture and transfer dissociation, and photodissociation. In these fragmentation methods, backbone C–C, C–N and N−C bonds are broken and produced a/x, b/y and c/z ions of positive or negative charge, respectively depending on the ion source polarity. These ions also undergo one/two hydrogen loss (denoted as $(a_n\text{-}1)^{\pm}$) or gain (presented as $(a_n\text{+}1)^{\pm}$) and forming hydrogen-rich and hydrogen-deficient fragment ions (see **Figure 1.11**). The fragment radical ions which generated from the so-called charge-reduced species of the peptide anions in UVPD are discussed in the chapter 2.

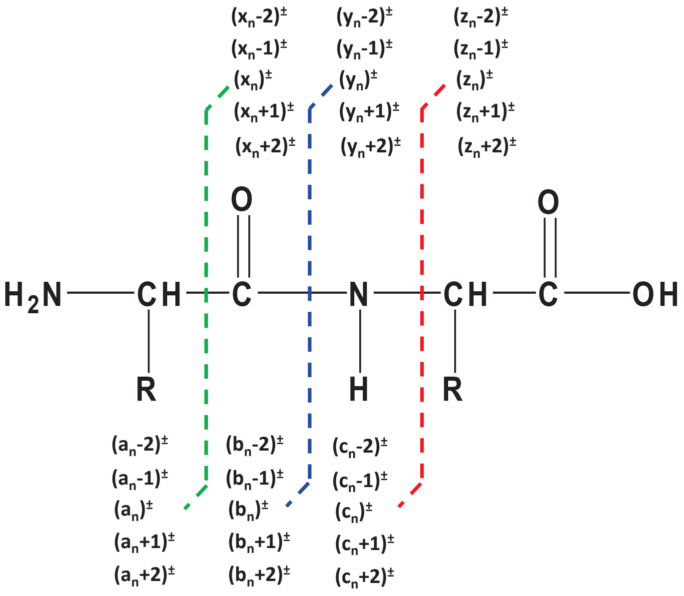

Figure 1.11 Nomenclature of fragment ions produced on breaking C–C, C–N and N−C bonds in peptides and proteins

1.3.1 Collision Activated Dissociation (CAD)

In order to obtain precise structural information at the single amino acid level, methods related to ion activation or fragmentation is very crucial. Collision activation dissociation (CAD) is frequently applied for fragmenting peptide and protein ions. This activation can generally be performed by two approaches: i) high-energy (kiloeletron volt) based collision dissociation and ii) low-energy (electron volt) based collision dissociation. In both approaches, the precursor ions are selected in the collision cell and allowed to collide with an inert gas such as helium, nitrogen, and argon (**Figure 1.12**). The collision between the precursor ion and a neutral target gas upturns the internal energy since some portion of the translational energy is transferred to the internal energy when an accelerated ion collides with the neutral gas in inelastic condition [84]. The maximum amount of available kinetic energy is transferred to the internal energy which depends on the mass of the precursor ion and target gas and can be represented by the following equation (applying center of mass considerations) [85]:

$$E_{com} = \left(\frac{m_t}{m_p + m_t}\right) E_{lab} \qquad (25)$$

where m_p and m_t are the masses of the precursor ion and target gas, respectively and E_{lab} is the kinetic energy of the ion in the laboratory frame. Increasing the kinetic energy of the ion or increasing the molecular weight of the collision gas will increase the available energy. However, the increasing mass of the precursor ion will decrease the available energy. The probability of interaction is also associated to the target gas pressure and the collision cross-sections of both precursor ion and target species [86]. At higher gas pressures, the collision rate between the precursor ions and the gas will increase in several folds.

Overall, the whole CAD process is accomplished by two consecutive steps (shown in **Figure 1.12**): i) very fast conversion (10^{-15}–10^{-14} s) of translational energy of the accelerated ion into the internal energy of both precursor ion and neutral gas target, and ii) relatively slow decomposition of the energized ion into fragment ions. Moreover, the fragment ions produced from the first dissociation can also be further activated by subsequent interactions and decomposed to secondary fragment ions.

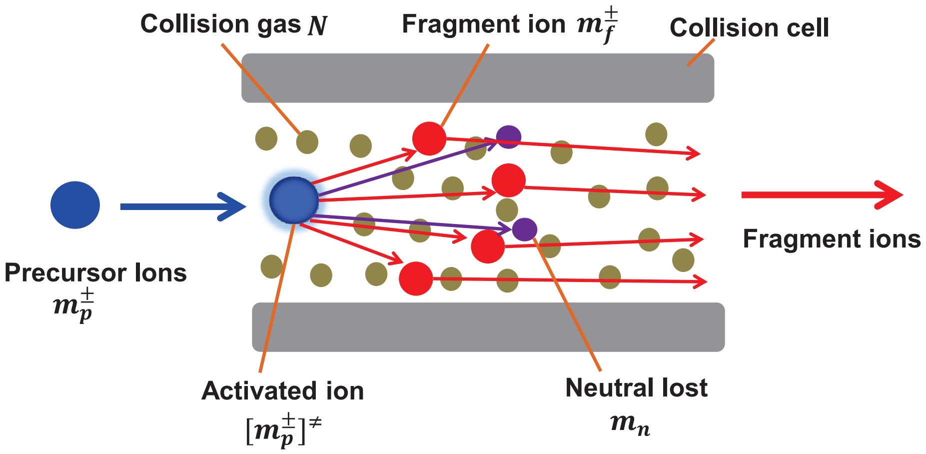

$$m_p^{\pm} + N \rightarrow [m_p^{\pm}]^{\neq} \rightarrow m_f^{\pm} + m_n$$

Figure 1.12 Collision Induced Dissociation and Fragmentation Pattern

In this slow-heating activation method, precursor ions mainly cleave at the C–N (peptide) bonds and generate b and y fragment ions (see **Figure 1.11** for nomenclature). Excitation of the precursor ion by CAD requires alternation of the kinetic energy which increases the neutral loss, in turn, provides limited structural information [87]. The inherent disadvantage of CAD in quadrupole ion trap mass spectrometry results from the competition between excitation and ejection [88]. In order to retain ions in the pseudopotential well, the velocity of the ions requires to be lowered. However, inducing dissociation, trap ions require to accomplish sufficient kinetic energy which can only be achieved from high velocity. The depth of the pseudopotential well, D, relates to the amplitude of RF trapping frequency and mass to charge ratio (*m/z*) described by the following simplified equation [89]:

$$D \propto \frac{(RF\ amplitude)^2}{(\frac{m}{z})^2} \qquad (26)$$

Elevating the RF frequency increases the depth of the well and subsequently decreases the value of *m/z,* which means low *m/z*-product ions cannot be trapped. It is estimated that approximately ions with an *m/z* one-third that of the precursor ions are not trapped and hence not detected. This shortcoming are improved by incorporating a separate high-energy collision dissociation (HCD) cell [90]. As this separate collision dissociation is independent of trapping parameter, the low-cutoff is not observed. In addition, the imparted-energy to the precursor ions is higher in a HCD cell than the traditional CAD in an ion trap mass spectrometer. However, despite these improvements, some challenges are remained on retaining the important post-translational modifications (PTMs) in the fragment ions.

1.3.2 Electron Capture and Electron Transfer Dissociations

Alternative to collision induced dissociation, electron based methods including electron capture dissociation (ECD) [91] and electron transfer dissociation (ETD) [92] have been developed. In the ECD method, instead of an inert gas, multiply-charged precursor ions are excited by a low energy electron (~1 eV) or an electron-rich anion (A$^-$) which are capable of transferring an electron as presented in **Figure 1.13** [93]. The reaction between the protonated precursor ion and electron (e$^-$) is exothermic (~4-6 eV) and nonergodic, meaning intermolecular oscillation energy is non-transferable [94]. Because of charge neutralization of the precursor ions following the electron capture/transfer, multiply charged ions are expected for ECD/ETD

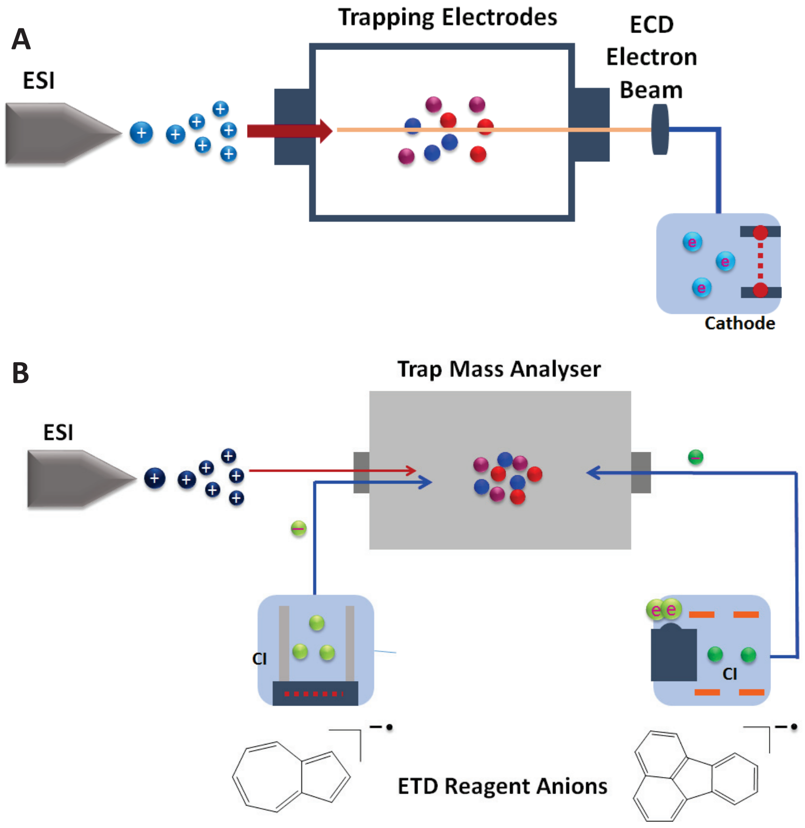

Figure 1.13 Schematic diagram of A) Electron capture and B) transfer dissociation methods (CI, chemical Ionization).

experiments. After reception of the electron, the excited precursor ions primarily break at N–C_α bonds and yield even-electron c (from N-terminal) and odd-electron radical z• ions (from C-terminal). Due to the breaking of N–C_α bond, labile PTMs are generally preserved. Occasionally, other minor fragmentation channel, *a* and *x* fragment ions can also be formed breaking C_α–C bonds. Although the fragmentation mechanism of ECD and ETD are similar, the instrumental set-up of these methods is quite different. ECD is performed at ultra-high vacuum (~10^{-10} Torr) whereas ion-ion reactions occurred in ETD at lower vacuum in ion trap. Lower vacuum promotes faster collisional cooling and thus decreases the interim energy of the post-electron attachment complex, offering additional energetic fragmentation channels [95].

ECD can straightforwardly be implemented within Fourier Transform ion cyclotron mass spectrometry (FTICR). Several studies confirmed that interfacing ECD with FTICR can successfully retain and detect the phosphorylation, glycosylation, sulfonation and others PTMs [96-100]. Although FTICR can provide high resolution and outstanding mass accuracy, it appears as a less viable option due to high cost and intricate operating system which requires more expertise than other MS instruments [81]. Moreover, integration of ECD with ion-trap instrument is very challenging since ECD has a small reaction cross section and low electron kinetic energy of ~1 eV [101]. Unlike ECD, ETD can be coupled with linear ion trap-Orbitrap hybrid mass spectrometer (QLT-Orbitrap) [102]. In this coupling, negative chemical ionization (NCI) source, which supplies reagent anions, is attached to a c-trap by an octopole and some modification is performed in QLT for ion/ion reactions. Moreover, ETD can be integrated with liquid chromatography (LC) for separating and analyzing protein and peptide [103, 104].

1.3.3 Ultraviolet Photodissociation (UVPD)

1.3.3.1 General Discussion

An alternative to collision [105-107] and electron [108, 109] based techniques, photon-based methods have emerged as relatively new powerful approaches for characterizing peptides, polysaccharides and proteins [110-116]. This technique can be employed with or without a chromophore which enable the excitation of all peptide without any sequence restriction [117, 118]. Ultraviolet photodissociation (UVPD) leads to intense fragmentation patterns. In this method, protein and peptide cations predominately dissociate to a/x ions and less frequently to c/z and b/y ions (see **Figure 1.11** for nomenclature). Different wavelengths such as 157, 193, 213, 220, and

280 nm have been implemented in UVPD. Above and at 280 nm, specific fragmentation have been reported following excitation of aromatic residues in peptides or proteins [119]. The number of fragment ions increases as the wavelength decreases from 280 nm to 213 nm [119, 120].

Among these wavelengths, 157 nm and 193 nm are most widely used for photodissociation experiment for peptide and protein characterization. Thompson *et al* employed vacuum photodissociation at 157 nm on singly protonated peptide ions to elucidate the unusual backbone cleavage [121]. Cui *et al* further revealed that basic residues in the C-terminal yields to x, v and w fragment ions whereas N-terminal produces a and d fragments ions [122]. Moreover, a+1 and x+1 radical ions are identified from the charge localized N- and C- terminals, respectively. Secondary radical elimination of hydrogen atom are detected from a+1 and x+1 ions to produce a and x ions, respectively. Satellite ions such as d, v and w are formed due to side chain eliminations. b, c and z fragment ions are also noticed but are less frequent than a and x ions. Hydrogen/deuterium exchange experiments further confirmed that both backbone amide and side-chain β-carbon hydrogen can undergo elimination to yield a and x ions [123]. Implementing time-resolved photodissociation at 157 nm revealed some unusual but stable x+2 fragment ion compared to less common a+2 ion [124]. They proposed that addition of one hydrogen to x+1 and a+1 radical ions can yield x+2 and a+2 ions. Migration and transfer of hydrogen atoms to radical ions have also been witnessed in ECD studies [125, 126].

In addition to 157 nm, 193 nm has been implemented in a hybrid linear ion trap-Orbitrap mass spectrometer for characterizing different peptide and proteins in positive polarity. Wide-ranging fragmentation yields a/x, b/y, c/z, y-1, v, w and d ions and thus provides nearly complete sequence coverage. Whole protein characterization has been achieved by this technique implementing direct infusion and/or chromatographic time scale [127, 128]. Along with common fragment ions, Madsen *et al* also observed some uncommon fragment ions such as a+2, c-1 and z+1 [129]. This study disclosed that fragmentation patterns varied with the protonation state of the peptide. When protonation takes place at the N-terminus, cleavage of the C_α-C bond occurred, however, N-C_α cleavage is favored with C-terminus protonation. Although the photodissociation technique yields various fragment ions, the core mechanism follows the excited state dissociation channel for ion activation.

1.3.3.2 Basics of UV Photodissociation

When UV photons interact with a peptide or protein (P), fast electronic transition occurs from an electronic ground state [S_0] to a high-energy state [S_n]. The process can be presented by

$$P + hv \rightarrow P^* \qquad (27)$$

Here h is the Planck constant, v is the frequency of radiation and P^* is the electronic excited state of P. *Pi* (π) electrons present in the highest occupied molecular orbital (HOMO) of peptide or protein can absorb the UV photons and promoted to the lowest unoccupied molecular orbital (LUMO) (anti-bonding molecular orbitals, π^*) in the higher-energy level. These relatively low energy transitions typically occur at 200 nm <λ<400 nm (UV) region. For peptide and protein, several amino acids such as phenylalanine, tyrosine, and tryptophan can act as UV chromophore (250-280 nm). Moreover, peptide bond (–OCNH–) can absorb UV photons in the 190-230 nm range.

Absorption of a single high energy photon is sufficient to induce dissociation of a peptide and protein in gas phase. High energy photon can cause photodissociation in two routes as shown in **Figure 1.14** [130]:

(i) promoting *vibronic transition* (simultaneous change in electronic and vibrational states) from the electronic ground state (S_0) to excited state (S_n) beyond the dissociation threshold

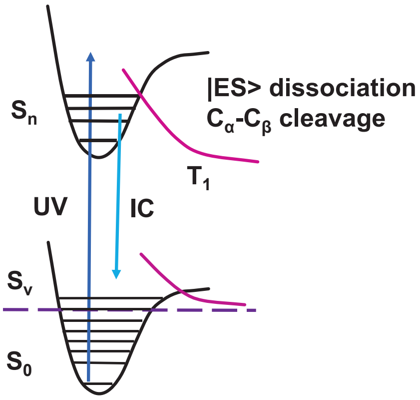

Figure 1.14 Excited state dissociation channels in Ultraviolent Photodissociation

(ii) Excitation leading to *internal conversion (IC)* from the excited state (S_n) to highly excited vibrational state (above the dissociation threshold) of S_0 by direct transition or *via* lower vibrational state of S_v.

For the fragmentation of peptide or protein, adequate photon energy is required to cross the photodissociation threshold, measured by the energy difference between transition state and the ground state of the molecule. Effective interaction between photons and the molecule is also governed by the Beer-Lambert Law:

$$-\ln\left(\frac{I}{I_0}\right) = \sigma l N \qquad (28)$$

$$\frac{I_0 - I}{I_0} = 1 - e^{-\sigma l N} \qquad (29)$$

where σ is the absorption cross-section (cm^2/molecule), l is the path length (cm), N is the number density (molecules/cm^{-3}) and $\frac{I_0 - I}{I_0}$ is the photon absorbed ratio. For inducing UV photodissociation, light source requires to produce ~10^{18} photons cm^{-2}s^{-1} for tryptophan amino acid cation [131].

1.3.3.3 Light source for UVPD

In general, a high-intensity laser-like light source is required for UV photodissociation experiment. In lasers, a system is promoted to an upper level from a lower lever in a highly reflective optical cavity by continuous pumping [132, 133]. In the upper level, the excited electron interacts with a photon causing relaxation by releasing a photon with same orientation and phase as the interacting one (see **Figure 1.15**). This photon then triggers stimulating emission of other photons providing ever-increasing photon flux similar to a chain reaction. The energy in the lasing cavity is stored in the form of a population inversion where the upper levels have more population compared to the lower level. The stored lasing energy can be used continuously (*cw*) or pulsed. In *cw*, one optical mirror is partially transparent which let the photons escape continuously from the cavity.

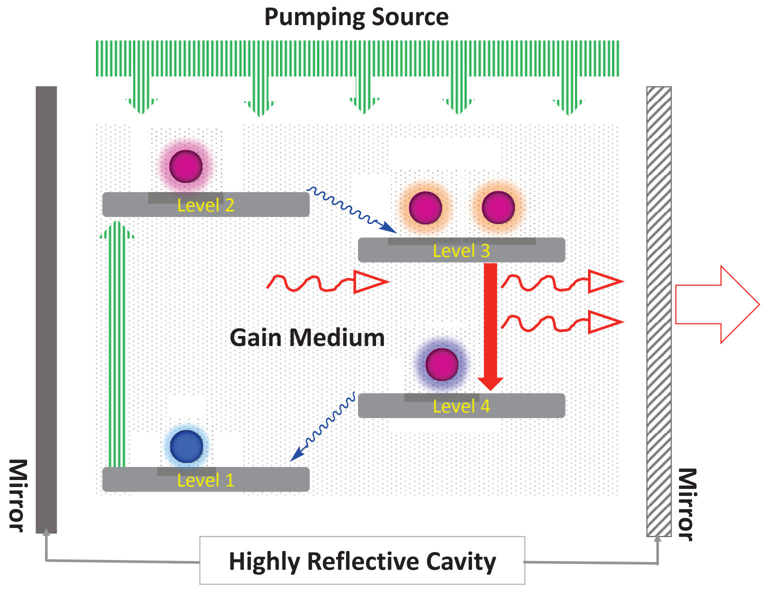

Figure 1.15 Essential component of laser with 4-level lasing systems with relative populations of levels.

However, in pulsed mode, photons are extracted in burst and controlled by a so-called quality factor (Q) switching [134] which can be defined by the following equation

$$Q = \frac{Energy\ stored}{Energy\ lost\ per\ cycle} 2\pi \qquad (30)$$

A low Q factor indicates that most of the stored energy in the cavity is lost whereas at high Q factor such loss is minimized. Therefore, Q-switch can toggle between high and low Q factors by either enabling or disabling light to resonate in the cavity at particular time.

UV lasers have many applications in industrial and medical application due to high photon energy and shorter wavelength [135]. Corrosive gas-based excimer lasers (ArF and KrF) are mainly used due to shortage of high power UV laser. This high power and high efficiency 2-level excimer laser only operated in pulse mode and has limited tenability of ±1 nm. High power all-solid-state UV lasers are highly regarded for its high gain factors, robustness, excellent efficiency, inexpensiveness, tenability and ease of operation [136]. High power and 4-level solid-state Nd:YAG laser is the best choice which provide primary output at 1064 nm with possible other lasing transitions. Nd:YAG laser is made of ytterbium aluminum garnet ($Y_3Al_5O_{12}$) crystal containing 0.1-1% of Nd^{3+}. For pumping the Nd:YAG laser, monochromatic diode laser are used.

The primary lasing transition occurs between the split-levels in the $^4F_{3/2}$ and $^4I_{11/2}$ states of Nb^{3+} [132] (**Figure 1.16**). Relaxation from the pump band to the $^4F_{3/2}$ level for promoting the population inversion and depopulation of the $^4I_{11/2}$ to the ground level is facilitated by the lattice vibration of the garnet.

As the Nd:YAG laser (BrillantB Nd:YAG, repetition rate of 20 Hz, Quantel, Les Ulis, France) provide the primary transition at 1064 nm, for generating high energy UV photon at 213 nm, one need to perform frequency doubling by higher harmonic generation (**Figure 1.17**). Harmonic generation is a non-linear process where high-intensity longer wavelength laser light interacts with non-linear optical crystal to produce shorter wavelength laser light. The obtained new frequency is integral multiple ($n\omega$) of the fundamental frequency (ω) of the original laser light. This phenomenon was first observed by Frankel *et al* when they shined their intense beam from the Ruby laser of 694 nm through quartz medium and obtained second harmonic at 347 nm [137]. Various nonlinear crystals such as γ-BaB_2O4 (BBO) and $CsLiB_6O_{10}$ (CLBO) are used for harmonic generation [138, 139]. For generating 213 nm UV light for our photodissociation experiment, the fundamental 1064 nm light is passed through the non-linear crystal to generate the second harmonic at 532 nm (**Figure 1.17**). Then the second harmonic is sent through the second crystal where fourth harmonic 266 nm is generated. The remaining fundamental is then allowed to interact with the fourth harmonic (266 nm) to produce the fifth harmonic 213 nm by sum-frequency generation (SFG).

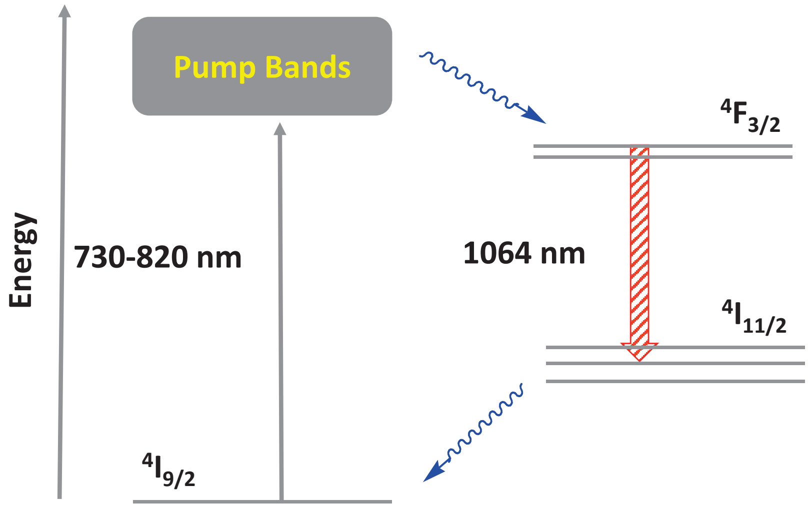

Figure 1.16 Energy diagram of Nd:YAG laser

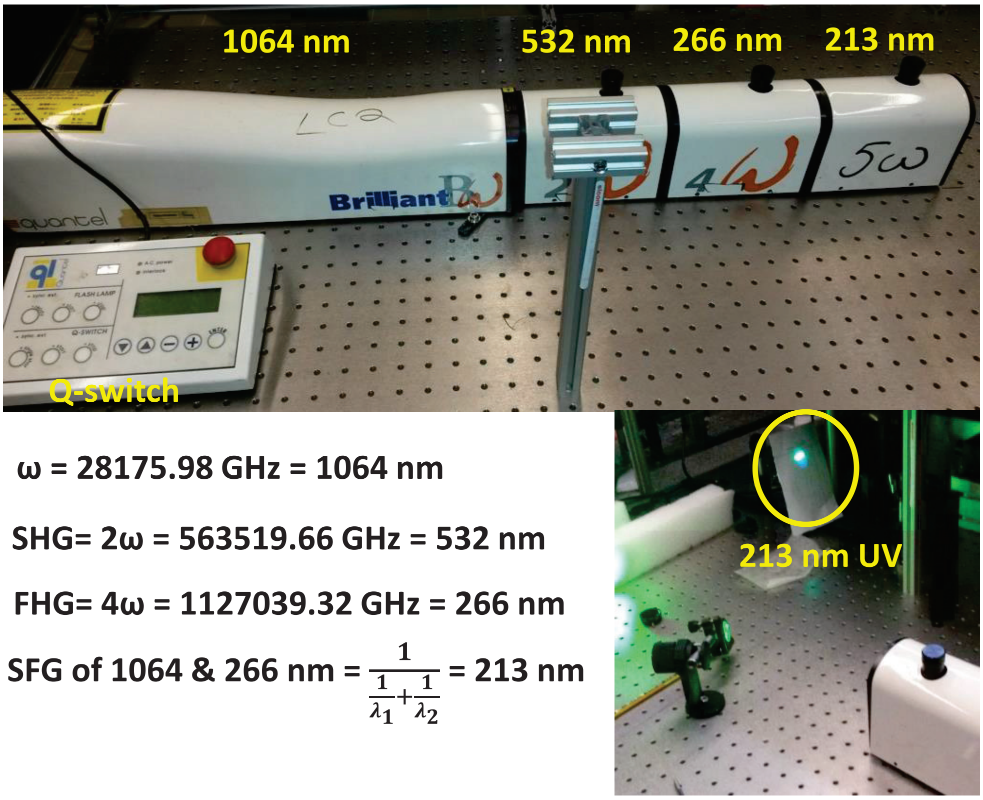

Figure 1.17 5th Harmonic Generation from Nd:YAG Laser

1.3.4 Infrared Multiphoton Dissociation (IRMPD)

1.3.4.1 General Discussion

Infrared Multiphoton dissociation (IRMPD) coupled with mass spectrometer has become a versatile tool for i) structural characterization of different class of molecules including peptide, proteins, carbohydrates and oligonucleotides [140] ii) probing unimolecular dissociation mechanism [141, 142] [143-145], and iii) performing mass-selected infrared spectroscopy [146].

As a structural characterization tool, unlike collision activation dissociation, IR activation is not associated to the trapping voltage, therefore, a low mass cutoff is not required. In addition, IR activation is not linked to collisional scattering or unstable trajectories thus can minimize the side chain and PTMs groups' loss during the photodissociation. Low energy IR photons (multiple) selectively break the most labile amide (C-N) bonds and generate b and y ions similar to the traditional slow-heating collision activation dissociation (CAD) method [147]. IRMPD has been implemented in the different instruments including quadrupole ion trap [148] and dual pressure linear ion trap [149-151]. Vasicek *et al* reported the execution of IRMPD in the HCD (High-energy Collision Dissociation) cell of a modified hybrid linear ion trap-Orbitrap mass spectrometer [152]. Numerous approaches including supercharging [153], linking IR-active ligands [154-157], increasing laser flux [157], elevating bath gas temperature [158], combining collision activation with laser irradiation [159] are employed to improve the IRMPD efficiency; however, the performance is still limited. Moreover, to explore the dissociation mechanism of proteins, oligonucleotides and polymer; continuous-wave CO_2 laser can act as black-body source for trapped ion and can promote unimolecular reaction.

1.3.4.2 Basics of Infrared Multiphoton Dissociation

From a classical point of view, molecular vibration is governed by Hooke's law:

$$F = -k\Delta r \qquad (31)$$

where F is the restoring force, k is the force constant and Δr displacement from equilibrium distance. However, the frequency of vibration (v) is related to the mass (m_A and m_B) and the force constant of the molecular spring between two atoms (A and B), it can be expressed by

$$v = \frac{1}{2\pi}\sqrt{\frac{k}{\frac{m_A\ m_B}{m_A + m_B}}} \qquad (32)$$

In the classical harmonic oscillator, the vibrational energy can be written as

$$E = \frac{1}{2}k\Delta r^2 = hv \qquad (33)$$

However, the vibrational motion is governed by quantum mechanics and only certain transitions are allowed based on the following equation [130]:

$$E\ (\boldsymbol{v}) = \left(\boldsymbol{v} + \frac{1}{2}\right) hv \qquad (34)$$

where v is the frequency of vibration and $\boldsymbol{v}$ is the vibrational quantum number (0, 1, 2…). Based on the selection rule, for allowed vibration the electric dipole moment must be changed or the transition dipole moment μ should be non-zero between two states i and j.

$$\mu = \int \psi_j^* \hat{\mu}\, \psi_i \neq 0 \qquad (35)$$

Here ψ represent the wavefunction of different states and $\hat{\mu}$ is the electric dipole moment operator. When this integral is non-zero, the transition will be allowed and vibrational mode is IR active.

Biomolecules such as peptide, protein and nucleic acids contain a permanent dipole moment and most of the vibrational modes (900-3600 cm^{-1}) are IR active. Some chemical moieties including phosphate, sulfonate, and carbohydrate, respectively are very prone to absorb IR photons. P–O, S–O and C–O groups show intense vibration near the 900-1200 cm^{-1} regions. To be absorbed by a bimolecular ion, IR photons required to be resonated with the fundamental transition ($v_0 \rightarrow v_1$) of a vibrational mode. Nonetheless, other transitions such as $v_1 \rightarrow v_2$ may not be resonant with photon due to anharmonicity which prohibits the dissociation by the so-called ladder-climbing process ($v_0 \rightarrow v_1 \rightarrow v_2$….dissociation) [146]. For this reason, the IR dissociation required multiple photons to surpass the dissociation threshold by several cycles of excitation and relaxation processes. Multiple absorption of low energy photons cause a slow and steady rise of the internal energy by very fast internal vibrational redistribution (IVR). Thus, normal modes couple with the initially absorbing normal modes to exceed the dissociation threshold and thus, induce cleavage of the liable bond (**Figure 1.18**). The dissociation mechanism of CAD, in which increase of internal energy depends on per collision, is similar to the IR photoactivation method [160].

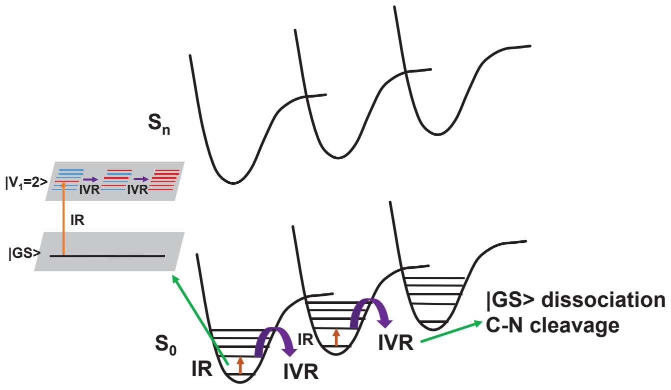

Figure 1.18 Ground state dissociation channel in infrared multiphoton dissociation

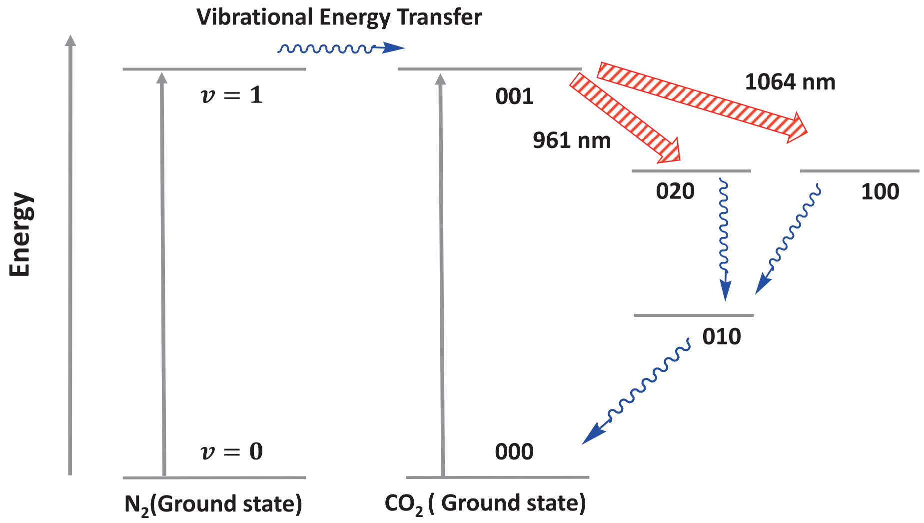

Figure 1.19 Energy diagram of CO_2 laser

1.3.4.3 Light Source for IRMPD

The CO_2 laser is particularly used for IR multiphoton dissociation experiment with mass spectrometry. The ease operation, high continuous power, high efficiency with output range of 900-1100 nm make the CO_2 laser the best candidate for photodissociation experiments. CO_2 is a gas discharge laser which occurred between a cathode and anode in a gas-filled tube [132]. The best operation requires a mixture of CO_2, N_2 and He. Collisions between excited N_2 and ground state CO_2 helps to excite the CO_2 to the first energy level. A CO_2 molecule has three mode of vibration: (i) symmetric stretching [i00], (ii) bending [0j0], and (iii) antisymmetric stretching [00k], where i, j, and k are integers [133] (**Figure 1.19**). Collision with N_2 excites CO_2 to the asymmetric stretching level 001. Lasing at 1064 nm happens from the 001 level (asymmetrical stretching) to the symmetric stretching level 100. Another lasing is also observed at 961 nm from 001 level to 020 level (bending). The relaxation happened from the two lasing states to the ground states (000) *via* an intermediate state (010). The fast relaxation process is observed when it makes collision with helium. This fast relaxation confirms the population inversion for the lasing transitions.

1.4 Presentation of the Thesis

This thesis focuses on method development and applications for characterizing peptide, proteins, post-translational modifications by the two laser light sources such as Nd:YAG (fifth harmonic at 213 nm) and CO_2 with a high resolution Q-Exactive hybrid quadrupole-Orbitrap mass spectrometer. Moreover, CO_2 laser source was also coupled with a charge-detection mass spectrometer to understand the fundamental aspect of unimolecular dissociation mechanism for megadalton polymer cations and anions. Besides laser-MS coupling, this thesis also employs charge-detection mass spectrometry to measure the mass and charge distributions of entire amyloid fibers involved in neurodegenerative diseases focusing on polymorphism mapping and population heterogeneity.

In chapter 2, the implementation of the coupling of 213 nm, 5th harmonic of Nd:YAG laser, with high resolution Q-Exactive mass spectrometer is presented for peptide anion characterization. Characterization of acidic peptides and proteins is challenging due to the deficiency of current mass spectrometry methods. This study showed some interesting and unexpected features for peptide anions fragmentation. We notice that hydrogen-deficient radical anions not only promote the cleavage of the C_α–C bond but also stimulate the breaking of N–C_α and C–N bonds. Site-specific side-chain loss is also detected abundantly irrespective of the nature of the peptide anions. Proline containing peptides exhibit unusual fragment ions similar to previous studies. To understanding such wide-spread fragmentation and hydrogen-deficient fragment ions, quantum calculation employing time-dependent density functional theory (TDDFT) was performed and thus rationalized our findings.

In chapter 3, a new method HiLoPD (high-low photodissociation) for top-down proteomics is developed in which two lasers such as 213 nm UV and 10.6 μm CO_2 are combined with high resolution mass spectrometer. The main theme of this project is to combine two distinctive ion activation channels as coupling of high and low energy activation pathways for whole protein characterization is expected to offer diverse, improved, efficient, and well-balanced fragmentation array. However, combining these two activation pathways with a mass spectrometer is very challenging as the working protocol continuous-wave of low-energy IR and pulse high-energy UV photoactivation is very different. Particularly implementing CO_2 laser with HCD cell has several issues on collision efficiency and vacuum pressure due to the presence of collision gas in the cell. Our results on the high-low energy photodissociation (HiLoPD) method indeed provide diverse fragment ions such as a/x, b/y, b-H_2O/y-H_2O, x+1, y-1, y-2, y-NH_3 ions, with a richness of secondary fragment ions including d, v and w, which can lead to identify the isomeric residues in a protein. In addition, we employed IRMPD, UVPD and HiLoPD methods to probe the secondary structure for elucidating the most flexible and the more rigid regions of ubiquitin in the gas phase.

In chapter 4, a comparative study is reported in which 10.6 μm IRMPD, 213 nm UVPD and HiLoPD methods were used for phospho-, sulfo- and glyco-peptides characterization. Characterizing PTMs in peptides and proteins is one of the most challenging task in structural biology. More efficient and sensitive mass spectrometry based methods are required to address the key issues for the characterizing PTMs. Herein, improvement of the ion activation methods in terms of backbone fragmentation, retention efficacy and detecting site-specific location of PTMs groups was described. Our results indicate that UVPD and HiLoPD can provide excellent fragmentation yield, good functional group retention efficiency and better site-specific information for phospho- and glyco- peptides; however, for sulfo-peptide, these methods remained very sensitive on retaining the SO_3 functional group.

In chapter 5, infrared multiphoton photodissociation coupled to charge-detection mass spectrometry was employed to understand the decay mechanism of an SO_3-containing poly (2-acrylamido-2-methyl-1-propanesulfonic acid) synthetic polymer known as PAMPS (2 MDa) in positive and negative polarities. A gated electrostatic ion trap (“Benner trap”) was used to store and detect single gaseous polymer ions generated by positive and negative polarity in an ESI source. The trapped ions are then vibrationally excited by multiple IR photons produced from a continuous-wave CO_2 laser, fragmenting the polymer ions with varying the laser intensities. We found difference in activation energy values for positive and negative ions. Quantum calculation is also performed to justify this difference.

In chapter 6, charge-detection mass spectrometer has been used to weigh megadalton amyloid fibrils associated to Alzheimer disease. Larger biological assemblies (nucleosomes, ribosome, transcription complex and virus) and aggregates (amyloid fibrils, antibodies, and protein-lipid complex) are very heterogeneous. Measuring their mass and charge distribution by means of traditional mass spectrometry is not feasible due to the lack of resolving power obtaining isotopic resolution of such large analytes at high *m/z*. The charge-detection mass spectrometry, an image current based singe-ion-detection technique, can offer a plausible solution for such assemblies and aggregates of mega-gigadalton masses. For the first time, we are able to weigh the amyloid beta, alpha-syn and tau fibrils detecting their masses of 15-150 megadalton (MDa). In addition, heterogeneity and polymorphism of these fibrils are also explained besides mass and charge measurements by CDMS.

Bibliography

1. Collins, F.S., Lander, E.S., Rogers, J., Waterston, R.H., Int Human Genome Sequencing, C.: Finishing the euchromatic sequence of the human genome. Nature. **431**, 931-945 (2004)
2. Berg, J.M., Tymoczko, J.L., Stryer, L. Biochemistry, W H Freeman, (2002)
3. Crick, F.: On Protein Synthesis. Symp. Soc. Experimen. Biol. **12**, 139-163 (1958)
4. Brenner, S., Jacob, F., Meselson, M.: An Unstable Intermediate Carrying Information from Genes to Ribosomes for Protein Synthesis. Nature. **190**, 576-581 (1961)
5. Cox, J., Mann, M.: Is Proteomics the New Genomics? Cell. **130**, 395-398
6. Altelaar, A.F.M., Munoz, J., Heck, A.J.R.: Next-generation proteomics: towards an integrative view of proteome dynamics. Nat Rev Genet. **14**, 35-48 (2013)
7. Luecke, H., Schobert, B., Richter, H., Cartailler, J., Lanyi, J.K.: Structure of Bacteriorhodopsin at 1.55 A Resolution. J. Mol. Biol. **291**, 899-911 (1999)
8. Arora, A., Abilgaard, F., Bushweller, J.H., Tamm, L.K.: Structure of outer membrane protein A transmembrane domain by NMR spectroscopy. Nat. Struct. Biol. **8**, 334-338 (2001)
9. Frank, J.: Advances in the field of single-particle cryo-electron microscopy over the last decade. Nat. Protocols. **12**, 209-212 (2017)
10. Jensen, O.N.: Interpreting the protein language using proteomics. Nat. Rev. Mol. Cell Biol. **7**, 391-403 (2006)
11. Nørregaard Jensen, O.: Modification-specific proteomics: characterization of post-translational modifications by mass spectrometry. Cur. Opin. Chem. Biol. **8**, 33-41 (2004)
12. Deribe, Y.L., Pawson, T., Dikic, I.: Post-translational modifications in signal integration. Nat. Struct. Mol. Biol. **17**, 666-672 (2010)
13. Heaton, A.L., Armentrout, P.B.: Thermodynamics and Mechanism of the Deamidation of Sodium-Bound Asparagine. J. Am. Chem. Soc. **130**, 10227-10232 (2008)
14. Liu, F., Iqbal, K., Grundke-Iqbal, I., Hart, G.W., Gong, C.-X.: O-GlcNAcylation regulates phosphorylation of tau: A mechanism involved in Alzheimer's disease. Proc. Natl. Acad. Sci. U. S. A. **101**, 10804-10809 (2004)
15. Seo, J., Lee, K.J.: Post-translational modifications and their biological functions: proteomic analysis and systematic approaches. J Biochem Mol Biol. **37**, 35-44 (2004)

16. Cohen, P.: The regulation of protein function by multisite phosphorylation – a 25 year update. Trends Biochem. Sci. **25**, 596-601 (2000)

17. Olsen, J.V., Vermeulen, M., Santamaria, A., Kumar, C., Miller, M.L., Jensen, L.J., Gnad, F., Cox, J., Jensen, T.S., Nigg, E.A., Brunak, S., Mann, M.: Quantitative Phosphoproteomics Reveals Widespread Full Phosphorylation Site Occupancy During Mitosis. Sci. Signal.**3**, ra3 (2010)

18. Kehoe, J.W., Bertozzi, C.R.: Tyrosine sulfation: a modulator of extracellular protein–protein interactions. Chem. Biol. **7**, R57-R61 (2000)

19. Varki, A., Esko, J.D., Colley, K.J. Cellular Organization of Glycosylation, Cold Spring Harbor Laboratory Press, (2009)

20. Lodish, H., Berk, A., Zipursky, S.L., Matsudaira, P., Baltimore, D., Darnell, J. Molecular Cell Biology, W. H. Freeman, (2000)

21. Gould, N., Doulias, P.T., Tenopoulou, M., Raju, K., Ischiropoulos, H.: Regulation of protein function and signaling by reversible cysteine s-nitrosylation. J. Biol. Chem. **288**, 26473-26479 (2013)

22. Choudhary, C., Kumar, C., Gnad, F., Nielsen, M.L., Rehman, M., Walther, T.C., Olsen, J.V., Mann, M.: Lysine Acetylation Targets Protein Complexes and Co-Regulates Major Cellular Functions. Science. **325**, 834-840 (2009)

23. Struhl, K.: Histone acetylation and transcriptional regulatory mechanisms. Genes Dev. **12**, 599-606 (1998)

24. Hoeller, D., Crosetto, N., Blagoev, B., Raiborg, C., Tikkanen, R., Wagner, S., Kowanetz, K., Breitling, R., Mann, M., Stenmark, H., Dikic, I.: Regulation of ubiquitin-binding proteins by monoubiquitination. Nat Cell Biol. **8**, 163-169 (2006)

25. Pickart, C. M., Eddins, M. J.: Ubiquitin: structures, functions, mechanisms Biochim. Biophys. Acta **1695**, 55-72, (2004)

26. Komander, D.: The emerging complexity of protein ubiquitination. Biochem. Soc. Trans. **37**, 937-953 (2009)

27. Hoeller, D., Crosetto, N., Blagoev, B., Raiborg, C., Tikkanen, R., Wagner, S., Kowanetz, K., Breitling, R., Mann, M., Stenmark, H., Dikic, I.: Regulation of ubiquitin-binding proteins by monoubiquitination. Nat. Cell Biol. **8**, 163-169 (2006)

28. Robinson, N.E., Robinson, A.B.: Deamidation of human proteins. Proc. Natl. Acad. Sci. **98**, 12409-12413 (2001)
29. Wilmarth, P.A., Tanner, S., Dasari, S., Nagalla, S.R., Riviere, M.A., Bafna, V., Pevzner, P.A., David, L.L.: Age-Related Changes in Human Crystallins Determined from Comparative Analysis of Post-translational Modifications in Young and Aged Lens: Does Deamidation Contribute to Crystallin Insolubility? J. Proteome Res. **5**, 2554-2566 (2006)
30. Mann, M., Jensen, O.N.: Proteomic analysis of post-translational modifications. Nat. Biotechnol. **21**, 255-261 (2003)
31. Zhao, Y., Jensen, O.N.: Modification-specific proteomics: Strategies for characterization of post-translational modifications using enrichment techniques. Proteomics. **9**, 4632-4641 (2009)
32. Min, D.-H., Mrksich, M.: Peptide arrays: towards routine implementation. Curr. Opin. Chem. Biol. **8**, 554-558 (2004)
33. Baumann, M., Meri, S.: Techniques for studying protein heterogeneity and post-translational modifications. Expert Rev. Proteomics. **1**, 207-217 (2004)
34. Steen, H., Jebanathirajah, J.A., Springer, M., Kirschner, M.W.: Stable isotope-free relative and absolute quantitation of protein phosphorylation stoichiometry by MS. Proc. Natl. Acad. Sci. U. S. A. **102**, 3948-3953 (2005)
35. Mann, M., Jensen, O.N.: Proteomic analysis of post-translational modifications. Nat. Biotechnol. **21**, 255-261 (2003)
36. Petkova, A.T., Leapman, R.D., Guo, Z., Yau, W.-M., Mattson, M.P., Tycko, R.: Self-Propagating, Molecular-Level Polymorphism in Alzheimer's ß-Amyloid Fibrils. Science. **307**, 262-265 (2005)
37. Catherman, A.D., Skinner, O.S., Kelleher, N.L.: Top Down proteomics: Facts and perspectives. Biochem. Biophys. Res. Commun. **445**, 683-693 (2014)
38. Progress in Top-Down Proteomics and the Analysis of Proteoforms. Annual Review of Anal. Chem.. **9**, 499-519 (2016)
39. Paravastu, A.K., Leapman, R.D., Yau, W.-M., Tycko, R.: Molecular structural basis for polymorphism in Alzheimer's β-amyloid fibrils. Proc. Natl. Acad. Sci. **105**, 18349-18354 (2008)

40. Knowles, T.P.J., Vendruscolo, M., Dobson, C.M.: The amyloid state and its association with protein misfolding diseases. Nat. Rev. Mol. Cell Biol. **15**, 384-396 (2014)
41. Koo, E.H., Lansbury, P.T., Kelly, J.W.: Amyloid diseases: Abnormal protein aggregation in neurodegeneration. Proc. Natl. Acad. Sci. **96**, 9989-9990 (1999)
42. Mangialasche, F., Solomon, A., Winblad, B., Mecocci, P., Kivipelto, M.: Alzheimer's disease: clinical trials and drug development. Lancet Neurol. **9**, 702-716 (2016)
43. Qiang, W., Yau, W.-M., Lu, J.-X., Collinge, J., Tycko, R.: Structural variation in amyloid-β fibrils from Alzheimer's disease clinical subtypes. Nature. **541**, 217-221 (2017)
44. Arosio, P., Knowles, T.P.J., Linse, S.: On the lag phase in amyloid fibril formation. Phys. Chem. Chem. Phys. **17**, 7606-7618 (2015)
45. Kodali, R., Wetzel, R.: Polymorphism in the intermediates and products of amyloid assembly. Curr. Opin. Struct. Biol. **17**, 48-57 (2007)
46. Cohen, S.I.A., Linse, S., Luheshi, L.M., Hellstrand, E., White, D.A., Rajah, L., Otzen, D.E., Vendruscolo, M., Dobson, C.M., Knowles, T.P.J.: Proliferation of amyloid-β42 aggregates occurs through a secondary nucleation mechanism. Proc. Natl. Acad. Sci.. **110**, 9758-9763 (2013)
47. Lomakin, A., Chung, D.S., Benedek, G.B., Kirschner, D.A., Teplow, D.B.: On the nucleation and growth of amyloid beta-protein fibrils: detection of nuclei and quantitation of rate constants. Proc. Natl. Acad. Sci. **93**, 1125-1129 (1996)
48. Jeong, J.S., Ansaloni, A., Mezzenga, R., Lashuel, H.A., Dietler, G.: Novel Mechanistic Insight into the Molecular Basis of Amyloid Polymorphism and Secondary Nucleation during Amyloid Formation. J. Mol. Biol. **425**, 1765-1781 (2013)
49. Andersen, C.B., Yagi, H., Manno, M., Martorana, V., Ban, T., Christiansen, G., Otzen, D.E., Goto, Y., Rischel, C.: Branching in Amyloid Fibril Growth. Biophys. J. **96**, 1529-1536
50. Langkilde, A.E., Vestergaard, B.: Methods for structural characterization of prefibrillar intermediates and amyloid fibrils. FEBS Lett. **583**, 2600-2609 (2009)
51. Nilsson, M.R.: Techniques to study amyloid fibril formation in vitro. Methods. **34**, 151-160 (2004)

52. Bouchard, M., Zurdo, J., Nettleton, E.J., Dobson, C.M., Robinson, C.V.: Formation of insulin amyloid fibrils followed by FTIR simultaneously with CD and electron microscopy. Protein Sci. **9**, 1960-1967 (2000)
53. Petkova, A.T., Ishii, Y., Balbach, J.J., Antzutkin, O.N., Leapman, R.D., Delaglio, F., Tycko, R.: A structural model for Alzheimer's β-amyloid fibrils based on experimental constraints from solid state NMR. Proc. Natl. Acad. Sci. **99**, 16742-16747 (2002)
54. Thomson, J.J.: XL. Cathode Rays. Phil. Mag. **44**, 293-316 (1897)
55. Fenn, J.B., Mann, M., Meng, C.K., Wong, S.F., Whitehouse, C.M.: Electrospray Ionization for Mass Spectrometry of Large Biomolecules. Science. **246**, 64-71 (1989)
56. Fenn, J.B.: Electrospray Wings for Molecular Elephants (Nobel Lecture). Angew. Chem. Int. Ed. **42**, 3871-3894 (2003)
57. Tanaka, K., Waki, H., Ido, Y., Akita, S., Yoshida, Y.: Protein and polymer analysis up to m/z 100.000 by laser ionization time-of-flight mass spectrometry. Rapid Commun. Mass Spectrom. **2**, 151-153 (1988)
58. Tanaka, K.: The Origin of Macromolecule Ionization by Laser Irradiation (Nobel Lecture). Angew. Chem. Int. Ed. **42**, 3861-3870 (2003)
59. Van Berkel, G.J., De La Mora, J.F., Enke, C.G., Cole, R.B., Martinez-Sanchez, M., Fenn, J.B.: Electrochemical processes in electrospray ionization mass spectrometry. J. Mass Spectrom. **35**, 939-952 (2000)
60. Wu, X., Oleschuk, R.D., Cann, N.M.: Characterization of microstructured fibre emitters: in pursuit of improved nano electrospray ionization performance. Analyst. **137**, 4150-4161 (2012)
61. Konermann, L., Ahadi, E., Rodriguez, A.D., Vahidi, S.: Unraveling the Mechanism of Electrospray Ionization. Anal. Chem. **85**, 2-9 (2013)
62. Fenn, J.B., Mann, M., Meng, C.K., Wong, S.F., Whitehouse, C.M.: Electrospray ionization-principles and practice. Mass Spectrom Rev. **9**, 37-70 (1990)
63. Wilm, M.: Principles of Electrospray Ionization. Mol. Cell. Proteomics. **10**, 94071-94078 (2011)
64. Banerjee, S.; Mazumdar, S.:Electrospray Ionization Mass Spectrometry: A Technique to Access the Information beyond the Molecular Weight of the Analyte, Int. J. Anal. Chem. Article ID 282574 (2012)

65. March, R.E.: An Introduction to Quadrupole Ion Trap Mass Spectrometry. J. Mass Spectrom. **32**, 351-369 (1997)
66. March, R.E.: Quadrupole ion traps. Mass Spectrom. Rev. **28**, 961-989 (2009)
67. Du, Z., Douglas, D.J.: A novel tandem quadrupole mass analyzer. J. Am. Soc. Mass Spectrom. **10**, 1053-1066 (1999)
68. Olsen, J.V., Macek, B., Lange, O., Makarov, A., Horning, S., Mann, M.: Higher-energy C-trap dissociation for peptide modification analysis. Nat Meth. **4**, 709-712 (2007)
69. Mann, M., Jensen, O.N.: Proteomic analysis of post-translational modifications. Nat Biotech. **21**, 255-261 (2003)
70. Zubarev, R.a., Makarov, A.: Orbitrap mass spectrometry. Anal. Chem. **85**, 5288-5296 (2013)
71. Makarov, A.: Electrostatic Axially Harmonic Orbital Trapping: A High-Performance Technique of Mass Analysis. Anal. Chem. **72**, 1156-1162 (2000)
72. Hardman, M., Makarov, A.: Interfacing the Orbitrap Mass Analyzer to an Electrospray Ion Source. Anal. Chem. **75**, 1699-1705 (2003)
73. Shelton, H., Jr., C.D.H., Wuerker, R.F.: Electrostatic Acceleration of Microparticles to Hypervelocities. J. Appl. Phys. **31**, 1243-1246 (1960)
74. Walsh, J.M., Stradling, G.L., Idzorek, G.C., Shafer, B.P., Wx, D.O., Curling, H.L.: Microparticle impacts at ultra-high velocities: Their relation to macroparticle impacts. Int. J. Impact Eng. **14**, 775-784 (1993)
75. Fuerstenau, S.D., Benner, W.H.: Molecular weight determination of megadalton DNA electrospray ions using charge detection time-of-flight mass spectrometry. Rapid Commun. Mass Spectrom. **9**, 1528-1538 (1995)
76. Pandey, A., Mann, M.: Proteomics to study genes and genomes. Nature. **405**, 837-846 (2000)
77. Masselon, C., Anderson, G.A., Harkewicz, R., Bruce, J.E., Pasa-Tolic, L., Smith, R.D.: Accurate mass multiplexed tandem mass spectrometry for high-throughput polypeptide identification from mixtures. Anal. Chem. **72**, 1918-1924 (2000)
78. McCormack, A.L., Schieltz, D.M., Goode, B., Yang, S., Barnes, G., Drubin, D., Yates, J.R.: Direct analysis and identification of proteins in mixtures by LC/MS/MS and database searching at the low-femtomole level. Anal. Chem.. **69**, 767-776 (1997)

79. Steen, H., Mann, M.: The ABC's (and XYZ's) of peptide sequencing. Nat Rev Mol Cell Biol. **5**, 699-711 (2004)
80. Chait, B.T.: Mass spectrometry: Bottom-up or top-down? Science. **314**, 65-66 (2006)
81. Cui, W.D., Rohrs, H.W., Gross, M.L.: Top-down mass spectrometry: Recent developments, applications and perspectives. Analyst. **136**, 3854-3864 (2011)
82. Lanucara, F., Eyers, C.E.: Top-down mass spectrometry for the analysis of combinatorial post-translational modifications. Mass Spectrom. Rev. **32**, 27-42 (2013)
83. Han, X., Jin, M., Breuker, K., McLafferty, F.W.: Extending Top-Down Mass Spectrometry to Proteins with Masses Greater Than 200 Kilodaltons. Science. **314**, 109-112 (2006)
84. McLuckey, S.A.: Principles of collisional activation in analytical mass spectrometry. J. Am. Soc Mass Spectrom. **3**, 599-614 (1992)
85. Sleno, L., Volmer, D.A.: Ion activation methods for tandem mass spectrometry. J Mass Spectrom. **39**, 1091-1112 (2004)
86. Hayes, R.N., Gross, M.L.: [10] Collision-induced dissociation. Methods Enzymol. **193**, 237-263 (1990)
87. Crowe, M.C., Brodbelt, J.S.: Infrared multiphoton dissociation (IRMPD) and collisionally activated dissociationof peptides in a quadrupole ion trapwith selective IRMPD of phosphopeptides. J. Am. Soc Mass Spectrom.**15**, 1581-1592 (2004)
88. Payne, A.H., Glish, G.L.: Thermally assisted infrared multiphoton photodissociation in a quadrupole ion trap. Anal. Chem. **73**, 3542-3548 (2001)
89. Charles, M.J., McLuckey, S.A., Glish, G.L.: Competition between resonance ejection and ion dissociation during resonant excitation in a quadrupole ion trap. J. Am. Soc. Mass Spectrom. **5**, 1031-1041 (1994)
90. Olsen, J.V.a.M.B.a.L.O.a.M.A.a.H.S.a.M.M.: Higher-energy C-trap dissociation for peptide modification analysis. Nature methods. **4**, 709-712 (2007)
91. Zubarev, R.A., Kelleher, N.L., McLafferty, F.W.: Electron capture dissociation of multiply charged protein cations. A nonergodic process. J Am. Chem. Soc. **120**, 3265-3266 (1998)
92. Syka, J.E.P., Coon, J.J., Schroeder, M.J., Shabanowitz, J., Hunt, D.F.: Peptide and protein sequence analysis by electron transfer dissociation mass spectrometry. Proc. Natl Acad Sci.USA. **101**, 9528-9533 (2004)

93. Zhurov, K.O., Fornelli, L., Wodrich, M.D., Laskay, U.A., Tsybin, Y.O.: Principles of electron capture and transfer dissociation mass spectrometry applied to peptide and protein structure analysis. Chem Soc. Rev. **42**, 5014-5030 (2013)
94. Wiesner, J., Premsler, T., Sickmann, A.: Application of electron transfer dissociation (ETD) for the analysis of posttranslational modifications. Proteomics. **8**, 4466-4483 (2008)
95. Zhurov, K.O., Fornelli, L., Wodrich, M.D., Laskay, U.A., Tsybin, Y.O.: Principles of electron capture and transfer dissociation mass spectrometry applied to peptide and protein structure analysis. Chem. Soc. Rev. **42**, 5014-5030 (2013)
96. Stensballe, A., Jensen, O.N., Olsen, J.V., Haselmann, K.F., Zubarev, R.A.: Electron capture dissociation of singly and multiply phosphorylated peptides. Rapid Comm. Mass Spectrom. **14**, 1793-1800 (2000)
97. Shi, S.D.H., Hemling, M.E., Carr, S.A., Horn, D.M., Lindh, I., McLafferty, F.W.: Phosphopeptide/Phosphoprotein Mapping by Electron Capture Dissociation Mass Spectrometry. Anal. Chem.. **73**, 19-22 (2000)
98. Mirgorodskaya, E., Roepstorff, P., Zubarev, R.A.: Localization of O-Glycosylation Sites in Peptides by Electron Capture Dissociation in a Fourier Transform Mass Spectrometer. Anal. Chem. **71**, 4431-4436 (1999)
99. Håkansson, K., Cooper, H.J., Emmett, M.R., Costello, C.E., Marshall, A.G., Nilsson, C.L.: Electron Capture Dissociation and Infrared Multiphoton Dissociation MS/MS of an N-Glycosylated Tryptic Peptide To Yield Complementary Sequence Information. Anal. Chem. **73**, 4530-4536 (2001)
100. Kelleher, N.L., Zubarev, R.A., Bush, K., Furie, B., Furie, B.C., McLafferty, F.W., Walsh, C.T.: Localization of Labile Posttranslational Modifications by Electron Capture Dissociation: The Case of γ-Carboxyglutamic Acid. Anal. Chemi. **71**, 4250-4253 (1999)
101. Baba, T., Hashimoto, Y., Hasegawa, H., Hirabayashi, A., Waki, I.: Electron Capture Dissociation in a Radio Frequency Ion Trap. Anal. Chem. **76**, 4263-4266 (2004)
102. McAlister, G.C., Berggren, W.T., Griep-Raming, J., Horning, S., Makarov, A., Phanstiel, D., Stafford, G., Swaney, D.L., Syka, J.E.P., Zabrouskov, V., Coon, J.J.: A Proteomics Grade Electron Transfer Dissociation-Enabled Hybrid Linear Ion Trap-Orbitrap Mass Spectrometer. J. Proteome Res. **7**, 3127-3136 (2008)

103. Udeshi, N.D., Shabanowitz, J., Hunt, D.F., Rose, K.L.: Analysis of proteins and peptides on a chromatographic timescale by electron-transfer dissociation MS. Febs Journal. **274**, 6269-6276 (2007)
104. Udeshi, N.D., Compton, P.D., Shabanowitz, J., Hunt, D.F., Rose, K.L.: Methods for analyzing peptides and proteins on a chromatographic timescale by electron-transfer dissociation mass spectrometry. Nat. Protoc. **3**, 1709-1717 (2008)
105. Zhurov, K.O., Fornelli, L., Wodrich, M.D., Laskay, U.A., Tsybin, Y.O.: Principles of electron capture and transfer dissociation mass spectrometry applied to peptide and protein structure analysis. Chem. Soc. Rev. **42**, 5014-5030 (2013)
106. McLuckey, S.A.: Principles of collisional activation in analytical mass spectrometry. J, Am. Soc. Mass Spectrom. **3**, 599-614 (1992)
107. Mitchell Wells, J., McLuckey, S.A.: Collision- Induced Dissociation (CID) of Peptides and Proteins. In: Burlingame AL (ed.). Academic Press, (2005)
108. Zubarev, R.A., Kelleher, N.L., McLafferty, F.W.: Electron capture dissociation of multiply charged protein cations. A nonergodic process. J. Am. Chem. Soc. **120**, 3265-3266 (1998)
109. Syka, J.E.P., Coon, J.J., Schroeder, M.J., Shabanowitz, J., Hunt, D.F.: Peptide and protein sequence analysis by electron transfer dissociation mass spectrometry. Proc Natl Acad Sci USA. **101**, 9528-9533 (2004)
110. Brodbelt, J.S.: Shedding Light on the Frontier of Photodissociation. J. Am. Chem. Soc. **22**, 197-206 (2011)
111. Brodbelt, J.S.: Photodissociation mass spectrometry: new tools for characterization of biological molecules. Chem. Soc. Rev. **43**, 2757-2783 (2014)
112. Antoine, R., Lemoine, J., Dugourd, P.: Electron Photodetachment Dissociation For Structural Characterization Of Synthetic And Bio-Polymer Anions. Mass Spectrom. Rev. **33**, 501-522 (2014)
113. Vasicek, L.A., Ledvina, A.R., Shaw, J., Griep-Raming, J., Westphall, M.S., Coon, J.J., Brodbelt, J.S.: Implementing Photodissociation in an Orbitrap Mass Spectrometer. J. Am. Soc. Mass Spectrom. **22**, 1105-1108 (2011)
114. Vasicek, L., Brodbelt, J.S.: Enhancement of Ultraviolet Photodissociation Efficiencies through Attachment of Aromatic Chromophores. Anal. Chem. **82**, 9441-9446 (2010)

115. Smith, S.I., Brodbelt, J.S.: Characterization of Oligodeoxynucleotides and Modifications by 193 nm Photodissociation and Electron Photodetachment Dissociation. Anal. Chem. **82**, 7218-7226 (2010)

116. Robinson, M.R., Madsen, J.A., Brodbelt, J.S.: 193 nm Ultraviolet Photodissociation of Imidazolinylated Lys-N Peptides for De Novo Sequencing. Anal. Chem. **84**, 2433-2439 (2012)

117. Reilly, J.P.: Ultraviolet photofragmentation of biomolecular ions. Mass Spectrom. Rev. **28**, 425-447 (2009)

118. Reilly, J.P.: Ultraviolet photofragmentation of biomolecular ions. Mass Spectrom Rev. **28**, 425-447 (2009)

119. Tabarin, T., Antoine, R., Broyer, M., Dugourd, P.: Specific photodissociation of peptides with multi-stage mass spectrometry. Rapid Comm. Mass Spectrom. **19**, 2883-2892 (2005)

120. Girod, M., Zeljka, S., Marin, V., Rodolphe, A., Luke, M., J., L., Bonacic-Koutecky, V., Philippe, D.: UV Photodissociation of Proline-containing Peptide Ions: Insights from Molecular Dynamics. J. Am. Soc. Mass Spectrom. **26**, 432--443 (2014)

121. Thompson, M.S., Weidong, C., P., R.J.: Fragmentation of singly charged peptide ions by photodissociation at lamda = 157 nm. Angew. Chem. Int. Ed. **43**, 4791--4794 (2004)

122. Cui, W., Thompson, M.S., Reilly, J.P.: Pathways of peptide ion fragmentation induced by vacuum ultraviolet light. J. Am. Soc. Mass Spectrom. **16**, 1384--1398 (2005)

123. Zhang, L., Cui, W., Thompson, M.S., Reilly, J.P.: Structures of α-Type Ions Formed in the 157 nm Photodissociation of Singly-Charged Peptide Ions. J. Am. Soc. Mass Spectrom. **17**, 1315-1321 (2006)

124. Kim, T.-Y., Reilly, J.P.: Time-Resolved Observation of Product Ions Generated by 157 nm Photodissociation of Singly Protonated Phosphopeptides. J. Am. Soc. Mass Spectrom. **20**, 2334-2341 (2009)

125. Zubarev, R.A., Horn, D.M., Fridriksson, E.K., Kelleher, N.L., Kruger, N.A., Lewis, M.A., Carpenter, B.K., McLafferty, F.W.: Electron Capture Dissociation for Structural Characterization of Multiply Charged Protein Cations. Anal. Chem. **72**, 563-573 (2000)

126. O'Connor, P.B., Lin, C., Cournoyer, J.J., Pittman, J.L., Belyayev, M., Budnik, B.A.: Long-Lived Electron Capture Dissociation Product Ions Experience Radical Migration via Hydrogen Abstraction. J. Am. Soc. Mass Spectrom. **17**, 576-585 (2006)

127. Shaw, J.B., Li, W.Z., Holden, D.D., Zhang, Y., Griep-Raming, J., Fellers, R.T., Early, B.P., Thomas, P.M., Kelleher, N.L., Brodbelt, J.S.: Complete Protein Characterization Using Top-Down Mass Spectrometry and Ultraviolet Photodissociation. J. Am. Chem. Soc. **135**, 12646-12651 (2013)
128. Cannon, J.R., Carnmarata, M.B., Robotham, S.A., Cotham, V.C., Shaw, J.B., Fellers, R.T., Early, B.P., Thomas, P.M., Kelleher, N.L., Brodbelt, J.S.: Ultraviolet Photodissociation for Characterization of Whole Proteins on a Chromatographic Time Scale. Anal. Chem. **86**, 2185-2192 (2014)
129. Madsen, J., Cheng, R.R., Kaoud, T.S., Dalby, K.N., Makarov, D.E., Brodbelt, J.S.: Charge-site-dependent dissociation of hydrogen-rich radical peptide cations upon vacuum UV photoexcitation. Chem. Eur. J. **18**, 5374--5383 (2012)
130. Stedwell, C.N.P., Nicolas C. Infrared Photodissociation of Biomolecualr Ion, Nicolas, C. Dugourd, P. eds. Springer, Heidelberg, London, New York (2013)
131. Mino, W.K., Gulyuz, K., Wang, D., Stedwell, C.N., Polfer, N.C.: Gas-Phase Structure and Dissociation Chemistry of Protonated Tryptophan Elucidated by Infrared Multiple-Photon Dissociation Spectroscopy. J. Phys. Chem. Lett. **2**, 299-304 (2011)
132. Shimoda, K. Introduction to laser physics Springer Berlin (2013)
133. Singh, S.C., Zeng, H., Guo, C., Cai, W.: Lasers: Fundamentals, Types, and Operations. Wiley-VCH Verlag GmbH & Co. KGaA, (2012)
134. Degnan, J.J.: Optimization of passively Q-switched lasers. IEEE J. Quan. Electron. **31**, 1890-1901 (1995)
135. Yap, Y.K., Inagaki, M., Nakajima, S., Mori, Y., Sasaki, T.: High-power fourth- and fifth-harmonic generation of a Nd:YAG laser by means of a CsLiB6O10. Opt. Lett. **21**, 1348-1350 (1996)
136. Lien-Bee, C., Wang, S.C., Kung, A.H.: Numerical Analysis of Fifth-Harmonic Conversion of Low-Power Pulsed Nd:YAG Laser with Resonance of Second Harmonic. Jpn. J. App. Phys. **42**, 4318 (2003)
137. Franken, P.A., Hill, A.E., Peters, C.W., Weinreich, G.: Generation of Optical Harmonics. Phys. Rev. Lett. **7**, 118-119 (1961)
138. New nonlinear optical crystal: Cesium lithium borate. App. Phys. Lett. **67**, 1818-1820 (1995)

139. Wang, L., Men, Y.: Comparison study of CsLiB6O10 and β-BaB2O4 as nonlinear media for optical parametric oscillators. App. Opt. **42**, 2720-2723 (2003)

140. Brodbelt, J.S., Wilson, J.J.: Infrared multiphoton dissociation in quadrupole ion traps. Mass Spectrom. Rev. **28**, 390-424 (2009)

141. Dunbar, R.C.: Infrared Radiative Cooling of Gas-Phase Ions. Mass Spectrom. Rev. **11**, 309-339 (1992)

142. Dunbar, R.C., McMahon, T.B.: Activation of Unimolecular Reactions by Ambient Blackbody Radiation. Science. **279**, 194-197 (1998)

143. Schnier, P.D., Klassen, J.S., Strittmatter, E.F., Williams, E.R.: Activation Energies for Dissociation of Double Strand Oligonucleotide Anions: Evidence for Watson-Crick Base Pairing in Vacuo. J. Am. Chem. Soc. **120**, 9605-9613 (1998)

144. Strittmatter, E., Schnier, P., Klassen, J., Williams, E.: Dissociation energies of deoxyribose nucleotide dimer anions measured using blackbody infrared radiative dissociation. J. Am. Soc. Mass Spectrom. **10**, 1095-1104 (1999)

145. Freitas, M.A., Hendrickson, C.L., Marshall, A.G.: Determination of Relative Ordering of Activation Energies for Gas-Phase Ion Unimolecular Dissociation by Infrared Radiation for Gaseous Multiphoton Energy Transfer. J. Am. Chem. Soc. **122**, 7768-7775 (2000)

146. Polfer, N.C.: Infrared multiple photon dissociation spectroscopy of trapped ions. Chem. Soc. Rev. **40**, 2211-2221 (2011)

147. McLuckey, S.A.: Principles of collisional activation in analytical mass spectrometry. J. Am. Soc. Mass Spctrom. **3**, 599-614 (1992)

148. Crowe, M.C., Brodbelt, J.S.: Infrared multiphoton dissociation (IRMPD) and collisionally activated dissociation of peptides in a quadrupole ion trap with selective IRMPD of phosphopeptides. J. Am. Chem. Soc. **15**, 1581-1592 (2004)

149. McAlister, G.C., Russell, J.D., Rumachik, N.G., Hebert, A.S., Syka, J.E.P., Geer, L.Y., Westphall, M.S., Pagliarini, D.J., Coon, J.J.: Analysis of the Acidic Proteome with Negative Electron-Transfer Dissociation Mass Spectrometry. Anal. Chem. **84**, 2875-2882 (2012)

150. Gardner, M.W., Smith, S.I., Ledvina, A.R., Madsen, J.A., Coon, J.J., Schwartz, J.C., Stafford Jr., G.C., Brodbelt, J.S.: Infrared multiphoton dissociation of peptide cations in a dual pressure linear ion trap mass spectrometer. Anal. Chem. **81**, 8109-8118 (2009)

151. Madsen, J., Brodbelt, J.: Comparison of infrared multiphoton dissociation and collision-induced dissociation of supercharged peptides in ion traps. J. Am. Soc. Mass Spctrom. **20**, 349-358 (2009)
152. Vasicek, L.A., Ledvina, A.R., Shaw, J., Griep-Raming, J., Westphall, M.S., Coon, J.J., Brodbelt, J.S.: Implementing Photodissociation in an Orbitrap Mass Spectrometer. J. Am. Soc. Mass Spctrom. **22**, 1105-1108 (2011)
153. Madsen, J.A., Gardner, M.W., Smith, S.I., Ledvina, A.R., Coon, J.J., Schwartz, J.C., Stafford, G.C., Brodbelt, J.S.: Top-Down Protein Fragmentation by Infrared Multiphoton Dissociation in a Dual Pressure Linear Ion Trap. Anal. Chem. **81**, 8677-8686 (2009)
154. Pikulski, M., Wilson, J.J., Aguilar, A., Brodbelt, J.S.: Amplification of Infrared Multiphoton Dissociation Efficiency in a Quadruple Ion Trap Using IR-Active Ligands. Anal. Chem. **78**, 8512-8517 (2006)
155. Vasicek, L., Wilson, J., Brodbelt, J.: Improved infrared multiphoton dissociation of peptides through N-terminal phosphonite derivatization. J. Am. Soc. Mass Spctrom. **20**, 377-384 (2009)
156. Gardner, M.W., Vasicek, L.A., Shabbir, S., Anslyn, E.V., Brodbelt, J.S.: Chromogenic Cross-Linker for the Characterization of Protein Structure by Infrared Multiphoton Dissociation Mass Spectrometry. Anal. Chem. **80**, 4807-4819 (2008)
157. Newsome, G.A., Glish, G.: Improving IRMPD in a quadrupole ion trap. J. Am. Soc. Mass Spctrom. **20**, 1127-1131 (2009)
158. Payne, A.H., Glish, G.L.: Thermally assisted infrared multiphoton photodissociation in a quadrupole ion trap. Anal. Chem. **73**, 3542-3548 (2001)
159. Hashimoto, Y., Hasegawa, H., Yoshinari, K., Waki, I.: Collision-Activated Infrared Multiphoton Dissociation in a Quadrupole Ion Trap Mass Spectrometer. Anal. Chem. **75**, 420-425 (2003)
160. Brodbelt, J.S.: Photodissociation mass spectrometry: new tools for characterization of biological molecules. Chem. Soc. Rev. **43**, 2757-2783 (2014)

Chapter Two:

Photodissociation of Peptide Anions

"Nor is the shadow equal with the sun's full heat;"

– 35:21

2.1 Introduction

Ultraviolet photodissociation (UVPD) methods, alternative to collision[1–3] and electron [4, 5] based techniques, have emerged as new powerful approaches for characterizing peptides, polysaccharides and proteins[6–12] as we have mentioned details in **chapter 1**. Here we have employed 213 nm UVPD for characterizing peptide anion. It is assumed that around 50% of naturally occurring peptides are acidic and prone to yield negative ions which are difficult to analyze with other means. However, most of the photon and electron based dissociation experiments were conducted on peptide and protein cations and very few were directed on negative polarity. Kjeldsen *et al* reported C_{α}–C backbone fragmentation by EDD (electron detachment dissociation) for peptide and observed more C-terminal species (x ions) than N–terminal fragments ($a^{\bullet}$ ions) [13]. Comparison of negative electron transfer dissociation (NETD) and UVPD for peptide anion disclosed that NETD usually produce simple set of a/x ions[14]. In NETD, along with a/x ions various neutral losses are observed from entire or partial side-chain cleavage of amino acids [15]. Activated ion negative electron transfer dissociation (AI-NETD) of doubly charged peptide ions also generates some hydrogen loss from a and x fragment ions [16].

Some previous electron photo-detachment dissociation (EPD) studies were performed with UV lasers on peptides and small proteins in negative polarity [17, 18]. Antoine *et al* investigated the electron photo-detachment dissociation of peptides using 262 nm with a linear ion trap [19]. Formation of $[M\text{-}2H]^{-\bullet}$ radical anion from the precursor ion was documented in this experiment. a/x and c/z fragment ions were observed. Comparative studies between EDD and EPD revealed significantly different fragment ion distributions in which EPD fragment ions are typically produced from tryptophan and histidine resides whereas in EDD backbone dissociation are favored. However, EDD on small proteins including ubiquitin and melittin suggests that basic resides may promote the formation of a/x fragment ions [20].

Radical containing peptides promote characteristic fragmentation pattern in mass spectrometry [21, 22]. Radical peptides are classified into two categories: hydrogen-deficient and hydrogen-rich radicals [23]. The former type is typically formed in UVPD, EDD and NETD routes whereas the later one is generated from ECD/ETD [8, 13, 24, 25]. Recently, formation of hydrogen-deficient species from the hydrogen-rich radical cation in ECD received great attention due to extensive fragmentation and wide-spread side-chain loss [22, 26]. Radical migration in hydrogen-deficient peptide radical promotes extensive neutral loss and allows remote backbone dissociation [27].

Here, we present the implementation of 213 nm UVPD in a Thermo Scientific Q Exactive hybrid quadrupole-Orbitrap mass spectrometer in negative polarity for peptide anions. We observed distinctive C_α–C, N–C_α and C–N backbone fragmentations from the hydrogen-deficient radical anions. Radical-driven extensive neutral loss is likewise evident in these experiments. Moreover, series of hydrogen-deficient and hydrogen-rich fragments are observed.

2.2 Material and Methods

2.2.1 Coupling UV laser with Mass Spectrometer

The hybrid quadrupole-Orbitrap Q-Exactive® mass spectrometer was modified to permit the laser irradiation to High Energy Collision Dissociation (HCD) cell. The generated fifth harmonic 213 nm laser beam (harmonic generation is described in **chapter 1**) passes through two dichroic mirrors, lenses, optical mirrors and then is introduced in the HCD cell (**Scheme 2.1**). As Nd:YAG and other similar lasers have multiple closely spaced emission wavelengths, dichroic filters are required to obtain the high purity of 213 nm light. A UV grade fused-silica window with wavelength range of 0.185–2.1 μm (provide increased transmission into the UV region) was fitted on the back of the HCD cell to allow irradiation of a laser beam. The laser beam energy irradiating the ions was ~1 mJ/ pulse. The laser was slightly off axis so as to avoid photofragmentation in the C-trap.

2.2 Photodissociation Mass Spectrometry

UVPD experiments were performed with hybrid quadrupole-Orbitrap Q-Exactive® mass spectrometer (Thermo Fisher Scientific, San Jose, CA, USA) equipped with a HESI ion source. Three small peptides YTIAALLSPYS, DYKDDDDK and RGDSPASSKP, which can produce

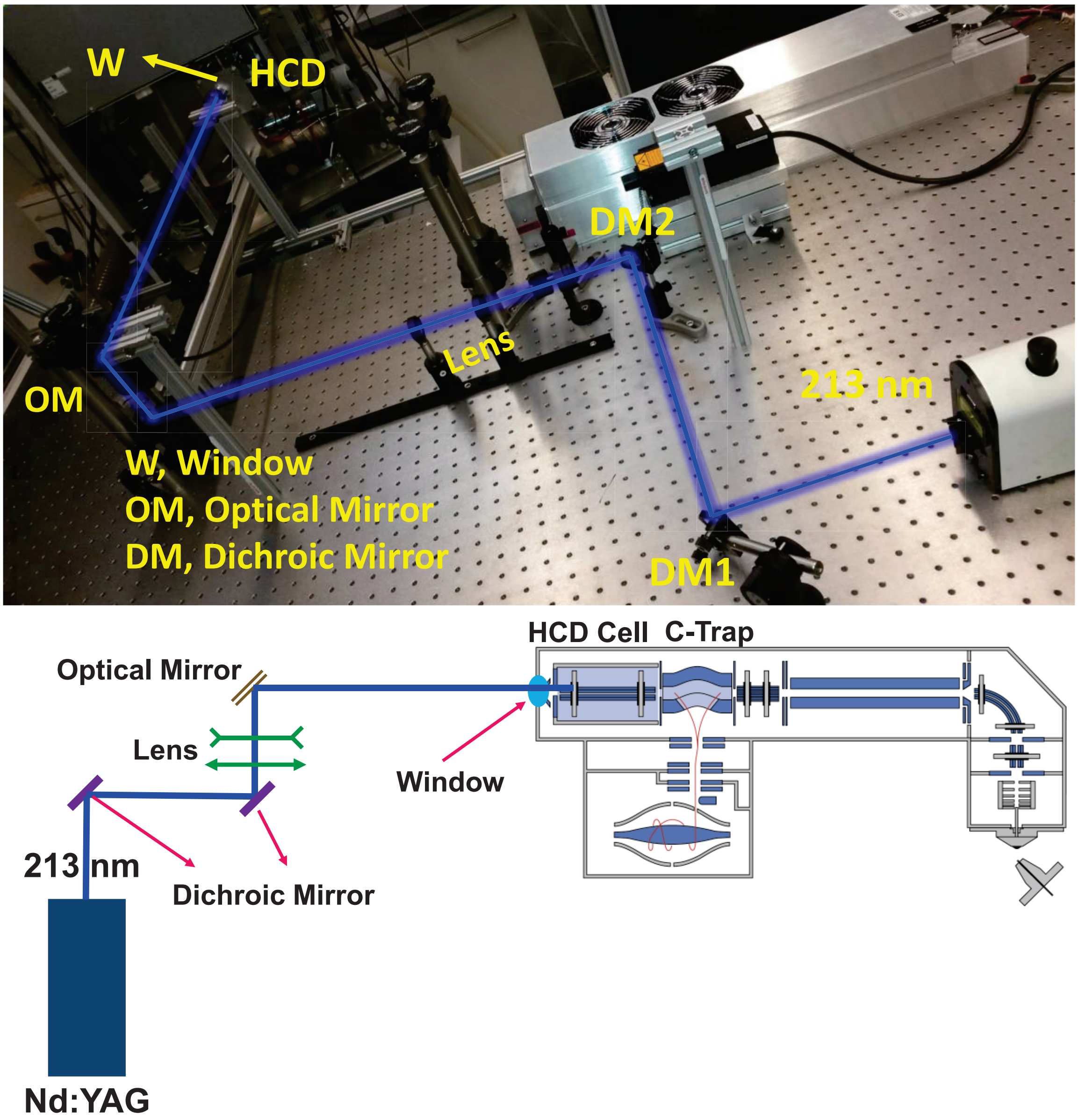

Scheme 2.1 Schematic representation of the execution of UVPD in the HCD cell of a hybrid quadrupole-Orbitrap mass spectrometer.

negative ions, were used without any further purification. Peptides samples were prepared at 1 μM concentration in 50/49/1 (v/v/v) acetonitrile/water/ammonium hydroxide and directly infused to MS at a flow rate of 5 µL/min. All spectra were acquired using a mass range of 100-1500 *m/z* and resolving power of 140000 at *m/z* 400 in negative polarity. Spray voltage, capillary temperature, and sheath gas flow rate were set to 3.5-4.0 kV and 250-320 ˚C, and 5-10, respectively. Experiments were performed on the different charge states such as -3, -2, and -1 of the precursor ions, all of these charge states produces nearly similar fragment ions. However, herein we only presented the fragmentation pattern of the doubly deprotonated precursor ions. The AGC (Automatic Gain Control) target for MS/MS was set to 1x10^6 and the maximum injection time was set at 250 ms. The isolation width was 2 Th. When required, the identification of fragment ions was confirmed by fragmentation of a single isotope (selection width 0.4 Th). The HCD collision energy was set to the minimum 2 eV in order to avoid collisions and provide photofragmentation spectra free of CID contamination. Different HCD (High Collision Dissociation) trapping times including 100, 500, 1000 and 2000 ms (2, 10, 20, 40 laser shots, respectively) were considered. All experiments were performed on 5 microscans mode with averaging 200 scans.

Manual analysis of UVPD data was performed with the aid of ChemCalc software [28]. Peak lists of three peptides were generated for all six major UVPD ion types (a, b, c, x, y, and z) including hydrogen-rich and -deficient radical ions. Fragments mass tolerance was set to 20 ppm.

2.2.3 Computation

All calculations were conducted with the Gaussian 09 software package [29]. Optimization and subsequent vibrational frequency calculation on the model amide system [$CH_3CONHCH_3$] were performed using density functional theory employing Becker's (B3) [30] exchange functional combining Lee, Yang, and Parr's (LYP) [31] correlation functional. Gaussian basis set 6-311+G (2d,p) was considered. Natural bond orbitals (NBO) [32, 33] calculations were computed at the same level of theory. For calculating the excited state properties, time-dependent density functional theory (TDDFT) [46] was employed with the B3LYP/6-311+G(2d,p) level of theory in gas phase. For TDDFT calculation, 20 excited states were considered.

2.3 Result and Discussion

2.3.1 The Photodissociation of Peptide 1 (YTIAALLSPYS)

The photodissociation spectrum of the doubly-deprotonated $[M-2H]^{2-}$ (*m/z* 597.8057) of this peptide is presented in **Figure 2.1A**. Exact masses and assignments of fragment ions of this peptide are summarized in **Table A2.1** (see in appendix). Similar to previous studies, the characteristic $[M-2H]^{-\bullet}$ charge-reduced radical species is detected at *m/z* 1195.6094 Da. This radical species is typically generated from photo-induced electron detachment from the selected peptide precursor. The photo-induced electron detachment event is assumed to be the main fragment channel for peptide dianion. Intense neutral losses are detected from this radical species (**Table A2.2 in appendix** and **Figure 2.2)**. Similar neutral losses are also demonstrated in previous studies [19, 20, 34–36]. The CH_3 radical (15.0242 Da) loss appears at *m/z* 1180.5852 from the side-chain of Ala [37]. Neutral loss of CO (27.9947 Da) and CH_3CH_2 (28.9995 Da) are noticed at *m/z* 1167.6147 and 1166.6099 Da, respectively. Removal of CH_3CH_2 can be used to distinguish the side chain loss of Ile (28.9995 Da) or Leu (43.0542 Da) [38]. Loss of CH_2O (30.0100 Da) and CH_2OH (31.0178 Da) are also observed from the side chain of Ser. NETD study on serine (Ser) containing peptide witnessed the loss of CH_2O when Ser is not phosphorylated [15]. The peak at *m/z* 1151.5829 can be assigned to the loss of C_2H_4O (44.0265 Da) from Thr side-chain [15, 37]. The sequential loss (61.9998 Da) of CO_2 and H_2O is also identified at *m/z* 1133.6099. Radical elimination of a C_3H_8ON from the Thr residue may lead to the fragment ion detected at *m/z* 1121.5759. Loss of tyrosylate groups from the side chain of Tyr (107.0472 and 106.0406 Da) is identified at *m/z* 1088.5622 and 1089.5688 Da, respectively. The phenoxy group of the tyrosylate produces an oxygen radical, which induces the cleavage of C_α-C_β side-chain of the tyrosine residue and promotes the formation of $O{=}C_6H_4{=}CH_2$ (exact mass 106.0413 Da) ion [8, 37, 39]. Two relatively weak peaks at *m/z* 1139.5855 and 1123.5910 can be assigned for the side-chain and related ion loss (56.0239 and 72.0184 Da) from Leu or Ile [15, 38–40]. Combined losses of tyrosylate and C_2H_4O from Tyr and Thr appear at *m/z* 1045.5419 and 1044.5346 respectively.

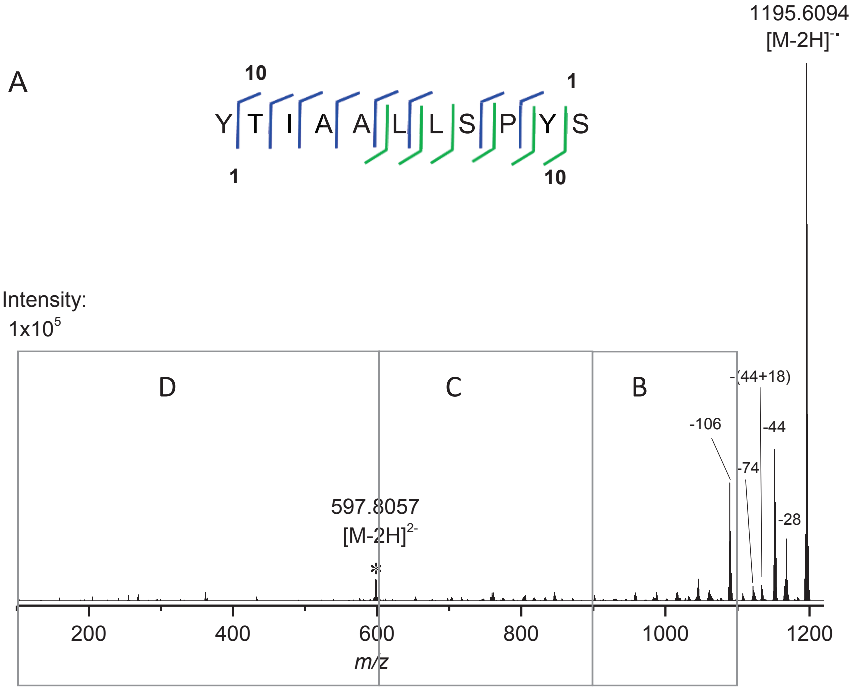
1195.6094
[M-2H]⁻•
A
10
1
Y T I A A L L S P Y S
1
10
Intensity:
1x10⁵
D
C
B
-(44+18)
-106
-44
-74
-28
597.8057
[M-2H]²⁻
*
200
400
600
800
1000
1200
m/z

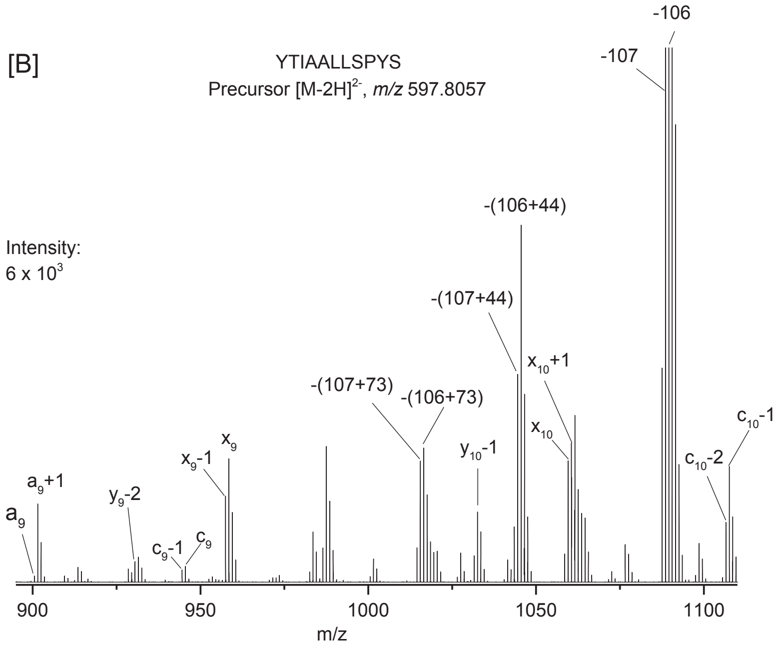
-106
-107
[B]
YTIAALLSPYS
Precursor [M-2H]²⁻, m/z 597.8057
-(106+44)
Intensity:
6 x 10³
-(107+44)
x10+1
-(107+73)
-(106+73)
c10-1
x10
y10-1
x9
c10-2
x9-1
a9+1
y9-2
a9
c9-1
c9
900
950
1000
1050
1100
m/z

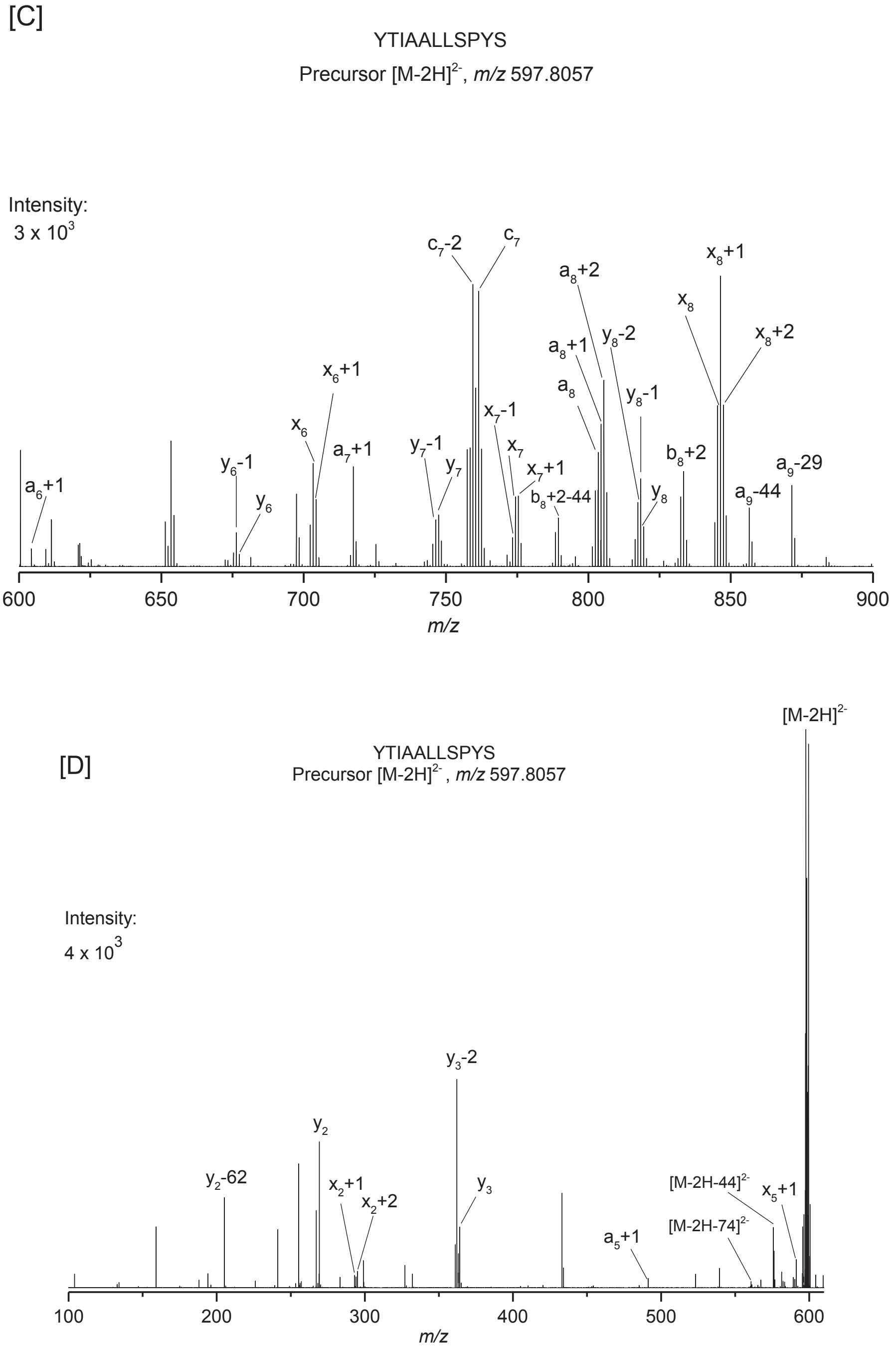

Figure 2.1 A) Photodissociation spectrum of the doubly-deprotonated [M-2H]$^{2-}$ ion (*m/z* 597.8057) of YTIAALLSPYS at 213 nm. The precursor ion is notified by * sign and the neutral losses are indicated by ion masses. The green and blue lines represent the a, b, c and x, y, z ions, respectively. B) Zoom of the 900-1100 *m/z*, C) Zoom of the 600-900 *m/z*, and D) Zoom of the 100-600 *m/z*.

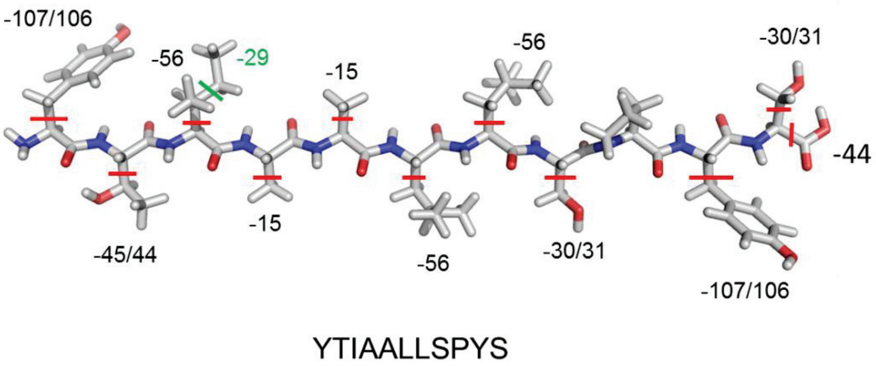

Figure 2.2 Side-chain losses detected from peptide 1, YTIAALLSPYS at 213 nm.

Zooms of **Figure 2.1A** are shown in **Figure 2.1B-2.1D**. Selected fragment ions from the single isotope selection of the doubly-deprotonated $[M-2H]^{2-}$ precursor ions are shown in **Figure 2.3**. For peptide 1, a series of radical $(a_n+1)^{-\cdot}$ fragment ions is observed for n=5, 6, 7, 8 and 9 These ions correspond to the elemental composition of a_n ions plus one hydrogen atom (explaining the +1 in the notation) and are radicals (dot in the notation). This nomenclature is in agreement with the one proposed recently by Chu *et al* [41], only exception is that we do not include the hydrogen symbol (H) after the number of losses or gains. Homolytic cleavage between the C_α and the carbonyl C from the precursor ion induced the formation of these radical ions, as shown in **Scheme 2.2**. Classical $(a_n)^-$ fragment ions are detected for n=8 and 9. These ions may mainly arise from the fragmentation of the doubly-deprotonated $[M-2H]^{2-}$ precursor ion. However, they can also be produced by secondary H elimination from the radical $(a_n+1)^{-\cdot}$ fragment ions [42]. Abundant a ions are favored by aromatic amino acids and in this case it is due to Tyr residue in N-terminal [18, 39]. An unusual fragment such as $(a_8+2)^-$ is additionally identified at *m/z* 805.4815 and which may be due to the presence of Pro residue [43, 44]. Detection of $(a+2)^-$ is also reported by Madsen *et al* in a high-throughput UVPD study in negative polarity for complex proteomic sample [45]. Two peaks at *m/z* 871.5031 and 856.4917 correspond to the loss of CH_3CH_2 (28.9995 Da from Ile) and C_2H_4O (44.0265 Da from Thr) from $(a_9)^-$ ion. Radical $(x_n+1)^{-\cdot}$ ions are also formed via homolytic cleavage of the C_α - carbonyl C bond, complementary to $(a_n+1)^{-\cdot}$ ions (**Scheme 2.2**). Series of radical $(x_n+1)^{-\cdot}$ ions are noticed at n= 2, 5, 6, 7, 8, and 10 whereas $(x_n)^-$ ions are detected at n= 6, 7, 8 and 9. Two unusual fragment types such as $(x_n+2)^-$ for n=2, 8 and radical $(x_n-1)^{-\cdot}$ for n=7 and 9 appear for peptide 1. $(x_2+2)^-$ ion detected at *m/z* 295.0924 is close to Pro residue [43]. Kim and Reilly found

x_n+2 fragment ions at 157 nm UVPD and concluded that some x+1 radical ions may take one hydrogen to form these new ions [46]. $(x_n+2)^-$ ions are also detected at 193 nm UVPD [45]. The proposed fragmentation pathway for the formation of $(x_2+2)^-$ ion is presented in **Scheme 2.3**. The formation of two $(x_n-1)^{-\cdot}$ ions are likewise owing to the radical elimination of hydrogen atom from the corresponding x_n ions. Shaw *et al* also observed some $(x_n-1)^{-\cdot}$ ions in activated ion negative electron transfer dissociation [16]. Moreover, classical fragmentation of the C_α-C bond with proton transfers from the charge-reduced $[M-2H]^{-\cdot}$ radical species also yields to the formation of $(x_n-1)^{-\cdot}$ ions. Indeed, these ions will contain the initial radical site and the negative charge. Fragmentation is then observed after electron photo-detachment.

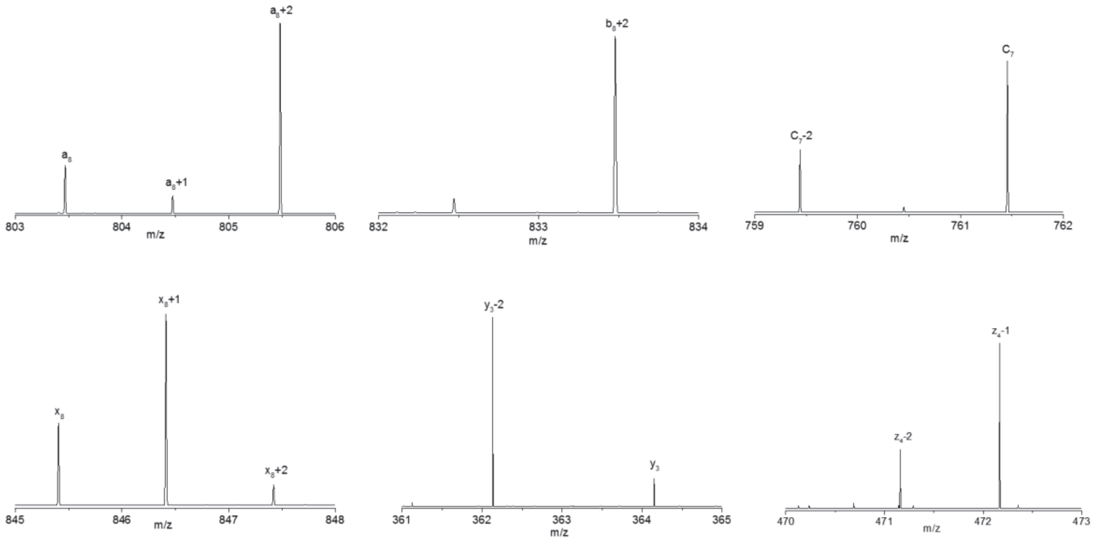

Figure 2.3 Selected fragment ions from the single isotope selection of the doubly-deprotonated $[M-2H]^{2-}$ precursor ions. a/x, b/y and c ions are from peptide 1 and z ion is from peptide 2.

Scheme 2.2 Proposed mechanism for the formation of $(a_n+1)^{-\cdot}$ and $(x_n+1)^{-\cdot}$ fragment ions during UVPD of doubly deprotonated peptide $[M-2H]^{2-}$.

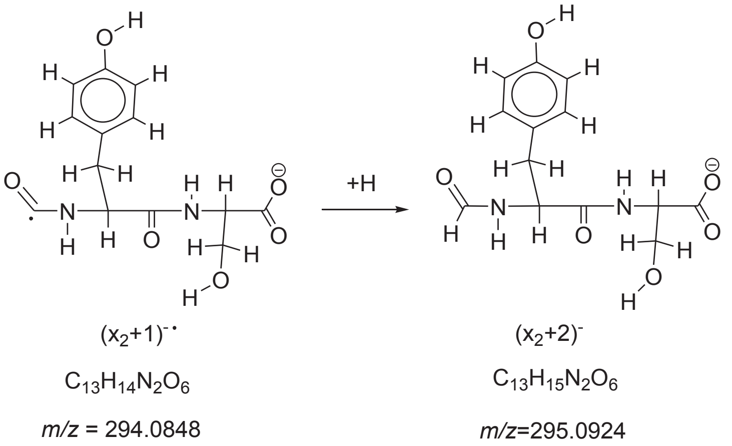

Scheme 2.3 Proposed mechanism for the formation of $(x_2+2)^-$ product ion from the $(x_1+1)^{-\cdot}$ fragment ions during the UVPD of the doubly deprotonated YTIAALLSPYS peptide.

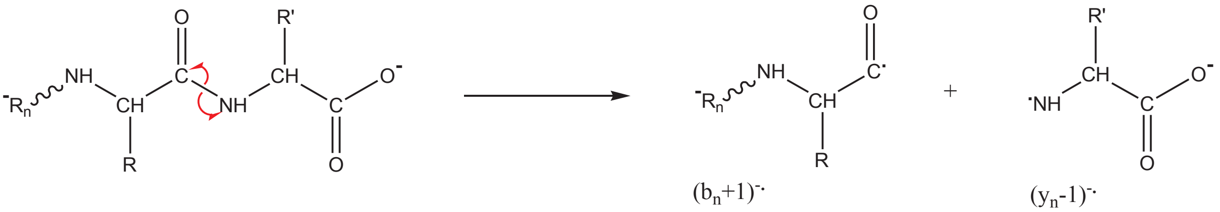

Scheme 2.4 Proposed mechanism for the formation of $(b_n+1)^{-\cdot}$ and $(y_n-1)^{-\cdot}$ fragment ions during UVPD of doubly deprotonated peptide $[M-2H]^{2-}$.

Series of $(y_n)^-$ ions are detected at n=2, 3, 6, 7, and 8. Radical $(y_n-1)^{-\cdot}$ ions are also observed at the positions n=6, 7, 8, and 10. These ions arise from the homolytic cleavage of the C-N bond from the precursor ion (**Scheme 2.4**). However, complementary $(b_n+1)^{-\cdot}$ radical ions are not detected. Fragmentation of the C-N bond from the charge-reduced $[M-2H]^{-\cdot}$ radical species may also leads to the formation of the $(y_n-1)^{-\cdot}$ ions, if the charge and the radical site after electron loss are located on the C-terminal side. As a general statement, the abundance of fragment ions results from both direct fragmentation of the precursor ions and fragmentation of the charge-reduced radical ions obtained after electron loss (EPD). $(y_n-1)^{-\cdot}$ radical ions could also be formed by H elimination from the $(y_n)^-$ ions. Three new $(y_n-2)^-$ ions are detected for this peptide at n=3, 8, and 9 positions and could be formed by H elimination from the $(y_n-1)^{-\cdot}$ ions. The fragmentation of the C-N bond close to the Pro residue can also explain the formation of the $(y_3-2)^-$ fragment ion [43]. Once again, these fragment ions could also arise from the homolytic cleavage of C-N bond fragmentation from the charge-reduced $[M-2H]^{-\cdot}$ radical species. One $(b_8+2)^-$ fragment ion is detected at *m/z* 833.4757 for this peptide due to the presence of the Pro residue. A neutral loss of 44.0264 Da corresponds to C_2H_4O of Thr observed at *m/z* 789.4493 from $(b_8+2)^-$ (**Figure 2.1C**).

c/z ions are less abundant for this peptide. Two $(c_n)^-$ ions are detected at n=7 and 9 positions. Moreover, two $(c_n-1)^{-\cdot}$ ions at n=9,10 positions and $(c_n-2)^-$ ions at n=7, 10 sites are observed. Radical $(c_n-1)^{-\cdot}$ ions could be produce via the homolytic cleavage of the N-C_α bond from the precursor ion (**Scheme 2.4**). Hydrogen abstraction from c ions are also detected in ECD [47–49]. The formation of the $(c_n-2)^-$ ions could be explained by the radical induced fragmentation of the N-C_α bond from the charge-reduced $[M-2H]^{-\cdot}$ radical species after electron loss.

2.3.2 The Photodissociation of Peptide 2 (DYKDDDDK)

The photodissociation spectrum of the doubly-deprotonated $[M-2H]^{2-}$ (*m/z* 505.1906) of peptide DYKDDDDK is presented in **Figure 2.4**. Exact masses and assignments of fragment ions of this peptide are summarized in **Table A2.3** (see in appendix). Intense neutral losses are also evident from this peptide (**Table A2.4**). Loss of H_2O from the charge-reduced radical species $[M-2H]^{-\bullet}$ is detected at *m/z* 992.3709. Losses of one, two and three CO_2 are identified at *m/z* 966.3913, 922.4019, and 878.4116, respectively. Madsen *et al* observed one and two CO_2 loss at 193 nm UVPD of singly and multiply charged peptide anions [36] Abundant CO_2 loss was moreover demonstrated in electron detachment dissociation for peptide and protein [17, 19]. Elimination of several CO_2 is a common feature related to aspartic and glutamic acid residues in NETD, Al-NETD, EDD and UVPD[16, 19]. The UVPD spectrum showed losses of 27.9955 Da from $[M-2H]^{-\bullet}$ that can be attributed to CO, similar to peptide 1. Loss of CO from radical species is also found in an earlier ECD study [50]. The peaks at *m/z* 903.3321 and 904.3394 correspond to the losses of tyrosylate groups of Tyr (107.0491 and 106.0418 Da) from the $[M-2H]^{-\bullet}$. Radical $C_3H_6O_2N$ (88.0371 Da) group elimination from the aspartic amino acid yields to the ion detected at *m/z* 922.3441. The ion observed at *m/z* 938.3961, can be assigned to the loss of $C_3H_4O_2$ (71.9851 Da) from Asp residue [15]. Loss of Lys residue (100.0736 Da) is also detected at *m/z* 910.3076. Moreover, a loss of 71.0713 Da (C_4H_9N) observed for the ion at *m/z* 939.3099 is from the Lys residue [15]. A combined loss of CO_2 and H_2O appears at *m/z* 948.3803.

A complete series of $(a_n)^-$ fragment ion is observed for this peptide for n=2-7. $(a_n+1)^{-\cdot}$ ions are detected for n=4, 5, 6 and 7. These ions are formed via homolytic cleavage from the precursor ion (**Scheme 2.2**). Radical $(a_n-1)^{-\cdot}$ ions are detected for n= 3, 5 and 6. Fragmentation of the C_α - C bond from the charge-reduced radical species $[M-2H]^{-\bullet}$ is involved to produce these series. Secondary radical elimination of hydrogen atom from $(a_n)^-$ ions could also yield to the formation of these ions. A complete series of $(x_n)^-$ fragment ions is detected at n=2-7 similar to complementary $(a_n)^-$ ions. Two radical $(x_n+1)^{-\cdot}$ ions (n=3 and 6) are detected at *m/z* 402.1380 and 760.2859, respectively. Moreover, two $(x_n+2)^-$ ions (n=2 and 6), which are formed by addition of one extra hydrogen atom to $(x_n+1)^-$ ions are detected. Additionally, $(x_7-1)^-$ ion is observed at *m/z* 921.3364. Same fragmentation mechanisms are proposed for the formation of these ions than for the peptide 1 described previously. A distinctive peaks at *m/z* 886.3281 corresponds to the loss of one and two H_2O molecules from $(x_7)^-$, respectively.

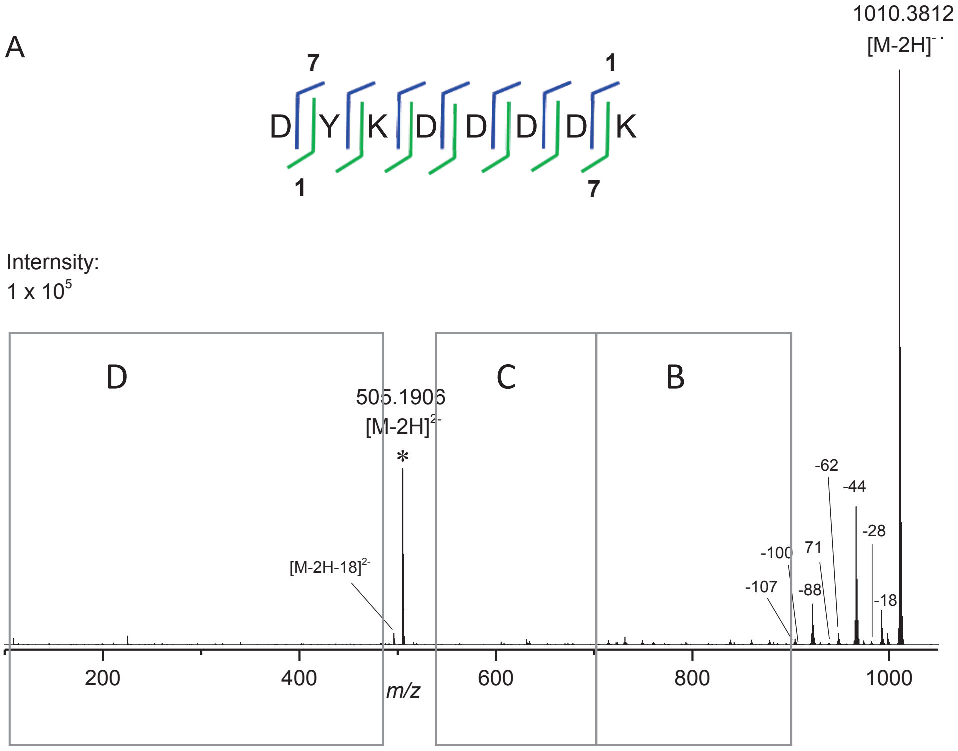

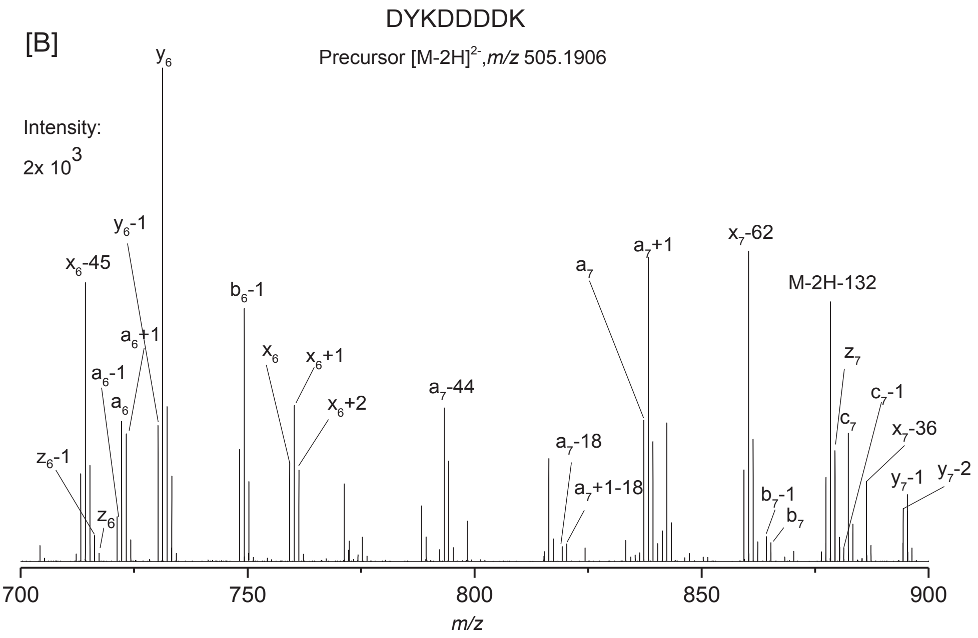
[B]
DYKDDDDK
Precursor [M-2H]2-, m/z 505.1906
Intensity:
2x 10^3
y6
y6-1
x6-45
b6-1
a6+1
a6-1
a6
x6
x6+1
x6+2
z6-1
z6
a7-44
a7-18
a7+1-18
a7
a7+1
x7-62
M-2H-132
z7
c7-1
c7
x7-36
b7-1
b7
y7-1
y7-2
700
750
800
850
900
m/z

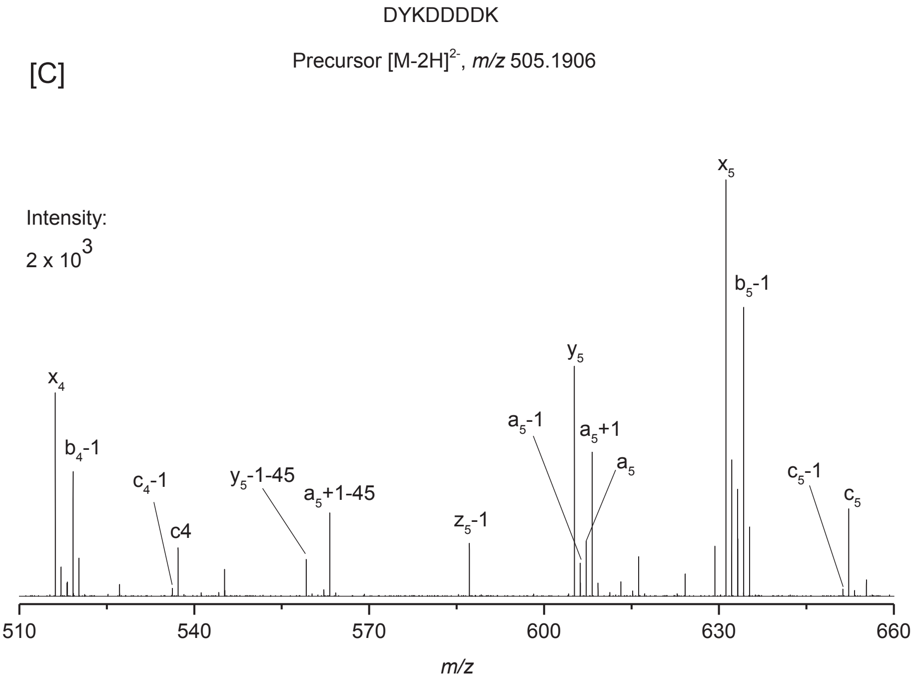
DYKDDDDK
Precursor [M-2H]2-, m/z 505.1906
[C]
Intensity:
2 x 10^3
x5
b5-1
y5
x4
b4-1
a5-1
a5+1
a5
c4-1
c4
y5-1-45
a5+1-45
z5-1
c5-1
c5
510
540
570
600
630
660
m/z

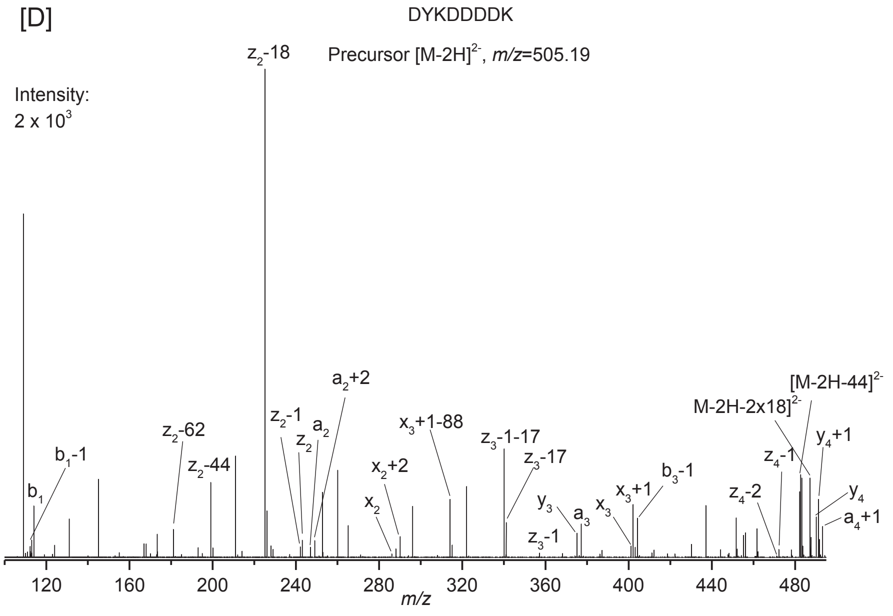

Figure 2.4 A) Photodissociation spectrum of the doubly-deprotonated $[M-2H]^{2-}$ ion (*m/z* 505.1906) of DYKDDDDK at 213 nm (the precursor ion is signified by * and neutral losses are indicated by ion masses). The green and blue lines represent the a, b, c and x, y, z ions, respectively. B) Zoom of the 700-900 *m/z*, C) Zoom of the 510-660 *m/z*, and D) Zoom of the 100-500 *m/z*.

Two $(b_n)^-$ fragment ions are observed at n=1 and 7 sites whereas very abundant radical $(b_n-1)^{-\cdot}$ ions are detected for n= 1, 3-7. These ions would come from the fragmentation of the C-N bond from the charge-reduced $[M-2H]^{-\bullet}$ radical species. Several $(y_n)^-$ ions appear at n= 3-6 positions. Some $(y_n-1)^{-\cdot}$ ions at n=3, 6, 7 sites are also detected (formed via the mechanism proposed **Scheme 2.4**) as well as $(y_7-2)^-$ ion. Specific radical induced fragmentation of the $[M-2H]^{-\bullet}$ radical species is then also observed, after electron loss, for this peptide.

Cleavage of N-C_α bonds produces series of c and z ions. Four $(c_n)^-$ ions and $(c_n-1)^{-\cdot}$ radical ions are noticed at n=4-7 positions. These ions arise from the homolytic cleavage of the N-C_α bond from the precursor ion (**Scheme 2.5**). However, complementary $(z_n+1)^{-\cdot}$ radical ions are not detected. $(z_n)^-$ ions are detected from 2, 3, 6 and 7 positions. Interestingly, complete series of radical $(z_n-1)^{-\cdot}$ ions (n=2-7) is observed for this peptide. Classical fragmentation of the N-C_α bond with proton transfers from the $[M-2H]^{-\bullet}$ radical species is proposed for the formation of these ions as well as the $(c_n-1)^{-\cdot}$ series. Compared to first peptide, abundance of c and z ions is noticeable for this peptide and may be due to the presence of five Asp residues. Removal of one H_2O, one CO_2 and combined CO_2 and H_2O from $(z_2)^-$ ion are detected at *m/z* 225.0868 199.1074, and 181.0967, respectively. Previous studies also noticed the losses of H_2O and CO_2 from z ion when peptide contained Asp residues [51].

Scheme 2.5 Proposed mechanism for the formation of $(c_n\text{-}1)^{-\bullet}$ and $(z_n\text{+}1)^{-\bullet}$ fragment ions during UVPD of doubly deprotonated peptide $[M\text{-}2H]^{2-}$.

2.3.3 The Photodissociation of Peptide 3 (RGDSPASSKP)

The photodissociation spectrum of the doubly-deprotonated $[M\text{-}2H]^{2-}$ (*m/z* 499.2393) of peptide RGDSPASSKP is presented in **Figure 2.5.** Exact masses and assignments of fragment ions of this peptide are summarized in **Table A2.5**. Intense neutral losses are summarized in **Table A2.6**.

The loss of H_2O from the charge-reduced radical species $[M\text{-}2H]^{-\bullet}$ (*m/z* 998.4767) is noticed at *m/z* 980.4673 (**Figure 2.5A**). There are three Ser residues in this peptides and loss of CH_2O (30.0095 Da) at *m/z* 968.4672 can be attributed to the side chain of Ser. The loss of 60.0540 Da observed for the peak at *m/z* 938.4227 corresponds to the C_2H_6ON group of the Ser residue. Loss of CO_2 (exact mass 43.9895 Da) from the carboxyl group located in C-terminal or side chain of aspartic acid appears at *m/z* 954.4872. Two distinctive peaks at *m/z* 899.3982 and 912.4072 correspond to the losses of 99.0785, and 86.0695 Da from the arginine side chain [15, 40]. Loss of 88.0498 Da which is detected at *m/z* 910.4269 is related to the side chain of Asp [51].

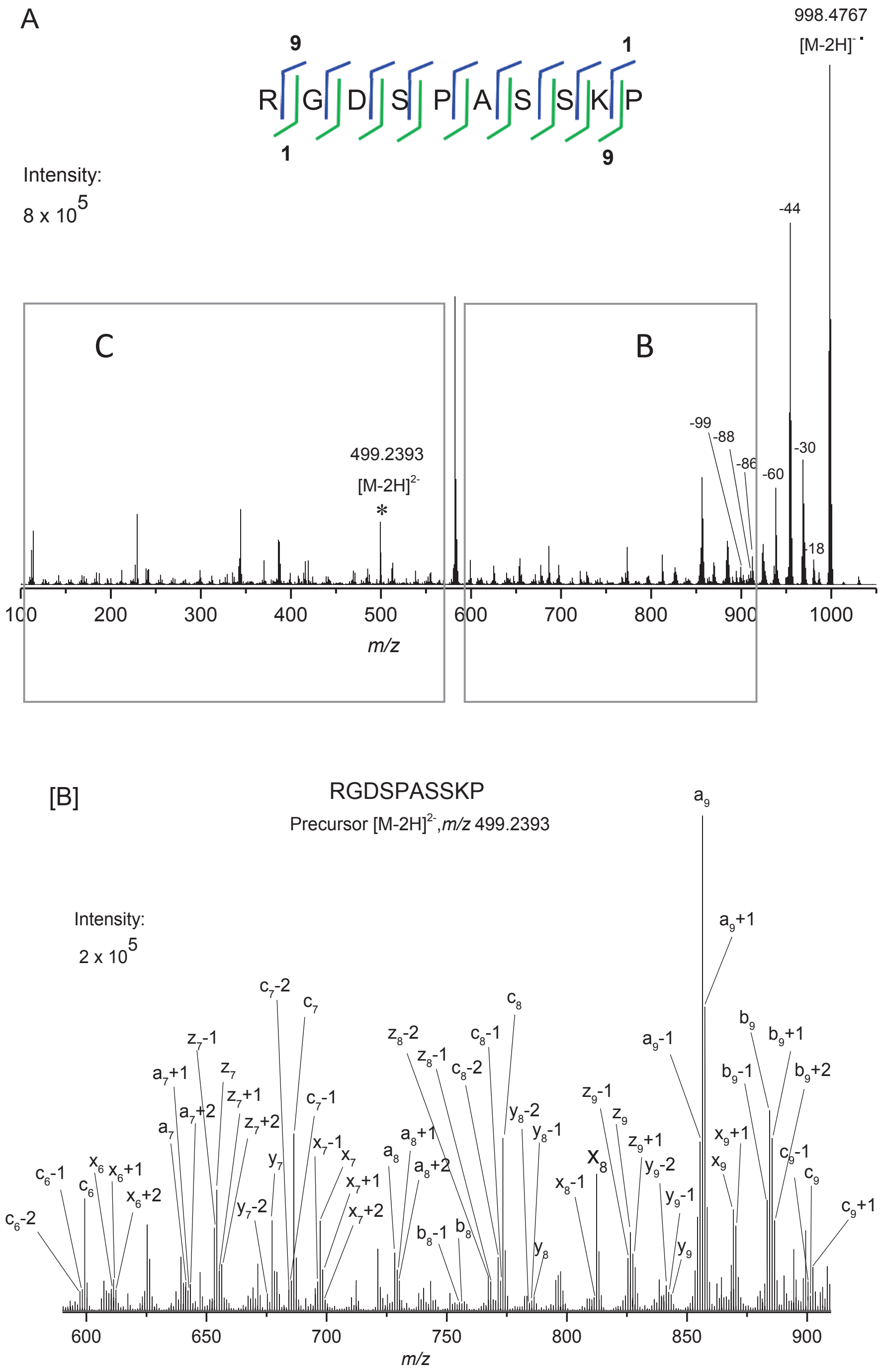
A
998.4767
[M-2H]⁻•
9
1
R G D S P A S S K P
1
9
Intensity:
8 x 10^5
-44
C
B
-99
-88
-86
-60
-30
-18
499.2393
[M-2H]2-
*
100
200
300
400
500
600
700
800
900
1000
m/z
[B]
RGDSPASSKP
Precursor [M-2H]2-, m/z 499.2393
Intensity:
2 x 10^5
a9
a9+1
a9-1
b9
b9+1
b9-1
b9+2
x9+1
x9
c9-1
c9
c9+1
c7-2
c7
c7-1
z7-1
z7
z7+1
z7+2
a7+1
a7+2
a7
y7
y7-2
x7-1
x7
x7+1
x7+2
c6-1
c6
c6-2
x6
x6+1
x6+2
z8-2
z8-1
c8-1
c8-2
c8
a8
a8+1
a8+2
b8-1
b8
y8-2
y8-1
y8
x8
x8-1
z9-1
z9
z9+1
y9-2
y9-1
y9
600
650
700
750
800
850
900
m/z

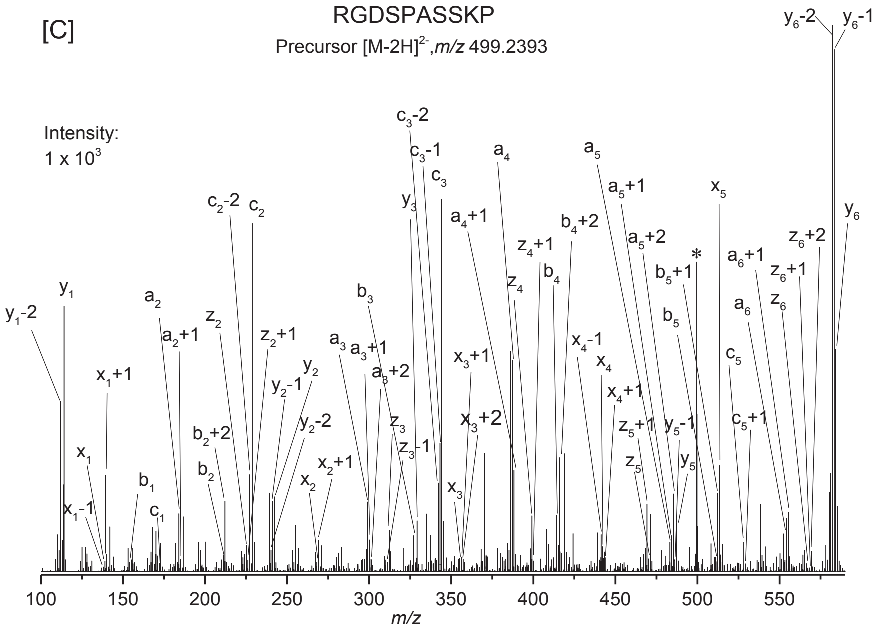

Figure 2.5 Photodissociation spectra of the doubly-deprotonated $[M\text{-}2H]^{2-}$ ion (*m/z* 499.2393) of RGDSPASSKP at 213 nm (the precursor ion is signified by * and neutral losses are indicated by ion masses). The green and blue lines represent the a, b, c and x, y, z ions, respectively. B) Zoom of the 600-900 *m/z* and C) Zoom of the 100-600 *m/z.*

Nearly complete series of $(a_n)^-$ fragment ions is observed for this peptide for n=2-9 whereas $(a_n\text{-}1)^{-\cdot}$ ions are detected for n= 6 and 9. Radical $(a_n+1)^{-\cdot}$ ions are detected for n=2-9 (**Scheme 2.2**). Addition of one hydrogen to $(a_n+1)^{-\cdot}$ radical ions (similar as shown in **Scheme 2.3** for the x_n+1 ions) which yield $(a_n+2)^-$ is also prevalent for n=3-5,7-9 positions. $(a_n+2)^-$ ions are also observed for Proline containing peptides [43, 52] and explain the formation of $(a_4+2)^{-\cdot}$ and $(a_9+2)^-$ ions. An almost complete series of $(x_n)^-$ fragment ions is detected at n=1-4, 6-9 similar to the complementary $(a_n)^-$ ions. Four $(x_n\text{-}1)^{-\cdot}$ ions are observed for n= 1, 4, 7-9 sites. Moreover, $(x_n+1)^{-\cdot}$ ions are detected for n=1-4, 6, 7, and 9. Four $(x_n+2)^-$ ions (n=2, 3, 6 and 7) are also formed via H addition on the $(x_n+1)^{-\cdot}$ ions.

$(b_n)^-$ and $(y_n)^-$ fragments ions are predominant in this peptides, which may be due to the presence of basic Arg and Lys amino acids [61]. $(b_n)^-$ ions are identified for n=1-5, 8, and 9 positions only missing n=6 and 7 related to Ala-Ser and Ser-Ser amide bonds. $(b_n+1)^{-\cdot}$ ions are detected for n= 4, 5, and 9 (**Scheme 2.4**). Three $(b_n\text{-}1)^{-\cdot}$ ions are observed at n= 3, 8 and 9.

Representative $(b_n+2)^-$ ions appear at 2, 4, 9 positions in which two sites (4 and 9) are closed to the Pro residues. $(b_2+2)^-$ ion could be explain by the H addition on the $(b_n+1)^{-\cdot}$ ion. Complete sequence of $(y_n)^-$ ions are found (n= 1-3, 5-9) whereas $(y_n-1)^{-\cdot}$ ions are noticed for n=2, 5-9. Distinctive $(y_n-2)^-$ ions are detected for n=1, 2, 6-9.

Homolytic cleavage and fragmentation, associated with proton transfers, of N-C_α bonds is also noticeable. Full sequence of $(c_n)^-$ ions located for n=1-3, 5-9 and $(c_n-1)^{-\cdot}$ ions are noticed at n= 3, 6-9. Fragment $(c_n-2)^-$ ions are detected for n= 2, 3, 6-8. Similar to peptide 2, complete series of $(z_n)^-$ ions (n=2-9) are generated from this peptide. $(z_n-1)^{-\cdot}$ ions are also observed for n=3,7-9. Moreover, $(z_n+1)^{-\cdot}$ ions are detected for n=2, 4, 6, 7 and 9 (**Scheme 2.5**).

2.3.4 Photo-induced Hydrogen loss at 213 nm

A general trend is observed for those three peptides with series of backbone cleavages leading to ions deficient in hydrogen. All three peptides produce the distinctive doubly-deprotonated $[M-2H]^{-\bullet}$ charge-reduced radical species upon irradiation of the monoisotopic precursor ion $[M-2H]^{2-}$, along with hydrogen loss from the charge-reduced radical species as shown in (**Figure 2.6**). Time-dependent density functional theory (TDDFT) calculation has been performed on a model amide system to elucidate the role of πσ* excited state in the photodissociation of peptide. The potential energy surface of the model amide system, π, π*, and σ* molecular orbitals are displayed in **Figure 2.7**. The lowest ππ*, πσ* and electronic group state (S_0) are shown with respect to the N-H stretching coordinate of the model amide. The ππ* excitation is observed for the amide system at 215 nm (5.75 eV) which relates with our UVPD experiment at 213 nm. The diffuse and polar character of σ* orbital is observed which is similar to the previous studies on pyrrole/indole system [53, 54]. The shallow barrier with respect to N-H stretch indicates the repulsive nature of this state [53]. For this amide system, the ππ* surface is above the πσ* surface which may allow the fast internal crossing from the ππ* to the πσ* states and lead to H atom dissociation [54–56]. The ππ* excitation-induced amide hydrogen loss then provides a general route for the formation of hydrogen-deficient ions in 213 nm UVPD. Repetition of this mechanism with absorption of several photons can lead to fragments displaying multiple H-loss. Moreover, the ππ* excitation-induced amide hydrogen loss may yield a nitrogen-centered amide anion intermediate and stimulate the wide-spread backbone fragmentation. However, details theoretical calculation are sought to elicit the mechanism of radical-driven side- chain loss and backbone fragmentation at 213 nm photodissociation on peptide and protein anions. Similar mechanism can also arise on other bonds from aromatic cycles or COO chromophore groups.

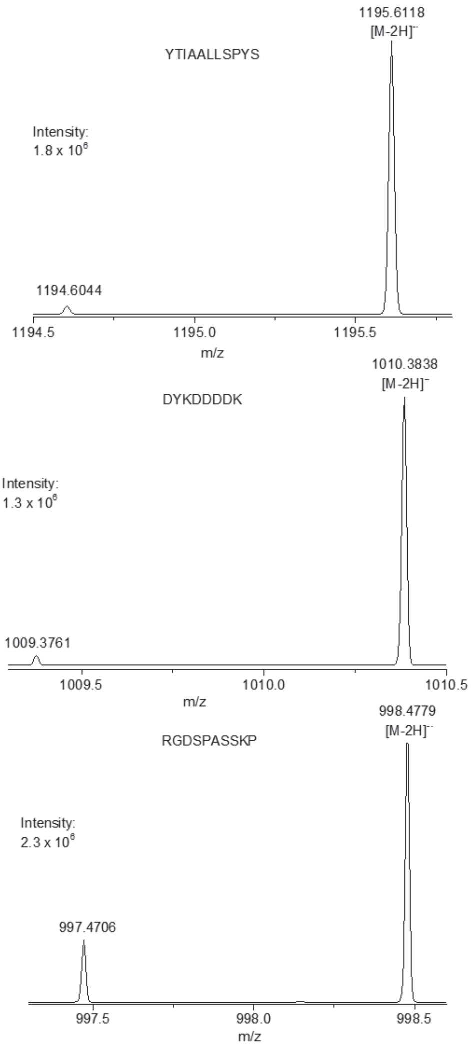

Figure 2.6 Photodissociation spectra of the doubly-deprotonated $[M\text{-}2H]^{2-}$ ion of three peptides. Loss of hydrogen is observed from the characteristic $[M\text{-}2H]^{-\bullet}$ charge-reduced radical at single isotope selection of the doubly-deprotonated $[M\text{-}2H]^{2-}$ precursor ions.

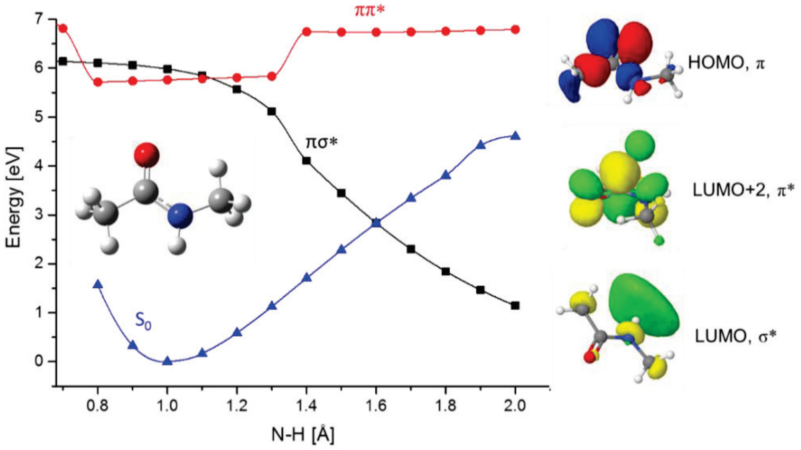

Figure 2.7. Potential Energy Surface of the lowest ππ*, πσ* and electronic ground state (S_0) as a function of the NH stretch reaction coordinate. The optimization, natural bond orbital (NBO) and TD-DFT calculations have been performed at B3LYP/6-311+G(2d,p) level of theory.

2.4 Summary

The key features of these experiments can be summarized as follows: (1) Extensive sequence specific side-chain losses are observed for all three peptides. (2) Near complete series of classical backbone cleavages (a/x, b/y, c/z) are observed. (3) Unusual fragment ions including $(x+1)^{-\cdot}$, $(x+2)^{-}$, $(x-1)^{-\cdot}$, $(y-1)^{-\cdot}$, $(y-2)^{-}$, $(z-1)^{-\cdot}$, $(z+1)^{-\cdot}$, $(z+2)^{-}$ and $(a-1)^{-\cdot}$, $(a+1)^{-\cdot}$, $(a+2)^{-}$, $(b-1)^{-\cdot}$, $(b+1)^{-\cdot}$, $(b+2)^{-}$, $(c-1)^{-\cdot}$, $(c-2)^{-}$ are consistently observed in these experiments and further confirmed by selecting single isotopic peak of the precursor ions. Some of these ions are coming from homolytic cleavages of the backbone from the precursor doubly charged ion. Classical fragmentation of backbone bonds concerted with proton transfers and homolytic cleavages are also observed for the charge-reduced $[M-2H]^{-\cdot}$ radical species after electron photo-detachment. Radical-induced specific fragment ions are then produced in these experiments of UVPD in the negative mode. Some of these ions may also result from secondary H eliminations. (4) Hydrogen-deficient ions may result from ππ* excitation-induced amide hydrogen loss. This ππ* excitation is reached upon absorption of a photon at 213 nm. The present study outlines the difficulty to interpret and systematically analyze the wealth of fragmentation produced by irradiation of peptide and protein anions at the onset of the amide bond absorption band, which may be different from VUV (vacuum ultraviolet) excitation.

Bibliography

1. Zhurov, K.O., Fornelli, L., Wodrich, M.D., Laskay, U.A., Tsybin, Y.O.: Principles of electron capture and transfer dissociation mass spectrometry applied to peptide and protein structure analysis. Chem. Soc. Rev. 42, 5014–5030 (2013). doi:10.1039/C3CS35477F

2. McLuckey, S.A.: Principles of collisional activation in analytical mass spectrometry. J. Am. Soc. Mass Spctrom. 3, 599–614 (1992). doi:10.1016/1044-0305(92)85001-Z

3. Mitchell Wells, J., McLuckey, S.A.: Collision- Induced Dissociation (CID) of Peptides and Proteins. In: Methods in Enzymology. pp. 148–185. Academic Press (2005)

4. Zubarev, R.A., Kelleher, N.L., McLafferty, F.W.: Electron capture dissociation of multiply charged protein cations. A nonergodic process. J. Am. Chem. Soc. 120, 3265–3266 (1998). doi:10.1021/ja973478k

5. Syka, J.E.P., Coon, J.J., Schroeder, M.J., Shabanowitz, J., Hunt, D.F.: Peptide and protein sequence analysis by electron transfer dissociation mass spectrometry. Pro. Natl. Acad. Sci. USA. 101, 9528–9533 (2004). doi:10.1073/pnas.0402700101

6. Brodbelt, J.S.: Shedding Light on the Frontier of Photodissociation. J. Am Soc. Mass Spectrom. 22, 197–206 (2011). doi:10.1007/s13361-010-0023-6

7. Brodbelt, J.S.: Photodissociation mass spectrometry: new tools for characterization of biological molecules. Chem. Soc. Rev. 43, 2757–2783 (2014). doi:10.1039/c3cs60444f

8. Antoine, R., Lemoine, J., Dugourd, P.: Electron photodetachment dissociation for structural characterization of synthetic and biopolymer anions. Mass Spectrom. Rev. 33, 501–522 (2014). doi:10.1002/mas.21402

9. Vasicek, L.A., Ledvina, A.R., Shaw, J., Griep-Raming, J., Westphall, M.S., Coon, J.J., Brodbelt, J.S.: Implementing Photodissociation in an Orbitrap Mass Spectrometer. J. Am. Soc. Mass Spctrom. 22, 1105–1108 (2011). doi:10.1007/s13361-011-0119-7

10. Vasicek, L., Brodbelt, J.S.: Enhancement of Ultraviolet Photodissociation Efficiencies through Attachment of Aromatic Chromophores. Anal. Chem. 82, 9441–9446 (2010). doi:10.1021/ac102126s

11. Smith, S.I., Brodbelt, J.S.: Characterization of Oligodeoxynucleotides and Modifications by 193 nm Photodissociation and Electron Photodetachment Dissociation. Anal. Chem. 82, 7218–7226 (2010). doi:10.1021/ac100989q

12. Robinson, M.R., Madsen, J.A., Brodbelt, J.S.: 193 nm Ultraviolet Photodissociation of Imidazolinylated Lys-N Peptides for De Novo Sequencing. Anal. Chem. 84, 2433–2439 (2012). doi:10.1021/ac203227y

13. Kjeldsen, F., Silivra, O. a., Ivonin, I. a., Haselmann, K.F., Gorshkov, M., Zubarev, R. a.: Cα-C backbone fragmentation dominates in electron detachment dissociation of gas-phase polypeptide polyanions. Chem. - A Eur. J. 11, 1803–1812 (2005). doi:10.1002/chem.200400806

14. Shaw, J.B., Madsen, J. a., Xu, H., Brodbelt, J.S.: Systematic comparison of ultraviolet photodissociation and electron transfer dissociation for peptide anion characterization. J. Am. Soc. Mass Spectrom. 23, 1707–1715 (2012). doi:10.1007/s13361-012-0424-9

15. Rumachik, N.G., McAlister, G.C., Russell, J.D., Bailey, D.J., Wenger, C.D., Coon, J.J.: Characterizing peptide neutral losses induced by negative electron-transfer dissociation (NETD). J. Am. Soc. Mass Spectrom. 23, 718–727 (2012). doi:10.1007/s13361-011-03315

16. Shaw, J.B., Kaplan, D.A., Brodbelt, J.S.: Activated Ion Negative Electron Transfer Dissociation of Multiply Charged Peptide Anions. Anal. Chem. 85, 4721–4728 (2013). doi:10.1021/ac4005315

17. Larraillet, V., Antoine, R., Dugourd, P., Lemoine, J.: Activated-Electron Photodetachment Dissociation for the Structural Characterization of Protein Polyanions. Anal. Chem. 81, 8410–8416 (2009). doi:10.1021/ac901304d

18. Larraillet, V., Vorobyev, A., Brunet, C., Lemoine, J., Tsybin, Y.O., Antoine, R., Dugourd, P.: Comparative dissociation of peptide polyanions by electron impact and photo-induced electron detachment. J. Am. Soc. Mass Spectrom. 21, 670–680 (2010). doi:10.1016/j.jasms.2010.01.015

19. Antoine, R., Joly, L., Tabarin, T., Broyer, M., Dugourd, P., Lemoine, J.: Photo-induced formation of radical anion peptides. Electron photodetachment dissociation experiments.

Rapid Commun. Mass Spectrom. 21, 265–268 (2007). doi:10.1002/rcm.2810

20. Ganisl, B., Valovka, T., Hartl, M., Taucher, M., Bister, K., Breuker, K.: Electron Detachment Dissociation for Top-Down Mass Spectrometry of Acidic Proteins. Chem. – A Eur. J. 17, 4460–4469 (2011). doi:10.1002/chem.201003709

21. Turecek, F., Julian, R.R.: Peptide Radicals and Cation Radicals in the Gas Phase. Chem. Rev. 113, 6691–6733 (2013). doi:10.1021/cr400043s

22. Moore, B.N., Ly, T., Julian, R.R.: Radical Conversion and Migration in Electron Capture Dissociation. J. Am. Chem. Soc. 133, 6997–7006 (2011). doi:10.1021/ja1096804

23. A Zubarev, R.: Peptide radical cations: gender determines dissociation chemistry. Mass Spectrom. (Tokyo, Japan). 2, S0004–S0004 (2013). doi:10.5702/massspectrometry.S0004

24. Coon, J.J., Shabanowitz, J., Hunt, D.F., Syka, J.E.P.: Electron Transfer Dissociation of Peptide Anions. J. Am. Soc. Mass Spectrom. 16, 880–882 (2005). doi:http://dx.doi.org/10.1016/j.jasms.2005.01.015

25. Oh, H. Bin, Moon, B.: Radical-Driven Peptide Backbone Dissociation Tandem Mass Spectrometry. Mass Spectrom. Rev. 34, 116–132 (2015). doi:10.1002/mas.21426

26. Kalli, A., Hess, S.: Electron Capture Dissociation of Hydrogen-Deficient Peptide Radical Cations. J. Am. Soc. Mass Spectrom. 23, 1729–1740 (2012). doi:10.1007/s13361-012-0433-8

27. Sun, Q., Nelson, H., Ly, T., Stoltz, B.M., Julian, R.R.: Side chain chemistry mediates backbone fragmentation in hydrogen deficient peptide radicals. J. Proteome Res. 8, 958–966 (2009). doi:10.1021/pr800592t

28. Patiny, L., Borel, A.: ChemCalc: A Building Block for Tomorrow's Chemical Infrastructure. J. Chem. Inf. Model. 53, 1223–1228 (2013). doi:10.1021/ci300563h

29. Gaussian09, R.A.: 1, MJ Frisch, GW Trucks, HB Schlegel, GE Scuseria, MA Robb, JR Cheeseman, G. Scalmani, V. Barone, B. Mennucci, GA Petersson et al., Gaussian. Inc., Wallingford CT. (2009)

30. Becke, A.D.: Density-functional exchange-energy approximation with correct asymptotic

behavior. Phys. Rev. A. 38, 3098–3100 (1988)

31. Lee, C., Yang, W., Parr, R.G.: Development of the Colle-Salvetti correlation-energy formula into a functional of the electron density. Phys. Rev. B. 37, 785–789 (1988)

32. Reed, A.E., Weinstock, R.B., Weinhold, F.: Natural population analysis. J. Chem. Phys. 83, 735–746 (1985)

33. Reed, A.E., Curtiss, L.A., Weinhold, F.: Intermolecular interactions from a natural bond orbital, donor-acceptor viewpoint. Chem. Rev. 88, 899–926 (1988)

34. Han, X., Jin, M., Breuker, K., McLafferty, F.W.: Extending Top-Down Mass Spectrometry to Proteins with Masses Greater Than 200 Kilodaltons. Science (80-.). 314, 109–112 (2006). doi:10.1126/science.1128868

35. Yoo, H.J., Wang, N., Zhuang, S., Song, H., Håkansson, K.: Negative-ion electron capture dissociation: Radical-driven fragmentation of charge-increased gaseous peptide anions. J. Am. Chem. Soc. 133, 16790–16793 (2011). doi:10.1021/ja207736y

36. Madsen, J. a., Kaoud, T.S., Dalby, K.N., Brodbelt, J.S.: 193-Nm Photodissociation of Singly and Multiply Charged Peptide Anions for Acidic Proteome Characterization. Proteomics. 11, 1329–1334 (2011). doi:10.1002/pmic.201000565

37. Bowie, J.H., Brinkworth, C.S., Dua, S.: Collision-induced fragmentations of the (M-H)− parent anions of underivatized peptides: An aid to structure determination and some unusual negative ion cleavages. Mass Spectrom. Rev. 21, 87–107 (2002). doi:10.1002/mas.10022

38. Han, H., Xia, Y., McLuckey, S.A.: Ion Trap Collisional Activation of c and z• Ions Formed via Gas-Phase Ion/Ion Electron-Transfer Dissociation. J. Proteome Res. 6, 3062–3069 (2007). doi:10.1021/pr070177t

39. Zhang, L., Reilly, J.P.: Radical-Driven Dissociation of Odd-Electron Peptide Radical Ions Produced in 157 nm Photodissociation. J. Am. Soc. Mass Spectrom. 20, 1378–1390 (2009). doi:http://dx.doi.org/10.1016/j.jasms.2009.03.026

40. Papayannopoulos, I.A.: The interpretation of collision-induced dissociation tandem mass

spectra of peptides. Mass Spectrom. Rev. 14, 49–73 (1995). doi:10.1002/mas.1280140104

41. Chu, I.K., Siu, C.-K., Lau, J.K.-C., Tang, W.K., Mu, X., Lai, C.K., Guo, X., Wang, X., Li, N., Xia, Y., Kong, X., Oh, H. Bin, Ryzhov, V., Tureček, F., Hopkinson, A.C., Siu, K.W.M.: Proposed nomenclature for peptide ion fragmentation. Int. J. Mass Spectrom. 390, 24–27 (2015). doi:10.1016/j.ijms.2015.07.021

42. Cui, W., Thompson, M.S., Reilly, J.P.: Pathways of peptide ion fragmentation induced by vacuum ultraviolet light. J. Am. Soc. Mass Spctrom. 16, 1384–1398 (2005). doi:10.1016/j.jasms.2005.03.050

43. Girod, M., Sanader, Z., Vojkovic, M., Antoine, R., MacAleese, L., Lemoine, J., Bonacic-Koutecky, V., Dugourd, P.: UV Photodissociation of Proline-containing Peptide Ions: Insights from Molecular Dynamics. J. Am. Soc. Mass Spctrom. 26, 432–443 (2014). doi:10.1007/s13361-014-1038-1

44. Madsen, J., Cheng, R.R., Kaoud, T.S., Dalby, K., Makarov, D.E., Brodbelt, J.: Charge-site-dependent dissociation of hydrogen-rich radical peptide cations upon vacuum UV photoexcitation. Chem. - A Eur. J. 18, 5374–5383 (2012). doi:10.1002/chem.201103534

45. Madsen, J. a., Xu, H., Robinson, M.R., Horton, a. P., Shaw, J.B., Giles, D.K., Kaoud, T.S., Dalby, K.N., Trent, M.S., Brodbelt, J.S.: High-throughput Database Search and Large-scale Negative Polarity Liquid Chromatography-Tandem Mass Spectrometry with Ultraviolet Photodissociation for Complex Proteomic Samples. Mol. Cell. Proteomics. 12, 2604–2614 (2013). doi:10.1074/mcp.O113.028258

46. Kim, T.-Y., Reilly, J.P.: Time-Resolved Observation of Product Ions Generated by 157 nm Photodissociation of Singly Protonated Phosphopeptides. J. Am. Soc. Mass Spectrom. 20, 2334–2341 (2009). doi:10.1016/j.jasms.2009.08.021

47. Zubarev, R.A., Horn, D.M., Fridriksson, E.K., Kelleher, N.L., Kruger, N.A., Lewis, M.A., Carpenter, B.K., McLafferty, F.W.: Electron Capture Dissociation for Structural Characterization of Multiply Charged Protein Cations. Anal. Chem. 72, 563–573 (2000). doi:10.1021/ac990811p

48. Fung, Y.M.E., Chan, T.W.D.: Experimental and theoretical investigations of the loss of

amino acid side chains in electron capture dissociation of model peptides. J. Am. Soc. Mass Spectrom. 16, 1523–1535 (2005). doi:10.1016/j.jasms.2005.05.001

49. Tureček, F., Syrstad, E.A.: Mechanism and Energetics of Intramolecular Hydrogen Transfer in Amide and Peptide Radicals and Cation-Radicals. J. Am. Chem. Soc. 125, 3353–3369 (2003). doi:10.1021/ja021162t

50. Cooper, H.J., Hudgins, R.R., Håkansson, K., Marshall, A.G.: Characterization of amino acid side chain losses in electron capture dissociation. J. Am. Soc. Mass Spectrom. 13, 241–249 (2002). doi:10.1016/S1044-0305(01)00357-9

51. Harrison, A.G., Tu, Y.P.: Ion chemistry of protonated aspartic acid derivatives. J. Mass Spectrom. 33, 532–542 (1998). doi:10.1002/(SICI)1096-9888(199806)

52. Kim, T.-Y., Valentine, S.J., Clemmer, D.E., Reilly, J.P.: Gas-Phase Conformation-Specific Photofragmentation of Proline-Containing Peptide Ions. J. Am. Soc. Mass Spectrom. 21, 1455–1465 (2010). doi:10.1016/j.jasms.2010.04.007

53. Sobolewski, A.L., Domcke, W., Dedonder-Lardeux, C., Jouvet, C.: Excited-state hydrogen detachment and hydrogen transfer driven by repulsive (1)pi sigma* states: A new paradigm for nonradiative decay in aromatic biomolecules. Phys. Chem. Chem. Phys. 4, 1093–1100 (2002). doi:10.1039/b110941n

54. Ashfold, M.N.R., King, G.A., Murdock, D., Nix, M.G.D., Oliver, T.A.A., Sage, A.G.: pi sigma* excited states in molecular photochemistry. Phys. Chem. Chem. Phys. 12, 1218–1238 (2010). doi:10.1039/b921706a

55. Ashfold, M.N.R., Cronin, B., Devine, A.L., Dixon, R.N., Nix, M.G.D.: The role of pi sigma* excited states in the photodissociation of heteroaromatic molecules. Science (80-.). 312, 1637–1640 (2006). doi:10.1126/science.1125436

56. Sage, A.G., Nix, M.G.D., Ashfold, M.N.R.: UV photodissociation of N-methylpyrrole: The role of (1)pi sigma* states in non-hydride heteroaromatic systems. Chem. Phys. 347, 300–308 (2008). doi:10.1016/j.chemphys.2007.09.038

Chapter Three:

Photodissociation of a Protein

“Light has many colors to discern structures and shapes.”

3.1 Introduction

Ultraviolet photodissociation (UVPD) [1–3] and infrared multiphoton dissociation (IRMPD)[4–6] have received great attention as an alternative to other top-down dissociation methods [7–11] for whole protein characterization [12–19]. High energy UV photons preferentially cleave C_α–C bond in peptides and proteins providing nearly complete sequence coverages [12, 20]. Contrasting to UVPD, multiple low energy IR photon excitation selectively breaks the most labile amide (C-N) bonds similar to the traditional slow-heating collision activation dissociation (CAD) method [21] (details are described in **chapter 1**). IRMPD has been implemented in different instruments including quadrupole ion traps [22] and dual pressure linear ion traps [6, 23, 24]. Vasicek *et al* reported the execution of IRMPD in the HCD (High-energy Collision Dissociation) cell of a modified hybrid linear ion trap-Orbitrap mass spectrometer [25].

The dissociation mechanisms involved after high and low energy photon excitations are quite different. Absorption of a single high energy photon (in the UV) is sufficient to induce dissociation of a peptide and protein in gas phase. On the other hand, multiple absorption of low energy photons (in the IR) are required before fragmentation. Excitation is followed by fast internal vibrational redistribution (IVR) and causes a slow and steady rise of the internal energy until it exceeds the dissociation threshold and thus induces cleavage of labile bonds [2].

Despite some analytical challenges, coupling of high and low energy activation pathways in a single MS/MS event is expected to offer diverse fragmentation arrays and thus deliver improved, efficient, and well-balanced fragmentation for whole protein characterization. Tsybin *et al* reported the implementation of IRMPD with electron capture dissociation (ECD) in FT-ICR mass spectrometer [26]. Electron and photon irradiation significantly improved the formation of sequence ions for peptides and proteins. Simultaneous IR photoactivation with ETD, known as activated ion electron transfer dissociation (AI–ETD), was also implemented in an ion trap-Orbitrap Elite system [27]. Moreover, tandem ETD spectra exhibited abundant peaks related to unreacted and charge reduced precursors. Hybrid AI-ETD showed better performance for lower charge states and produce specific fragment ions. The combination of UVPD with ETD (known as ETUVPD) in an ion trap-Orbitrap has also been reported [28]. The combined ETUVPD method showed balanced fragment ions with increased number of c and z ions. The fragmentation efficiency of ETD can also be enhanced by other means such as additional activation with CID and

HCD, known as ETciD and EThcd [29,30]. These hybrid methods showed rich fragmentation spectra compared to CID, HCD and ETD alone.

Although a few studies are coupling electron and photon based methods, integrating electron-driven technique with low or high collision activation approaches, so far there is no study reporting the combination of high and low energy photons for characterizing protein. Here, we report the implementation of a method combining solid-state 5th harmonic 213 nm laser excitation with 10.6 μm CO_2 laser excitation in a hybrid quadrupole-Orbitrap mass spectrometer using different excitation schemes (consecutive IR+UV, UV+IR and simultaneous UV/IR) for top-down characterization of ubiquitin. This high-low energy photon based method (HiLoPD) improves the fragmentation pattern providing well-proportioned a/x, b/y and z-ions with richness of secondary fragment ions including d, v and w.

3.2 Materials and Methods

3.2.1 Coupling CO_2 and UV lasers with Mass Spectrometer

A 50 W cw-CO_2 laser (ULR-50, Universal Laser System®, Scottsdale, AZ) was used as a light source for IRMPD experiments. The wavelength of the CO_2 laser is 1060 nm with a beam diameter and divergence (full angle) of 4±1 mm and 5±1 mrad, respectively. The IR beam is directed to the HCD cell using gold mirrors and a half-moon (D-shaped) mirror (See **Scheme 3.1**). The IR beam was gated on an external TTL signal. Irradiation times from 0.1 to 1 s were tested. The N_2 pressure in the HCD cell was adjusted to optimize the IR fragmentation while avoiding significant loss of signal (pressure controller set to ~0.09 MPa). Also, a BaF_2 window (wavelength range 0.2-12 μm, Ø 25.4 mm, thickness 5 mm) was placed at the rear of the HCD cell, which transmit both IR (10.6 μm) and UV (213 nm) beams with 90 and 85% efficiency, respectively. A simple schematic presentation of the coupling of combined CO_2 and UV lasers in the HCD cell of a hybrid quadrupole-Orbitrap is presented in **Scheme 3.1**.

For UVPD experiment combined with IRMPD, the fifth harmonic (λ=213 nm, ~1 mJ/pulse) of a 20 Hz BrillantB solid-state Nd:YAG laser (Quantel, Les Ulis, France) source was used **as mentioned in the chapter 2**. A mechanical shutter (SH05/TSC001, Thorslab) was installed between the optical mirror and the half-moon mirror to control UV laser pulses. This shutter allows, on demand, the UV beam in the HCD cell. For UVPD, the optimal shutter open time was determined to be 0.2 s (4 laser shots). In order to irradiate ions only when ions are in the HCD cell, the voltage on test-point 18 (TP18), located on Q-Exactive electronic board, was monitored. In our experimental conditions, the falling edge (-10 V → -350 V) on the TP18 is used to determine the moment when ions are ejected from the C-trap to the HCD-cell (see **Figure 3.1**). Two independent TTL pulses are then generated, with width and delay adjustable with regards to the TP18 trigger. The TTL pulses are used to lift the gate on the CO_2 laser and open the shutter on the UV beam path.

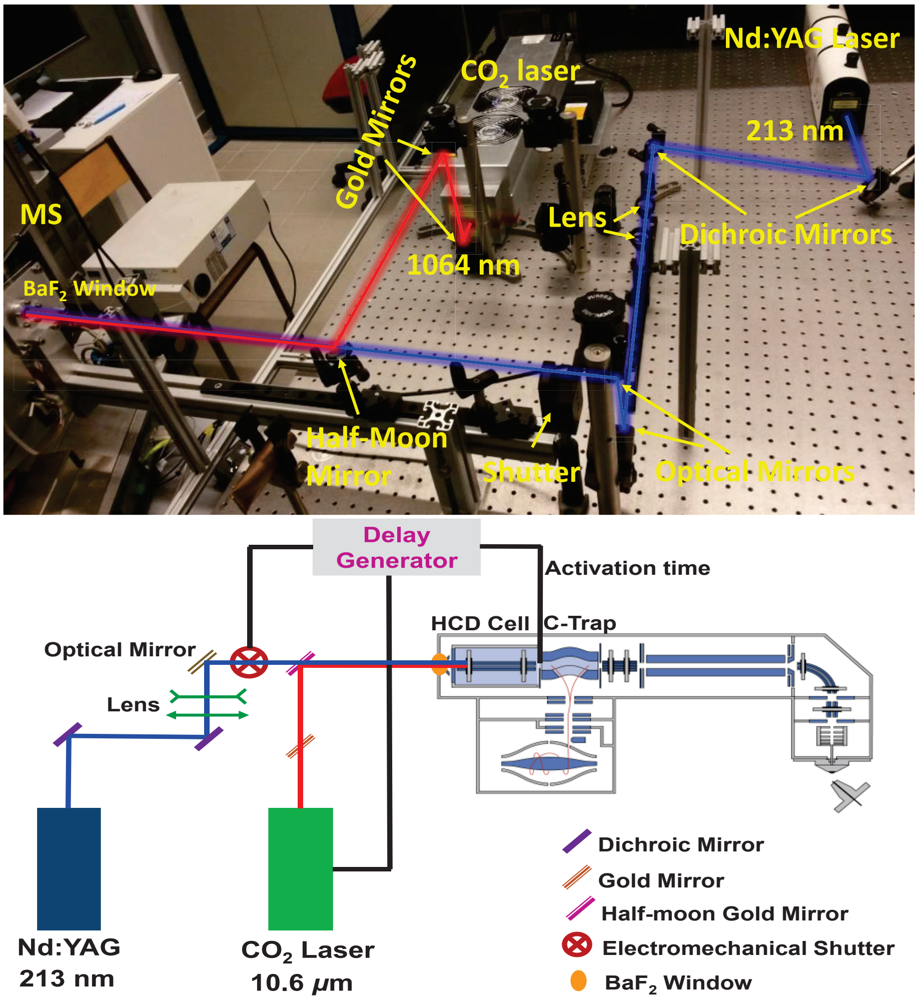

Scheme 3.1 Schematic representation of the execution of combined IRMPD and UVPD in the HCD cell of a hybrid quadrupole-Orbitrap mass spectrometer.

For combined IRMPD+UVPD experiment, three different coupling schemes between IR and UV were implemented (**Figure 3.1**). In scheme I, CO_2 laser was *ON* for 1 s and then followed by 4 UV pulses (0.2 s). In scheme II, 4 pulses of UV were admitted in the HCD cell first, and followed by 1 s of CO_2 laser. In those first two schemes, IR and UV were used consecutively: when CO_2 laser was *ON*, the UV laser was *OFF* and *vice versa*. In scheme III, the CO_2 laser was turned *ON* and the UV shutter was open concomitantly. As in previous schemes, IR was left *ON* for 1 s while the UV shutter was left open for 0.2 s (4 pulses). In each scheme, the coupled IR/UV irradiation takes place during single HCD events in MS^2 sequences.

3.2.2 Mass Spectrometry

All experiments were performed on a hybrid quadrupole-Orbitrap Q-Exactive® mass spectrometer (Thermo Fisher Scientific, San Jose, CA, USA) equipped with a HESI ion source. Ubiquitin (76 residues, 8.6 kDa) from bovine erythrocytes was obtained from Sigma-Aldrich and used without any further purification. Ubiquitin samples were prepared at 10 μM concentration in 50/49/1 (v/v/v) methanol/water/acetic acid and directly infused to MS at a flow rate of 5 μL/min. All mass spectra were acquired using a mass range of 200-2000 *m/z* and resolving power of 140000 at *m/z* 400. Spray voltage, capillary temperature, and sheath gas flow rate were set to 4.0 kV and 320 ˚C, and 20 respectively. The AGC (Automatic Gain Control) target was set to $5x10^6$ and the maximum injection time was set at 250 ms. The isolation width was 8-10 Th. To avoid collisions and CID contamination, HCD collision energy was set to the minimum 2 eV. All experiments were performed for 3 microscans and averaging for 50 scans.

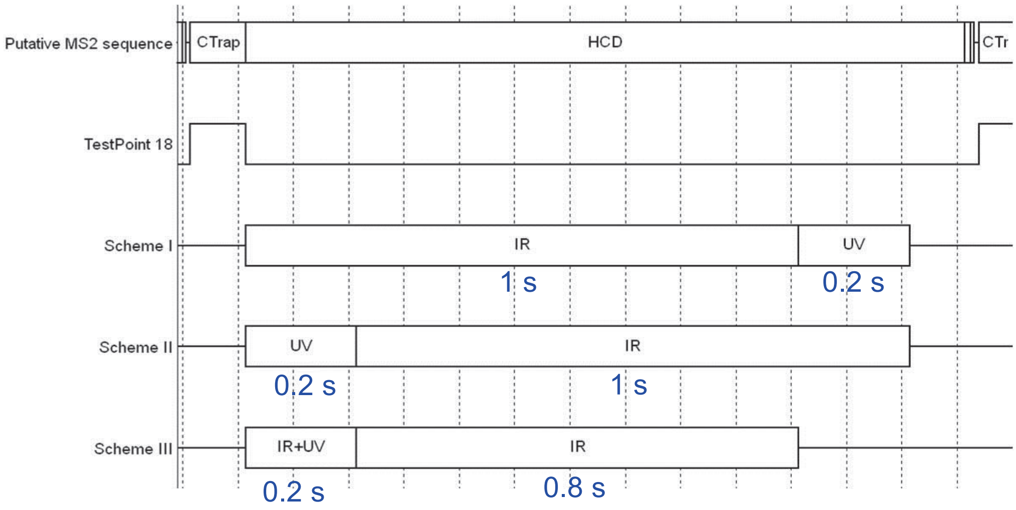

Figure 3.1 Consecutive and simultaneous irradiations of UV and IR laser in the combined high-low energy photon based method.

3.2.3 Data Analysis

Raw files were deconvoluted and deisotoped to the neutral monoisotopic masses using Xtract algorithm provided by Thermo Scientific Inc. Manual analysis of IRMPD, UVPD, and combined UVPD and IRMPD data was performed with the aid of ProSight Light software [31] and Protein Prospector V5.14.4. (http://prospector.ucsf.edu/prospector/mshome.htm). All major ion types (a, a+1, a+2, b-1, b, b+1, b+2, c-1, c, c+1, x-1, x, x+1, x+2, y, y-1, y-2, z-1, z, z+1) were considered. We observed substantial number of secondary fragment ions including d, v and w which were analyzed by Protein Prospector. H_2O and NH_3 losses from the fragment ions were also considered. Single protein mode with a fragment mass tolerance set to 15 ppm was used for all methods.

3.3 Results and Discussion

3.3.1 Optimization of IRMPD on Intact Protein.

The overall performance of IRMPD is hindered by the failure to provide adequate fragmentation of peptide or proteins at the standard pressure in the HCD cell. Although relatively high pressure is desirable for collision cooling during the ion accumulation to obtain maximum trapping efficiency, it is disadvantageous to ion activation and dissociation [32]. In the Q-Exactive mass spectrometer, the HCD cell and C-trap are filled with N_2 gas with chamber pressure of ~10^{-5} mbar known as High Vacuum (HV) region whereas Orbitrap kept the low pressure at ~10^{-10} mbar designated as Ultra High Vacuum (UHV) region. A pressure regulator allows control of the collision gas valve and hence the pressure in the HCD cell. The position of the pressure controller also has an effect on the High Vacuum pressure value. Here, where we discuss high and low pressure it is the HCD cell pressure governed by the pressure controller position and estimated *via* High Vacuum gauge that is being considered. A previous study on hybrid QLT-Orbitrap indicated that the level of the collision gas (N_2) must be lowered [33]. At high pressure in the chamber (HV ~4.6×10^{-5} mbar, pressure controller 0.5 MPa), there is no noticeable photodissociation observed for +12 charge state ion of ubiquitin even at longer (1 s) irradiation time (**Figure 3.2)**. The collision frequency, which is associated with the collision cross-section [34] of the protein, of +12 charge state ion of ubiquitin is typically around 6700 s^{-1} at high pressure of 10^{-4} mbar (**Figure 3.3**). This high collision rate promotes collision deactivation and cooling of the protein before it can undergo fragmentation, resulting in limited photodissociation being observed. The fragmentation efficiency improves as the pressure is reduced. At low pressure (HV ~9.3 x 10^{-6} mbar, pressure controller

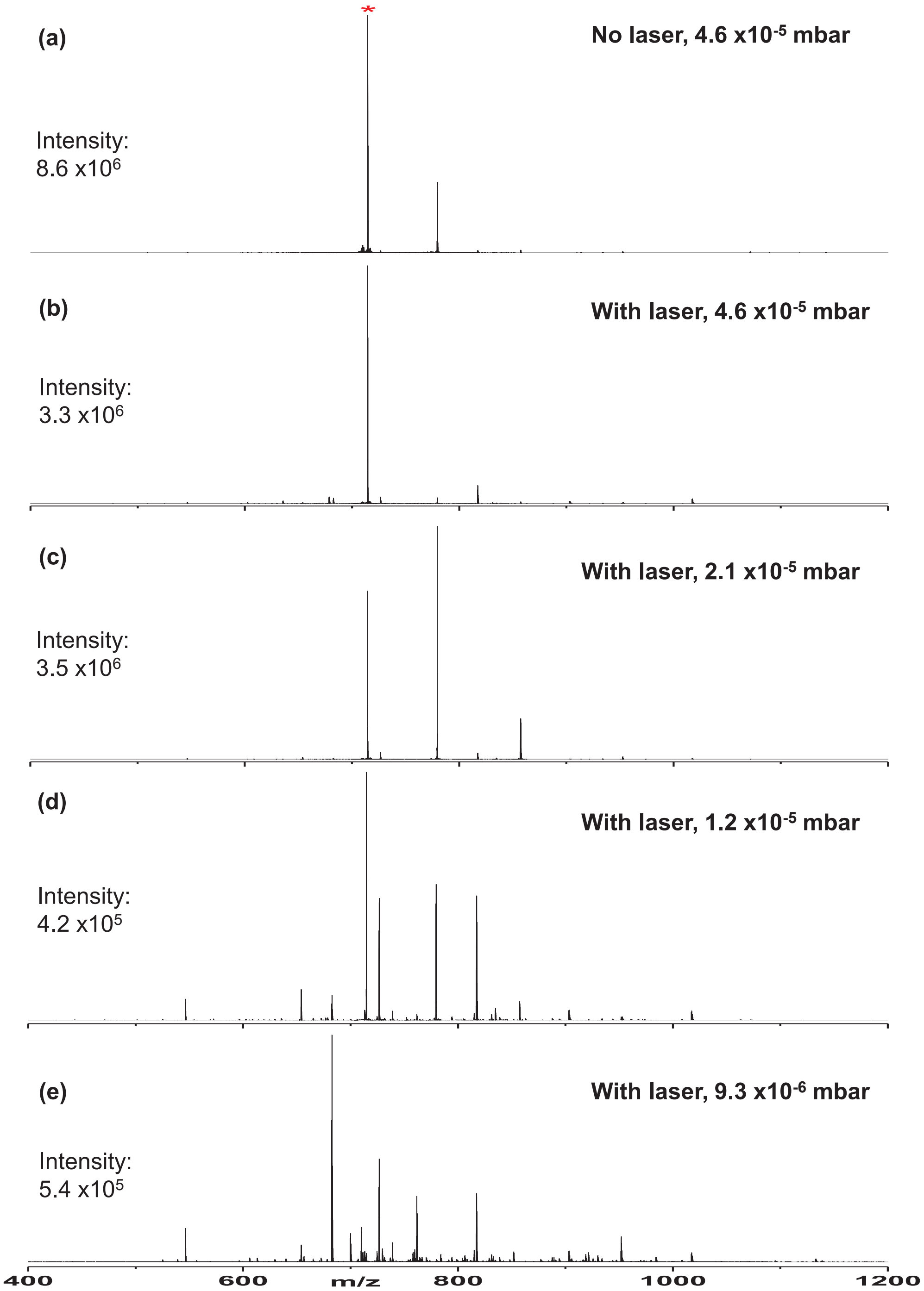

Figure 3.2 Impact of pressure on the fragmentation of the +12 charge state precursor ion (*m/z*=714.7279) of ubiquitin at 1 s irradiation time by IRMPD. The precursor ion is indicated as star (*) sign.

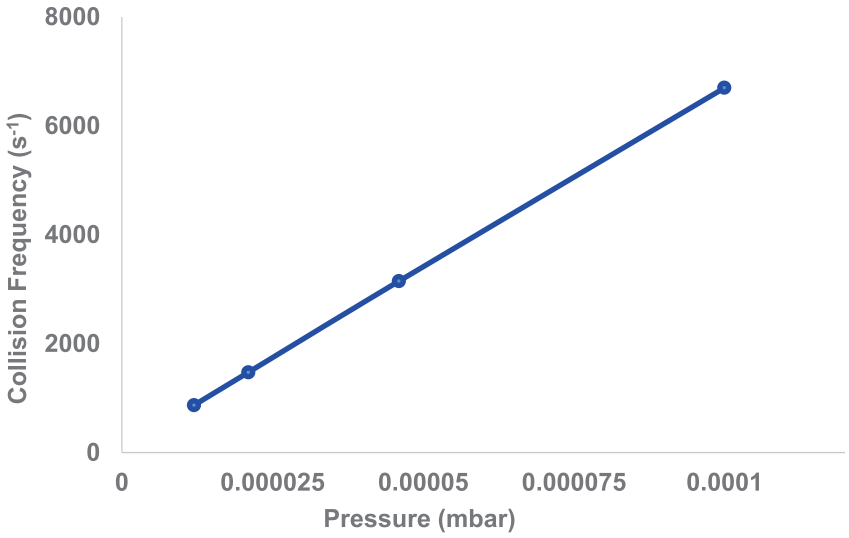

Figure 3.3 Effect of pressure on the collision frequency (s^{-1}) of the +12 (*m/z*=714.7279) ion of ubiquitin. Collision Cross-Section (CCS) value was taken from the ref. 34.

~0.09 MPa), the dissociation efficiency is augmented significantly for +12 charged precursor ion of ubiquitin. At ~9.3 x 10^{-6} mbar pressure, the collision frequency of +12 ion of ubiquitin is reduced. It is noticed that pressure lower than ~0.09 MPa on the pressure controller can lead to more fragment ions, however, the signal is not very stable at this range and moreover sensitivity and resolution are also decreased. The irradiation time also has a major impact on the photodissociation yield of ubiquitin (**Figure 3.4**). At lower pressure, when ubiquitin is irradiated for 0.1 s, the fragmentation efficiency is only about 25% which is considerably improved to 68% for 1 s irradiation time **(Figure 3.5**). Most previous studies related to IRMPD used a laser irradiation time less than 0.1 s in LIT [6 , 27]. As is evident from other studies, higher laser power is required for superior fragmentation efficiency of larger peptides and intact proteins [6,35,33,36].

The IRMPD on the +12 charge state ion of ubiquitin shows a total of 141 fragment ions of which 41 are b-type and 98 are y-type ions. Exact masses and assignments of the ions detected in the IRMPD of the 12+ precursor ion (*m/z*=714.7279) of ubiquitin are summarized in **Table A3.1** (see in appendix). For this charge state, twice as many of y-type ions are identified as compared to b-type ions. The sequence coverage for the +12 ion is 59% (44 bonds break) which is significantly higher than the coverage 24% (18 bonds break) reported earlier when IRMPD was first implemented in high resolution Orbitrap mass spectrometer (**Figure 3.6**) [25]. We found that 60%

of the nominal laser power with combination of lower pressure (HV ~9.3 x 10^{-6} mbar) and longer irradiation time (~1 s) are optimal for characterization of intact protein by IRMPD in a quadrupole-Orbitrap system.

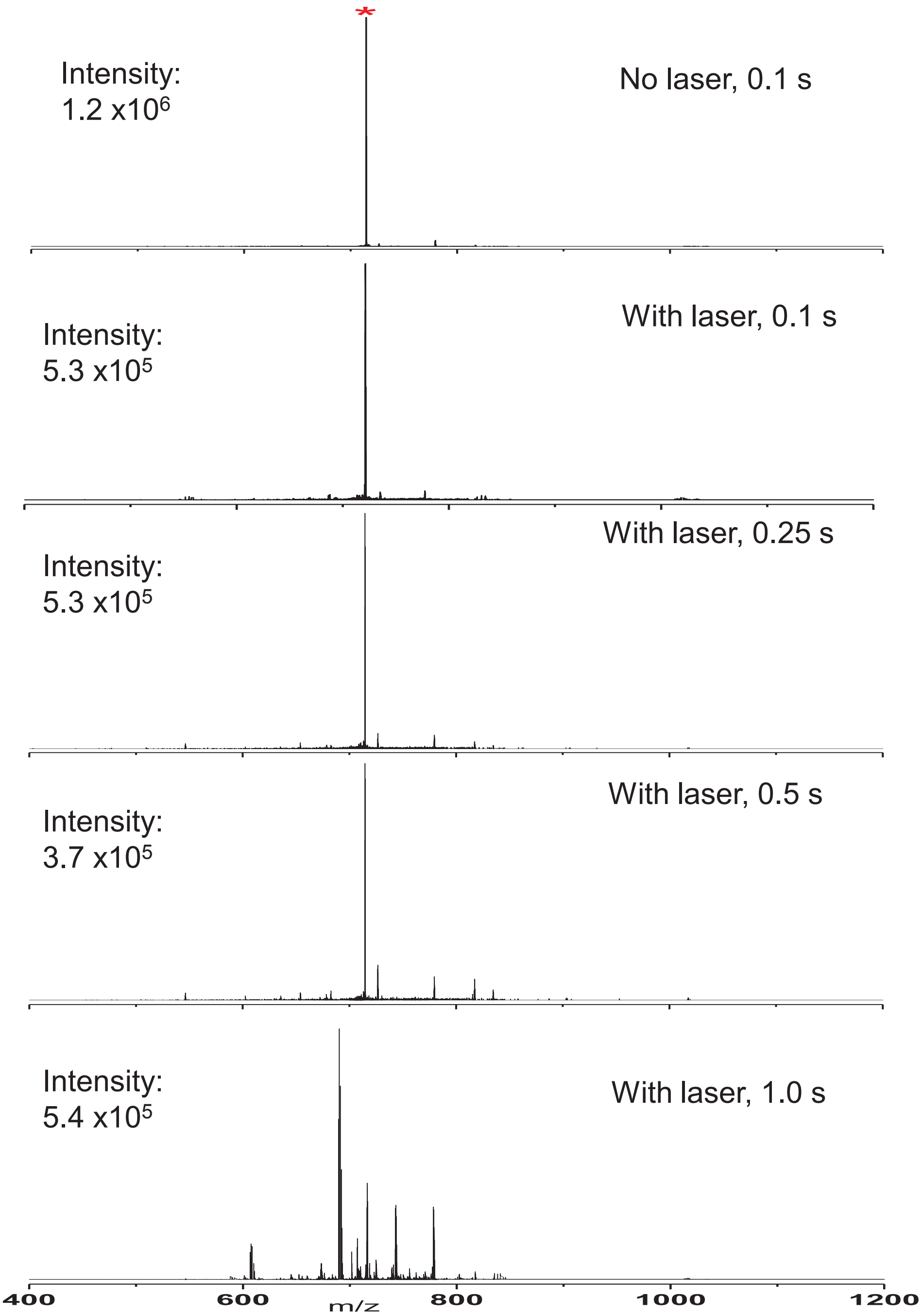

Figure 3.4 Effect of IRMPD irradiation time (s) on the +12 charge state precursor ion (*m/z*=714.7279) of ubiquitin at low pressure in the HCD cell (9.3 x10^{-6} mbar). The precursor ion is indicated as star (*) sign.

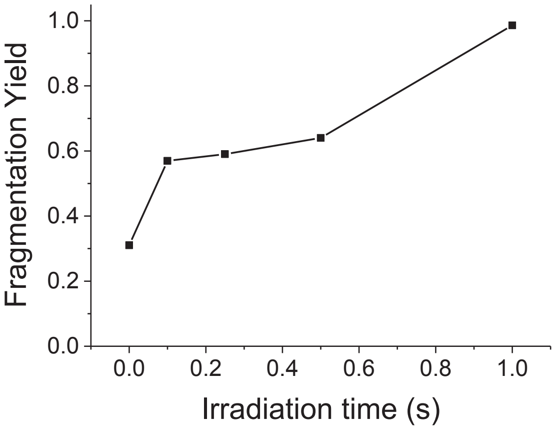

Figure 3.5 Fragmentation yield based on the IRMPD irradiation time (s) for the +12 charge state precursor ion (*m/z*=714.7279) of ubiquitin at the lowest HCD pressure (~9.3 x10^{-6} mbar). Fragmentation yield = Σ(photofragments)/Σ(photofragments+precursor).

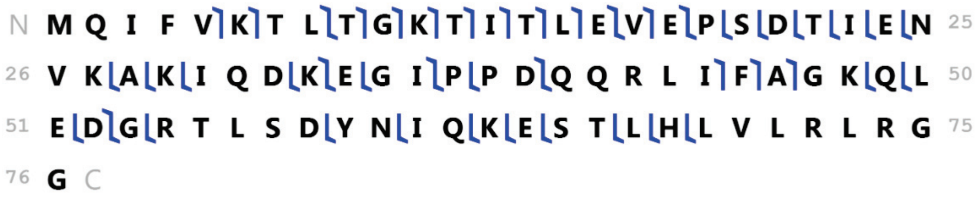

Figure 3.6 IRMPD sequence coverage (59%) of the +12 charge state precursor ion (*m/z*=714.7279) of ubiquitin.

3.3.2 UVPD, IRMPD and HiLoPD on Ubiquitin.

The photodissociation mass spectra using IRMPD, UVPD and combined IR and UV (scheme I, II, III**)** of the +13 precursor ion of ubiquitin are presented in **Figure 3.7**.

First of all, the +13 precursor ion of ubiquitin was subjected to UVPD only. All 213 nm UVPD experiments have been performed in the low pressure regime (~9.3 x 10^{-6} mbar) to make unbiased comparison with consecutive or simultaneous irradiation of IRMPD and UVPD. Even at low pressure, the 213 nm UVPD on the +13 charge state ion identifies a total of 209 fragment ions (**Figure 3.8a**) including 68 a-type, 5 b-type, and 10 c-type ions as well as 38 x-type, 59 y-type and 28 z-type ions (**Table A3.2**, in appendix). Along with traditional a/x, y and c/z ions, a+1/x+1, x+2, y-1, y-2, c-1, and c+1 ions of ubiquitin are also detected. Recently, we reported that the radical-driven backbone fragmentation provides 22 distinctive fragment ion types for peptide anions at 213 nm UVPD [15].

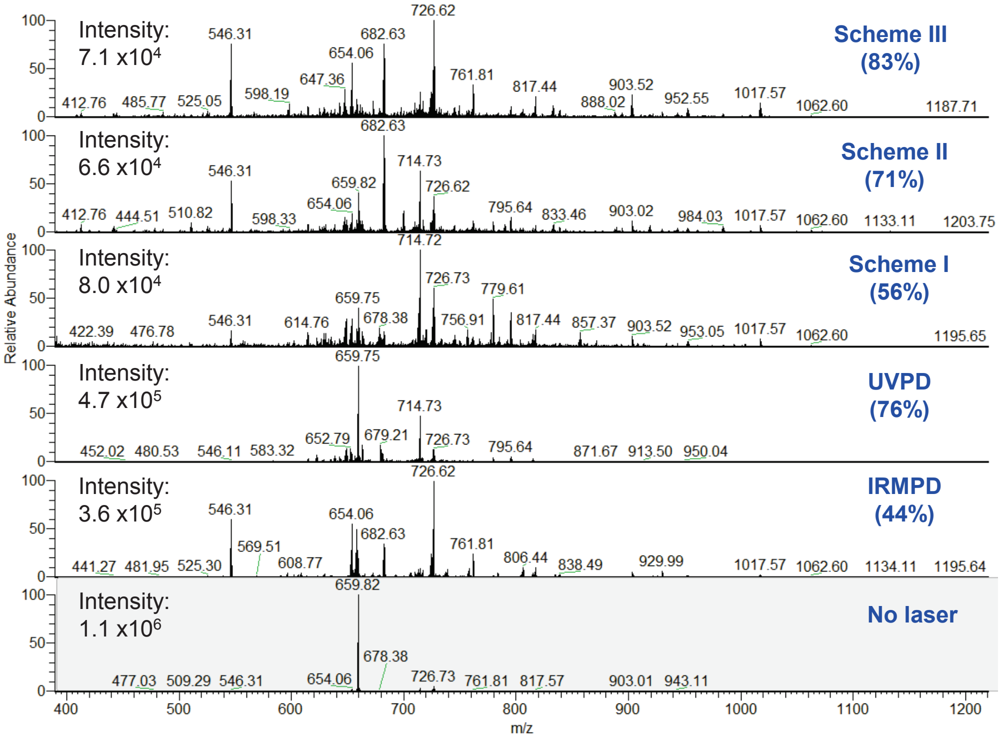

Figure 3.7 Combined IR and UV (schemes I, II, III), IRMPD and UVPD spectra of the +13 charge state precursor ion (m/z=659.8249) of ubiquitin. Isolation spectrum with no activation is also presented. Sequence coverages are indicated in brackets.

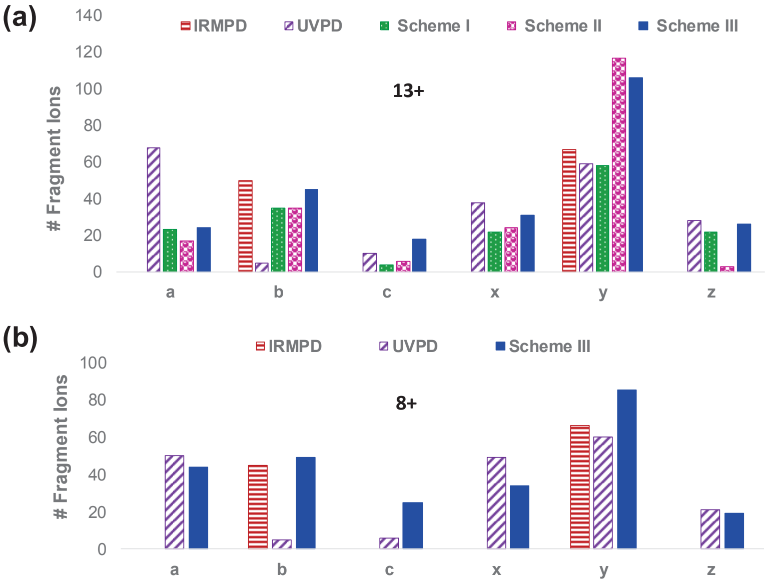

Figure 3.8 (a) Number of fragment ions detected by IRMPD, UVPD, and combined IR and UV (scheme I, II and III) of the +13 charge state precursor ion (m/z=659.8249) of ubiquitin. (b) Number of fragment ions detected by IRMPD, UVPD and HiLoPD (scheme III) of the +8 charge states precursor ion (m/z=1071.5864) of ubiquitin.

High energy UVPD (157 and 193 nm) reported abundant formation of the radical a+1 and x+1 ions [37,38,39]. Here we observed the similar feature at 213 nm (5.8 eV) UVPD which produces significant number of a+1/x+1 ion. The mechanism of the homolytic cleavage of the C_α-C(O) bond which produces a+1/x+1 ions has been proposed elsewhere [15]. Moreover, the formation of y-1 and y-2 occur from the secondary dissociation of the x+1 radical and is associated with presence of proline residues [38,18]. Neutral losses of NH_3 are detected from a and y ions. The UVPD sequence coverage achieved for the +13 precursor ion is 76%.

The IRMPD experiment on the +13 ion of ubiquitin detects a total of 121 fragment ions (**Figure 3.8a**). Exact masses and assignments of ions detected in the IRMPD of the +13 ion (*m/z*=659.8249) of ubiquitin are summarized in **Table A3.3** (in appendix). Among them, 49 ions are b–type and 67 ions are y-type fragments. The formation of only b and y-type ions is expected from cleavages of C-N bonds proceeding *via* vibrationally-excited ground state dissociation. H_2O and NH_3 losses from the b and y ions are also noticed, with H_2O losses being more widespread than NH_3 loss. The loss of water is energetically favorable from the protonated acidic group [40]. Ubiquitin has 7 threonine (T), 6 glutamic acid (E), 5 aspartic acid (D) and 3 serine (S) residues which may promote the widespread water loss. Low (z = +1) to high charge states (z = +12) of the b and y ions are observed, with the same fragment ion often being observed in many different charge states. For example, b_{17} ion with +2, +3, and +4 charge states are detected at *m/z* 952.5491, 635.3695, and 476.7778, respectively. The IRMPD sequence coverage of this charge state precursor ion is 44%.

The same precursor ion (z = +13) was then fragmented with UVPD in combination to IRMPD. In the consecutive scheme I, in which first IR then UV irradiation was performed (see **Figure 3.1**), the total number of detected fragment ions is remarkably declined compared to UVPD (**Figure 3.8a**) alone. Despite this decrease, the number of b-type ions detected is significantly increased. The y-type ions remain same as UVPD alone. The a/x and c/z ions are also remarkably suppressed. Overall, the sequence coverage using this scheme is only 56 % (**Figure 3.7**). In scheme I, IR laser pulses produce ubiquitin in its vibrationally hot electronic ground state (**Figure 3.9a**). Excitation promotes formation of hot ions and eventually ground state dissociation. And thus less parent ions are then available for UV fragmentation. UV excitation of hot ions is also possible.

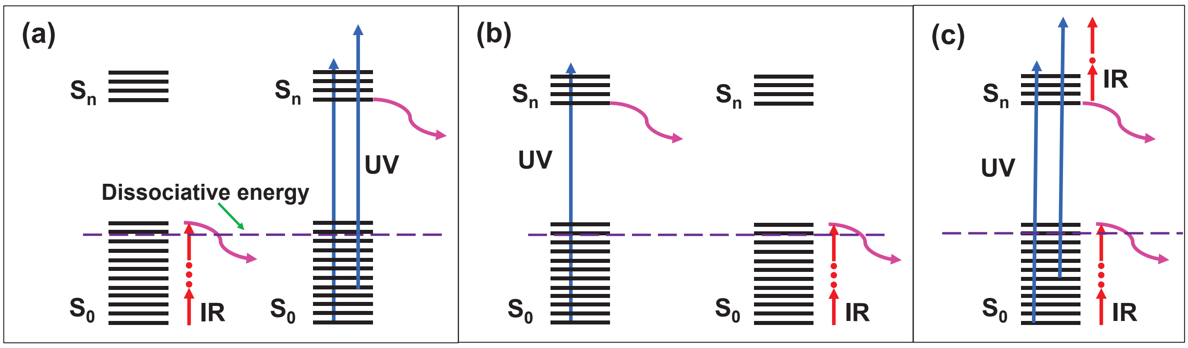

Figure 3.9 Ground and excited state dissociation channels in scheme I (a), scheme II (b) and scheme III (c)

In the consecutive scheme II (**Figure 3.1**), when irradiation with UV laser pulses is followed by IR irradiation, the overall number of detected fragment ions is considerably higher compared to scheme I (**Figure 3.8a**). The number of b and y-type ions is sharply increased as compared to both UVPD and scheme I. The relaxation following electronic excitation either by light emission, internal conversion through a conical intersection or via fragmentation is expected to be fast (typically ranging from fs to ns timescales). In scheme II, IR excitation is occurring after electronic excitation and relaxation has occurred. The UV laser promotes excited states dissociation whereas IR laser subsequently leads to the ground state dissociation (**Figure 3.9b**). The combination of the two dissociation mechanisms explains the large amount of detected fragment ions in scheme II. In this case, the sequence coverage for this charge state precursor ion is 71% and is comparable to the one observed in UVPD.

The simultaneous introduction of UV and IR lasers (HiLoPD, high-low photodissociation, scheme III, shown in **Figure 3.1**), on the +13 ion of ubiquitin produces a more diverse range of fragment ions than any of IRMPD, UVPD, Scheme I and Scheme II (**Figure 3.8a**). Exact masses and assignments of the ions detected in the combined UVPD and IRMPD of the +13 ion (*m/z*=659.8249) of ubiquitin are summarized in **Table A3.4** (in appendix). Compare to UVPD, a substantial increase in b and y ions is observed in scheme III. The number of b-type ions increases from 5 to 48 while the number of y-type ions raises from 59 to 106 ions. The number of c-type ions is increased slightly from 10 to 18.

The number of x and z-type of ions remained nearly same as UVPD, whereas the number of a-type ions is decreased noticeably from 68 to 24 ions with respect to UVPD. Secondary fragmentation leads to the formation of d, v, and w ions. It is noticed that w ions are significantly increased in scheme III compared to UVPD, scheme I and II (**Figure 3.10**). Due to the excess energy in scheme III, elimination of other groups such as R, CO and CONH are observed near the position of primary cleavage. High energy 157 and 193 nm UVPD has also reported the side-chain losses from the a+1/x+1 ions to form d, v and w ions [39]. Kjeldsen *et al* noticed the formation of d and w ions from the Leu and Ile comprising peptide in hot electron capture dissociation [41]. Zhang and Reilly also observed the formation of v, w_a, and w_b ions from x+1 ion of Leu and Ile containing peptides by UVPD at 157 nm [42]. It is interesting to note that ubiquitin has a total of 16 Leu and Ile residues, and thus formation of these secondary ions allows to distinguish isomeric residues. In addition, HiLoPD can be applied for *de novo* sequencing of peptides [43]. The sequence coverage of the +13 ion of ubiquitin obtained at scheme III is 83%. The photophysical interpretation of this increase in fragmentation yield is that IR irradiation concomitant to UV irradiation can lead to vibrational excitation as well as excitation of higher electronic states and thus produce a rich fragmentation array (**Figure 3.9c**). **Figure 3.11** shows the sequence maps obtained for the +13 charge state precursor ion in IRMPD, UVPD and HiLoPD (scheme III). The sequence coverage is improved in HiLoPD thanks to the combination of IR and UV irradiation. While IRMPD yields more fragment ions from the N-terminal, UVPD produces ions from the mid and C-terminal regions. Interestingly, HiLoPD able to produce fragments ions from all regions.

For a lower charge state (z = +8), the simultaneous irradiation of scheme III (HiLoPD) also showed a balanced fragmentation pattern. The total number of detected fragment ions of this charge state in scheme III is higher than both IRMPD and UVPD (**Figure 3.8b**) alone. A considerable number of b and y ions are observed in this lower charge state, and c-type ions are also detected. Only z-type ions remain essentially the same as in UVPD. The sequence coverage of the +8 ion of ubiquitin obtained with HiLoPD (scheme III) is 85%. Formation of d, v and w ions also is noticed for these charge states similar to +13 precursor ion.

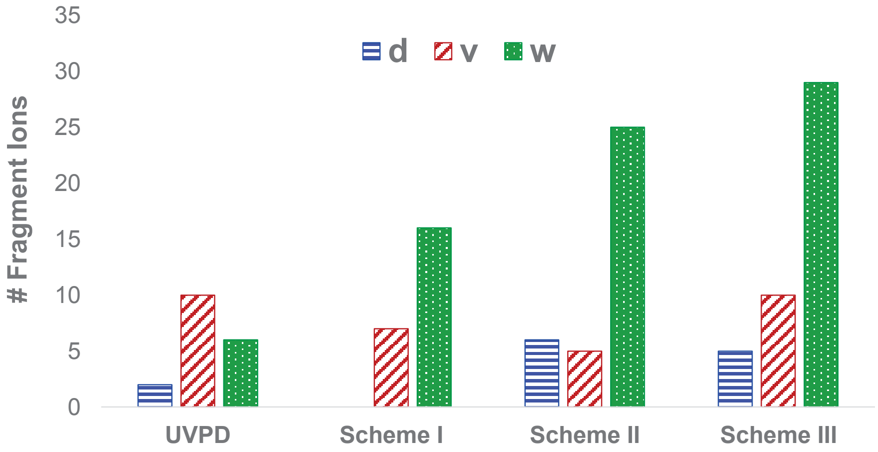

Figure 3.10 Number of secondary fragment ions (d, v and w) detected by UVPD, and combined IR and UV (scheme I, II and III) of the +13 charge state precursor ion (m/z=659.8249) of ubiquitin.

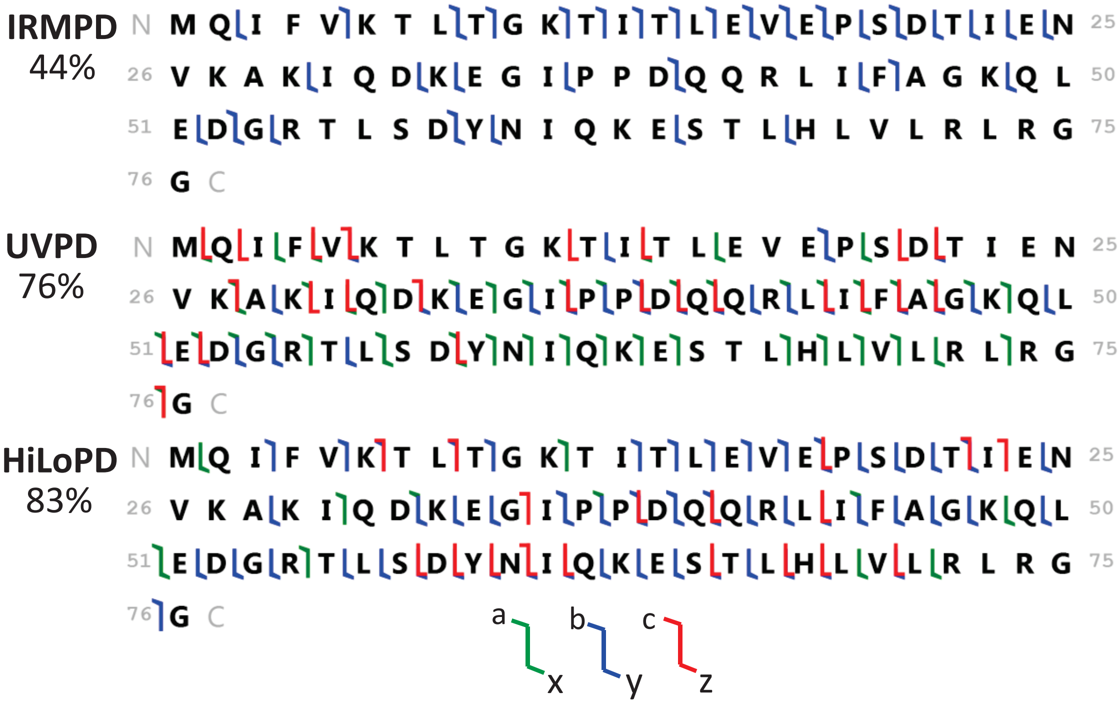

Figure 3.11 Sequence coverage of the +13 charge state precursor ion (m/z=659.8249) of ubiquitin observed by IRMPD, UVPD and HiLoPD (scheme III).

Overall, IRMPD selectively produces b/y, and b-H_2O/y-H_2O ions whereas UVPD preferentially yields a+1/x+1, a/x, y-1, y-NH_3, z, v and w ions (**Figure 3.12a**). The hybrid HiLoPD (scheme III) method generates b/y, b-H_2O/y-H_2O, x, x+1, y-1, y-2, y-NH_3, z, v and w ions. Bond breaking and sequence coverage of high (z = +13) and low (z = +8) ions of ubiquitin obtained by IRMPD, UVPD and HiLoPD (scheme III) are shown in **Figure 3.12b and 3.12c**. HiLoPD allows to improve the efficiency of structural characterization of ubiquitin compared to IRMPD and UVPD. Moreover, sequence coverages obtained with HiLoPD are similar to those theoretically expected by combining UVPD and IRMPD (calculated IR+UV, see **Figure 3.12c**).

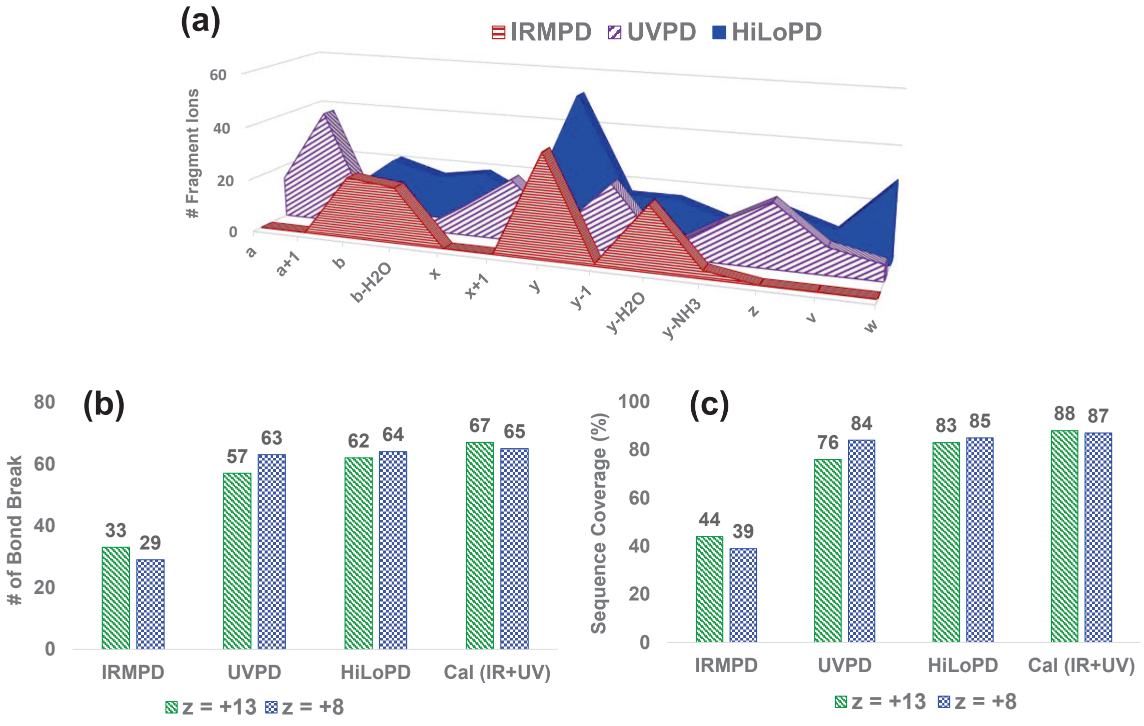

Figure 3.12 (a) Comparative view of fragment ion types generated by IRMPD, UVPD and HiLoPD (scheme III) of the +13 charge state precursor ion (*m/z*=659.8249) of ubiquitin. (b) Number of bond breaks (c) Sequence coverage (%) obtained by IRMPD, UVPD, HiLoPD (scheme III), and theoretically combined IR and UV (Calculated (IR+UV)) of the +13 (*m/z*=659.8249) and +8 (*m/z*=1071.5864) charge state precursor ions of ubiquitin.

3.3.3 Amino Acid Specific Fragmentation

Ubiquitin contains 76 amino acid residues. The residue specific fragmentation pattern of high (+13) and low (+8) charge states of ubiquitin observed in IRMPD and UVPD are presented in **Figure 3.13**. In IRMPD, most of the b/y fragment ions are obtained from the N-terminal region whereas in UVPD a/x, y and z ions are detected from the C-terminal region. In addition, UVPD produces more fragment ions closed to Pro37, Pro38 and two aromatic residues at Phe45 and Tyr59.

For region-specific fragmentation, the 76 amino acid residues of ubiquitin are divided into region I (1-18), region II (19-35), region III (36-48) and region IV (49-76). In IRMPD, region I (1-18) shows more b and y ions compared to other regions (**Figure 3.14a**). High (+13) charge state shows more b/y ions than low (+8) charge state in region I. Ubiquitin has five β-strands (1-7, 10-17, 40-45, 48-50, 64-72 residues) and four of them are located in the region I and IV. In gas phase, β sheets are less stable and prompt to fragmentation compared to α-helix structure which are stabilized by the supplementary salt bridges [44]. Less fragment ions are detected from the region II (19-35) and III (36-48) which may be due to the fact that these regions can form six and five salt bridges in gas phase, respectively [45]. At low pH, the C-terminal of the ubiquitin native states is transformed to an extended α-helix (A state) [46, 47]. In this state, half of the N-terminal existed as β-sheet whereas half of the C-terminal elongated with high α-helical propensity in presence of methanol (**Figure 3.15**). This could explain that in IRMPD, less fragment ions are observed from the C-terminal region for high (+13) charge state.

In UVPD, more fragment ions are detected from region III (36-48) and IV (49-76). Reduced number of UVPD fragment ion is observed in region I (1-18) which is very different as compared to IRMPD. High charge (+13) state show significant number of a/x, y, and z ions in region III (36-48) compared to low (+8) charge state (**Figure 3.14b**). For region IV (49-76), nearly same number of fragment ions are identified for +13 and +8. For all charge states, more ions detected from the C-terminal.

In vacuum (157 nm and 193 nm) UVPD, the backbone cleavage of peptide and protein occurred before the intramolecular vibrational redistribution [12, 48]. However, 213 nm UVPD may adopt different photofragmentation mechanism. The regions III and IV which produce more fragment ions have one phenylalanine (Phe) at 45 and one tyrosine (Tyr) residue at 59, respectively.

In HiLoPD (scheme III), the overall fragmentation dynamics is similar to UVPD. More fragment ions a/x, b/y and c/z are produced from the C-terminal regions III and IV compared to the N-terminal regions I and II (**Figure 3.14c**). More b-type ions are generated from region I similar to IRMPD. In addition, significant number of y-type ions are produced from C-terminal. For small peptides, when Tyr is located in the C-terminal, y-type ions are observed [49].

Our results suggest that the photofragmentation yield of IRMPD not only depends on the conformation of the ubiquitin but also relates to the α-helical, β-strand characters and salt-bridged formation in the secondary structure. Nonetheless, UVPD and HiLoPD fragmentation yields are affected by the local environment of the aromatic residues. However, further studies are required to employ these techniques for larger protein to confirm these findings.

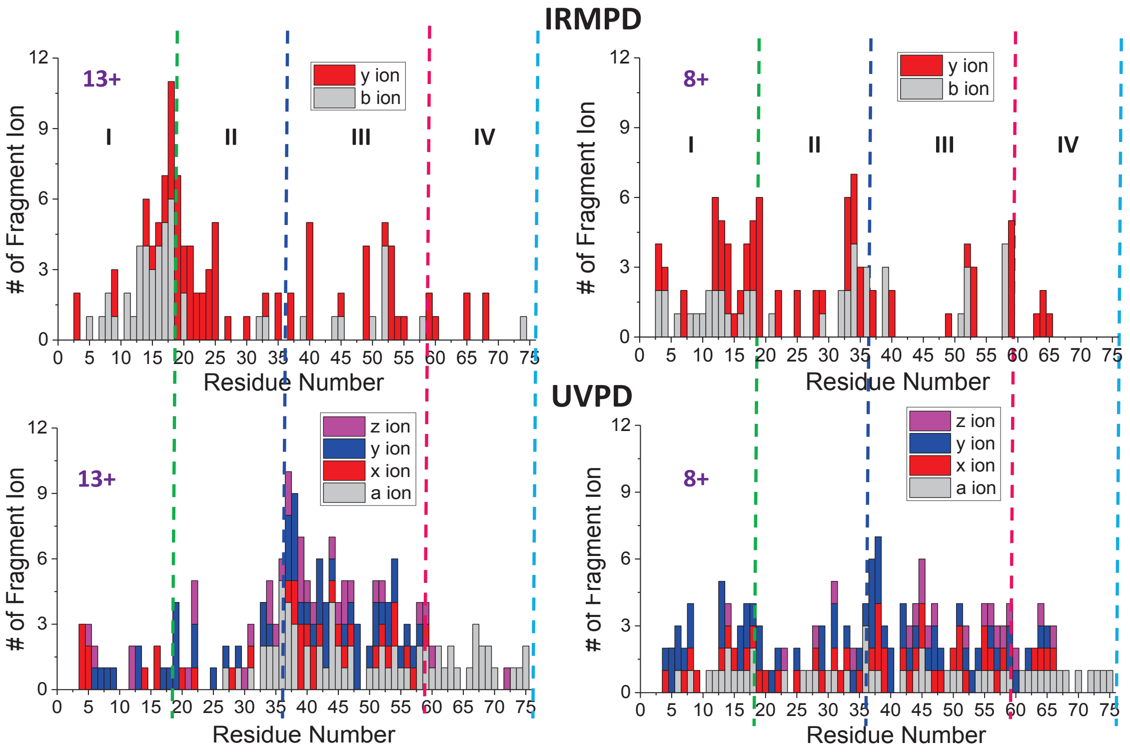

Figure 3.13 Amino acid specific fragmentation pattern observed in IRMPD and UVPD for the high (+13) and low (+8) charge states of ubiquitin.

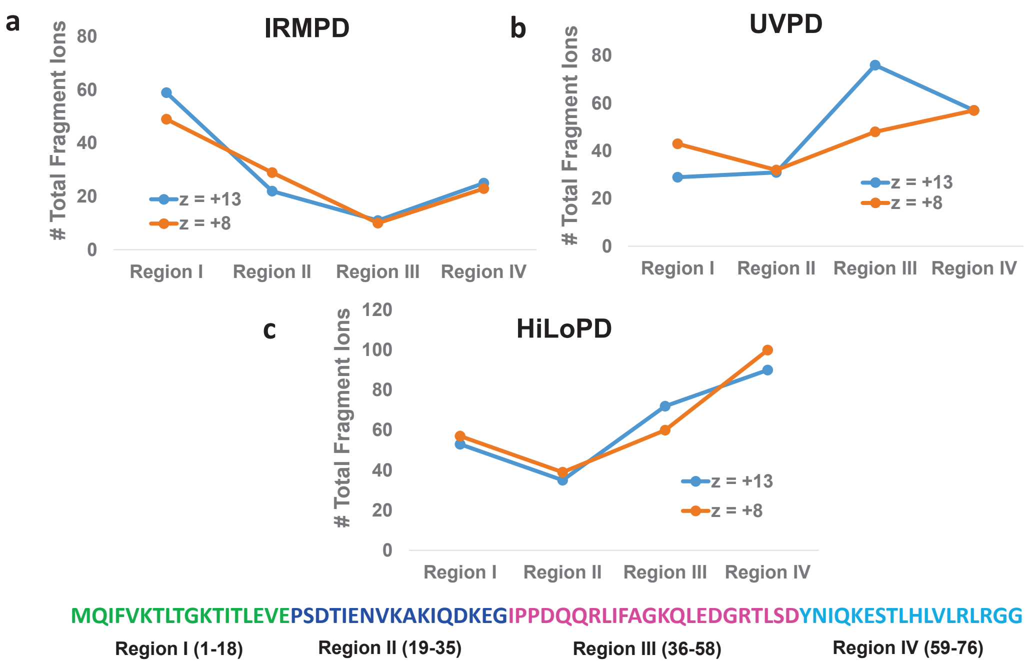

Figure 3.14 Region specific fragmentation pattern observed in IRMPD, UVPD and HiLoPD for the high (+13) and low (+8) charge states of ubiquitin.

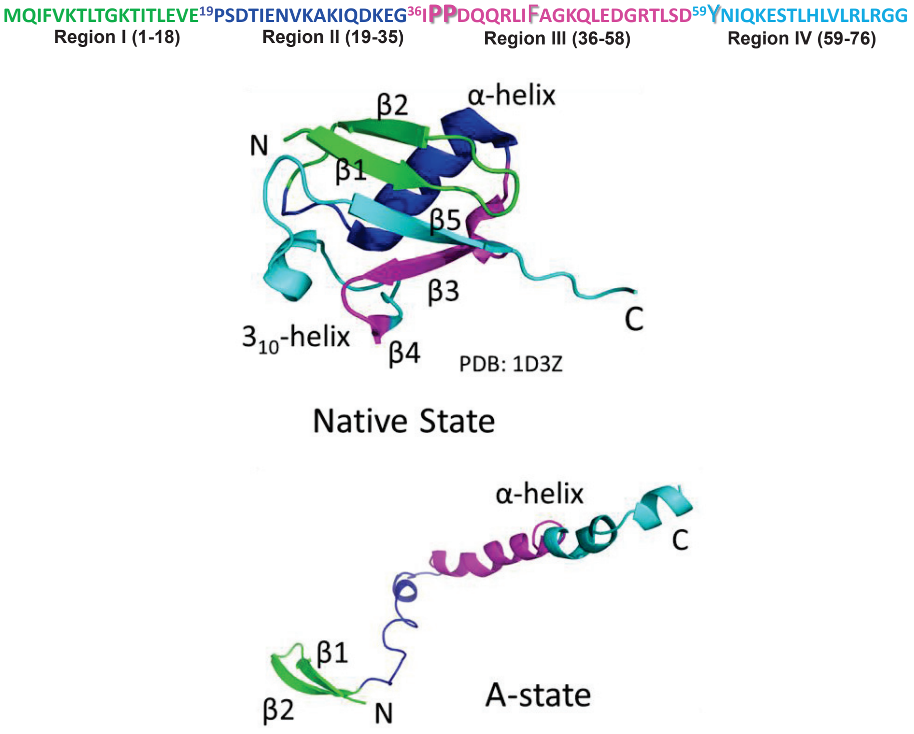

Figure 3.15 Native and A-State of Ubiquitin

3.4 Summary

We have reported IRMPD, 213 nm UVPD, and HiLoPD patterns of ubiquitin in a hybrid quadrupole-Orbitrap mass spectrometer. Improved performance of IRMPD is observed when we use high laser powers coupled with a combination of very low pressure and longer irradiation time in the HCD cell. Significant numbers of b/y ions and neutral losses of NH_3 and H_2O are detected by IRMPD. Similar to excimer 193 nm UVPD, solid-state 213 nm UVPD can promote C_α–C cleavage generating abundant a/x, y, and z fragment ions for ubiquitin.

The coupling of low-energy IRMPD and high-energy UVPD was implemented using three different irradiation schemes. In scheme I, where IR irradiation is followed by UV, the detected fragment ions are decreased as compared to UVPD only, which is mainly due to intense IR fragmentation prior to UV excitation. When UV irradiation was followed by IR (scheme II), the total number of detected fragment ion is slightly increased. In scheme III, while UV and IR lasers irradiation is simultaneous, the total number of detected fragment ions is increased. Excited and ground state dissociation channels promote widespread fragmentation in ubiquitin. Compared to UVPD, b/y-type ions are increased. We observed that, while a/x fragment ions are decreasing, nearly equal number of d, v and w ions emerge, which can lead to identify the isomeric residues in a protein.

Finally, the relation between regions of a protein that displayed high fragmentation yields and its conformational flexibility was explored in IRMPD, UVPD and HiLoPD. While for IRMPD, the conformational ensemble of gaseous ubiquitin cations preserve some memory of the solution phase structure, UVPD and HiLoPD fragmentation yields are affected by the local environment of the aromatic residues within the protein. In particular for ubiquitin, substantial fragmentation occurs at the half of the C-terminal region III and IV closed to Pro37, Pro38, Phe45 and Tyr59, respectively.

Bibliography

1. Reilly, J.P.: Ultraviolet photofragmentation of biomolecular ions. Mass Spectrom Rev. 28, 425–447 (2009). doi:10.1002/mas.20214

2. Brodbelt, J.S.: Photodissociation mass spectrometry: new tools for characterization of biological molecules. Chem. Soc. Rev. 43, 2757–83 (2014). doi:10.1039/c3cs60444f

3. Antoine, R., Lemoine, J., Dugourd, P.: Electron photodetachment dissociation for structural characterization of synthetic and biopolymer anions. Mass Spectrom. Rev. 33, 501–522 (2014). doi:10.1002/mas.21402

4. Gardner, M.W., Smith, S.I., Ledvina, A.R., Madsen, J.A., Coon, J.J., Schwartz, J.C., Stafford Jr., G.C., Brodbelt, J.S.: Infrared multiphoton dissociation of peptide cations in a dual pressure linear ion trap mass spectrometer. Anal. Chem. 81, 8109–8118 (2009). doi:10.1021/ac901313m

5. Raspopov, S.A., El-Faramawy, A., Thomson, B.A., Siu, K.W.M.: Infrared multiphoton dissociation in quadrupole time-of-flight mass spectrometry: top-down characterization of proteins. Anal. Chem. 78, 4572–7 (2006). doi:10.1021/ac052248i

6. Ledvina, A.R., Lee, M.V., McAlister, G.C., Westphall, M.S., Coon, J.J.: Infrared multiphoton dissociation for quantitative shotgun proteomics. Anal. Chem. 84, 4513–4519 (2012). doi:10.1021/ac300367p

7. Zhurov, K.O., Fornelli, L., Wodrich, M.D., Laskay, U.A., Tsybin, Y.O.: Principles of electron capture and transfer dissociation mass spectrometry applied to peptide and protein structure analysis. Chem. Soc. Rev. 42, 5014–5030 (2013). doi:10.1039/C3CS35477F

8. Zubarev, R.A., Kelleher, N.L., McLafferty, F.W.: Electron capture dissociation of multiply charged protein cations. A nonergodic process. J. Am. Chem. Soc. 120, 3265–3266 (1998). doi:10.1021/ja973478k

9. Syka, J.E.P., Coon, J.J., Schroeder, M.J., Shabanowitz, J., Hunt, D.F.: Peptide and protein sequence analysis by electron transfer dissociation mass spectrometry. Pro. Natl. Acad. Sci. USA. 101, 9528–9533 (2004). doi:10.1073/pnas.0402700101

10. Breuker, K., Oh, H., Lin, C., Carpenter, B.K., McLafferty, F.W.: Nonergodic and conformational control of the electron capture dissociation of protein cations. Proc. Natl. Acad. Sci. U.S.A. 101, 14011–14016 (2004)

11. Breuker, K., Oh, H., Horn, D.M., Cerda, B.A., McLafferty, F.W.: Detailed Unfolding and Folding of Gaseous Ubiquitin Ions Characterized by Electron Capture Dissociation. J. Am. Chem. Soc. 124, 6407–6420 (2002). doi:10.1021/ja012267j

12. Shaw, J.B., Li, W., Holden, D.D., Zhang, Y., Griep-Raming, J., Fellers, R.T., Early, B.P., Thomas, P.M., Kelleher, N.L., Brodbelt, J.S.: Complete protein characterization using top-down mass spectrometry and ultraviolet photodissociation. J. Am. Chem. Soc. 135, 12646–12651 (2013). doi:10.1021/ja4029654

13. Cannon, J.R., Cammarata, M.B., Robotham, S.A., Cotham, V.C., Shaw, J.B., Fellers, R.T., homas, P.M., Kelleher, N.L., Brodbelt, J.: Ultraviolet photodissociation for characterization of whole proteins on a chromatographic time scale. Anal. Chem. 86, 2185–2192 (2014). doi:10.1021/ac403859a

14. Cammarata, M.B., Brodbelt, J.S.: Structural characterization of holo- and apo-myoglobin in the gas phase by ultraviolet photodissociation mass spectrometry. Chem. Sci. 6, 1324–1333 (2015). doi:10.1039/C4SC03200D

15. Halim, M.A., Girod, M., MacAleese, L., Lemoine, J., Antoine, R., Dugourd, P.: 213 nm Ultraviolet Photodissociation on Peptide Anions: Radical-Directed Fragmentation Patterns. J. Am Soc. Mass Spectrom. 27, 474–486 (2016). doi:http://dx.doi.org/10.1007/s13361-015-1297-5

16. Cammarata, M.B., Thyer, R., Rosenberg, J., Ellington, A., Brodbelt, J.S.: Structural Characterization of Dihydrofolate Reductase Complexes by Top-Down Ultraviolet Photodissociation Mass Spectrometry. J. Am. Chem. Soc. 137, 9128–9135 (2015). doi:10.1021/jacs.5b04628

17. Cannon, J.R.., Martinez-Fonts, K., Robotham, S., Matouschek, A., Brodbelt, J.S.: Top-Down 193-nm Ultraviolet Photodissociation Mass Spectrometry for Simultaneous Determination of Polyubiquitin Chain Length and Topology. Anal. Chem. 87, 1812–1820 (2015). doi:10.1021/ac5038363

18. Girod, M., Sanader, Z., Vojkovic, M., Antoine, R., MacAleese, L., Lemoine, J., Bonacic-Koutecky, V., Dugourd, P.: UV Photodissociation of Proline-containing Peptide Ions: Insights from Molecular Dynamics. J. Am. Soc. Mass Spctrom. 26, 432–443 (2014). doi:10.1007/s13361-014-1038-1

19. Fort, K.L., Dyachenko, A., Potel, C.M., Corradini, E., Marino, F., Barendregt, A., Makarov, A.A., Scheltema, R.A., Heck, A.J.R.: Implementation of Ultraviolet Photodissociation on a Benchtop Q Exactive Mass Spectrometer and Its Application to Phosphoproteomics. Anal. Chem. 88, 2303–2310 (2016). doi:10.1021/acs.analchem.5b04162

20. Brodbelt, J.S.: Ion Activation Methods for Peptides and Proteins. Anal. Chem. 88, 30–51 (2016). doi:10.1021/acs.analchem.5b04563

21. McLuckey, S.A.: Principles of collisional activation in analytical mass spectrometry. J. Am. Soc. Mass Spctrom. 3, 599–614 (1992). doi:http://dx.doi.org/10.1016/1044-0305(92)85001-Z

22. Crowe, M.C., Brodbelt, J.S.: Infrared multiphoton dissociation (IRMPD) and collisionally activated dissociation of peptides in a quadrupole ion trap with selective IRMPD of phosphopeptides. J. Am. Chem. Soc. 15, 1581–1592 (2004). doi:10.1016/j.jasms.2004.07.016

23. Gardner, M.W., Smith, S.I., Ledvina, A.R., Madsen, J.A., Coon, J.J., Schwartz, J.C., Stafford Jr., G.C., Brodbelt, J.S.: Infrared multiphoton dissociation of peptide cations in a dual pressure linear ion trap mass spectrometer. Anal. Chem. 81, 8109–8118 (2009). doi:10.1021/ac901313m

24. Madsen, J.A., Gardner, M.W., Smith, S.I., Ledvina, A.R., Coon, J.J., Schwartz, J.C., Stafford, G.C., Brodbelt, J.S.: Top-Down Protein Fragmentation by Infrared Multiphoton Dissociation in a Dual Pressure Linear Ion Trap. Anal. Chem. 81, 8677–8686 (2009). doi:10.1021/ac901554z

25. Vasicek, L.A., Ledvina, A.R., Shaw, J., Griep-Raming, J., Westphall, M.S., Coon, J.J., Brodbelt, J.S.: Implementing Photodissociation in an Orbitrap Mass Spectrometer. J. Am. Soc. Mass Spctrom. 22, 1105–1108 (2011). doi:10.1007/s13361-011-0119-7

26. Tsybin, Y.O., Witt, M., Baykut, G., Kjeldsen, F., Håkansson, P.: Combined infrared multiphoton dissociation and electron capture dissociation with a hollow electron beam in Fourier transform ion cyclotron resonance mass spectrometry. Rapid Commun. Mass Spectrom. 17, 1759–1768 (2003). doi:10.1002/rcm.1118

27. Riley, N.M., Westphall, M.S., Coon, J.J.: Activated Ion Electron Transfer Dissociation for Improved Fragmentation of Intact Proteins. Anal. Chem. 87, 7109–7116 (2015). doi:10.1021/acs.analchem.5b00881

28. Cannon, J.R., Holden, D.D., Brodbelt, J.S.: Hybridizing Ultraviolet Photodissociation with Electron Transfer Dissociation for Intact Protein Characterization. Anal. Chem. 86, 10970–10977 (2014)

29. Swaney, D.L., McAlister, G.C., Wirtala, M., Schwartz, J.C., Syka, J.E.P., Coon, J.J.: Supplemental Activation Method for High-Efficiency Electron-Transfer Dissociation of Doubly Protonated Peptide Precursors. Anal. Chem. 79, 477–485 (2007). doi:10.1021/ac061457f

30. Frese, C.K., Altelaar, A.F.M., van den Toorn, H., Nolting, D., Griep-Raming, J., Heck, A.J.R., Mohammed, S.: Toward Full Peptide Sequence Coverage by Dual Fragmentation Combining Electron-Transfer and Higher-Energy Collision Dissociation Tandem Mass Spectrometry. Anal. Chem. 84, 9668–9673 (2012). doi:10.1021/ac3025366

31. Fellers, R.T., Greer, J.B., Early, B.P., Yu, X., LeDuc, R.D., Kelleher, N.L., Thomas, P.M.: ProSight Lite: Graphical software to analyze top-down mass spectrometry data. Proteomics. 15, 1235–1238 (2014). doi:10.1002/pmic.201400313

32. Hashimoto, Y., Hasegawa, H., Waki, I.: High sensitivity and broad dynamic range infrared multiphoton dissociation for a quadrupole ion trap. Rapid. Comm. Mass Spectrom. 18, 2255–2259 (2004). doi:10.1002/rcm.1619

33. Ledvina, A.R., Rose, C.M., Mcalister, G.C., Syka, J.E.P., Westphall, M.S., Griep-raming, J., Schwartz, J.C., Coon, J.J.: Activated Ion ETD Performed in a Modified Collision Cell on a Hybrid QLT-Oribtrap Mass Spectrometer. J. Am. Soc. Mass Spctrom. 1623–1633 (2013). doi:10.1007/s13361-013-0621-1

34. Bush, M.F., Hall, Z., Giles, K., Hoyes, J., Robinson, C. V, Ruotolo, B.T.: Collision Cross Sections of Proteins and Their Complexes: A Calibration Framework and Database for Gas-Phase Structural Biology. Anal. Chem. 82, 9557–9565 (2010). doi:10.1021/ac1022953

35. Brodbelt, J.S., Wilson, J.J.: Infrared multiphoton dissociation in quadrupole ion traps. Mass Spectrom. Rev. 28, 390–424 (2009). doi:10.1002/mas.20216

36. Ledvina, A.R., Beauchene, N.A., McAlister, G.C., Syka, J.E.P., Schwartz, J.C., Griep-Raming, J., Westphall, M.S., Coon, J.J.: Activated-Ion Electron Transfer Dissociation Improves the Ability of Electron Transfer Dissociation to Identify Peptides in a Complex Mixture. Anal. Chem. 82, 10068–10074 (2010). doi:10.1021/ac1020358

37. Zhang, L., Cui, W., Thompson, M.S., Reilly, J.P.: Structures of alpha-Type Ions Formed in the 157 nm Photodissociation of Singly-Charged Peptide Ions. J. Am. Soc. Mass Spctrom. 17, 1315–1321 (2006). doi:10.1016/j.jasms.2006.06.007

38. Madsen, J., Cheng, R.R., Kaoud, T.S., Dalby, K., Makarov, D.E., Brodbelt, J.: Charge-site-dependent dissociation of hydrogen-rich radical peptide cations upon vacuum UV photoexcitation. Chem. Eur. J. 18, 5374–5383 (2012). doi:10.1002/chem.201103534

39. Cui, W., Thompson, M.S., Reilly, J.P.: Pathways of peptide ion fragmentation induced by vacuum ultraviolet light. J. Am. Soc. Mass Spctrom. 16, 1384–1398 (2005). doi:10.1016/j.jasms.2005.03.050

40. Van Stipdonk, M., Kullman, M., Berden, G., Oomens, J.: IRMPD and DFT study of the loss of water from protonated 2-hydroxynicotinic acid. Int. J. Mass Spectrom. 330–332, 134–143 (2012). doi:http://dx.doi.org/10.1016/j.ijms.2012.06.026

41. Kjeldsen, F., Haselmann, K.F., Budnik, B.A., Jensen, F., Zubarev, R.A.: Dissociative capture of hot (3–13 eV) electrons by polypeptide polycations: an efficient process accompanied by secondary fragmentation. Chem. Phys. Lett. 356, 201–206 (2002). doi:http://dx.doi.org/10.1016/S0009-2614(02)00149-5

42. Zhang, L., Reilly, J.P.: Peptide Photodissociation with 157 nm Light in a Commercial Tandem Time-of-Flight Mass Spectrometer. Anal. Chem. 81, 7829–7838 (2009).

doi:10.1021/ac9012557

43. Zhang, L., Reilly, J.P.: De Novo Sequencing of Tryptic Peptides Derived from Deinococcus radiodurans Ribosomal Proteins Using 157 nm Photodissociation MALDI TOF/TOF Mass Spectrometry. J. Proteom. Res. 9, 3025–3034 (2010). doi:10.1021/pr901206j

44. Breuker, K., Brüschweiler, S., Tollinger, M.: Electrostatic stabilization of a native protein structure in the gas phase. Angew. Chem. Int. Ed. 50, 873–7 (2011). doi:10.1002/anie.201005112

45. Skinner, O.S., Mclafferty, F.W., Breuker, K.: How Ubiquitin Unfolds after Transfer into the Gas Phase. J. Am. Soc. Mass Spctrom. 23, 1011–1014 (2012). doi:10.1007/s13361-012-0370-6

46. Harding, M.M., Williams, D.H., Woolfson, D.N.: Characterization of a Partially Denatured State of a Protein by Two-Dimensional NMR: Reduction of the Hydrophobic Interactions in Ubiquitin. Biochemistry. 30, 3120–3128 (1991)

47. Wilkinson, K.D., Mayer, A.N.: Alcohol-Induced Conformational Changes of Ubiquitin. Arch. Biochem. Biophys. 250, 390–399 (1986)

48. Kim, T.-Y., Thompson, M.S., Reilly, J.P.: Peptide photodissociation at 157 nm in a linear ion trap mass spectrometer. Rapid Comm. Mass Spectrom. 19, 1657–1665 (2005). doi:10.1002/rcm.1969

49. Dehon, C., Soorkia, S., Pedrazzani, M., Jouvet, C., Barat, M., Fayeton, J.A., Lucas, B.: Photofragmentation at 263 nm of small peptides containing tyrosine: the role of the charge transfer on CO. Phys. Chem. Chem. Phys. 15, 8779–8788 (2013). doi:10.1039/C3CP50720C

Chapter 4:

Photodissociation of PTM peptides

"Function relies in diversity."

4.1 Introduction

Identification and mapping of the post-translational modifications (PTMs) in peptides and proteins is challenging because of their low abundance, lability and unique chemical properties [1, 2]. Mass spectrometry based analysis of phosphorylation [3], sulfonation [4], and glycosylation [5] have great importance to understand their diverse biological functions. Phosphorylation by protein kinases regulates signal transduction for diverse intracellular processes [6, 7]. Many diseases such as cancer, inflammatory, metabolic disorders, and neurological diseases are also interlinked to kinase protein phosphorylation [8]. The key functions of tyrosine sulfation are to regulate the protein-protein interactions, hormonal regulation and hemostasis [9, 10]. Due to the very acidic nature and labile sulfo-ester bond, it is difficult to characterize the sulfoproteome [11]. In glycoproteins, an oligosaccharide chain (glycan) is covalently attached to the polypeptide side-chain [12]. Glycosylation is associated with plasma-membrane and secretory proteins [13]. Moreover, proteins that have an extracellular segment are often glycosylated. Glycosylation has been linked with several human diseases such as inflammatory [14], cancer [15], genetic disorders [16] and neurodegenerative [17, 18]. Due to low-abundance, the complexity and heterogeneity of glycan structures, glycoproteins are difficult to characterize [19].

Tandem Mass Spectrometry (MS/MS) has emerged as an indispensable tool for analyzing protein PTMs as it can provide structural information at a single amino acid resolution and high accuracy, relative speed and sensitivity [20, 21]. In order to obtain precise structural information at single amino acid level, methods related to ion activation are crucial. Collision induced dissociation (CID) is frequently applied for fragmenting peptide ions. Although CID can pinpoint the presence of phosphate (especially from pSer and pThr) in a peptide or protein by identifying the loss of a phosphate (-80 HPO_3 or -98 H_3PO_4) group from the precursor ion, the exact site determination is challenging [22]. The neutral loss of phosphate groups is not always observed from tyrosine due to the strong phosphate-tyrosine binding energy and lower abundance of pTyr phosphorylation compared to pSer and pThr [23, 24]. Moreover, as sulfonation (SO_3) and phosphorylation (HPO_3) both result in the loss of 80 Da it makes the PTM identification more challenging. One inherent problem with CID is that excitation of precursor ion requires alteration of kinetic energy which increases the neutral loss, and in turn, provides limited structural information [22]. However, metastable atom-activated dissociation (MAD) and higher-energy collision dissociation (HCD) experiments on phosphorylated and sulfonated peptides in negative ion mode show significant improvement [25, 26]. Recently, using dual spray ion/ion reactions, traditional collision induced dissociation

(CID) showed significant improvement in terms of fragmentation and retention of phosphate group [27].

Electron-driven methods based on ‘ion-electron’ activation in electron capture dissociation (ECD) [28] and ‘ion-ion’ activation in electron transfer dissociation (ETD) [29] have been developed as an alternative to CID. In ECD and ETD, instead of an inert gas, precursor ions are excited by low energy electron (~1 eV) or electron-rich anions which are capable of transferring electrons [30]. After reception of an electron, the excited precursor ions specifically break the N–C_α bonds and yield c and z ions without abundant side-chain loss, allowing the identification of PTM site location [31, 32]. However, ECD and ETD methods require multiply charged ions, which is difficult to form for the acidic phosphate and sulfonate groups in PTMs [30, 33, 34]. Incorporating metal ion for phospho and sulfo sites can improve the localization and fragmentation by generating multiple charge states [35, 36]. The acidic nature of phospho- and sulfo- groups in the PTM peptide can show improved ionization in negative ion mode and is able to provide good fragmentation while retaining the PTM groups [37–39]. However, irrespective of activation methods peptide anions produce more complex MS/MS spectra arising from manifold fragmentation events with widespread side chain losses making it difficult to process, interpret and analyze the complex data-set [40–45].

As an alternative to ‘ion-ion’ activation technique, various UV photon-based methods including 157 nm [46], 193 nm [47–50], 220 nm [51], 266 nm [52] ultraviolet photodissociation (UVPD), electron detachment dissociations (EDD) [53] are also available. Kim *et al* observed series of a/x ions in 157 nm VUVPD on phospho-peptides which can retain the phosphate group [46]. They also found that phospho-tyrosine is more stable compared to phosphoserine or phosphothreonine. 193 nm UVPD with negative polarity can disclose some interesting features such as excellent sequence coverage and retaining H_3PO_4 and SO_3 groups from product ions of phospho- and sulfo- peptides [50, 54, 55]. 220 nm UVPD on protonated tyrosine containing phospho-peptides showed characteristic aromatic side chain losses of the tyrosine residue [51]. Aromatic side chain loss was also observed at 266 nm for electron detachment dissociation (EDD) for peptide anions [53]; however, such loss was suppressed for phospho-peptide cation [52]. Compared to high-energy UV photodissociation, relatively few studies are directed by 10.6 μm infrared multiphoton dissociation (IRMPD) [56–59] for PTM characterization. Despite some challenges and difficulties, IRMPD has some potentials [60–62] since this method i) requires no alternation of the stable trajectory or kinetic energy of the trapped ion for excitation; ii) is not associated to low cutoff *m/z;* iii) can provide reasonable fragmentation efficiency; iv) can operate without collision gas v) is compatible with the vibrational modes of PO_4^{3-} and SO_3 groups present in PTMs.

Although various wavelengths between 157-266 nm were employed in ultraviolet photodissociation for post-translational modification characterization, 213 nm UVPD [41, 63] has never been used before for such characterization. Moreover, a new method HiLoPD (high-low photodissociation), [64] which combined high-energy UV and low-energy IR lasers with a high resolution Q-Exactive mass spectrometer encompassing high and low photoactivation channels, has not been previously employed for PTM characterization. In this study, we attempt to evaluate the performance of 10.6 μm IRMPD, 213 nm UVPD and HiLoPD for phospho-, sulfo- and glyco-peptide cation characterization specifying three goals: i) obtaining adequate backbone fragmentation with good sequence coverage; ii) identifying the exact position of PTM groups; and iii) comparing the loss and retain events of the labile PTM groups in the fragment ions.

4.2 Materials and Methods

4.2.1 Sample Preparation

Phospho-, sulfo-, and glyco-peptides such as RRLIEDAEY(H_2PO_4) AARG from tyrosine kinase peptide, RDY(SO_3)TGWLDF and EAISPPDAAS(GalNAc)AAPLR from GalNAc-Ser Erythropoietin (177-131) were obtained from GeneCust Europe. All peptides were used without any further purification. All peptide samples were prepared at 2μM concentration in 50/49/1 (v/v/v) methanol/water/acetic acid.

4.2.2 Mass Spectrometry

All experiments were performed on a hybrid quadrupole-Orbitrap Q-Exactive® mass spectrometer (Thermo Fisher Scientific, San Jose, CA, USA) equipped with a HESI ion source which is described in **chapter 3**. Positive polarity was used for all peptides.

4.2.3 Photodissociation and Computation

IRMPD experiments were performed with a 50 W continuous-wave CO_2 laser (Model ULR-50, Universal Laser System®, Scottsdale, AZ) described in **chapter 3**. To compete with backbone fragmentation and retaining PTM groups, various nominal laser powers from 10-60% were used. However, we noticed that 10-30% laser power is enough attaining excellent

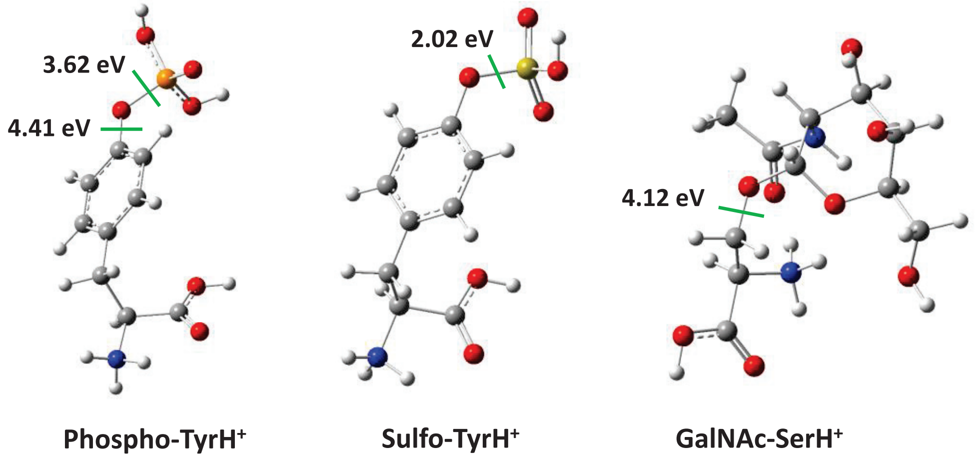

Scheme 4.1 Optimized structures of the model systems of phospho-TyrH$^+$, sulfo-TyrH$^+$ and GalNAc-SerH$^+$ calculated at the B3LYP/6-31G (d, p) level of theory in the gas phase. Green lines represent the cleavage of bonds and corresponding bond dissociation energies are presented in eV.

fragmentation and comparable PTM loss and retain events. Although high laser power can provide a significant number of fragment ions, it is difficult to retain the PTM groups. Compared to protein sample, peptides generally required shorter irradiation times from 50 ms to 500 ms. As we already discussed in the earlier **chapter 3** that for IRMPD experiment N_2 gas pressure in the HCD cell is required to be adjusted to optimize the IR fragmentation while avoiding significant loss of signal. For the PTM peptides, the pressure controller was set to ~0.1-0.15 MPa for efficient trapping and good signal.

For the UVPD experiments, similar to the previous experiment, the fifth harmonic (λ=213 nm, ~1 mJ/pulse) of a 20 Hz BrillantB solid-state Nd:YAG laser (Quantel, Les Ulis, France) was used. However, the optimal shutter open time used here was 50-100 ms (1-2 laser shots) as the PTM peptides require fewer UV laser shots.

HiLoPD experiments were performed with combined IRMPD and UVPD irradiation in the HCD cell of a hybrid quadrupole-Orbitrap mass spectrometer. The details set up were described in the **chapter 3**. Coupling schemes between IR and UV were implemented by simultaneous irradiation of the CO_2 laser (50-200 ms) with 10-30% of nominal laser power and 1-2 shots of UV laser.

Theoretical calculations were performed with the Gaussian09 program [65]. Model systems of phospho-TyrH$^+$, sulfo-TyrH$^+$ and GalNAc-SerH$^+$ and their corresponding fragments (including loss of PTMs phospho, sulfo and GalNAc groups) (see **scheme 4.1**) are optimized at the B3LYP/6-31G (d, p) level of theory in the gas phase. Bond dissociation energy (eV) is calculated by the following equation: $\Delta E = (E_A + E_B) - E_{AB}$ where E_A, E_B and E_{AB} are the electronic energies of fragments (A and B) and the model systems (AB), respectively.

4.2.4 Data Analysis

Manual interpretation of the IRMPD, UVPD, and HiLoPD data were performed with the assistance of Protein Prospector V5.14.4. (http://prospector.ucsf.edu/prospector/mshome.htm). All major ion types (a, a+1, a+2, b-1, b, b+1, b+2, c-1, c, c+1, x-1, x, x+1, x+2, y, y-1, y-2, z-1, z, z+1) were considered. To identify the loss of PTMs, the exact mass of the labile groups were subtracted from the precursor and fragment ions and a mass list was manually created in excel. Then these values were searched for throughout the spectra. H_2O and NH_3 losses from the fragment ions were also considered.

For the PTM loss and retention assessments, the position of PTM site relative to N- and C-terminals' ions of a/b/c and x/y/z, respectively were considered. For the losses of similar groups (such as H_3PO_4 and HPO_3) from the same fragment ion are counted as a 'one loss' event. For instance, if both H_3PO_4 and HPO_3 are lost from the y_5 ion, it is counted as 'one loss' event not 'two losses'. In addition, detection of several y-1, y, y+1 or a, a+2 ions from the same backbone position is counted as 'one retain' event, not several. PTMs loss and retain are calculated by following equations:

$$\% \, Loss = \frac{\sum number\ of\ PTMs\ loss\ detected}{\sum number\ of\ PTMs\ loss\ detected + \sum number\ of PTMs\ retain\ detected} \times 100$$

$$\% \, Retain = \frac{\sum number\ of\ PTMs\ retain\ detected}{\sum number\ of\ PTMs\ loss\ detected + \sum number\ of PTMs\ retain\ detected} \times 100$$

4.3 Result and Discussion

4.3.1 IRMPD, UVPD and HILOPD on RRLIEDAEY(H_2PO_4)AARG

In general, the activation of phospho-peptide molecular ion induces the cleavage of C–O–P ester bridge. If the cleavage of C–O bond occurred with hydrogen transfer, phosphoric acid (H_3PO_4) loss occurs whereas breaking of the O–P bond promotes the loss of HPO_3 group. In collision activation of tyrosine phosphorylated peptide, it is usually neutral loss of the HPO_3 (79.9657 Da) group that is observed [66];and , the loss of the H_3PO_4 group is less likely to occur. Since the bond dissociation energy of a C–O bond adjacent to an aromatic ring is quite high compared to a P–O bond and the secondly aromatic group does not promote E2-

elimination or S_N2-neighbouring group participation reaction [67]. Our density functional theory (DFT) calculation also confirms higher bond dissociation energy of the C–O (4.41 eV) compared to the O–P bond (3.62 eV). Previous studies reported that removal of H_3PO_4 group can occur from phosphorylated tyrosine by the concurrent or sequential loss of HPO_3 from the tyrosine residue and H_2O from somewhere else of the peptide [68, 69].

The IRMPD, UVPD and HiLoPD photodissociation spectra of the triply-protonated $[M+3H]^{3+}$ (*m/z* 533.9346) of peptide RRLIEDAEY(H_2PO_4)AARG is presented in **Figure 4.1**. Theoretical and observed *m/z* for fragment ions detected in IRMPD, UVPD and HiLoPD experiments on this peptide are summarized in **Table A4.1** (see in appendix). Abundance of fragment ions excluding phosphate losses in all three methods is compared in **Figure 4.2**.

Since the stretching of the P–O bond (9.6–11 μm or 1042-909 cm^{-1}) is in resonance with 10.6 μm wavelength, the phosphate group can stimulate chromophore-driven efficient dissociation [70]. The IRMPD spectrum provides a good overall sequence coverage of 83%, including sequence information in the low *m/z* region. IRMPD shows greater sequence coverage with N- terminal ions (75%) than C-terminal ions (66%). The neural losses of 98.0118 Da and 79.9986 Da, which correspond to the elimination of H_3PO_4 and HPO_3 groups, are observed from the precursor ions at *m/z* 501.2637 and 507.2681, respectively. The neutral loss of H_2O is detected at *m/z* 527.9238. In addition, IRMPD exhibits substantial backbone fragmentation (excluding phosphate losses) producing 30 b ions and 13 y ions (**Figure 4.2**). In the site-specific PTM losses, 5 are detected for y_n ions (n=5-9) while only 2 are identified from b_n ions (n = 9, 10) (**Figure 4.3**). Moreover, phosphate groups are retained in 4 y_n ions (n=5, 6, 7, 8). Overall phosphate loss in IRMPD is 63.6% which delivers 36.4% of phosphate retention efficiency.

The UVPD experiment on the +3 ion of this peptide allows detection of a total of 87 fragment ions (excluding phosphate losses) with 1 pulse which is nearly double the number of fragment ions detected in IRMPD (**Table A4.1**, in appendix). The neutral loss peaks at *m/z* 527.9256, 506.9291 and 501.2650 correspond to the elimination of H_2O, H_2PO_3 and H_3PO_4 from the precursor ion $[M+3H]^{3+}$. The neutral loss of CH_3CH_2 noticed at *m/z* 524.2445 Da, represents the side chain of Ile [71]. There is a peak at *m/z* 498.5760 corresponding to the loss of $O=C_6H_4=CH_2$ (106.0836 Da) from tyrosine [72]. However, compare to IRMPD only 14 b ions are identified in UVPD. Besides traditional a/x, y and c/z ions, a+1/x+1, x+2, y-1, y-2, c-1, and c+1 ions of this peptide are also detected. Despite the absence of a proline residue, we notice y-1 and y-2 ions from secondary detachment of the x+1 radical [38,18]. The UVPD spectrum provides 83% overall sequence coverage and with significant number of fragment ions. However, equal sequence coverage (66%) is observed with N- and C-terminal ions.

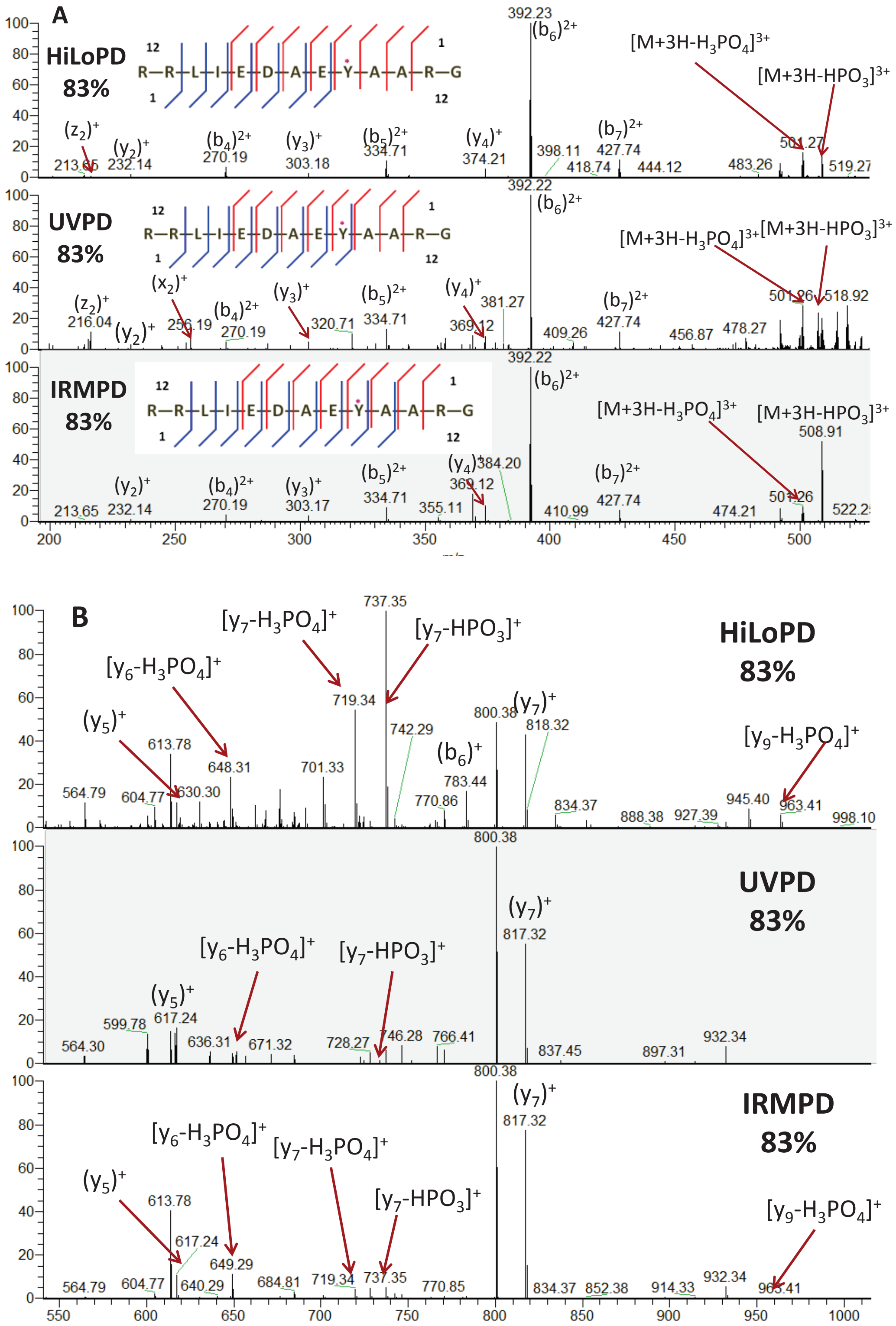

Figure 4.1 IRMPD, UVPD and HiLoPD spectra of the +3 charge state precursor ion (*m/z* 533.9356) of RRLIEDAEY(H_2PO_4)AARG peptide A) 200-530 *m/z* and B) 550-1000 *m/z*. Detail assignments of the fragment ions are summarized in **Table A4.1.**

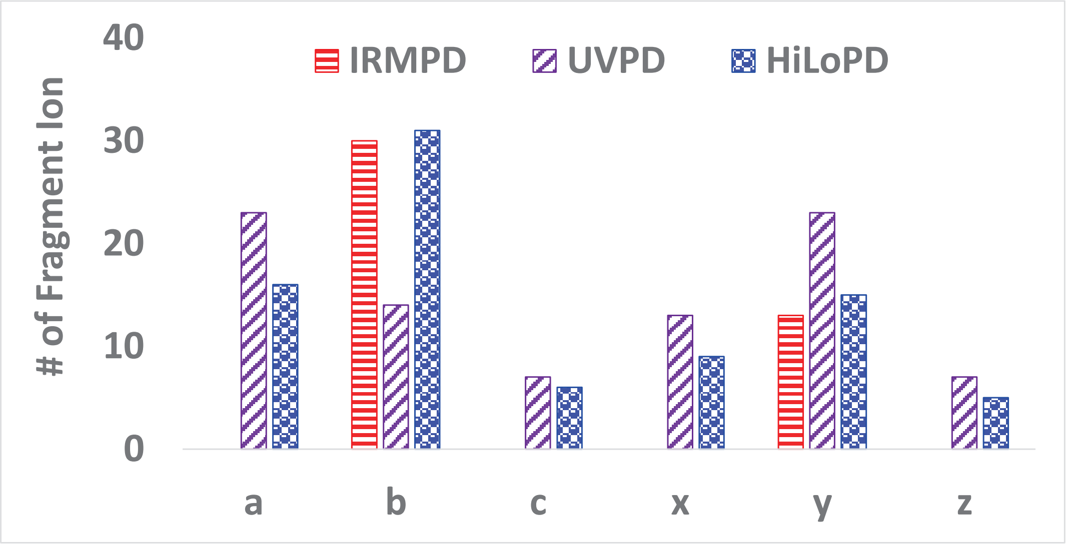

Figure 4.2 Number of fragment ions (without phosphate loss) detected by IRMPD, UVPD and HiLoPD spectra of the +3 charge state precursor ion (*m/z* 533.9356) of RRLIEDAEY(H_2PO_4)AARG peptide.

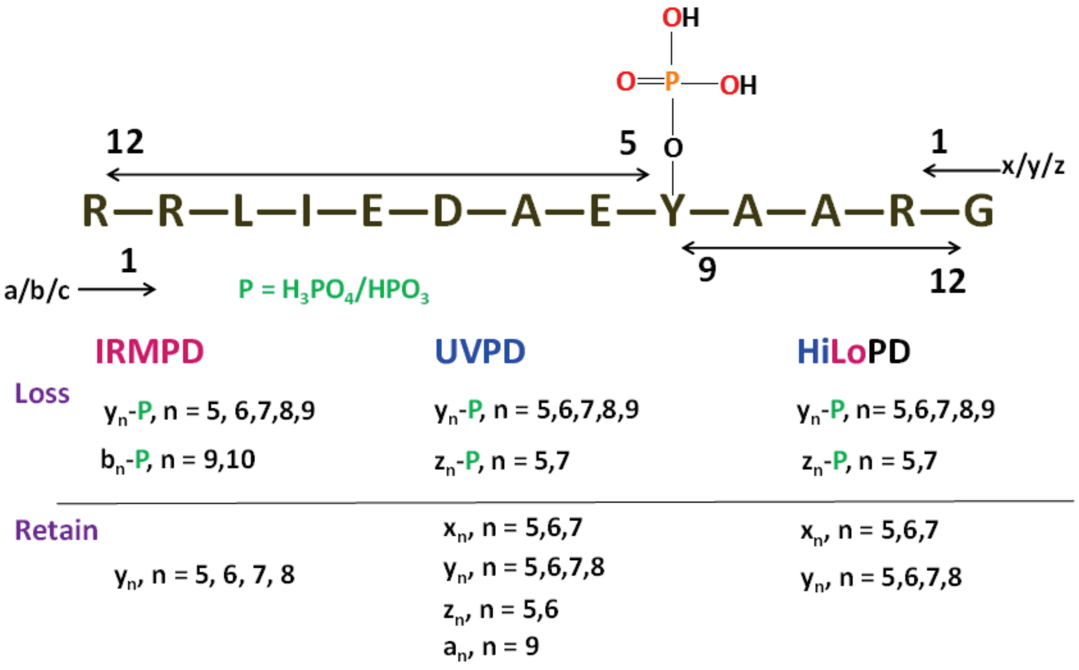

	IRMPD	UVPD	HiLoPD
Loss	y_n-P, n = 5, 6,7,8,9 b_n-P, n = 9,10	y_n-P, n = 5,6,7,8,9 z_n-P, n = 5,7	y_n-P, n= 5,6,7,8,9 z_n-P, n = 5,7
Retain	y_n, n = 5, 6, 7, 8	x_n, n = 5,6,7 y_n, n = 5,6,7,8 z_n, n = 5,6 a_n, n = 9	x_n, n = 5,6,7 y_n, n = 5,6,7,8

Figure 4.3 Fragment-specific phosphate loss and retain events detected in IRMPD, UVPD and HiLoPD for +3 charge state precursor ion (*m/z* 533.9356) of RRLIEDAEY(H_2PO_4)AARG peptide. Loss of H_3PO_4 or HPO_3 group from the same fragment ion counted as ‘one loss’. For example, both H_3PO_4 and HPO_3 are lost from y_7 in IRMPD which is counted as ‘one loss’ event not ‘two loss’.

In UVPD, the neutral losses of H_3PO4 and HPO_3 groups from the fragment ions are observed from y_n ions of position n = 5-9. Only two such losses are identified for z_n ions (n = 5,7). Surprisingly, there is no such phosphate loss detected for a, b, c or x ions. Significant number of phosphate retain is identified in x_n (n=5,6,7), y_n (n=5,6,7,8), z_n (n=5,6) and a_n(n=9) ions (**Figure 4.3**). The overall loss of phosphate in UVPD is 41.2%, which shows retention efficiency of 58.8%.

HiLoPD on the same peptide produces a wider range of fragmentation types, a, b, c, x, y, and z, owing to its high and low activation channels combining UV and IR photodissociation. While UVPD and HiLoPD produce identical sequence coverage (83%), HiLoPD shows diverse array of fragment ions from N and C-terminals. While significant number of b ions (31 fragments) are identified similar to IRMPD, many of them are absent in UVPD (**Figure 4.2**). However, compared to UVPD, the number of a/x ions are decreased in HiLoPD. In addition to the traditional ion types, the spectrum also contains highly abundant ions corresponding to neutral losses of water and ammonia from the fragment ions (**Table A4.1**). Similar to UVPD, phosphate losses are observed for y_n (n = 5-9) and z_n (n=5, 7) ions and no loss is detected from a, b, c and x ions in HiLoPD (**Figure 4.3**). It appears that loss of HPO_3 from y ions is more frequent in HiLoPD and UVPD compared to IRMPD. The overall phosphate retention efficiency in HiLoPD is 50.0%.

Although significant losses of phosphate groups from the product ions are not desirable, some of these losses and along with high sequence coverage can certainly confirm the phosphate location on a phospho-peptide. In IRMPD, the elimination of H_3PO_4 group is identified from the b_{9-10} as well as from y_{5-9} ions (**Figure 4.3**). In UVPD and HiLoPD, the neutral losses of H_3PO4 and HPO_3 groups are only found from y_{5-9}, z_5 and z_7 fragment ions. As evident from these results, no phosphate loss is detected from y_{1-4} and b_{1-8} ions, which can confirm that phosphate group is attached to the tyrosine at position 9 or 5 corresponding to N- and C-terminals, respectively.

4.3.2 IRMPD, UVPD and HiLoPD on RDY(SO$_3$)TGWLDF

The IRMPD, UVPD and HiLoPD photodissociation spectra of the doubly-protonated $[M+2H]^{2+}$ (*m/z* 626.7492) of peptide RDY(SO_3)TGWLDF are presented in **Figure 4.4.** Observed *m/z* and assignment of fragment ions of this peptide are summarized in **Table A4.2** (in appendix). The number of fragment ions (excluding sulfonate loss) detected by IRMPD, UVPD and HiLoPD is summarized in **Figure 4.5**. Singly and doubly protonated precursor ions provide nearly the same fragment ions in UVPD; however, the singly protonated charge state is not stable and difficult to analyze during the isolation state prior to MS/MS activation in IRMPD and HiLoPD methods. Similar event is also witnessed in a previous study [47]. However, the doubly-protonated charge state of this peptide is worked well with all three methods. Moreover, earlier studies reported that higher charge states can increase the sulfonate retention [39]. In all cases, neutral loss of SO_3 (79.9573 Da) is observed at *m/z* 1172.5388 from the $[M+H]^+$ ions and at *m/z* 586.7710 from the precursor ion, respectively. Moreover, sequential loss of SO_3 and H_2O is detected at *m/z* 577.7677 from the precursor ion.

The vibrational frequencies of C–O(SO_3) and symmetrical O=S=O are in the range 9.4-10 μm [75] which is very closed to the wavelength of (10.6 μm) CO_2 laser. The IRMPD spectrum provides overall 87% of sequence coverage and is dominated by series of y-ions, as well as minor contributions from b-ions (**Figure 4.5**). Although more fragment ions are generated from C-terminal, high sequence coverage is observed for N-terminal (87.5%) compared to C-terminal (62.5%). Most of the y ions are formed from the C-terminal residues particularly aspartic acid at position 2. Previous collision induced dissociation (CID) studies have shown that acidic residues near to the C-terminus may promote the formation of y ion in sulfonated peptides [76]. Some y ions in IRMPD eliminate a molecule of water (18 Da) in secondary fragmentation. Interestingly, loss of SO_3 is predominantly seen from b_{3}-$_{8}$ ions but no such loss is detected from y ions; however, for phospho-peptide more phosphate losses are detected from y ions. Widespread losses of SO_3 are attributed to the low bond dissociation energy of the O–S bond (2.02 eV) in sulfo-peptide (**Scheme 4.1**).

UVPD and HiLoPD of the doubly protonated precursor ion provide 100% sequence coverage with a/x, b/y and c/z ions. 20 and 28 fragment ions (excluding SO_3 loss) are detected in UVPD and HiLoPD, respectively. In UVPD and HiLoPD, more a/b ions are discovered from aspartic acid at position 2 related to N-terminal which is closed to the SO_3-containing tyrosine. In addition to the typical fragment ions types, the UVPD and HiLoPD spectra also comprise abundant ions corresponding to neutral losses of water and ammonia. The losses of 171.0099 and 129.0141 Da from the precursor ions correspond to the removal of the related ion of tryptophan at *m/z* 541.2400 and immonium ion of arginine at *m/z* 562.2380, respectively (**Table A4.2**). Hydrogen deficient and hydrogen rich fragment ions are prevalence in UVPD and HiLoPD. Loss of SO_3 is noticed from the backbone a/b/c fragment ions in UVPD and HiLoPD. Similar to IRMPD, the overall SO_3 retention efficiency obtained by these two methods are very poor.

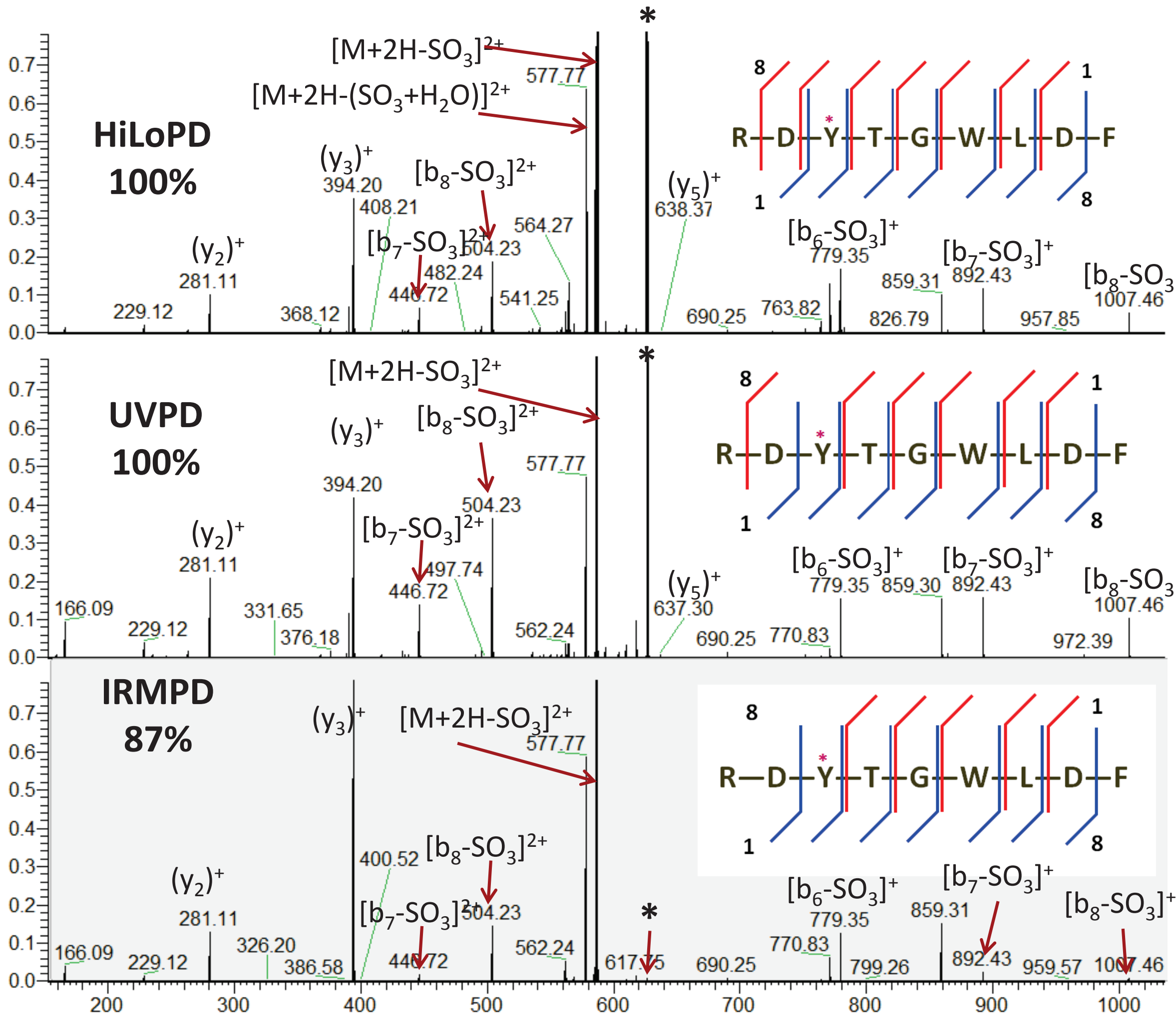

Figure 4.4 IRMPD, UVPD and HiLoPD spectra of the +2 charge state precursor ion (*m/z* 626.7492) of RDY(SO_3)TGWLDF peptide. The precursor ions are indicated by star (*) sign. Detailed assignment of the fragment ions are summarized in **Table A4.2**.

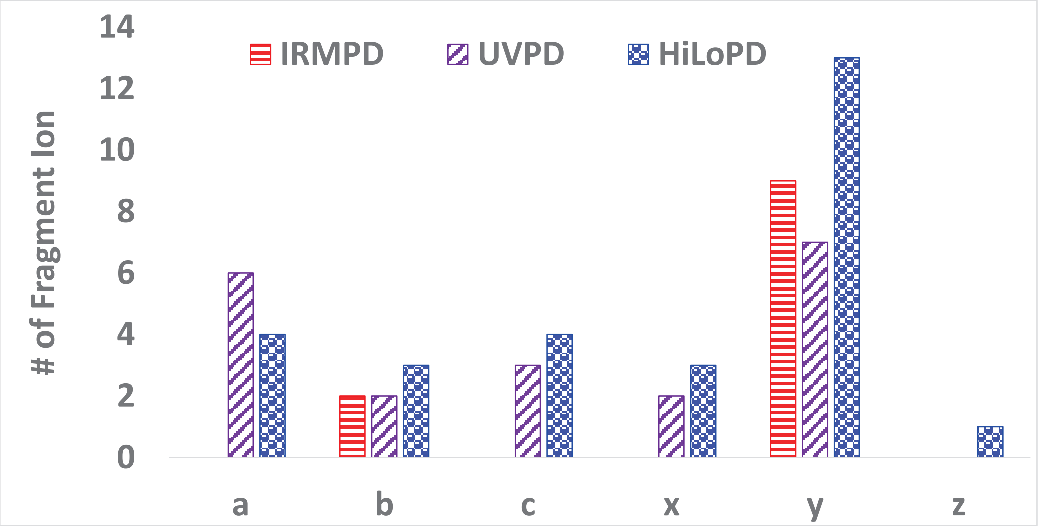

Figure 4.5 Number of fragment ions detected by IRMPD, UVPD, and HiLoPD of the +2 charge state precursor ion (*m/z* 626.7492) of RDY(SO_3)TGWLDF peptide.

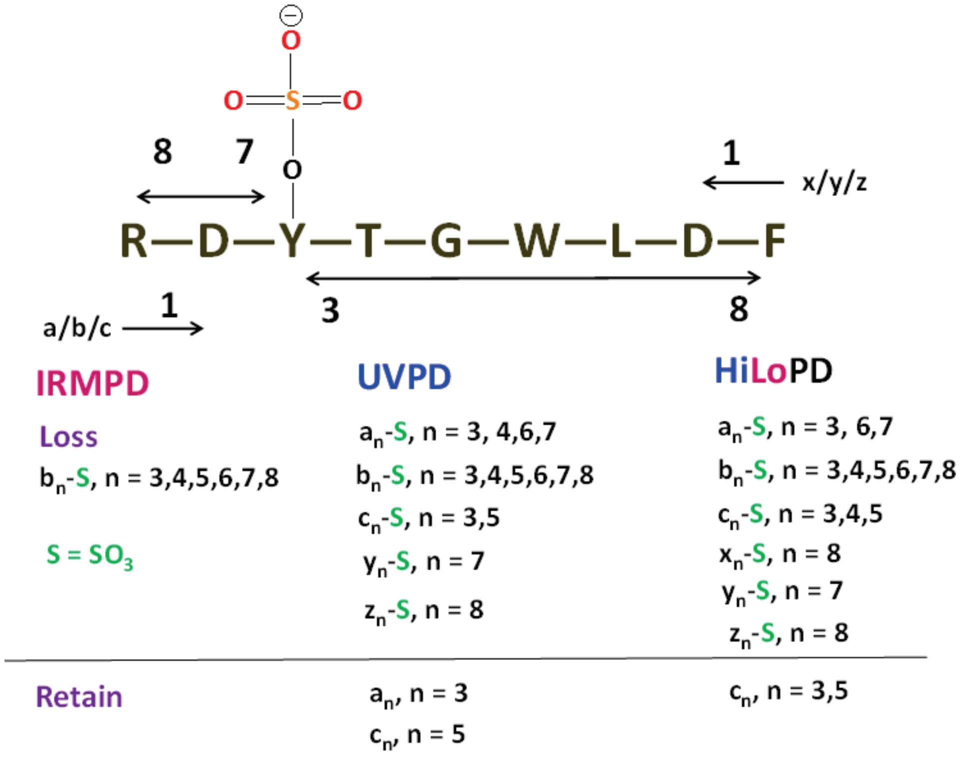

Figure 4.6 Fragment-specific phosphate loss and retain events in IRMPD, UVPD and HiLoPD on the +2 charge state precursor ion *(m/z* 626.7492) of RDY(SO_3)TGWLDF peptide.

In addition to sequence coverage and retention efficiency, the actual site of sulfation is required to be pinpointed. Although CID method has routinely been utilized to confirm the presence of sulfo group detecting the neural loss of SO_3 from the precursor ion, however, fragment ions are required to confirm the position [47]. In UVPD and HiLoPD, there is no SO_3 loss detected from $a_{1-2}/b_{1-2}/c_{1-2}$ and only such loss is noticed from $a_3/b_3/c_3$ and onward. In addition, there is no loss of SO_3 witnessed from $x_{1-6}/y_{1-6}/z_{1-6}$ ions and only such losses are started to happen from y_7 and x_8/z_8 ions which confirmed that SO_3 group is present at position 3 with tyrosine related to N-terminal.

4.3.3 IRMPD, UVPD and HiLoPD on EAISPPDAAS (GalNAc) AAPLR

High throughput and residue-specific investigation of the O-glycosylation is challenging since the O-glycan core structure is very heterogeneous compared to the N-glycan and there is no straightforward protein sequence available for the O-glycan [5, 77, 78]. In a given protein, the O-glycan can be found on several serine/threonine residues. Collision induced dissociation (CID) technique is routinely used for deducing the glycan composition, however, determining the exact position of glycosylation on a peptide sequence is difficult to achieve. Although IRMPD provides nearly similar fragment ions to CAD, a previous study disclosed that low photon energy based method can provided informative side chain losses from the non-glycosylated serine and threonine residues, which indirectly implicated sites of the glycan attachment [77]. The IRMPD photodissociation spectrum obtained for the triply-protonated $[M+3H]^{3+}$ (*m/z* 556.9529) of peptide EAISPPDAAS(GalNAc)AAPLR is presented in **Figure 4.7.** Theoretical and observed *m/z* values of fragment ions of this peptide are summarized in **Table A4.3.** The sequence coverage obtained by IRMPD is 86%. The neutral losses of GalNAc (221.0999 Da) and GalNAc-H_2O (203.0899 Da) are observed from the precursor ion at *m/z* 483.2556 and 489.2591, respectively. For all methods, the sequential losses of GalNAc and H_2O are specifically observed from b_{10}-b_{12} positions. In IRMPD, nearly equal numbers of b and y ions are noticed (**Figure 4.8**). The neutral losses of GalNAc and GalNAc-H_2O are observed from $b_{10\text{-}12}$ ions whereas for y_n ions these are occurred from n=7, 8, 10, and 12 (**Figure 4.9**). There is no such neutral losses observed for b_{1}-$_{9}$ and y_{1}-$_{5}$, which unambiguously confirmed that the GalNAc group attached to serine at 10 or 6 position relative to N- and C-terminals. Some GalNAc groups are also retained in y/b ions. Overall, IRMPD shows 41.6% retention efficiency (**Figure 4.9**), which is better than the sulfo-peptide and may be due to the high bond dissociation energy related to the C–O bond (4.12 eV) in glyco-peptide (**Scheme 4.1**).

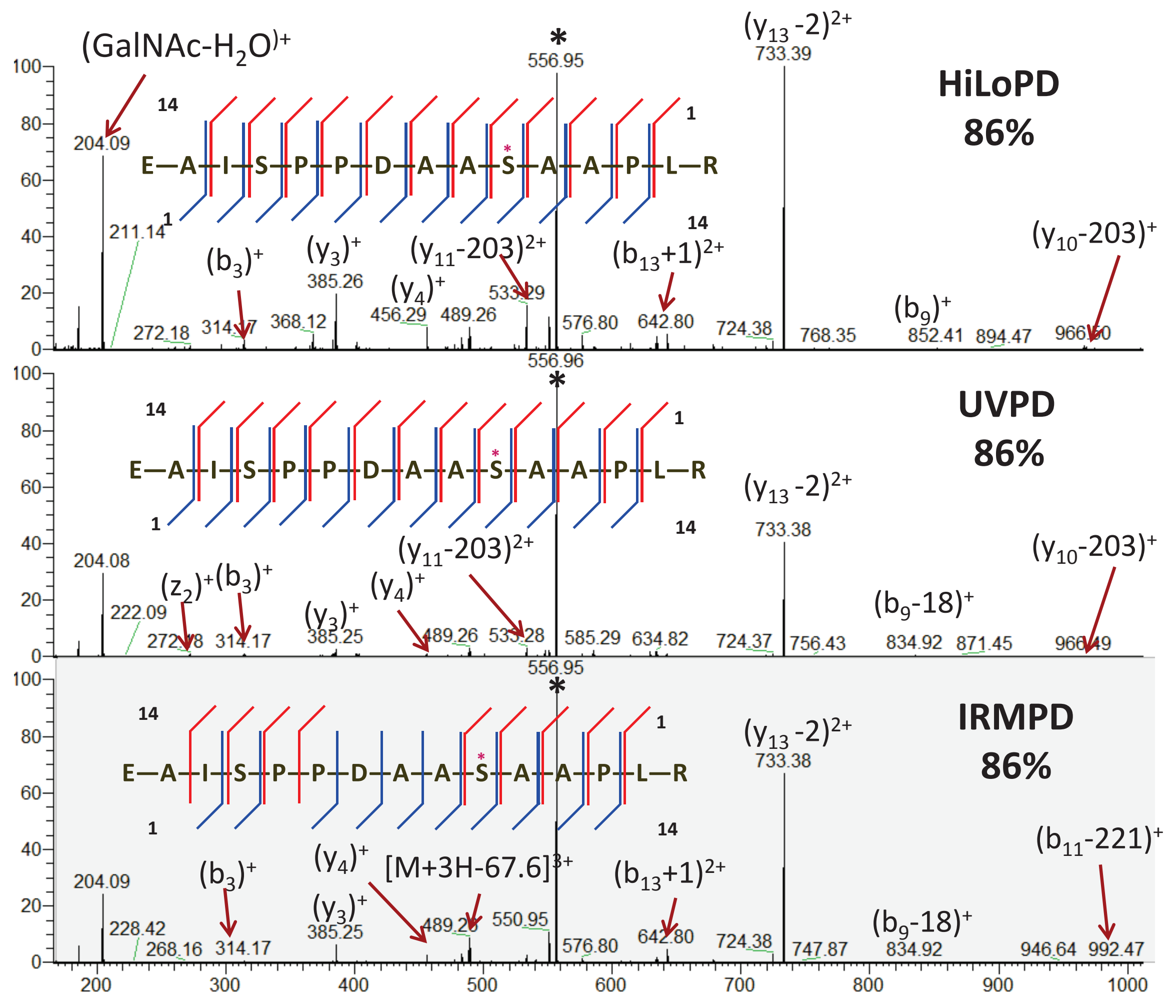

Figure 4.7 IRMPD, UVPD and HiLoPD spectra of the +3 charge state precursor ion (*m/z*=556.9529) of EAISPPDAAS(GalNAc)AAPLR peptide. The precursor ions are indicated by star (*) sign. Detailed assignment of the fragment ions are summarized in **Table A4.3**.

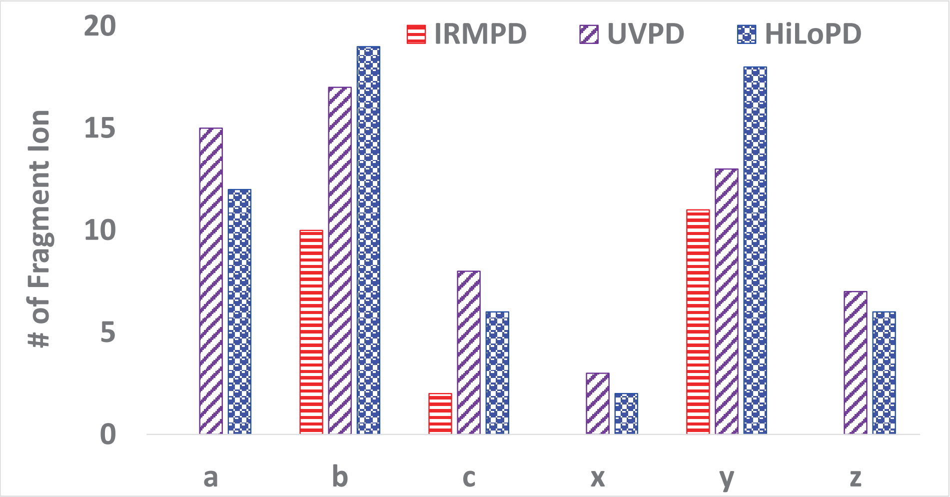

Figure 4.8 Number of fragment ions detected by IRMPD, UVPD and HiLoPD spectra of the +3 charge state precursor ion (*m/z*=556.9529) of EAISPPDAAS(GalNAc)AAPLR peptide.

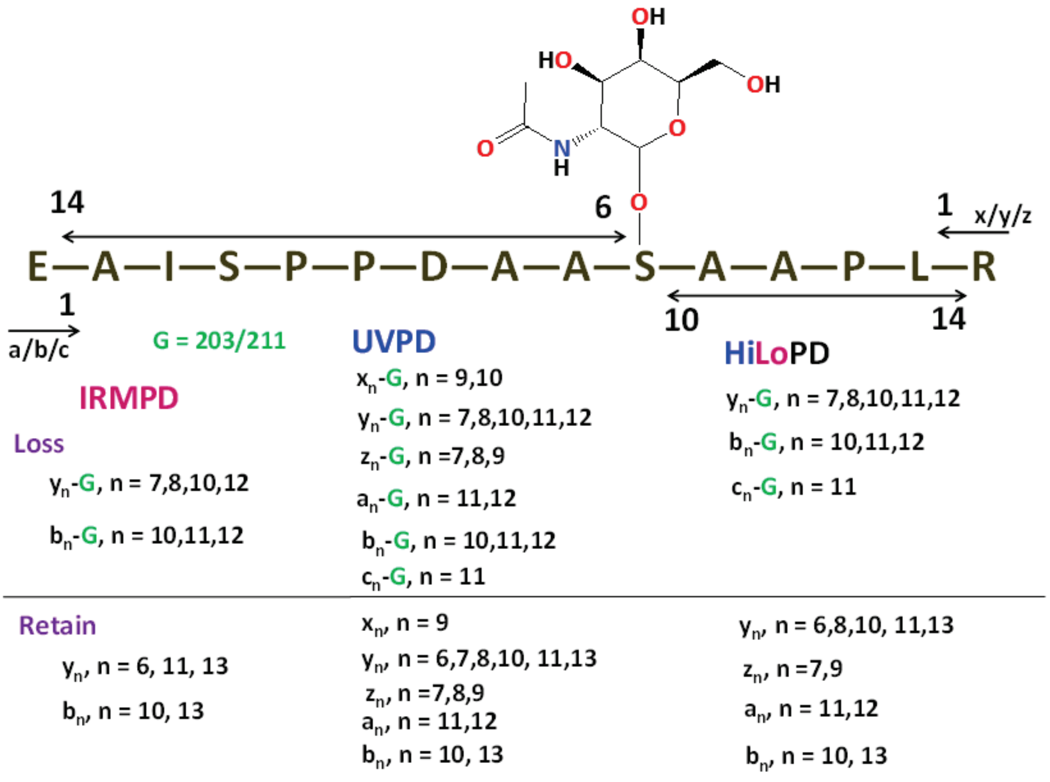

Figure 4.9 Fragment-specific phosphate loss and retain events in IRMPD, UVPD and HiLoPD on the +3 charge state precursor ion (*m/z* 556.9529) of EAISPPDAAS (GalNAc)AAPLR peptide.

The UVPD spectrum provides a wealth of fragment ions with sequence coverage of 86%. Significant number of a/x and b/y ions are detected which retain the GalNAc group. Compared to IRMPD (23 ions), the UVPD spectrum provides more fragment ions (63 ions). In addition, some c and z ions are also observed. Moreover, the neutral losses of GalNAc (221.0999Da) and GalNAc-H_2O (203.0899 Da) groups are observed from y ions compared to other ions (**Figure 4.9**). To be specific, loss of GalNAc and GalNAc-H_2O groups starts from the 10 and 7 positions related to N- and C-terminals, respectively. More losses are detected from y/b ions compared other fragment ions. The overall PTM retention efficiency is 46.6 %.

In HiLoPD, significant number of a/x, b/y and c/z ions are identified with similar sequence coverage (86%) from N- and C-terminals. The number of b ions detected in HiLoPD is higher than UVPD and IRMPD. Similar to our previous studies, a ion number is decreased compared to UVPD, which may be due to the secondary fragmentation of these ions [64]. Interestingly, very few x ions are generated in HiLoPD as well as UVPD. Compared to UVPD, the neutral losses of GalNAc and GalNAC-H_2O groups are significantly diminished at HiLoPD. Such losses are only observed for b/y and c ions (**Figure 4.9**). All a/x and z ions retain the glycan groups. Similar to UVPD, the neutral losses start to happen from the 10 and 7 position relative to N- and C-terminals, which confirm the position of glycan group (in serine at 10 position related to N-terminal) in this peptide. The GalNAc retention efficiency of HiLoPD is the highest 55.0%, compared to IRMPD (41.6%) and UVPD (46.6%), respectively (**Figure 4.9**).

4.4 Summary

In this work, we report the IRMPD, UVPD and HiLoPD investigations for characterizing phospho-, sulfo- and glyco- peptides in the gas phase. Compare to the whole protein, characterization of these PTMs peptides require lower CO_2 laser power and fewer UV laser shots. Controlled and tunable parameters can improve the performance of these techniques. The IRMPD results demonstrate that sufficient backbone fragmentation and sequence coverage can be accomplished by these techniques. The sequence coverage for phospho-, sulfo- and glyco-peptides is 83, 87 and 86%, respectively. The exact location of the PTM groups in a peptide can be pinpointed. However, fragment-specific and overall PTMs retention efficiency in IRMPD is somewhat reduced for all peptides. Compared to phospho- and glyco- peptides, IRMPD is very sensitive to the SO_3 group, which may be due to the low bond dissociation energy associated to the O–S bond. Herein, we also present the first study of 213 nm UVPD and HiLoPD for characterizing different PTM peptides. UVPD and HiLoPD show excellent sequence coverage of 83, 100 and 86%, for phospho-, sulfo- and glyco-peptides. Photodissociation at 213 nm UVPD and HiLoPD on peptide cation offers several promising benefits including i) can produce more array of fragment ions with excellent sequence coverage ii) can identify the exact PTM position iii) can provide balanced PTM loss and retain events, and iv) no widespread side-chain losses. Our first set of results has shown that UVPD and HiLoPD have more to offer for characterizing phospho- and glyco-proteomics.

Bibliography

1. Mann, M., Jensen, O.N.: Proteomic analysis of post-translational modifications. Nat. Biotechnol. 21, 255–261 (2003). doi:doi:10.1038/nbt0303-255

2. Zhao, Y., Jensen, O.N.: Modification-specific proteomics: Strategies for characterization of post-translational modifications using enrichment techniques. Proteomics. 9, 4632–4641 (2009). doi:10.1002/pmic.200900398

3. Macek, B., Mann, M., Olsen, J. V: Global and Site-Specific Quantitative Phosphoproteomics: Principles and Applications. Annu. Rev. Pharmacol. Toxicol. 49, 199–221 (2009). doi:10.1146/annurev.pharmtox.011008.145606

4. Önnerfjord, P., Heathfield, T.F., Heinegård, D.: Identification of Tyrosine Sulfation in Extracellular Leucine-rich Repeat Proteins Using Mass Spectrometry. J. Biol. Chem. . 279 , 26–33 (2004). doi:10.1074/jbc.M308689200

5. Christiansen, M.N., Kolarich, D., Nevalainen, H., Packer, N.H., Jensen, P.H.: Challenges of determining o-glycopeptide heterogeneity: A fungal glucanase model system. Anal. Chem. 82, 3500–3509 (2010). doi:10.1021/ac901717n

6. Cohen, P.: The origins of protein phosphorylation. Nat Cell Biol. 4, E127–E130 (2002). doi:10.1038/ncb0502-e127

7. Ubersax, J.A., Ferrell Jr, J.E.: Mechanisms of specificity in protein phosphorylation. Nat Rev Mol Cell Biol. 8, 530–541 (2007). doi:10.1038/nrm2203

8. Pearce, L.R., Komander, D., Alessi, D.R.: The nuts and bolts of AGC protein kinases. Nat Rev Mol Cell Biol. 11, 9–22 (2010). doi:10.1038/nrm2822

9. Bettelheim, F.R.: TYROSINE-O-SULFATE IN A PEPTIDE FROM FIBRINOGEN. J. Am. Chem. Soc. 76, 2838–2839 (1954). doi:10.1021/ja01639a073

10. Moore, K.L.: Protein tyrosine sulfation: A critical posttranslation modification in plants and animals. Proc. Natl. Acad. Sci. . 106 , 14741–14742 (2009). doi:10.1073/pnas.0908376106

11. Yu, Y., Hoffhines, A.J., Moore, K.L., Leary, J.A.: Determination of the sites of tyrosine O-sulfation in peptides and proteins. Nat Meth. 4, 583–588 (2007). doi:10.1038/nmeth1056

12. Steen, P. Van den, Rudd, P.M., Dwek, R.A., Opdenakker, G.: Concepts and Principles of O-Linked Glycosylation. Crit. Rev. Biochem. Mol. Biol. 33, 151–208 (1998). doi:10.1080/10409239891204198

13. Gill, D.J., Clausen, H., Bard, F.: Location, location, location: new insights into O-GalNAc protein glycosylation. Trends Cell Biol. 21, 149–158 (2017). doi:10.1016/j.tcb.2010.11.004

14. Kreisman, L.S.C., Cobb, B.A.: Infection, inflammation and host carbohydrates: A Glyco-Evasion Hypothesis. Glycobiology. 22, 1019–1030 (2012). doi:10.1093/glycob/cws070

15. Pinho, S.S., Reis, C.A.: Glycosylation in cancer: mechanisms and clinical implications. Nat Rev Cancer. 15, 540–555 (2015). doi:10.1038/nrc3982

16. Freeze, H.H., Eklund, E.A., Ng, B.G., Patterson, M.C.: Neurological Aspects of Human Glycosylation Disorders. Annu. Rev. Neurosci. 38, 105–125 (2015). doi:10.1146/annurev-neuro-071714-034019

17. Schedin-Weiss, S., Winblad, B., Tjernberg, L.O.: The role of protein glycosylation in Alzheimer disease. FEBS J. 281, 46–62 (2014). doi:10.1111/febs.12590

18. Hwang, H., Zhang, J., Chung, K.A., Leverenz, J.B., Zabetian, C.P., Peskind, E.R., Jankovic, J., Su, Z., Hancock, A.M., Pan, C., Montine, T.J., Pan, S., Nutt, J., Albin, R., Gearing, M., Beyer, R.P., Shi, M., Zhang, J.: Glycoproteomics in neurodegenerative diseases. Mass Spectrom. Rev. 29, 79–125 (2010). doi:10.1002/mas.20221

19. Pan, S., Chen, R., Aebersold, R., Brentnall, T.A.: Mass Spectrometry Based Glycoproteomics—From a Proteomics Perspective. Mol. Cell. Proteomics . 10 , (2011). doi:10.1074/mcp.R110.003251

20. Masselon, C., Anderson, G.A., Harkewicz, R., Bruce, J.E., Pasa-Tolic, L., Smith, R.D.: Accurate mass multiplexed tandem mass spectrometry for high-throughput polypeptide identification from mixtures. Anal. Chem. 72, 1918–1924 (2000). doi:10.1021/ac991133+

21. Pandey, A., Mann, M.: Proteomics to study genes and genomes. Nature. 405, 837–846 (2000). doi:10.1038/35015709

22. Crowe, M.C., Brodbelt, J.S.: Infrared multiphoton dissociation (IRMPD) and

collisionally activated dissociationof peptides in a quadrupole ion trapwith selective IRMPD of phosphopeptides. J. Am. Soc. Mass Spectrom. 15, 1581–1592 (2004). doi:10.1016/j.jasms.2004.07.016

23. Zolodz, M.D., Wood, K. V: Detection of tyrosine phosphorylated peptides via skimmer collision-induced dissociation/ion trap mass spectrometry. J. Mass Spectrom. 38, 257–264 (2003). doi:10.1002/jms.435

24. Affolter, M., Watts, J.D., Krebs, D.L., Aebersold, R.: Evaluation of Two-Dimensional Phosphopeptide Maps by Electrospray Ionization Mass Spectrometry of Recovered Peptides. Anal. Biochem. 223, 74–81 (1994). doi:10.1006/abio.1994.1549

25. Cook, S.L., Jackson, G.P.: Metastable Atom-Activated Dissociation Mass Spectrometry of Phosphorylated and Sulfonated Peptides in Negative Ion Mode. J. Am. Soc. Mass Spectrom. 22, 1088–1099 (2011). doi:10.1007/s13361-011-0123-y

26. Edelson-Averbukh, M., Shevchenko, A., Pipkorn, R., Lehmann, W.D.: Discrimination Between Peptide O-Sulfo- and O-Phosphotyrosine Residues by Negative Ion Mode Electrospray Tandem Mass Spectrometry. J. Am. Soc. Mass Spectrom. 22, 2256–2268 (2011). doi:10.1007/s13361-011-0248-z

27. Cotham, V.C., McGee, W.M., Brodbelt, J.S.: Modulation of phosphopeptide fragmentation via dual spray ion/ion reactions using a sulfonate-incorporating reagent. Anal. Chem. 88, 8158–8165 (2016). doi:10.1021/acs.analchem.6b01901

28. Zubarev, R.A., Kelleher, N.L., McLafferty, F.W.: Electron capture dissociation of multiply charged protein cations. A nonergodic process. J. Am. Chem. Soc. 120, 3265–3266 (1998). doi:10.1021/ja973478k

29. Syka, J.E.P., Coon, J.J., Schroeder, M.J., Shabanowitz, J., Hunt, D.F.: Peptide and protein sequence analysis by electron transfer dissociation mass spectrometry. Pro. Natl. Acad. Sci. USA. 101, 9528–9533 (2004). doi:10.1073/pnas.0402700101

30. Zhurov, K.O., Fornelli, L., Wodrich, M.D., Laskay, U.A., Tsybin, Y.O.: Principles of electron capture and transfer dissociation mass spectrometry applied to peptide and protein structure analysis. Chem. Soc. Rev. 42, 5014–5030 (2013). doi:10.1039/C3CS35477F

31. Coon, J.J.: Collision or Electron? Protein Sequence Analysis on the 21st Century. Anal.

Chem. 81, 3208–3215 (2009). doi:10.1021/ac802330b

32. Shi, S.D.H., Hemling, M.E., Carr, S.A., Horn, D.M., Lindh, I., McLafferty, F.W.: Phosphopeptide/Phosphoprotein Mapping by Electron Capture Dissociation Mass Spectrometry. Anal. Chem. 73, 19–22 (2000). doi:10.1021/ac000703z

33. Good, D.M., Wirtala, M., McAlister, G.C., Coon, J.J.: Performance Characteristics of Electron Transfer Dissociation Mass Spectrometry. Mol. Cell. Proteomics. 6, 1942–1951 (2007). doi:10.1074/mcp.M700073-MCP200

34. Frese, C.K., Altelaar, A.F.M., Hennrich, M.L., Nolting, D., Zeller, M., Griep-Raming, J., Heck, A.J.R., Mohammed, S.: Improved Peptide Identification by Targeted Fragmentation Using CID, HCD and ETD on an LTQ-Orbitrap Velos. J. Proteome Res. 10, 2377–2388 (2011). doi:10.1021/pr1011729

35. Asakawa, D., Takeuchi, T., Yamashita, A., Wada, Y.: Influence of Metal–Peptide Complexation on Fragmentation and Inter-Fragment Hydrogen Migration in Electron Transfer Dissociation. J. Am. Soc. Mass Spectrom. 25, 1029–1039 (2014). doi:10.1007/s13361-014-0855-6

36. Asakawa, D., Osaka, I.: High-Confidence Sequencing of Phosphopeptides by Electron Transfer Dissociation Mass Spectrometry Using Dinuclear Zinc(II) Complex. Anal. Chem. 88, 12393–12402 (2016). doi:10.1021/acs.analchem.6b03645

37. Loo, J.A., Loo, R.R.O., Light, K.J., Edmonds, C.G., Smith, R.D.: Multiply Charged Negative Ions by Electrospray Ionization of Polypeptides and Proteins. Anal. Chem. 64, 81–88 (1992). doi:10.1021/ac00025a015

38. Huzarska, M., Ugalde, I., Kaplan, D.A., Hartmer, R., Easterling, M.L., Polfer, N.C.: Negative Electron Transfer Dissociation of Deprotonated Phosphopeptide Anions: Choice of Radical Cation Reagent and Competition between Electron and Proton Transfer. Anal. Chem. 82, 2873–2878 (2010). doi:10.1021/ac9028592

39. Hersberger, K.E., Kristina, H.: Characterization of O -Sulfopeptides by Negative Ion Mode Tandem Mass Spectrometry: Superior Performance of Negative Ion Electron Capture Dissociation. Anal. Chem. 84, 6370–6377 (2012)

40. Madsen, J.A., Xu, H., Robinson, M.R., Horton, A.P., Shaw, J.B., Giles, D.K., Kaoud, T.S., Dalby, K.N., Trent, M.S., Brodbelt, J.S.: High-throughput Database Search and

Large-scale Negative Polarity Liquid Chromatography-Tandem Mass Spectrometry with Ultraviolet Photodissociation for Complex Proteomic Samples. Mol. Cell. Proteomics. 12, 2604–2614 (2013). doi:10.1074/mcp.O113.028258

41. Halim, M., Girod, M., MacAleese, L., Lemoine, J., Antoine, R., Dugourd, P.: 213 nm Ultraviolet Photodissociation on Peptide Anions: Radical-Directed Fragmentation Patterns. J. Am. Soc. Mass Spctrom. 27, 474–486 (2016). doi:10.1007/s13361-015-1297-5

42. Riley, N.M., Rush, M.J.P., Rose, C.M., Richards, A.L., Kwiecien, N.W., Bailey, D.J., Hebert, A.S., Westphall, M.S., Coon, J.J.: The Negative Mode Proteome with Activated Ion Negative Electron Transfer Dissociation (AI-NETD). Mol. Cell. Proteomics . 14 , 2644–2660 (2015). doi:10.1074/mcp.M115.049726

43. Riley, N.M., Bern, M., Westphall, M.S., Coon, J.J.: Full-Featured Search Algorithm for Negative Electron-Transfer Dissociation. J. Proteome Res. 15, 2768–2776 (2016). doi:10.1021/acs.jproteome.6b00319

44. Bowie, J.H., Brinkworth, C.S., Dua, S.: Collision-induced fragmentations of the (M-H)− parent anions of underivatized peptides: An aid to structure determination and some unusual negative ion cleavages. Mass Spectrom. Rev. 21, 87–107 (2002). doi:10.1002/mas.10022

45. Shaw, J.B., Kaplan, D.A., Brodbelt, J.S.: Activated Ion Negative Electron Transfer Dissociation of Multiply Charged Peptide Anions. Anal. Chem. 85, 4721–4728 (2013). doi:10.1021/ac4005315

46. Kim, T.-Y., Reilly, J.P.: Time-Resolved Observation of Product Ions Generated by 157 nm Photodissociation of Singly Protonated Phosphopeptides. J. Am. Soc. Mass Spectrom. 20, 2334–2341 (2009). doi:10.1016/j.jasms.2009.08.021

47. Robinson, M.R., Moore, K.L., Brodbelt, J.S.: Direct Identification of Tyrosine Sulfation by using Ultraviolet Photodissociation Mass Spectrometry. J. Am. Soc. Mass Spectrom. 25, 1461–1471 (2014). doi:10.1007/s13361-014-0910-3

48. Madsen, J. a., Kaoud, T.S., Dalby, K.N., Brodbelt, J.S.: 193-Nm Photodissociation of Singly and Multiply Charged Peptide Anions for Acidic Proteome Characterization. Proteomics. 11, 1329–1334 (2011). doi:10.1002/pmic.201000565

49. Fort, K.L., Dyachenko, A., Potel, C.M., Corradini, E., Marino, F., Barendregt, A., Makarov, A.A., Scheltema, R.A., Heck, A.J.R.: Implementation of Ultraviolet Photodissociation on a Benchtop Q Exactive Mass Spectrometer and Its Application to Phosphoproteomics. Anal. Chem. 88, 2303–2310 (2016). doi:10.1021/acs.analchem.5b04162

50. Robinson, M.R., Taliaferro, J.M., Dalby, K.N., Brodbelt, J.S.: 193 Nm Ultraviolet Photodissociation Mass Spectrometry for Phosphopeptide Characterization in the Positive and Negative Ion Modes. J. Proteome Res. 15, 2739–2748 (2016). doi:10.1021/acs.jproteome.6b00289

51. Lemoine, J., Tabarin, T., Antoine, R., Broyer, M., Dugourd, P.: UV photodissociation of phospho-seryl-containing peptides: Laser stabilization of the phospho-seryl bond with multistage mass spectrometry. Rapid Commun. Mass Spectrom. 20, 507–511 (2006). doi:10.1002/rcm.2333

52. Park, S., Ahn, W.-K., Lee, S., Han, S.Y., Rhee, B.K., Oh, H. Bin: Ultraviolet photodissociation at 266 nm of phosphorylated peptide cations. Rapid Commun. Mass Spectrom. 23, 3609–3620 (2009). doi:10.1002/rcm.4184

53. Antoine, R., Joly, L., Tabarin, T., Broyer, M., Dugourd, P., Lemoine, J.: Photo-induced formation of radical anion peptides. Electron photodetachment dissociation experiments. Rapid Commun. Mass Spectrom. 21, 265–268 (2007). doi:10.1002/rcm.2810

54. Madsen, J.A., Kaoud, T.S., Dalby, K.N., Brodbelt, J.S.: 193-nm photodissociation of singly and multiply charged peptide anions for acidic proteome characterization. Proteomics. 11, 1329–1334 (2011). doi:10.1002/pmic.201000565

55. Robinson, M.R., Moore, K.L., Brodbelt, J.S.: Direct identification of tyrosine sulfation by using ultraviolet photodissociation mass spectrometry. J. Am. Soc. Mass Spectrom. 25, 1461–1471 (2014). doi:10.1007/s13361-014-0910-3

56. Crowe, M.C., Brodbelt, J.S.: Infrared multiphoton dissociation (IRMPD) and collisionally activated dissociation of peptides in a quadrupole ion trap with selective IRMPD of phosphopeptides. J. Am. Chem. Soc. 15, 1581–1592 (2004). doi:10.1016/j.jasms.2004.07.016

57. Wilson, J.J., Brodbelt, J.S.: Infrared Multiphoton Dissociation for Enhanced de Novo

Sequence Interpretation of N-Terminal Sulfonated Peptides in a Quadrupole Ion Trap. Anal. Chem. 78, 6855–6862 (2006). doi:10.1021/ac060760d

58. Pikulski, M., Hargrove, A., Shabbir, S.H., Anslyn, E. V, Brodbelt, J.S.: Sequencing and Characterization of Oligosaccharides Using Infrared Multiphoton Dissociation and Boronic Acid Derivatization in a Quadrupole Ion Trap. J. Am. Soc. Mass Spectrom. 18, 2094–2106 (2007). doi:/10.1016/j.jasms.2007.09.005

59. Li, B., Russell, S.C., Zhang, J., Hedrick, J.L., Lebrilla, C.B.: Structure determination by MALDI-IRMPD mass spectrometry and exoglycosidase digestions of O-linked oligosaccharides from Xenopus borealis egg jelly. Glycobiology. 21, 877–894 (2011). doi:http://dx.doi.org/10.1093/glycob/cwr003

60. Park, Y., Lebrilla, C.B.: Application of Fourier transform ion cyclotron resonance mass spectrometry to oligosaccharides. Mass Spectrom. Rev. 24, 232–264 (2005). doi:10.1002/mas.20010

61. Brodbelt, J.S., Wilson, J.J.: Infrared multiphoton dissociation in quadrupole ion traps. Mass Spectrom. Rev. 28, 390–424 (2009). doi:10.1002/mas.20216

62. Zhou, Wen and Hakansson, K.: Structural Characterization of Carbohydrates by Fourier Transform Tandem Mass Spectrometry. Curr. Proteomics. 8, 297–308 (2011). doi:10.2174/157016411798220826

63. Girod, M., Sanader, Z., Vojkovic, M., Antoine, R., MacAleese, L., Lemoine, J., Bonacic-Koutecky, V., Dugourd, P.: UV Photodissociation of Proline-containing Peptide Ions: Insights from Molecular Dynamics. J. Am. Soc. Mass Spctrom. 26, 432–443 (2014). doi:10.1007/s13361-014-1038-1

64. Halim, M.A., Girod, M., MacAleese, L., Lemoine, J., Antoine, R., Dugourd, P.: Combined Infrared Multiphoton Dissociation with Ultraviolet Photodissociation for Ubiquitin Characterization. J. Am. Soc. Mass Spectrom. 27, 1435–1442 (2016). doi:10.1007/s13361-016-1419-8

65. Frisch, M., Trucks, G., Schlegel, H.: Gaussian 09, Revision D. 01; Gaussian: Wallingford, CT, USA, 2009.

66. DeGnore, J., Qin, J.: Fragmentation of phosphopeptides in an ion trap mass spectrometer. J. Am. Soc. Mass Spectrom. 9, 1175–1188 (1998). doi:10.1016/S1044-

0305(98)00088-9

67. Tholey, A., Reed, J., Lehmann, W.D.: Electrospray tandem mass spectrometric studies of phosphopeptides and phosphopeptide analogues. J Mass Spectrom. 34, 117–123 (1999). doi:3.0.CO;2-V

68. Moyer, S.C., VonSeggern, C.E., Cotter, R.J.: Fragmentation of cationized phosphotyrosine containing peptides by atmospheric pressure MALDI/Ion trap mass spectrometry. J. Am. Soc. Mass Spectrom. 14, 581–592 (2003). doi:10.1016/S1044-0305(03)00142-9

69. Annan, R.S., Carr, S. a: Phosphopeptide analysis by matrix-assisted laser desorption time-of-flight mass spectrometry. Anal. Chem. 68, 3413–3421 (1996)

70. Flora, J.W., Muddiman, D.C.: Determination of the relative energies of activation for the dissociation of aromatic versus aliphatic phosphopeptides by ESI-FTICR-MS and IRMPD. J. Am. Soc. Mass Spectrom. 15, 121–127 (2004). doi:10.1016/j.jasms.2003.10.004

71. Han, H., Xia, Y., McLuckey, S.A.: Ion Trap Collisional Activation of c and z• Ions Formed via Gas-Phase Ion/Ion Electron-Transfer Dissociation. J. Proteome Res. 6, 3062–3069 (2007). doi:10.1021/pr070177t

72. Antoine, R., Lemoine, J., Dugourd, P.: Electron Photodetachment Dissociation for Structural Characterization of Synthetic and Bio-Polymer Anions. Mass Spectrom. Rev. 33, 501–522 (2014). doi:10.1002/mas.21402

73. Madsen, J., Cheng, R.R., Kaoud, T.S., Dalby, K., Makarov, D.E., Brodbelt, J.: Charge-site-dependent dissociation of hydrogen-rich radical peptide cations upon vacuum UV photoexcitation. Chem. Eur. J. 18, 5374–5383 (2012). doi:10.1002/chem.201103534

74. Girod, M., Sanader, Z., Vojkovic, M., Antoine, R., MacAleese, L., Lemoine, J., Bonacic-Koutecky, V., Dugourd, P.: UV Photodissociation of Proline-containing Peptide Ions: Insights from Molecular Dynamics. J. Am. Soc. Mass Spctrom. 26, 432–443 (2014). doi:10.1007/s13361-014-1038-1

75. Paciotti, R., Coletti, C., Re, N., Scuderi, D., Chiavarino, B., Fornarini, S., Crestoni, M.E.: Serine O-sulfation probed by IRMPD spectroscopy. Phys. Chem. Chem. Phys. 17, 25891–25904 (2015). doi:10.1039/C5CP01409C

76. Budnik, B. a., Haselmann, K.F., Zubarev, R. a.: Electron detachment dissociation of peptide di-anions: An electron-hole recombination phenomenon. Chem. Phys. Lett. 342, 299–302 (2001). doi:10.1016/S0009-2614(01)00501-2

77. Seipert, R.R., Dodds, E.D., Lebrilla, C.B.: Exploiting differential dissociation chemistries of O-linked glycopeptide ions for the localization of mucin-type protein glycosylation. J. Proteome Res. 8, 493–501 (2009). doi:10.1021/pr8007072

78. Zhu, Z., Su, X., Clark, D.F., Go, E.P., Desaire, H.: Characterizing O-Linked glycopeptides by electron transfer dissociation: Fragmentation rules and applications in data analysis. Anal. Chem. 85, 8403–8411 (2013). doi:10.1021/ac401814h

Chapter Five:

Photodissociation of Polymer Ions: Cation *vs* Anion

"The spectral density of back-body radiation represents something absolute. Searching the absolute is the highest form of research."

– Max Planck

5.1 Introduction

Understanding the mechanism of unimolecular reactions especially for larger chemical and biological systems with mass spectrometry is an active area of research. For any chemical reaction, reactants are required to overcome a barrier gaining internal energy by means of collision or photo-activation. However, the unimolecular reaction follows a first-order kinetic which demands a plausible explanation. Black-body radiation-induced and slow heating collision-induced activation mechanisms can provide reasonable elucidation of unimolecular reactions for cluster ions, peptide or protein ions, and small segments of DNA [1, 2] . However, the unimolecular reactions performed in traditional trapped-ion mass spectrometry cannot detect individual ions and deals only with the cloud of ions. Although one would like to use single-ion measurements [3, 4] to analyze and compare the different decay mechanisms of large versus small chemical and biological systems. Indeed, information gained at the single molecule level is much richer than the mere averages, as it notably provides much more insight into the physical mechanisms through the correlation between various observables [5]. This limitation can be overcome if one can measure each ion independently, which may offer more physical insights to the dissociation mechanism.

Charge-detection Mass Spectrometry (CDMS) is a single ion detection technique in which mass-to-charge ratio (*m/z*) and charge (z) of each ion can be detected individually [6]. Since this technique is not associated to the charge state resolution, it can be applied to weigh large chemical and biological systems of megadalton or higher species [7, 8] (details are already discussed in **chapter 1**). In addition, this technique can equally be employed for intrinsic and extrinsically heterogeneous systems. Since the first coupling of this concept with electrospray ionization (ESI) by Brenner and co-workers [6], application of the CD-MS technique has significantly increased for weighing megadalton species such as DNAs, synthetic polymers, block copolymer micelles, vesicles, nanoparticles, viruses, and fibrils [8-19].

In 1997, W. Henry Benner proposed an extension of the CD-MS technique by combining the charge-detection device with an electrostatic ion trap ("Benner" trap) [20]. Due to the trapping capability of this MS device, individual plasmid DNA ions in the megadalton range (i.e. with masses greater than 10^6 Da) were detected and measured with high accuracies. Furthermore, this technique opened the way to directly measuring the kinetics of dissociation of large macro ions after activation, as well as providing a direct correlation between precursor and product ions [8, 11]. Stepwise vibrational excitation in infrared multiphoton dissociation (IRMPD) has been used to study the chemistry of small molecules for decades [21]. Infrared Multiphoton dissociation (IRMPD) is an indispensable tools for studying unimolecular reaction mechanisms as this reaction can be treated as a thermal reaction which equilibrates ions thermally at a known temperature in the collision cell through multiphoton absorption. The previous studies of Dunbar et al. showed that continuous-wave CO_2 laser dissociation can drive a reaction and can be compared with a black-body source [22, 23], an idea which has been exploited for the quantitative characterization of unimolecular dissociation processes [24-26]. Low energy IR photons can thus promote vibrationally induced excitation, which has been utilized to explore the dissociation mechanism of small molecules, proteins and large oligonucleotides for years. However, very few studies are employed for megadalton species [5]. Recently our group pushed the limit of IRMPD to megadalton-size DNA ions, by coupling a CO_2 laser to a “Benner” Trap. In this study on IRMPD for double and single strands of DNA cations disclosed that activation energy elevated slightly with increases of mass [27]. The experiment also revealed several fragmentation pathways having distinct signatures at the single molecule level which would not be accessible from studies based on statistically averaged reaction rates only. Indeed, the waveforms recorded under laser irradiation revealed several fragmentation patterns having distinct signatures at the single-molecule level. Three types of fragmentation patterns have been observed: “sudden loss”, “funnel”, and “staircase” behavior [5, 27]. Moreover, the fragmentation pattern is quite different for double and single strands DNAs with different repartition in the three types of fragmentation patterns. A similar pattern is also observed for polyethylene oxide (PEO) cations having an average molecular weight of 7 megadalton [5].

The unimolecular dissociation mechanism may also depend on the nature of the charge of the molecular ions. Indeed, both binding energy and branching ratio in dissociation channels can be different for anions and cations. Previous studies on carbon clusters such as fullerenes showed different patterns of decay mechanisms for cations and anions [28-30]. For fullerene cation, the decay mechanism leads to sequential emission of neutral C_2 fragments, whereas the decay process of anionic fullerene involves the loss of one or more of its excess electrons through delayed electron (thermionic) emission [31].

Herein, we aim at exploring the unimolecular gas phase ion chemistry, in particular its dependence on the sign of the charge, in the megadalton range. We employ infrared multiphoton photodissociation coupled to a gated electrostatic ion trap for studying the decay mechanism of SO_3-containing poly(2-acrylamido-2-methyl-1-propanesulfonic acid) synthetic polymer known as PAMPS (with an average molecular weight ~2 MDa) in positive and negative polarities. We notice that the activation energy of PAMPS positive and negative ions is quite different. The fragmentation patterns revealed by analyzing the waveforms recorded under laser irradiation are also compared.

5.2 Materials and Methods

5.2.1 Coupling CO_2 Laser with Charge-detection Mass Spectrometer

A cw CO_2 laser (λ = 10.6 μm, output power of 25 W) was used for coupling with CDMS (**Scheme 5.1**). The beam shape is circular with a near Gaussian profile. The beam diameter is 3.5 mm at the output aperture and has a full angle divergence of 4 mrad. The laser beam is reflected by three gold-coated copper mirrors, after which it is injected on the rear side of the CDDs through a ZnSe window that is installed on the rear of the CDD chamber. For laser power dependence experiments, the laser was operated at 5 kHz, and the photon flux was varied by changing the duty cycle of the laser (from 10 to 50%).

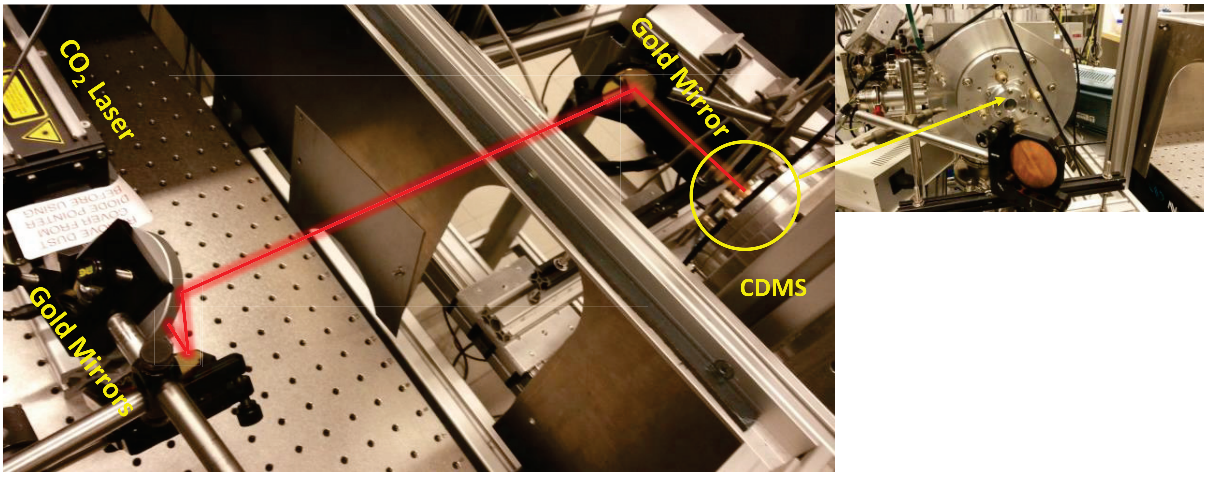

Scheme 5.1 Schematic representation of the coupling CO_2 laser with charge-detection mass spectrometer.

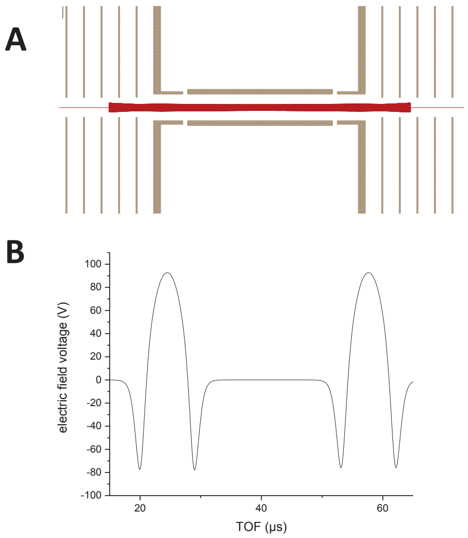

Figure 5.1 A) A simulated trajectory B) time of flight (TOF) *vs* electric field voltage diagram of a positively charged ion with a mass and charge of 2x10^6 Da and +700, respectively. The ion velocity is 2400 m/s.

5.2.2 Gated Electrostatic Ion Ttrap: "Benner" Trap

When an ion enters the trap device, it triggers a circuit that enables the potentials on the entrance and exit electrodes (ion mirrors) to predetermined values designed to reflect ions. In this device, the image charge, at each passage of the ion, is collected by the 'pick-up' tube (high impedance) and is transmitted to a field effect transistor (2SK152) which is already discussed in **chapter 1**. Transmission between the mechanics of the "Benner" trap and the PCB is made by a copper rigid connector. In addition to limit ground currents, this rigid link allows to minimize noise. The equivalent capacity of the link between the pick-up tube and the JFET is approximately 1 pF.

In order to find the correct potentials to apply on the entrance and exit electrodes to optimally reflect and focus ions of a given energy toward the detector tube, we conducted ion trajectory simulation with SIMION 7.0 (http://simion.com/). SIMION was used to build electrode geometries and determine DC contributions to the fields. **Figure 5.1A** shows a trajectory simulation of a positively charged ion with a mass of 2x10^6 Da holding +700 charges and moving with an initial velocity of 2400 m/s, reflecting a few hundred times through the detector. The lens numbering system progresses from 1a), the end cap, to 6, the electrode farthest from the end cap of the detector. The detector tube is separated from the endcaps by a small space. In **Figure 5.1**, the following voltages are applied to the electrodes: L1 = 0 V, L2 = -122 V, L3 = 52 V, L4 = 131 V, L5 = 187V andL6 = 220 V. The optimal voltages obtained in this simulation are similar to those proposed by Benner. For negatively charged ions, the following voltages are applied to the electrodes: L1 = 0 V, L2 = +120 V, L3 = -52 V, L4 = -131 V, L5 = -187V andL6 = -220 V. Only ions in a specific range of initial velocity are trapped by the potential valley provided by ion mirrors. With the optimal voltages applied on the ion mirrors, the ion trajectory oscillates between the two mirrors. Ion trajectories are reflected between L2 and L3 electrodes. The electric field voltage seen by the single trapped ion is displayed as a function of the time of flight in **Figure 5.1B**. Interestingly, the ion spends about half of the TOF in the field-free region (charge detection tube) and the other half of the TOF is spent in the ion mirrors.

5.2.3 Electrospray Instrumentation and Sample Preparation

An electrospray ion source and vacuum interface were used to generate the ion beam. Sample solutions, at flow rates typically of 0.6-1.0 mL/h, enter the electrospray chamber through a 0.1 mm internal diameter stainless steel capillary tube located inside the needle tip. Nitrogen drying gas is injected between the end cap and the transfer glass capillary. It is used to enhance electrospray droplet desolvation and flows through a heater typically set at 200°C. We used poly(2-acrylamido-2-methyl-1-propanesulfonic acid) synthetic polymer known as PAMPS, with an average molecular weight ~2 MDa (Sigma-Aldrich). Solutions were prepared in water: methanol (50:50, v/v) at a concentration of 0.2-0.3 g/L (agitated for 24 h) and electrosprayed in both positive and negative ESI ionization modes. Sulfonate backbone is known to have a high affinity for sodium ions, and we postulate that sodium adducts are responsible for charging in PAMPS polymers in positive ESI mode, as it has been observed for phosphate backbone in DNAs [6, 13, 14]. In the negative ESI mode, easy deprotonation of sulfonate backbone is likely responsible for charging in PAMPS (see **Scheme 5.2**). A spray voltage of ~±2800 V is used for both ESI ionization modes. Gas-phase ions were transmitted through an ionic train containing a hexapole ion guide and ionic lenses and directed toward the “Benner” trap. The distribution of mass for these ions recorded by electrospray-charge-detection mass spectrometry exhibits a maximum at 2.8 MDa, as well as a high-mass tail. The high-mass tail is due to the dispersion in the degree of polymerization for such macromolecules and extends up to ~12 MDa [26]. The polarity of all voltages (with the same absolute values) was reversed when negatively charged ions were studied.

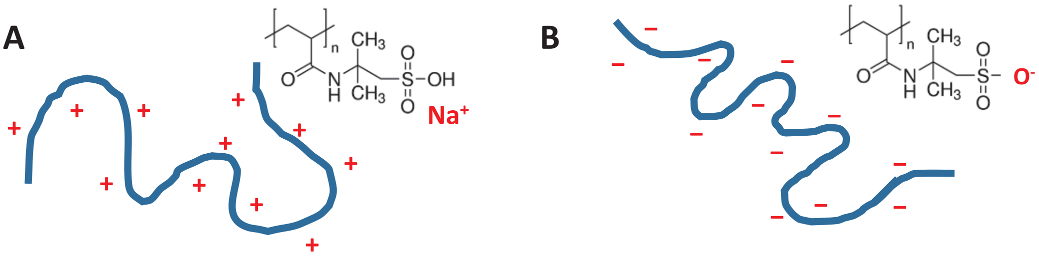

Scheme 5.2 A) Positive and B) Negative PAMPS ions

5.2.4 Quantum Calculations

All calculations were performed with Gaussian09 program [32]. Model systems of PAMPS polymer cation (Na^+), anion, and their corresponding fragments (see **Figure 5.2**) are optimized at the B3LYP/6-31G(d) level of theory. Vibrational frequencies of all ions were also calculated to confirm that all systems are in the minima of the potential energy surface. Ionization potential and electron detachment energy of the corresponding ions are also calculated by removing and adding an electron from or to the model systems. Infrared spectra of positive and negative PAMPS monomer ions were calculated at B3LYP/6-31G(d) level of theory. A scaling factor of 0.9613 was used for IR frequencies.

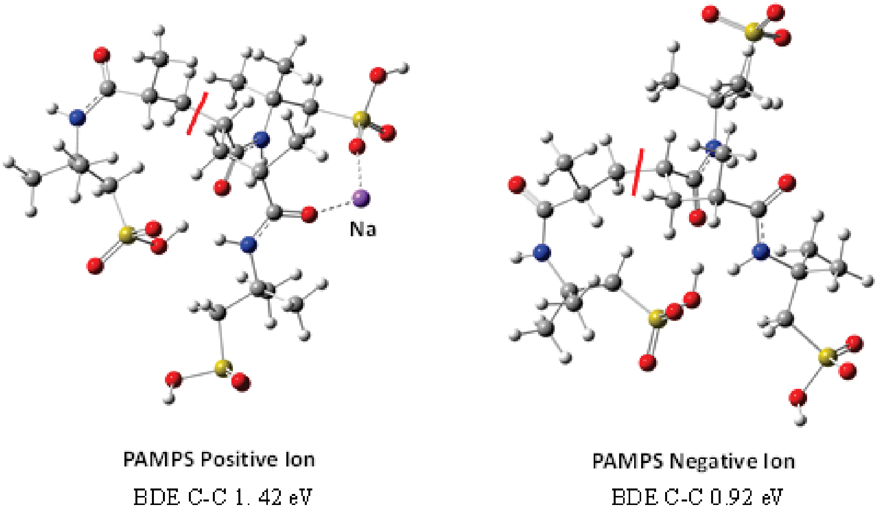

Figure 5.2 Optimized structure of PAMPS positive and negative ions calculated at B3LYP/6-31G(d) level of theory.

5.3 Result and Discussion

5.3.1 Fragmentation Signatures at the Single Molecule Level

With and without laser, the single trapped ions undergoes several hundred round trips between the ion mirrors in the "Benner" trap. The corresponding single ion image current generated by the round trips of ions in the trap (oscillations) is then recorded as a function of time. **Figure 3A** shows the experimental raw time domain signal for a trapped ion created by a single highly charged electrospray ion of PAMPS (in positive mode) as it travelled back and forth through the ion trap. The single ion has been trapped for ~18 ms during which time it cycled ~380 times through the detector tube. The shape and amplitude of the raw signal are roughly constant, which means that no significant charge loss is observed during the trapping time.

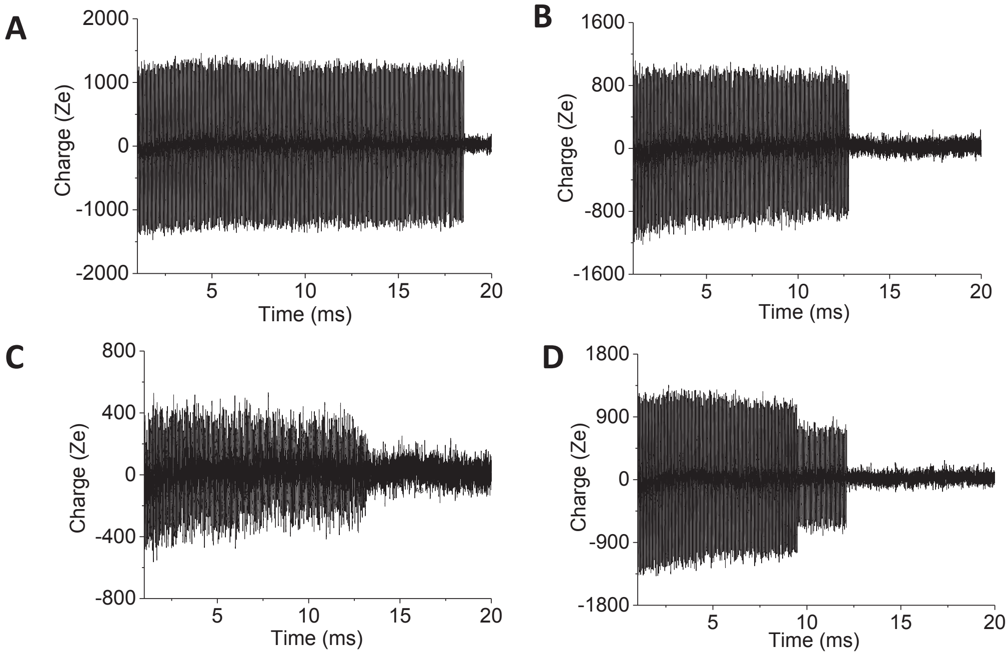

Figure 5.3 A) Ion wavelet for PAMPS positive ion a stored in the electrostatic ion trap without laser irradiation. Ion wavelet of B) "sudden loss" C) "funnel" and D) "stair case" types of decay recorded for a PAMPS positive ion stored in the electrostatic ion trap under continuous irradiation by the CO_2 laser. In the "funnel" type of decay, the total charge of the ion gradually decreased before the loss of the particle.

As the laser is switched on during the ion trapping time, drastic changes are observed both in the trapping duration and the shape of the oscillations. Charge decay patterns are individually analyzed according to their shape, and can be classified in three families. If the shape and amplitude of the raw signal is roughly the same with shorter trapping duration than the one recoded without laser, the charge decay profile is classified as "sudden loss" (**Figure 5.3B**). If modification in the charge decay patterns occurs at the end of the trapping duration, decay shapes are then classified in two different categories: i) decay shapes named "funnel" (**Figure 5.3C**) are assigned to those that lose progressively charges until disappearance, ii) "staircase"-type decays (**Figure 5.3D**) correspond to a sudden loss of a certain amount of charges from the parent ion leading to a stable fragment that stays as produced within the trap longer than 500 μs (or six oscillations). Note that the noise level in the pick-up signal has been improved as compared to our previous work [5, 8, 27] and now is as low as ~200 e. In our analysis, we only observed single fragment ions corresponding to the largest fragmentation product.

When photofragmentation occurs, and considering the "stair-case"-type of decay, both the *m/z* ratio and the kinetic energy E_0 of the photofragments can be different from the precursor ion and then accurate measurements of m/*z* for photofragments are difficult to extract. If photofragments are generated when the precursor is traveling in the region of the ion mirrors, the trapping stability is non-trivial and must satisfy both spatial and temporal focusing conditions [33]. Trajectory simulations using SIMION 7.0 indicate that fragment ions are less efficiently trapped when they are generated in the ion mirrors than fragments generated in the field free region. Such fragments are usually not stable and will be lost suddenly in the trap leading to a "sudden-loss"-type of decay. One the other hand, it the fragment ion is generated in the field-free region, it will have the same velocity as the precursor ion. Trajectory simulations using SIMION 7.0 indicate that fragment ions are efficiently trapped when they are generated in the field-free region. If the *m/z* ratio of the photofragment is equal to the *m/z* ratio for precursor ion, the TOF of photofragment is equal to the TOF of precursor. If the *m/z* ratio of the photofragment is higher (lower) than that of the precursor, then the TOF of photo fragments will be higher (lower) than that of the precursor as shown in **Figure 5.4**. A linear dependence is obtained between the *m/z* ratio and the observed TOF for fragments. Thus the Benner trap behaves like a MS/MS instrument, where both the *m/z* of precursor and fragments can be extracted from "stair-case"-type of decay. As two distinct population of ions are observed in stair-case, one can detect the charge and time of flight of precursor and fragment ions separately. We collected, from traces belonging to “stair-case”-type of decay, both TOF of precursor and fragment ions (see **Figure 5.5 A**), for positively charged ions). It appears that TOFs of precursor are lower than TOFs of fragment ions. This means that the largest fragmentation products generated from IR multiphoton absorption of megadalton PAMPS have *m/z* ratios higher than the *m/z* of their precursor ions. Again, from traces belonging to “stair-case”-type of decay, we collected both the total charges of precursor and fragment ions (see **Figure 5.5B**), for positively charged ions. On the average, the largest fragment ions hold ~75 % of the total precursor charge. Results are similar for both cations and anions.

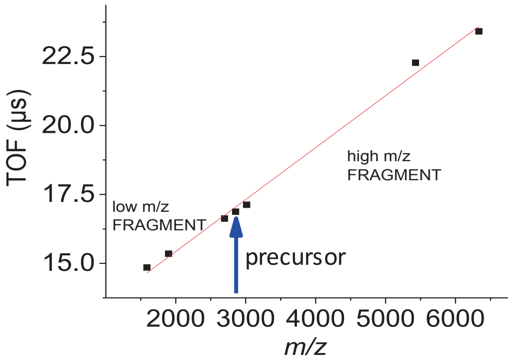

Figure 5.4 SIMION simulation of the time of flight (µs) vs *m/z* of high and low fragments generated from dissociation of a precursor ion in the center of the field-free region of the “Benner” trap. The precursor ion is a positively charged ion with a mass and charge of 2x10^6 Da and +700, respectively. The ion velocity is 2400 m/s.

5.3.2 Fragmentation signatures and activation energy: Statistical analysis

As already observed for (bio)polymer macroions [5, 8, 27], the waveforms recorded under laser irradiation reveal several fragmentation pathways having distinct signatures at the single-molecule level. Three types of fragmentation patterns have been observed, as shown in **Figure 5.3(b-d)**. The shape of the oscillation adopted three distinctive patterns such as ‘Funnel-Like’, ‘Stair-Case’ and ‘Sudden-Loss’ as we also witnessed in our previous studies on megadalton DNA and polyethylene oxide (PEO). It appeared that the shapes of the oscillations are inherent properties related to megadalton species when they are exposed to IR photons. After analysis all distinctive patterns for all laser powers for positively and negatively charged ions we see nearly similar trend on abundance of those patterns. However, the funnel shape has lower charge compared to stair-case and sudden-loss patterns, as shown in **Figure 5.6**. In particular, stair-case pattern is only observed when PAMPS ions have charges higher than 600 e.

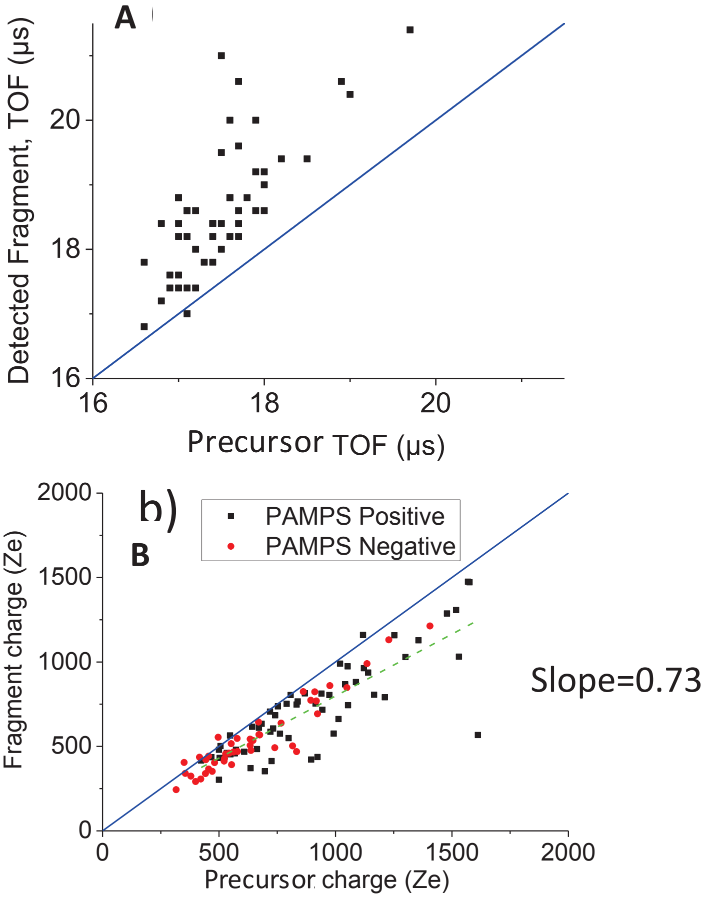

Figure 5.5 A) Experimental time of flight of precursor and fragment for positively charged ions B) Charge distribution of precursor and fragment ions in stair-case type of patterns for positive and negative PAMPS ions.

A statistical analysis of the abundance of the three family of decay pattern permits us to notice that for both ions characteristic stair-case traces are relatively less frequent than other traces. In negative mode, 11% traced are stair-case whereas in positive mode only 9% are such a type (**Figure 5.7**.). For negative ions, 60% of traces are funnel-like, and 58% are detected for positive ions. The sudden-loss traces for positive and negative ions are 29% and 33%,

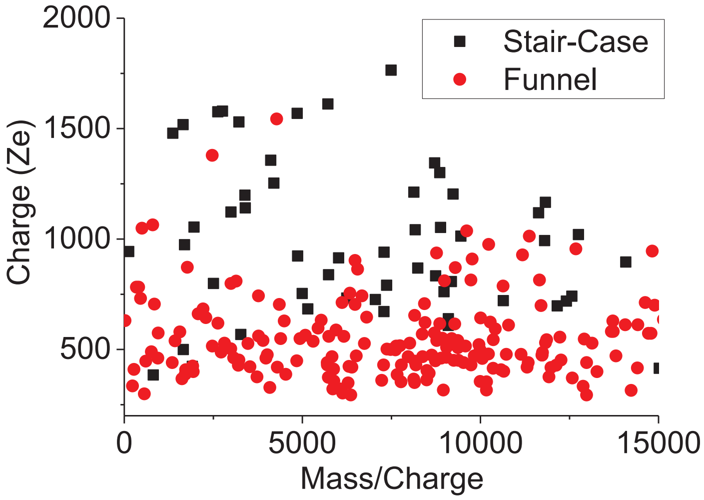

Figure 5.6 Charge and mass/charge distribution of stair-case and funnel traces.

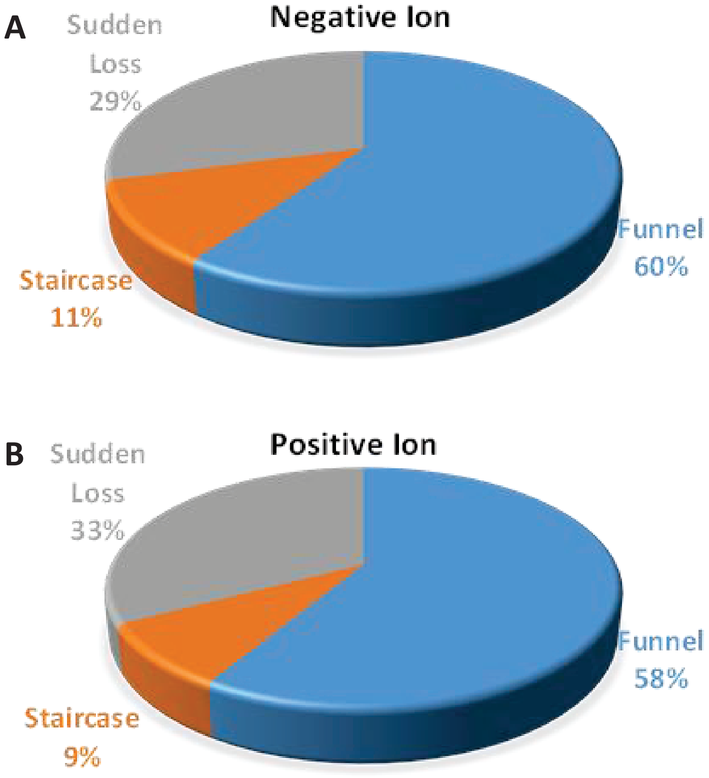

Figure 5.7 Distributions of the shapes of the decay wavelets for PAMPS A) positive and B) negative ions under CO_2 laser irradiation.

respectively (**Figure 5.7**). In contrast to our previous studies, we notice that for all traces there is a slight continuing decrease of amplitude over trapping time while the laser was switched on.

Interpreting the observed kinetics for the dissociation of PAMPS ions requires monitoring a large set of traces of individual ions to construct a density distribution of dissociation rates for a collection of ions. For each laser power, ~100 traces of individual ions were analyzed, and the normalized ion count at a given time (ranging from 1 to 20 ms) was obtained by the number of traces for which the ion was still detectable at this time, further normalized by the initial number of traces considered. The decaying relative ion abundances of positive PAMPS ion as a function of irradiation time using different laser intensities from 11.9 to 29.9 W/cm^2 are depicted in **Figure 5.8**. Nearly similar trends are observed for negative time (data is not shown). With increase of laser intensity, the rate of dissociation increases. The initiation of dissociation is detected after an induction time, after which the rate is treated as a log-linear decay. The rate of dissociation is calculated from the linear fit of $k_{diss} = -d\ \ln(CI)/dt$, where CI is the ion count. For calculating the activation energy E_a for positive and negative ion photodissociation, we first obtain the first order rate constants at various laser intensities (**Figure 5.8A**). Then we plot the natural logarithm of the rate constant against the natural logarithm of the laser intensities, which has been estimated to provide the E_a value according to the following equation [8, 34, 35]:

$$E_a = 0.22 \frac{d \ln k_{diss}}{d \ln \rho(\nu_{laser})} \quad (1)$$

Assuming, sk_B=0.22 (as reported for proteins and DNAs) [34, 36], for positive ion, the activation energy of the photodissociation is 0.65 eV, compared with the lower activation energy of 0.26 eV for negative ions.

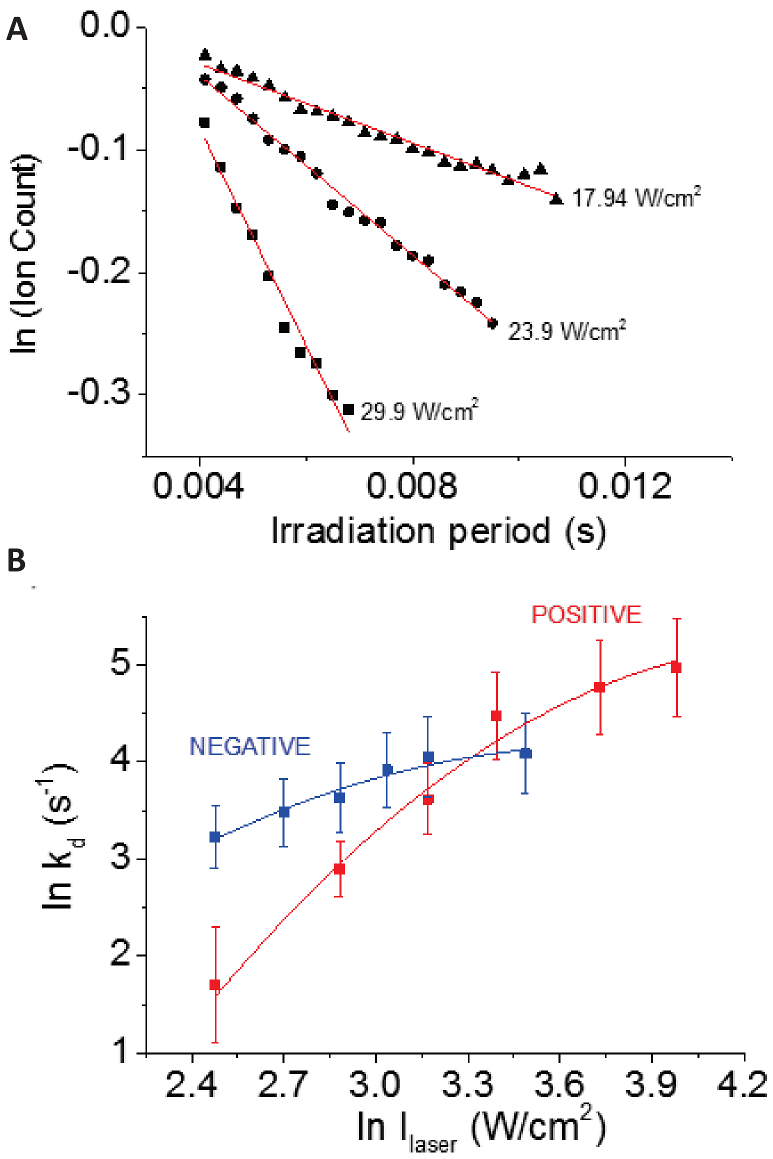

Figure 5.8 A) Logarithm of ion count versus time for the dissociation of PAMPS position ions under different laser powers. The plots were constructed by analyzing ~300 wavelets of individual ions at each laser power in order to construct a frequency histogram of the distribution of ion counts. The line corresponds to a linear fit of the data. B) Respective plots of the logarithm of the first-order unimolecular dissociation rate constant, k_{diss}, versus the logarithm of the laser intensity for both positive and negative PAMPS ions. The activation energy for dissociation, E_a, is obtained from the slope of the linear fit (see Equation 1).

5.3.3 Decay Pathways

In general, photoexcited molecular cations $(M^{n+})^*$ can decay via the following channels:

$$M^{n+*} + nh\upsilon \longrightarrow (M^{n+})^* \longrightarrow \begin{cases} M^{(n+m)+} + me^- & (a) \\ F_1^{p+} + F_2^{q+} & (b) \\ M^{n+} + nh\upsilon' & (c) \end{cases}$$

Similarly for anions

$$M^{n-*} + nh\upsilon \longrightarrow (M^{n-})^* \longrightarrow \begin{cases} M^{(n-m)-} + me^- & (d) \\ F_1^{p-} + F_2^{q-} & (e) \\ M^{n-} + nh\upsilon' & (f) \end{cases}$$

provided the internal energy of excited molecular ions, determined by the multiphoton absorption energy and the internal energy of the ion before the excitation, exceeds the barrier energy. Channels (a) and (d) are respectively (multi)ionization and (multi) electron emission. Channels (b) and (e) are fragmentation (which can be fission or evaporation of small fragments from precursor ions).

Finally, channels (c) and (f) are radiative transitions. This last process is supposed to be a major process at low internal energy when fragmentation and ionization are not open. Channels (a) and (d) are respectively related to the ionization potential and the detachment energy of PAMPS polymers. We calculated the second ionization potential for PAMPS trimers, i.e. 10.7 eV (calculated for single charged cation at the B3LYP/6-31G(d) level of theory) and the detachment energy of the acidic group in PAMPS trimers, i.e. 4.5 eV (calculated for single charged anion at the B3LYP/6-31G (d) level of theory). For channels (b) and (e) corresponding to fragmentation, an estimation of the bond dissociation energy (BDE) is required. For this purpose, the structure of the PAMPS of positive and negative ions has been calculated and the optimized structures are shown in the **Figure 5.2**. In positive mode, sodium cation forms two distinct non-bonding interactions. The Na---O=C/S bond distance is 2.102-2.187 Å. The Mulliken partial charge on the Na and adjacent oxygen are +0.65 (a. u) and -0.55 (a. u), respectively. However, in negative ions such interactions are absent. Our quantum calculation on the bond dissociation energy (BDE) associated to the breaking of a C–C bond (see red line in the **Figure 5.2)** for positive and negative ions are different. For positive ion, the BDE is 1.42 eV whereas for negative ion it is 0.92 eV which indicates that sodium (Na^+) cation play a significant role on the stabilizing the system and thus the polymeric C−C bonds compared to negative ions. Moreover, calculated IR spectra of positive and negative PAMPS ions disclosed that stretching frequency of the S=O bond appeared at 955 cm^{-1} (correlate with CO_2 laser wavelength, 10.64 μm = 939 cm^{-1}) whereas such stretching mode for positive ion is shifted to 1086 cm^{-1} (**Figure 5.9**). These values are in a reasonable trend with the values obtained for activation energy for megadalton PAMPS ions. The difference observed in activation energy values between positively and negatively charged ions may be due to different binding energy depending on the nature of the charge on the polymer.

Note that successive electron detachment would lead to the observation of gradual loss of charge from the decay traces (see **Figure 5.3**) and then a majority of funnel-like decay traces for negatively charged ions. The fact that the branching ratio between the 3 different families of traces (sudden-loss, funnel and stair-case) is similar for both positively and negatively charged ions preclude this hypothesis (see **Figure 5.7**).

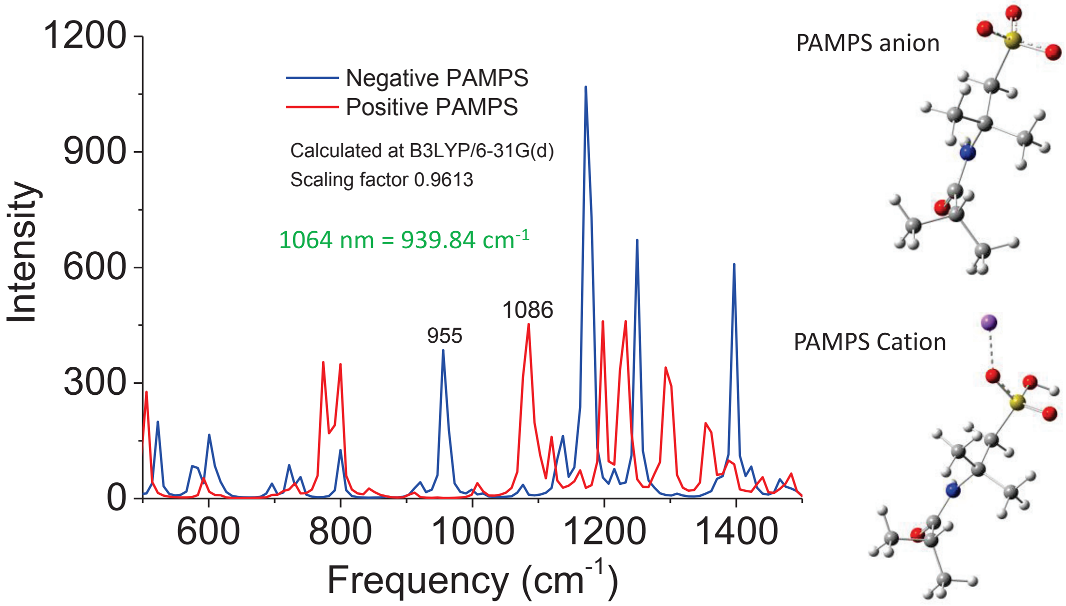

Figure 5.9 IR spectra of positive and negative PAMPS monomer ions calculated at B3LYP/6-31G(d) level of theory.

5.4 Summary

Herein we coupled infrared multiphoton dissociation with charge-detection ion trap mass spectrometry to study the decay mechanism of megadalton polymer cation and anion. Simulation and quantum calculations have been performed to investigate the thermal dissociation of large polymer ions. Our study discloses that photodissociation pathways of megadalton polymer cation and anion are different in which positive ions require overcoming a higher activation barrier while negative ions follow a lower activation channel. Density functional theory calculation also supports those pathways since bond dissociation energies of positive and negative polymer ions are different. Na^+ ion plays a pivotal role in stabilizing the PAMPS cations by introducing non-bonding interactions; however; such an interaction is not present for negative ions. Moreover, irradiation of the trapped ions with IR photons produced three different shapes for the ion-decay profiles. Highly charged precursor ions characteristically adopt a distinctive "stair-case" pattern whereas low charge species follow a "funnel like" shape.

Bibliography

1. Dunbar, R.C.: BIRD (blackbody infrared radiative dissociation): Evolution, principles, and applications. Mass Spectrom. Rev. **23**, 127-158 (2004)
2. Laskin, J., Futrell, J.H.: Activation of large ions in FT-ICR mass spectrometry. Mass Spectrom. Rev. **24**, 135-167 (2005)
3. Chen, R., Cheng, X., Mitchell, D.W., Hofstadler, S.A., Wu, Q., Rockwood, A.L., Sherman, M.G., Smith, R.D.: Trapping, Detection, and Mass Determination of Coliphage T4 DNA Ions of 108 Da by Electrospray Ionization Fourier Transform Ion Cyclotron Resonance Mass Spectrometry. Anal. Chem. **67**, 1159-1163 (1995)
4. Smith, R.D., Cheng, X., Bruce, J.E., Hofstadler, S.A., Anderson, G.A.: Trapping, Detection and Reaction of Very Large Single Molecular-Ions by Mass-Spectrometry. Nature. **369**, 137-139 (1994)
5. Antoine, R., Doussineau, T., Dugourd, P., Calvo, F.: Multiphoton dissociation of macromolecular ions at the single-molecule level. Phys. Rev. A. **87**, 013435 (2013)
6. Fuerstenau, S.D., Benner, W.H.: Molecular weight determination of megadalton DNA electrospray ions using charge detection time-of-flight mass spectrometry. Rapid Commun. Mass Spectrom. **9**, 1528-1538 (1995)
7. Keifer, D.Z., Jarrold, M.F.: Single-molecule mass spectrometry. Mass Spectrom. Rev. DOI: 10.1002/mas.21495, (2016)
8. Doussineau, T., Antoine, R., Santacreu, M., Dugourd, P.: Pushing the Limit of Infrared Multiphoton Dissociation to Megadalton-Size DNA Ions. J. Phys. Chem. Lett. **3**, 2141-2145 (2012)
9. Loumaigne, M., Midelet, C., Doussineau, T., Dugourd, P., Antoine, R., Stamboul, M., Debarre, A., Werts, M.H.V.: Optical extinction and scattering cross sections of plasmonic nanoparticle dimers in aqueous suspension. Nanoscale. **8**, 6555-6570 (2016)
10. Faucon, A., Benhelli-Mokrani, H., Fleury, F., Dubreil, L., Hulin, P., Nedellec, S., Doussineau, T., Antoine, R., Orlando, T., Lascialfari, A., Fresnais, J., Lartigue, L., Ishow, E.: Tuning the architectural integrity of high-performance magneto-fluorescent core-shell nanoassemblies in cancer cells. J. Colloid Interface Sci. **479**, 139-149 (2016)

11. Doussineau, T., Bao, C.Y., Clavier, C., Dagany, X., Kerleroux, M., Antoine, R., Dugourd, P.: Infrared Multiphoton Dissociation Tandem Charge Detection-Mass Spectrometry of Single Megadalton Electrosprayed Ions. Rev. Sci. Intrum. **82**, 084104 (2011)
12. Fuerstenau, S.D., Benner, W.H., Thomas, J.J., Brugidou, C., Bothner, B., Siuzdak, G.: Mass spectrometry of an intact virus. Angew. Chem.-Int. Edit. **40**, 542-544 (2001)
13. Schultz, J.C., Hack, C.A., Benner, W.H.: Mass determination of megadalton-DNA electrospray ions using charge detection mass spectrometry. J. Am. Soc. Mass Spectrom. **9**, 305-313 (1998)
14. Schultz, J.C., Hack, C.A., Benner, W.H.: Polymerase chain reaction products analyzed by charge detection mass spectrometry. Rapid Commun. Mass Spectrom. **13**, 15-20 (1999)
15. Pierson, E.E., Keifer, D.Z., Asokan, A., Jarrold, M.F.: Resolving Adeno-Associated Viral Particle Diversity With Charge Detection Mass Spectrometry. Anal. Chem. **88**, 6718-6725 (2016)
16. Pierson, E.E., Keifer, D.Z., Selzer, L., Lee, L.S., Contino, N.C., Wang, J.C.Y., Zlotnick, A., Jarrold, M.F.: Detection of Late Intermediates in Virus Capsid Assembly by Charge Detection Mass Spectrometry. J. Am. Chem. Soc. **136**, 3536-3541 (2014)
17. Warren, N.J., Mykhaylyk, O.O., Ryan, A.J., Williams, M., Doussineau, T., Dugourd, P., Antoine, R., Portale, G., Armes, S.P.: Testing the Vesicular Morphology to Destruction: Birth and Death of Diblock Copolymer Vesicles Prepared via Polymerization-Induced Self-Assembly. J. Am. Chem. Soc. **137**, 1929-1937 (2015)
18. Doussineau, T., Désert, A., Lambert, O., Taveau, J.-C., Lansalot, M., Dugourd, P., Bourgeat-Lami, E., Ravaine, S., Duguet, E., Antoine, R.: Charge Detection Mass Spectrometry for the Characterization of Mass and Surface Area of Composite Nanoparticles. J. Phys. Chem. C. **119**, 10844-10849 (2015)
19. Doussineau, T., Mathevon, C., Altamura, L., Vendrely, C., Dugourd, P., Forge, V., Antoine, R.: Mass Determination of Entire Amyloid Fibrils by Using Mass Spectrometry. Angew. Chem. Int. Ed. **128**, 2386-2390 (2016)
20. Benner, W.H.: A gated electrostatic ion trap to repetitiously measure the charge and m/z of large electrospray ions. Anal. Chem. **69**, 4162-4168 (1997)
21. Dunbar, R.C.: New approaches to ion thermochemistry via dissociation and association. In: In: BabcockLM A, editors (ed.). JAI Press, Greenwich, CT, (1996)

22. Dunbar, R.C.: Infrared Radiative Cooling of Gas-Phase Ions. Mass Spectrom. Rev. **11**, 309-339 (1992)
23. Dunbar, R.C., McMahon, T.B.: Activation of Unimolecular Reactions by Ambient Blackbody Radiation. Science. **279**, 194-197 (1998)
24. Schnier, P.D., Klassen, J.S., Strittmatter, E.F., Williams, E.R.: Activation Energies for Dissociation of Double Strand Oligonucleotide Anions: Evidence for Watson-Crick Base Pairing in Vacuo. J. Am. Chem. Soc. **120**, 9605-9613 (1998)
25. Strittmatter, E., Schnier, P., Klassen, J., Williams, E.: Dissociation energies of deoxyribose nucleotide dimer anions measured using blackbody infrared radiative dissociation. J. Am. Soc. Mass Spectrom. **10**, 1095-1104 (1999)
26. Freitas, M.A., Hendrickson, C.L., Marshall, A.G.: Determination of Relative Ordering of Activation Energies for Gas-Phase Ion Unimolecular Dissociation by Infrared Radiation for Gaseous Multiphoton Energy Transfer. J. Am. Chem. Soc. **122**, 7768-7775 (2000)
27. Doussineau, T., Paletto, P., Dugourd, P., Antoine, R.: Multiphoton Dissociation of Electrosprayed MegaDalton-Sized DNA Ions in a Charge-Detection Mass Spectrometer. J. Am. Soc. Mass Spectrom. **26**, 7-13 (2015)
28. Walsh, N., Lassesson, A., Martinez, F., Marx, G., Schweikhard, L.: Comparison of the low-energy decay mechanisms of C70+ and C70−. Vacuum. **83**, 761-767 (2008)
29. Lifshitz, C.: Energetics and dynamics of ionization and dissociation of fullerene carbon clusters. Mass Spectrom. Rev. **12**, 261-284 (1993)
30. Lifshitz, C.: C2 binding energy in C60. Int. J. Mass Spectrom. **198**, 1-14 (2000)
31. Lifshitz, C.: Some recent aspects of unimolecular gas phase ion chemistry. Chem. Soc. Rev. **30**, 186-192 (2001)
32. Frisch, M., Trucks, G.W., Schlegel, H.B., Scuseria, G.E., Robb, M.A., Cheeseman, J.R., Scalmani, G., Barone, V., Mennucci, B., Petersson, G.A.: Gaussian 09, Revision A. 02, Gaussian. Inc., Wallingford, CT. **200**, (2009)
33. Rockwood, A.L.: Stability conditions for multiply reflecting electrostatic ion traps. J. Am. Soc. Mass Spectrom. **10**, 241-245 (1999)
34. Paech, K., Jockusch, R.A., Williams, E.R.: Slow infrared laser dissociation of molecules in the rapid energy exchange limit. J. Phys. Chem. A. **106**, 9761-9766 (2002)

35. Paech, K., Jockusch, R.A., Williams, E.R.: Slow infrared laser dissociation of biomolecules in the rapid energy exchange limit J. Phys. Chem. A. **107**, 2596-2596 (2003)
36. Doussineau, T., Antoine, R., Santacreu, M., Dugourd, P.: Pushing the Limit of Infrared Multiphoton Dissociation to Megadalton-Size DNA Ions. J. Phys. Chem. Lett. **3**, 2141-2145 (2012)

Chapter 6:

Weighing Amyloid Fibrils

“Symptoms that hide in polymorphs are difficult to fight with”

6.1 Introduction

Age-related neurodegenerative diseases including the Alzheimer and Parkinson are associated to the accumulation of amyloid deposits due to the aggregation of few specific peptides and proteins [1, 2] (details are discussed in **chapter 1**). The proteins involved in these deposits are in the so-called amyloid state, with common structural features whatever the peptides and proteins involved [3–5]. These peptides and proteins undergo slow but steady formation of the oligomers, short protofibrils and mature (protofilaments) fibers in the brain of the neurodegenerative patient [6, 7].

The amyloid formation shows distinctive polymorphisms [8–11]. Metastable intermediates are observed during the formation process whereas mature fibrils are often seen at the endpoint *via* self-propagation with high dependability on the amyloid elongation [5, 12, 13]. The diameter of the elongated fibers varies from a few nanometers and lengths around a micrometer. The core structure of these fibers is stabilized by hydrogen-bonded β-strands perpendicular to the fiber axis and forming β-sheets, either parallel or anti-parallel, along the fiber axis [14]. The development of amyloid fibers follows a slow nucleation/growth mechanism, where the formation of oligomers acts as nuclei for the growth of the protofibrils and thus of the mature (protofilaments) fibers [15–17]. Electron microscopy shows that the fibrils are composed of several ‘protofilaments’, which twist around one another to form the mature fibril [18]. The heterogeneity of amyloid fibrils show different types of polymorphisms depending on the i) number of the protofilaments (2) arrangement of protofilaments and (3) conformation of polypeptide [19]. Determining the molecular structure of protofibrils and protofilaments at atomic resolution is challenging, however, their structures are crucial for elucidating the aggregation pathway involved in fibril formation and for developing therapeutic and diagnostic agents [20]. Some studies suggested that the most toxic species are not the amyloid deposits but the oligomers and/or protofibrils [21–24]. These toxic species could be continuously produced by the interactions between newly generated monomeric peptides ($A\beta_{1\text{-}42}$ peptide) and amyloid fibers accumulated within the amyloid deposits. In addition, the high ratio of preformed fibers leads to polymorphism which has a strong connection to amyloid deposits lead to the neuronal death and severe dementia condition among patient.

We recently showed that CDMS is capable of measuring masses of amyloid fibrils of lactalbumin [25]. Previous MS-based studies of fibrillation have been limited to the early steps in aggregation [26, 27]. The CDMS measurements provided rapid access to information like mass and charge distribution, and when coupled with measurements of the average length of the fibrils from TEM/AFM, the mass-per-length (MPL) is determined. The mass and length distributions are found to be log-normal which is characteristic of nonspecific aggregation. We report here the characterization by charge detection mass spectrometry (CDMS) of amyloid fibers made of the proteins involved in neurodegenerative diseases. Mass and charge distribution of amyloid fibers made of Aβ_{1-42} peptides, tau protein and α-synuclein are evaluated. Beside the mass distribution for the different amyloid fibers, this technique allows to distinguish and characterize different populations within a sample, as illustrated in the case of Aβ_{1-42} peptide and Tau protein fibrils. These experiments allow also to highlight how the mechanism of fiber formation affects the fiber population. In the case of α-synuclein, we show how the polymorphism affects the mass and charge distributions, in relation with important changes on the fiber structure.

6.2 Materials and Methods

6.2.1 Fibrils Sample Preparation

Aβ_{1-42} Fibrils: Lyophilized Aβ_{1-42} peptide (Genecust, Luxembourg) was dissolved in distilled water at pH 12.0, adjusted with 5 M NaOH. The solution was filtrated through a spin 0.2 µm membrane filter (Millipore, n°146560) to remove any aggregated species. The solution was stored at −20 °C. Aβ_{1-42} fibrils were prepared by incubating monomer Aβ_{1-42} peptide solution (final concentration at 100 µM) in Tyrode's buffer (150 mM NaCl, 3 mM KCl, 10 mM HEPES pH 7.4, 10 mM glucose filtrated with a spin 0.2µm) at 310°K in a 500 µL reaction volume on a rotating shaker (300 rpm) at pH 6.5 for 72 hours.

α-synuclein Fibrils: Wt human α-Synuclein was expressed in *E coli* and purified according to previously published protocol with few modifications [28]. First, *E. coli* cells were lyzed by three passages on a French press instead of by successive freeze-thaw cycles and sonication. Secondly, the ammonium sulphate precipitation step was omitted. Finally after the ion-exchange chromatography, the protein was further purified by gel filtration using a Sephacryl-S100HR column and milliQ water was used as running buffer. The protein was lyophilized and stored at -20°C. The integrity of the protein was checked by SDS-PAGE and MS. The purity of the protein was estimated to be higher than 95% based on the densitometry analysis of the SDS-PAGE.

Lyophilized protein was dissolved into 3mL of 10 mM NaP buffer pH 7.5 containing 100 mM NaCl and 0.1% sodium azide. The solution was filtered through a 0.22 µm cut-off syringe filter and the concentration of the protein was determined by absorbance measurement at 280 nm from the extinction coefficient (5960 cm^{-1} M^{-1}). The protein solution was incubated in a 14 mL polypropylene round-bottom corning falcon tube on a New Brunswick Innova 44 incubator at 37°C under orbital agitation at 226 rpm for 12 days. At given time points (roughly every 24 or 48 h), an aliquot was taken to monitor the formation of amyloid fibrils by thioflavin-T fluorescence using previously published protocol [29].

Tau Fibrils: Lyophilized hTau40 was dissolved at 110µM, in MOPS buffer (3-(N-morpholino) propanesulfonic acid), 20 mM pH 7.4. The fibrils were prepared in MOPS by adding heparin to hTau40 monomers (molar ratio 1:2.2) at 310°K in a 600 μL reaction volume on a rotating shaker (300rpm), pH 7.4 for 72 hours.

Heparin (average molecular mass of 7 kDa), sodium chloride (NaCl, >99.5%), sodium hydroxide (NaOH, 99.99%), 3-(N-morpholino)propanesulfonic acid (MOPS, >99.5%) and 4-(2-hydroxyethyl)-1-piperazineethanesulfonic acid (HEPES, 99.5%), were purchased from Sigma-Aldrich (France). Potassium chloride (KCl, 99.5%) was purchased from SDS Carlo Erba (France).

6.2.2 Negative Stain Electron Microscopy

Fibril suspensions were diluted in buffer to around 1 mg/mL concentration and adsorbed into glow-discharged carbon-coated copper grid for 30 seconds. Grids were stained with 2 % uranyl acetate, dried with filter paper and observed with Phillips CM12 transmission electron microscope.

6.2.3 Atomic Force Microscopy (AFM)

Fibrils were diluted to a final concentration of 0.28 µM in HCl 0.1 mM and let adsorb over night at 4°C onto plasma O_2 cleaned glass slides. After removal of the solution, the samples were left to dry. Images were recorded at a scanning speed of 0.5 Hz in the tapping mode in air with a Dimension 3100 (Brucker) using Si_3N_4 cantilevers of a spring constant of 0.4 $N.m^{-1}$, and were analysed using Nanoscope (Brucker). PeakForce Tapping AFM analysis of the thick film was performed on Dimension ICON (Bruker). ScanAsyst Air tip (Bruker) with a spring constant of 0.35 $N.m^{-1}$, as determined by the thermal tune method, was used. The used Peak Force Set point value was 150 pN.

6.2.4 Charge-Detection Mass Spectrometry (described in **chapter 1**)

6.2.5 Data Processing and Analysis

A home-developed, VISUAL C++, Windows-based software was used to record the signals. The program calculates the time between the maxima of the positive and negative pulses, the amplitudes of the two pulses and the ratio between their absolute values. A high-frequency filter was added to the data processing of traces in order to remove peak artefacts. Residual droplets are excluded by using post-processing thresholds for TOF (> 80 μs). For Aβ1-42 peptides and Tau fibrils, two populations were separated based on time of flight values. In this work, only ions (with charges higher than ~300 e) that both enter and exit the tube are counted. Events for which the absolute value of the amplitude ratio between the first and the second pulses is greater than 1.5 or less than 0.75 are automatically excluded. These events may result either from an ion that enters but does not exit the detector (due to fragmentation or loss in the charge detector) or from non-single events including two or more different ions entering the charge detector during a time-of flight measurement. This procedure precludes, in particular, the detection of more than one ion with the charge-detection device. Finally, the corresponding ion counting rate ranges around 100 ions per second.

For each ion, the mass is deduced from its *m/z* and *z* values. Each displayed mass distribution compiles about 8,000-10,000 individual ion measurements. The mass distributions are histogrammed using a given bin-size (5-10 MDa). Each bar represents the number of counted ions having mass corresponding to the mass range of the bar. The mass and length distributions were found to be log-normal which is characteristic of nonspecific aggregation [25]. The shape of the molecular weight distribution (MWD) of fibrils was thus fitted by a log-normal distribution ($P(\ln M) = \frac{1}{\sqrt{2\pi}\sigma} \exp\left[-\frac{\ln^2(M/m_0)}{2\sigma^2} \right]$), where m_0 is the median and σ is the width of the distribution. m_{max} is the mass corresponding to the maximum of the log-normal distribution.

6.2.6 ESI Conditions

Aqueous mother dispersions of fibrils were prepared in two ways i) one without adding any organic solvent ii) another with diluting in 75/25 water: methanol solvent mixture before injection into the ESI source. Final concentrations range between 25-50 μM in fibrils. Dispersions were injected at flow rates of typically 0.2-0.6 mL/h, and entered the electrospray chamber through a 0.1

mm internal diameter stainless steel capillary tube located inside the needle tip. Carrier nitrogen gas was injected between the end cap and the transfer glass capillary and was flown through a heater typically set at 200 °C. The ESI source generates highly charged macro-ions which are guided by an ionic train to the mass spectrometer. Ions are guided up to a vacuum stage chamber (~10^{-6} mbar) and directed through the CDD (charge-detection device).

In general, one may be concerned that the conditions of ESI are too harsh with diluting in 75/25 water: methanol solvent mixture before injection into the ESI source. Would not native spray (pure water) be more appropriate? CDMS experiments on A$\beta_{1\text{-}42}$ fibrils were performed in two conditions with and without organic solvent, methanol. Time of flight, mass and charge distribution (**Figure 6.1A**) of two samples are almost similar which indicates that small amounts (25%) of organic solvent do not disrupt the fibrils' overall population. In our case, the studied fibrils are very stable and the addition of methanol or acetic acid should not affect their conformation during the time of the MS measurements. Note that the ion signal in pure water is very unstable (due to unstable spray) and the addition of methanol allows for a better stability of the spray.

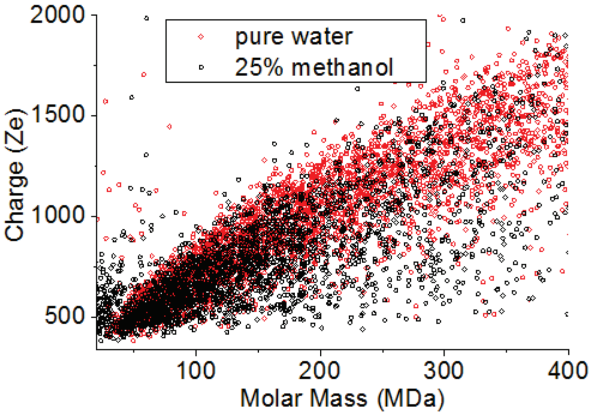

Figure 6.1 Mass vs charge distribution of A$\beta_{1\text{-}42}$ fibril in pure water and 25% methanol

6.3 Result and Discussion

6.3.1 A$\beta_{1\text{-}42}$ peptide Fibrils

Amyloid fibers which formed from A$\beta_{1\text{-}42}$ peptides were obtained upon incubation at pH 6.5 and 37°C. The transmission electron microscopy image (**Figure 6.2A**) showed two distinctive types of fibril population: nearly spherically-shaped short protofibrils and elongated fibers. Within one sample, different morphologies for A$\beta_{1\text{-}42}$ peptides fibril are evident. Biophysical studies of Aβ amyloids disclosed the existence of various polymorphs within a single sample [30]. The length of the protofibrils is centered on 250 nm (**Figure 6.2B**). The shorter population is assigned to the protofibrils and tentatively related to the low-mass population. Protofibrils of Aβ peptides can grow to 500 nm in length contrast to spherical oligomers [31]. In comparison with mature fibrils, protofibrils are curvi-linear and lack a periodic (twisting) sub-structure. Herein, protofibrils of A$\beta_{1\text{-}42}$ peptides exhibited no substantial growth similar to previous study on A$\beta_{1\text{-}40}$ peptides [32]. However, protofibrils can show growth with monomer addition, however, such growth rate is significantly slower than that of mature fibers [33].

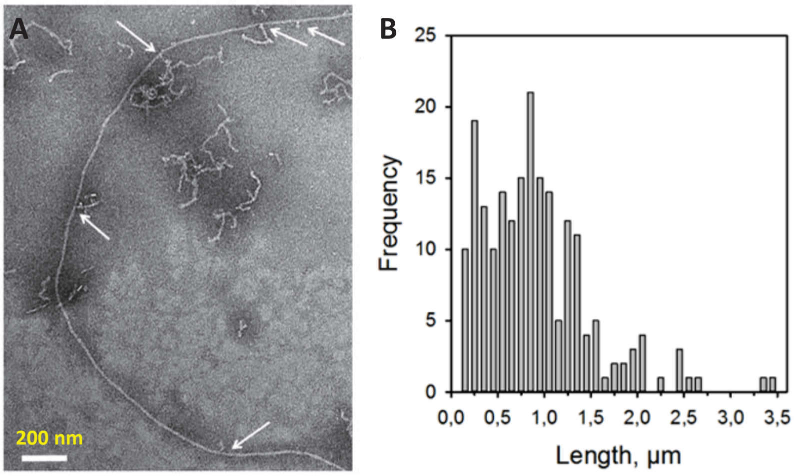

Figure 6. 2 A) TEM image of Aβ1-42 amyloid fibers, scale bar: 200 nm B) Length distribution of A$\beta_{1\text{-}42}$ amyloid fibers extracted from TEM clichés. The two types of fibrils are distinguished from the length distribution.

The elongated mature fibril has an average length of 900 nm. Previous transmission electron microscopy (TEM) and atomic force microscopy (AFM) analysis have shown that mature amyloid fibrils can have a length of >1000 nm [18]. For structural determination of an amyloid fibril, mass-per-length (MPL) measurement by scanning transmission electron microscopy (STEM) [34–36] provides valuable information. It is well-know that A$\beta_{(1\text{–}42)}$ amyloid fibrils show an in-register intermolecular parallel cross–β-sheet entity with a repetition rate at every 0.48 nm (i.e., the distance between two β-strands across the β-sheets). Considering this value of 0.48 nm, the number of molecules per layer can be estimated. Previous studies disclose that amyloid fibrils can have 2-5 peptides per repeat in one protofilament [37–39]. However, for short protofibrils the estimated of the mass-per-length (MPL) value is around 80 kDa/nm. Using theoretical molar mass of an Aβ$_{1\text{-}42}$ peptide (4.514 kDa), this MPL value translates into 8.5 Aβ1$_{\text{-}42}$ peptide for each 0.48 nm repeat of the fibril. The second population of larger length and mass was assigned to elongated fibers; the MPL value is estimated around 60 kDa/nm which indicates 6.38 peptide per cross-β repeat. Both MPL values associated to short and elongated fibers are significantly larger than the average values based on electron cryo-microscopy image processing, i.e. ~ 20 kDa/nm. High MPL values are also detected, albeit not often, in some cases. MPL value obtained for a previous Aβ$_{1\text{-}42}$ fibril is 23.5±0.1 kDa/nm [40] which is incubated for 48 hours; however, higher mass Aβ$_{1\text{-}40}$ fibrils also show MPL values of 46 kDa/nm [41] and 60-100 kDa/nm [33] for longer incubation time of four and seven days, respectively. The exact reason of this apparent discrepancy is unclear. However, the sampling in our case was larger by several orders of magnitude than the one used for cryo-microscopy experiments; several thousand of unselected fibers in our case compare to a few selected on their aspects on a cryo-microscopy cliché. Other physico-chemical factors such as pH, temperature, agitation, salt and other co-solutes [42–46] may have impact on the morphologies and thus on the mass-per-length (MPL) values of the short and mature fibrils.

Mature fibrils can have one or more protofilaments, however, here we noticed only one long protofilament for Aβ$_{1\text{-}42}$ fibril. Usually Aβ$_{1\text{-}42}$ fibril contains one protofilament [40] whereas Aβ$_{1\text{-}40}$ comprises two such filaments [47]. This single protofilament is fully solvent-exposed and structurally disordered as can be seen from **Figure 6.2A**. Although Aβ fibrils are often, but not always, twisted [48, 49]; couple of twisting is evident from the TEM image. One key feature of this sampling is that several 'branching' or 'breaking' are noticed (arrow sign in **Figure 6.2A**) in the elongated protofilament indicating that some secondary nucleation may be occurring within the nucleation process. Similar branching events, not often, were also detected for glucagon (peptide hormone) [50], lithostathine (Reg-1, a protein of 144 amino acids) [51], prion protein [52] and Aβ$_{1\text{-}40}$ peptides [53] fibrils. In some cases, branching and/or breaking allow amplification and exponential grow of the fibril structures [54]. Twisting may be a perquisite for such branching or breaking. This phenomenon also suggests that the final state of our sample may be the result of a competition between primary and secondary nucleation mechanisms. Moreover, fibril unwinding and branching may be a requirement for post-nucleation grown for these fibrils.

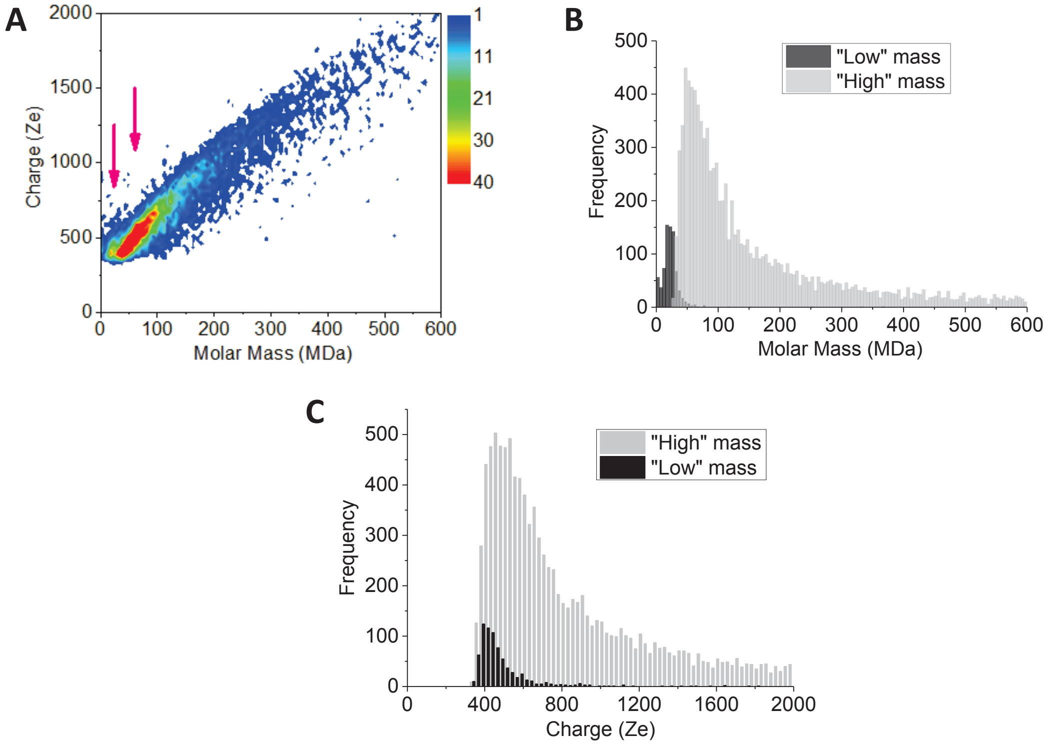

Figure 6.3 A) 2D-graph of CD-MS measurements performed on A$\beta_{1\text{-}42}$ amyloid fiber sample. B) Mass distribution drawn from A. The two populations have been distinguished based on their different time of flight. The mass distribution is histogrammed using a given bin-size (5 MDa). Each bar represents the number of measured ions whose masses correspond to the mass range of the bin. C) Charge distribution drawn from A. The two populations have been distinguished thanks to their different time of flight. The charge distribution is histogrammed using a given bin-size (25 e). Each bar represents the number of measured ions whose charges correspond to the charge range of the bin.

The mass measurement results on single Aβ fiber macro-ions in presence of 25% of methanol are gathered into a 2D graph (charge vs mass) (**Figure 6.3 A**). The mass distribution extracted from the 2D-graph was quite broad (**Figure 6.3B**), with a shoulder at low mass. This corresponded to a low mass population that could be seen also on the 2D-graph, suggesting that they have a different charge density. The mean charge of the protofibrils (low mass) is 410e whereas the charge distribution of the elongated mature (high mass) fibril is 500e (**Figure 6.3C**). The number of ions for low-mass and high-mass populations (used for histograms) are respectively 759 and 9642 giving a “population” ratio of ~8 % for short fibrils compared to long fibrils. Despite small population ratio, the charge difference between the protofibrils and elongated fibrils is not large. After separated them based on the time of flight, two populations could be clearly observed (**Figure 6.3B**): a first one with a molar mass centered on 20 MDa and a second one with a peak maximum around 55 MDa. According to the molar mass of Aβ_{1-42} peptide (0.004514 MDa), this provides around 4431 peptides per fiber for the first population and 12184 peptides per fiber for the second one. Considering the length of short (250 nm) and elongated (900 nm) fibrils and β-cross repetition at 0.48 nm, the CDMS experiment provide 8.50 and 6.49 peptide per 0.48 nm for short and elongated fibrils which support our MPL results.

6.3.2 Alpha (α)-Synuclein

Alpha-synuclein, a small (14.5 kDa) intrinsically disordered protein expressed in neurons, is believed to be responsible for Lewy body disease such as Parkinson disease (PD) [55–57]. Similar to Aβ_{1-42} peptide, this protein also exhibits a cross-β structure with a repetition spacing of 0.48 nm [58]. Some recent findings showed that amyloids associated with neurodegenerative diseases can spread in a prion-like approach analogous to prion protein (PrP) [59, 60] and particularly α- synuclein assemblies can act as seed and spread from one cell to another which is confirmed in cell cultures as well as in animal models [61, 62]. Polymorphism of α-synuclein is often observed, however, clarification of their difference is still needed to be addressed [63–65]. In our study, two types of α-synuclein fibers have been obtained. We notice two distinctive types of fibers, one is regular isolated fibers, so-called type I, (**Figure 6.4A**), while other one is irregular ribbons, so-called type II (**Figure 6.4B**). These ribbons are made of the heterogeneous association of fibrils of variable lengths. Moreover, fibers involved in ribbon are obviously shorter than those observed in the sample with isolated fibers. According to their respective length distributions (**Figure 6.5**), isolated fibers of the first sample type has a mean length of 900 nm, while those involved within ribbons had a mean length of 500 nm. These distinctive morphologies related to isolated fibers and high-mass ribbons are also obtained in previous studies [28, 66–68]. Both types of fibers are further characterized by atomic force microscopy

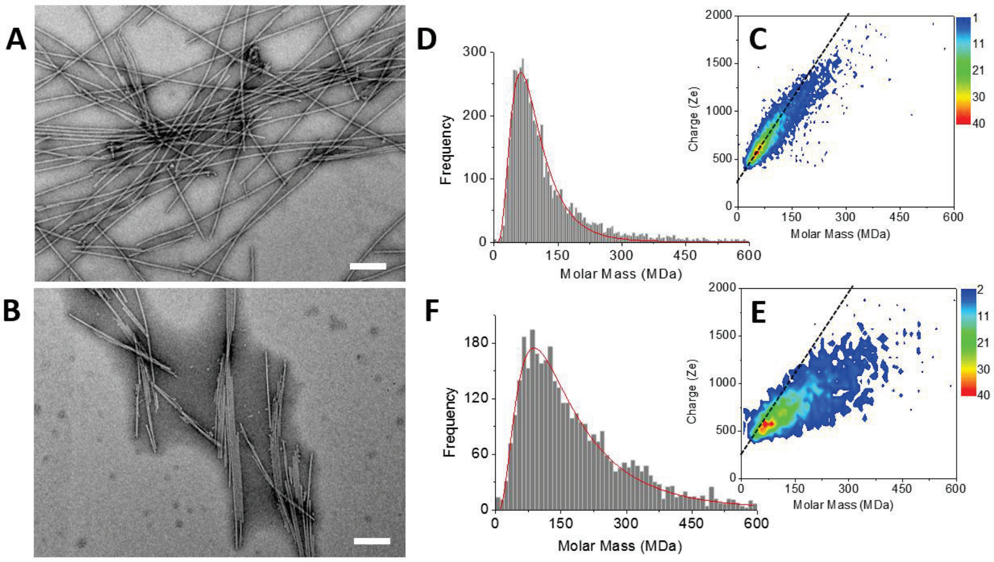

Figure 6.4 ***α-synuclein amyloid fibers.*** **(A&B)** TEM image of type I (**A**) and type II **(B)** α-synuclein amyloid fibers, scale bar: 200 nm. **(C&E)** 2D-graph of CD-MS measurements performed on type I (**C)** and type II **(E)** α-synuclein amyloid fiber sample. **(D&F)** Mass distribution drawn from **C&E)** for type I (**D**) and type II **(F)** α-synuclein amyloid fibers. The mass distribution is histogrammed using a given bin-size (10 MDa). Each bar represents the number of measured ions whose masses correspond to the mass range of the bin.

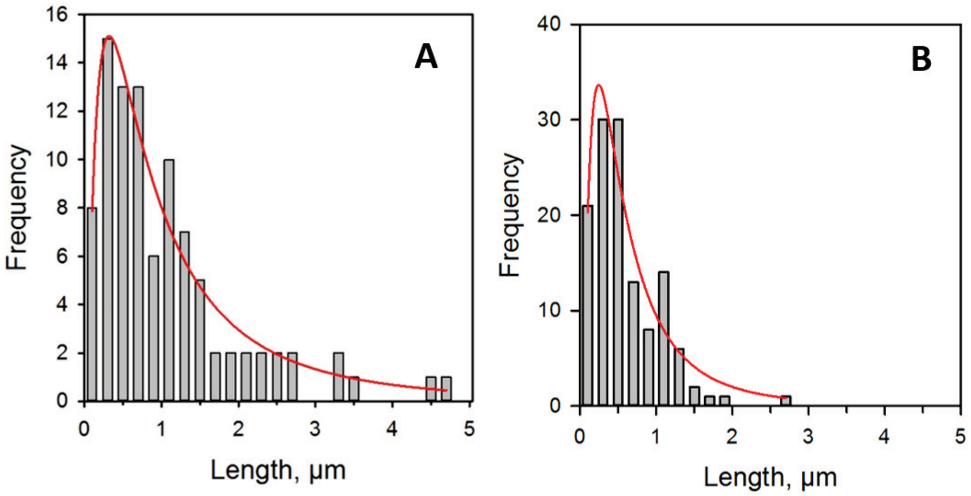

Figure 6.5 Length distribution of type I (**A**) and type II **(B)** α-synuclein amyloid fibers extracted from TEM clichés. The red curve represents the LogNormal function fitting the experimental distribution from which mean length values were extracted.

(AFM) (**Figure 6.6**). The height profiles of isolated fibers showed a single maximum around 8 nm. In the case of the ribbons, the profiles are much broader, with several peaks corresponding to aligned fibers. At the exception of regions with overlapping fibers, it is obvious that the average height of the ribbons is significantly lower than that of the single fibers: 5.5 ± 0.9 nm *vs* 8.3 ± 0.9 nm, for ribbons and single fibers respectively. A previous AFM study [69] on the wide-type and mutants (A30P and E46K) reported the height of 10.0±1.1, 8.1±1.2 and 9.0±0.8 nm, respectively which are agreed well with our result for the isolated single fibers. The relatively short height of the ribbon fibers can be explained by fact that these fibers might have longer periodicity

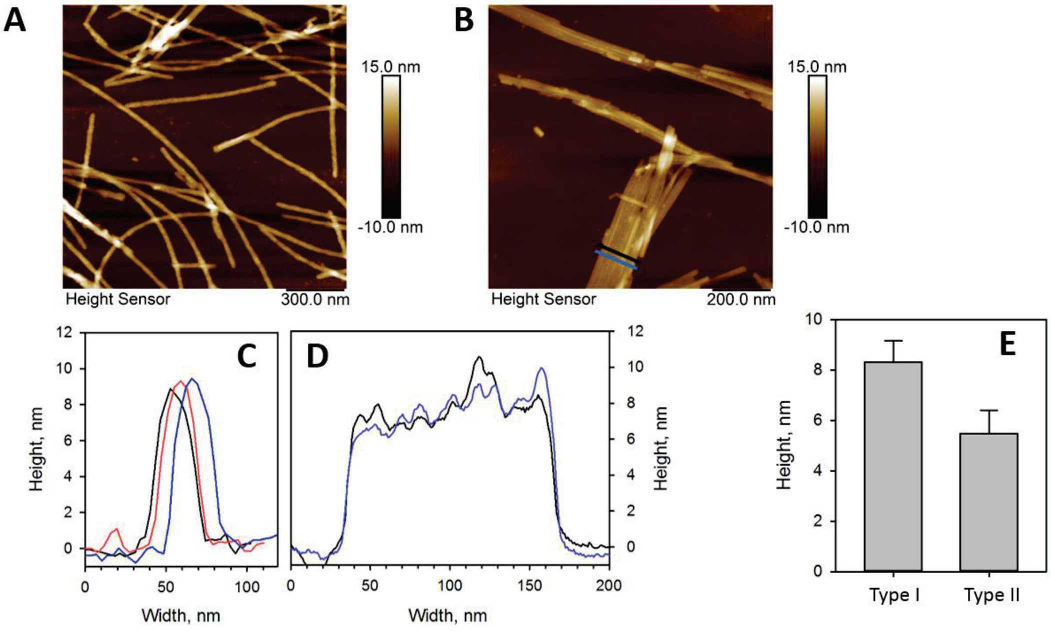

Figure 6.6 (A&B) AFM images of type I (**A)** and type II **(B)** α-synuclein amyloid fibers. **C)** Typical height profiles extracted from image shown on **A)** for type I α-synuclein amyloid fibers. **D)** Height profiles along the blue and black lines drawn on **B)** for type II α-synuclein amyloid fibers. **E)** Mean heights extracted from AFM images recorded for each type of α-synuclein amyloid fibers.

compared to the shorter periodicity of the isolated single fibers. The compactness of the fibers may depend on the change in the periodicity of the fibril twist. A loose twist may shorten the height of the ribbon fibers. In this case, the loosely twisted ribbon-like fibers (type II) and the tightly twisted rod like fibers (type I) are different forms of the same structure. This alternative explanation is also supported by Chamberlain *et al* [70] for SH_3 domain fibrils where they also witnessed a similar event in the short-height ribbon like fibers.

Although the morphology of α-synuclein aggregates is highly sensitive to solution condition including pH, temperature, incubation time, salt concentration, and buffer conditions[71]; the origin of the differences between the two samples (type I and type II) are not understood. The only notable difference is the initial concentration of monomeric protein: 51 μM in the case of the isolated fibers and 83 μM for the ribbons. As a consequence the fiber formation was faster at higher concentration. This could have an effect on the formation mechanism, by enabling some secondary nucleation for instance. Another possibility is that significant structure changes have been reported during the maturation of α-synuclein fibers, i.e. after their formation. The total incubation time being the same for both samples, the maturation phase must have been longer in the case of the higher protein concentration sample, because of a faster fibrillation, allowing more reorganization.

The CDMS 2D graph recorded with the isolated fibers showed a well-defined charge *vs* mass dependency (**Figure 6.4C**). According to the mass distribution (**Figure 6.4D**), the mean mass is 85.4 MDa, with a mean charge at 700 e. Hence, these α-synuclein amyloid fibers is made of 5905 proteins on average ($M_{\alpha\text{-syn.}}$ = 0.01446 MDa). According to the length distribution estimated from transmission electron microscopy (TEM) (**Figure 6.5**), the average fiber length was 900 nm, giving a MPL value around 95 kDa/nm. Using the theoretical mass of a α-synuclein (14.460 kDa), this MPL value translates into 3.15 protein for each β-cross repetition at 0.48 nm. However, previous study reported this value of 2 protein per 0.47 nm [72]. Considering the length of the isolated fibers (900 nm), CDMS experiment provide 3.14 α-synuclein per 0.48 nm for the isolated fibers which is exactly same as the MPL result obtained from EM.

In the case of the ribbons, the charge *vs* mass dependency was not so well defined anymore (**Figure 6.4E**), resulting in a much broader mass distribution, with a mean mass at 147.8 MDa (**Figure 6.4F**). The broadness reflected the heterogeneity of the sample, with ribbons of varying length and width. It is obvious on the 2D-graph that the charge of the fibers is significantly lower than in the case of the type I sample; a dashed line corresponding to the charge *vs* mass dependency of the type I fibers is reported on both 2D-graphs for comparison. The pH being identical for both types of sample, this suggested that charges were at least partially hidden due to the organization of the fibers into ribbons. To explain the charge reduction phenomena for the ribbon fibers we propose a model (**Figure 6.7A**). The slope ratio of the type I and II fibers in **Figures 6.4C** vs **6.4E** is approximately ~1.7. If we consider the charge of an individual fiber is 4 (assuming 4 faces of a square). So for n fibrils one will expect $4n$ charges. However, in case of stacked or assembled fibrils if the charge of one fibril is 4 (4 faces) then for n fibrils one would expect $4 + 2 \times (n - 1)$ charges due to the charge off of the two adjacent faces during the assembling or stacking. If we then plot the charge ratio of individual fibrils/stacked fibrils in terms of the number of fibrils (**Figure 6.7B**), the number of fibril per assembly is ~6 at 1.7 ratio which is also be confirmed from the AFM height processing data of the ribbon fibers, type II (**Figure 6.6D**). Another important insight can be drawn from the lateral bonding of fibrils into ribbons is that there may be some kind of electrostatic interactions involved which promote such assemblies. This also suggests that the newly formed fibers are propitious to electrostatic interactions on their sides, and this could be an important feature for their toxicity through the disruption of neuron extracellular cell membranes.

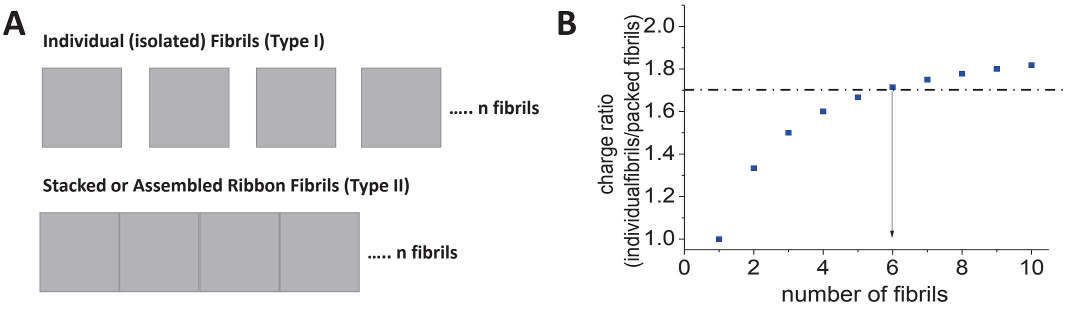

Figure 6.7 A) Proposed model for isolated and ribbon fibrils B) Charge ratio vs number of fibrils.

6.3.3 Tau fibrils

Although extracellular amyloid fibrils are mainly formed from Aβ protein, however, intracellular neurofibrillary tangles are generated primarily from a microtubule-binding and intrinsically disordered Tau protein [73, 74]. Tau protein has six isoforms which differ with three to four 'repeat domain' (RD) in the C-terminal region. The longest isoform in our central nervous system, hTau40 (441 amino acids), contains a repeat domain of four (R1 to R4) [75]. In solution, Tau remains as random coil, however, in amyloid state it generally forms distinctive paired helical filament (PHFs) and straight filaments [76, 77]. In Alzheimer disease (AD), Tau is assumed to be hyper-phosphorylated and aggregated to form neurofibrillary tangles (NFTs) [78]. However, *in vitro* Tau amyloid fibril formation is very slow in absence of phosphorylation. The polyanion glycosaminoglycan heparin (to mimic the hyperphosphorylation) normally used for Tau aggregation *in vitro* to create a model system close to pathological one isolated from AD-disease brain [79–81].

The formation of amyloid fibers by Tau is triggered by the addition of heparin at a molar ratio of Tau/heparin 2.2. Various types of fibers are observed by electron microscopy (**Figure 6.8A**) and the length distribution is quite broad 0.1 to 3.3 μm (**Figure 6.8B**). Different curled, twisted, thin and thick human Tau fibrils of 2-4.3 μm are also observed earlier [82]. Various lengths of the Tau fibrils may be due to their diverse morphology varied in bending, periodicity, twisting, thickness, and substructure as evident from the TEM image. The characteristic paired helical filaments (PHF) [83, 84] are also appeared in some fibrils. Moreover, some small spherical oligomers could

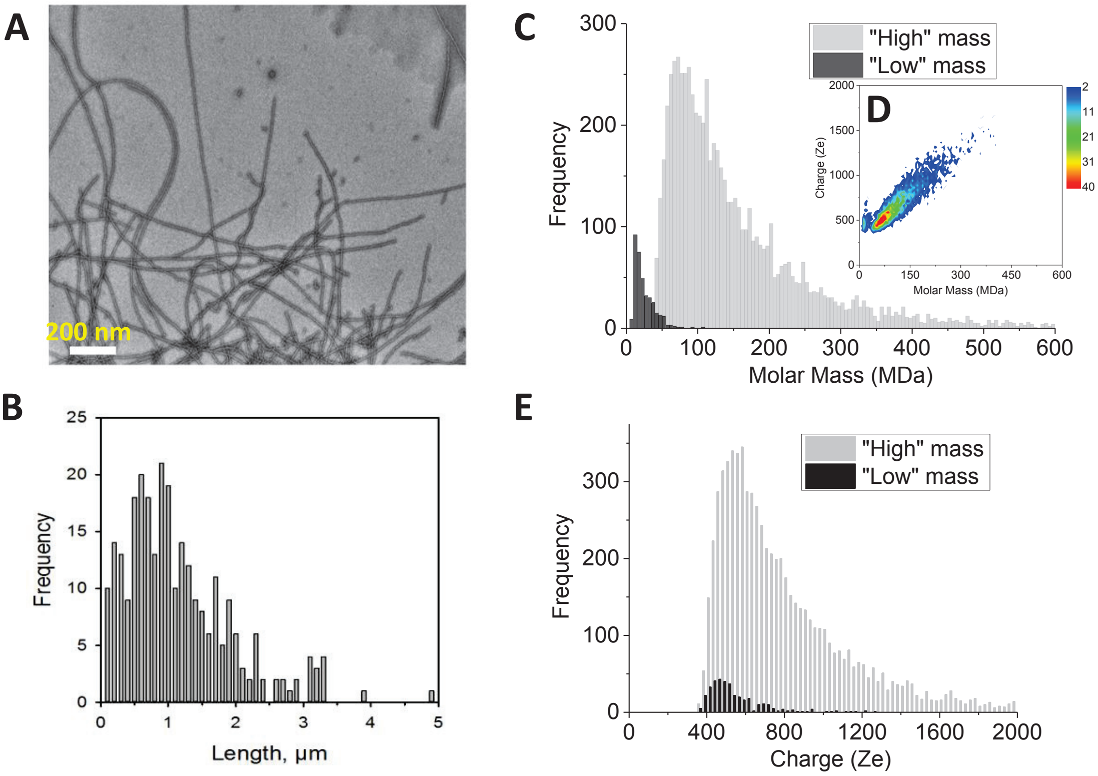

Figure 6.8 A) TEM image of Tau amyloid fibers, scale bar: 200 nm. **B)** Length distribution of Tau amyloid fibers extracted from TEM clichés. **C)** Mass distribution of two population based on different time of flight drawn from **B**). **D)** 2D-graph of CD-MS measurements performed on Tau amyloid fiber sample. The mass distribution is histogrammed using a given bin-size (5 MDa). Each bar represents the number of measured ions whose masses correspond to the mass range of the bin. **E)** Charge distribution drawn from **B**). The two populations have been distinguished thanks to their different time of flight. The charge distribution is histogrammed using a given bin-size (25 e). Each bar represents the number of measured ions whose charges correspond to the charge range of the bin.

be distinguished (**Figure 6.8A**), but they are not considered for the length distribution estimation. Mass distribution of two populations based on different time of flight is presented in Figure **8C**. Within the CDMS 2D-graph (**Figure 6.8D**), a small population of low mass (around 15 MDa) could be observed, that could be due to either the high order oligomers or the short-length protofibrils population. The formation of protofibrils of Tau has not been observed so far, only two exceptions reported by Ramachandran *et al* [81] and Xu *et al* [85]. The previous heparin mediated rod-like protofibrils are assumed to be off-pathway products [81].

The main population has a mean mass of 113.5 MDa (**Figure 6.8C** and **6.8D**). As the presence of heparin is essential for the formation of fiber by tau, mostly for screening charges, the estimation of the number of proteins per fibrils was not straightforward. Only an estimation can be given, if we hypothesize that the ratio tau/heparin is the same within the fibers and in the bulk, i.e. 2.2. Considering the theoretical mass of hTau40 (45.8 kDa) and heparin (15.4 kDa at 2.2 ratio), we can estimate that around 1837 and 245 proteins per fiber are available for the high mass mature fibrils and low mass protofibrils, respectively.

One can notice that, as it is already the case with the Aβ_{1-42} fibers (**Figure 6.3C**), the charge density of Tau is only slighted reduced in the case of the low mass fibrils (466 e) compared to the high mass fibrils (540 e) (**Figure 6.8E**). Previous study proposed that core PHFs consists of stacked β-strands formed by the repeat domains of Tau [86]. This region is stabilized by hydrophobic interaction and highly protease-resistant; however, the disordered region of Tau fibrils is largely charged or polar [87]. This disordered region of the Tau fibrils is also known as 'fuzzy coat'[88]. Nearly similar charge of the 15 MDa and 113.5 MDa populations indicate that this short protofibrils may adopt large 'fuzzy coat' region which is highly charged with no or very small hydrophobic core region. Whereas high mass mature fibrils may contain a hydrophobic core (which reduces the charge contain) with fuzzy disorder region. Other possibilities cannot be ruled out that the two populations may be driven by different shapes: cylinder *vs* spherical and/or different ratio of tau/heparin that can modulate the charge screening. In addition, this relative charge density could be a reason for a higher toxicity of these oligomers/short protofibrils. Indeed, interactions with lipid membranes are thought to be central for the toxicity and electrostatic interactions are important for the interactions of polypeptides with membranes and their further destabilization.

6.4 Summary

In summary, charge-detection-mass-spectrometry provides a wealth of information on amyloid fiber samples along with electron microscopy results. Beside the mass and charge of individual fibers, this technique enables to characterize the homogeneity and heterogeneity of the populations and to detect the presence of different types of fibers of $A\beta_{1-42}$ peptides, α-synuclein and tau proteins. CDMS detects the mass and charge distribution of two distinctive $A\beta_{1-42}$ fibril populations with mean mass of 20 and 55 MDa, respectively which are also evident from TEM images. Interestingly, CDMS experiment is also able to identify 8.50 and 6.49 peptides per β-cross repetition at 0.48 nm for short and elongated fibrils which support our MPL results. Despite their mass differences, these short and elongated species retain nearly same charge. For α-synuclein, we notice two distinctive types of fibers: regular isolated and irregular ribbons fibers. The mass of these fibers are 85.4 and 147.8 MDa since the number and arrangement of the protofilaments are very different, the key parameters of polymorphisms in amyloid fibrils. The arrangement of protofilaments also has great implication on charge distribution and such arrangement through assembling or stacking may be responsible for partial charge reduction in the ribbon fibrils of α-synuclein. Unlike $A\beta_{1-42}$ peptides and α-synuclein fibrils, polymorphism of Tau fibril is quite different. Beside paired helical (PHFs) and straight filaments, Tau fibrils also show diverse morphology with bending, periodicity, twisting, thickness, and substructure. High order oligomer or short protofibrils are detected along with high mass mature fibrils in CDMS. Similar to $A\beta_{1-42}$ peptides fibrils, the charge density of the short protofibrils is relatively higher than the mature fibrils.

This study further reveals the prime importance to use alternative approaches to measure amyloid fiber samples, well-known to be highly heterogeneous and, as a consequence, difficult to accurately characterize. In association with time-resolved experiment this will allow to investigate the mechanisms of formation and maturation of amyloid fibers, important to get insight into the development of the neurodegenerative diseases. At last, this technique should be particularly powerful to characterize amyloid deposits extracted from patients. However, the structure and heterogeneity in the fibril formation process remain difficult to assess by any traditional MS-based methods. A further step will require coupling between charge-detection mass spectrometry and separation techniques. In asymmetrical flow field-flow fractionation (AF4), there is no stationary phase able to induce mechanical or shear stress on the protein molecules, and the mobile phase composition can be chosen to preserve the native state. In particular, in vitro Aβ_{1-42} peptide aggregation was recently monitored by AF4 [89]. A possibility would be to couple asymmetrical flow field-flow fractionation (AF4) with charge detection mass spectrometry to profile the time-dependent aggregation pattern, in order to better decipher population heterogeneity. Work along these lines is currently underway in our laboratory.

Bibliography

1. Jakob-Roetne, R., Jacobsen, H.: Alzheimer's Disease: From Pathology to Therapeutic Approaches. Angew. Chemie Int. Ed. 48, 3030–3059 (2009). doi:10.1002/anie.200802808
2. Makin, O.S., Serpell, L.C.: Structures for amyloid fibrils. FEBS J. 272, 5950–5961 (2005). doi:10.1111/j.1742-4658.2005.05025.x
3. Pedersen, J.S., Andersen, C.B., Otzen, D.E.: Amyloid structure – one but not the same: the many levels of fibrillar polymorphism. FEBS J. 277, 4591–4601 (2010). doi:10.1111/j.1742-4658.2010.07888.x
4. Chiti, F., Dobson, C.M.: Protein Misfolding, Functional Amyloid, and Human Disease. Annu. Rev. Biochem. 75, 333–366 (2006)
5. Chiti, F., Dobson, C.M.: Amyloid formation by globular proteins under native conditions. Nat. Chem. Biol. 5, 15–22 (2009)
6. Fändrich, M., Schmidt, M., Grigorieff, N.: Recent progress in understanding Alzheimer's Beta-amyloid structures. Trends Biochem. Sci. 36, 338–345 (2017). doi:10.1016/j.tibs.2011.02.002
7. Ahmed, M., Davis, J., Aucoin, D., Sato, T., Ahuja, S., Aimoto, S., Elliott, J.I., Van Nostrand, W.E., Smith, S.O.: Structural conversion of neurotoxic amyloid-[beta]1-42 oligomers to fibrils. Nat Struct Mol Biol. 17, 561–567 (2010)
8. Eichner, T., Radford, S.E.: A Diversity of Assembly Mechanisms of a Generic Amyloid Fold. Mol. Cell. 43, 8–18 (2011). doi:http://doi.org/10.1016/j.molcel.2011.05.012
9. Fändrich, M., Meinhardt, J., Grigorieff, N.: Structural polymorphism of Alzheimer Aβ and other amyloid fibrils. Prion. 3, 89–93 (2009). doi:10.4161/pri.3.2.8859
10. Meinhardt, J., Sachse, C., Hortschansky, P., Grigorieff, N., Fändrich, M.: Aβ(1-40) Fibril Polymorphism Implies Diverse Interaction Patterns in Amyloid Fibrils. J. Mol. Biol. 386, 869–877 (2009). doi:10.1016/j.jmb.2008.11.005
11. Wetzel, R., Shivaprasad, S., Williams, A.D.: Plasticity of Amyloid Fibrils. Biochemistry. 46, 1–10 (2007). doi:10.1021/bi0620959
12. Kodali, R., Wetzel, R.: Polymorphism in the intermediates and products of amyloid assembly. Curr. Opin. Struct. Biol. 17, 48–57 (2007). doi:10.1016/j.sbi.2007.01.007
13. Petkova, A.T., Leapman, R.D., Guo, Z., Yau, W.-M., Mattson, M.P., Tycko, R.: Self-Propagating, Molecular-Level Polymorphism in Alzheimers ß-Amyloid Fibrils. Science

(80-.). 307, 262 LP – 265 (2005)

14. Fitzpatrick, A.W.P., Debelouchina, G.T., Bayro, M.J., Clare, D.K., Caporini, M.A., Bajaj, V.S., Jaroniec, C.P., Wang, L., Ladizhansky, V., Müller, S.A., MacPhee, C.E., Waudby, C.A., Mott, H.R., De Simone, A., Knowles, T.P.J., Saibil, H.R., Vendruscolo, M., Orlova, E. V, Griffin, R.G., Dobson, C.M.: Atomic structure and hierarchical assembly of a cross-β amyloid fibril. Proc. Natl. Acad. Sci. . 110 , 5468–5473 (2013). doi:10.1073/pnas.1219476110
15. Cohen, S.I.A., Linse, S., Luheshi, L.M., Hellstrand, E., White, D.A., Rajah, L., Otzen, D.E., Vendruscolo, M., Dobson, C.M., Knowles, T.P.J.: Proliferation of amyloid-β42 aggregates occurs through a secondary nucleation mechanism. Proc. Natl. Acad. Sci. . 110 , 9758–9763 (2013). doi:10.1073/pnas.1218402110
16. Lomakin, A., Chung, D.S., Benedek, G.B., Kirschner, D.A., Teplow, D.B.: On the nucleation and growth of amyloid beta-protein fibrils: detection of nuclei and quantitation of rate constants. Proc. Natl. Acad. Sci. U. S. A. 93, 1125–1129 (1996)
17. Jeong, J.S., Ansaloni, A., Mezzenga, R., Lashuel, H.A., Dietler, G.: Novel Mechanistic Insight into the Molecular Basis of Amyloid Polymorphism and Secondary Nucleation during Amyloid Formation. J. Mol. Biol. 425, 1765–1781 (2013). doi:http://doi.org/10.1016/j.jmb.2013.02.005
18. Makin, O.S., Serpell, L.C.: Structures for amyloid fibrils. FEBS J. 272, 5950–5961 (2005). doi:10.1111/j.1742-4658.2005.05025.x
19. Fändrich, M., Meinhardt, J., Grigorieff, N.: Structural polymorphism of Alzheimer Aβ and other amyloid fibrils. Prion. 3, 89–93 (2009). doi:10.4161/pri.3.2.8859
20. Ahmed, M., Davis, J., Aucoin, D., Sato, T., Ahuja, S., Aimoto, S., Elliott, J.I., Van Nostrand, W.E., Smith, S.O.: Structural conversion of neurotoxic amyloid-[beta]1-42 oligomers to fibrils. Nat Struct Mol Biol. 17, 561–567 (2010)
21. Qiang, W., Yau, W.-M., Lu, J.-X., Collinge, J., Tycko, R.: Structural variation in amyloid-β fibrils from Alzheimer’s disease clinical subtypes. Nature. 541, 217–221 (2017)
22. Caughey, B., Lansbury, P.T.: Protofibrils, Pores, Fibrils, and Neurodegeneration: Separating the Responsible Protein Aggregates from The Innocent Bystanders. Annu. Rev. Neurosci. 26, 267–298 (2003). doi:10.1146/annurev.neuro.26.010302.081142
23. Glabe, C.G.: Common mechanisms of amyloid oligomer pathogenesis in degenerative

disease. Neurobiol. Aging. 27, 570–575 (2017). doi:10.1016/j.neurobiolaging.2005.04.017

24. Goldsbury, C., Frey, P., Olivieri, V., Aebi, U., Müller, S.A.: Multiple Assembly Pathways Underlie Amyloid-β Fibril Polymorphisms. J. Mol. Biol. 352, 282–298 (2005). doi:http://doi.org/10.1016/j.jmb.2005.07.029
25. Doussineau, T., Mathevon, C., Altamura, L., Vendrely, C., Dugourd, P., Forge, V., Antoine, R.: Mass Determination of Entire Amyloid Fibrils by Using Mass Spectrometry. Angew. Chemie. 128, 2386–2390 (2016). doi:10.1002/ange.201508995
26. Bleiholder, C., Dupuis, N.F., Wyttenbach, T., Bowers, M.T.: Ion mobility–mass spectrometry reveals a conformational conversion from random assembly to β-sheet in amyloid fibril formation. Nat Chem. 3, 172–177 (2011)
27. Hoffmann, W., von Helden, G., Pagel, K.: Ion mobility-mass spectrometry and orthogonal gas-phase techniques to study amyloid formation and inhibition. Curr. Opin. Struct. Biol. 46, 7–15 (2017). doi:http://doi.org/10.1016/j.sbi.2017.03.002
28. Hoyer, W., Antony, T., Cherny, D., Heim, G., Jovin, T.M., Subramaniam, V.: Dependence of α-Synuclein Aggregate Morphology on Solution Conditions. J. Mol. Biol. 322, 383–393 (2002). doi:10.1016/S0022-2836(02)00775-1
29. Scarafone, N., Pain, C., Fratamico, A., Gaspard, G., Yilmaz, N., Filée, P., Galleni, M., Matagne, A., Dumoulin, M.: Amyloid-Like Fibril Formation by PolyQ Proteins: A Critical Balance between the PolyQ Length and the Constraints Imposed by the Host Protein. PLoS One. 7, e31253 (2012)
30. Wälti, M.A., Ravotti, F., Arai, H., Glabe, C.G., Wall, J.S., Böckmann, A., Güntert, P., Meier, B.H., Riek, R.: Atomic-resolution structure of a disease-relevant Aβ(1–42) amyloid fibril. Proc. Natl. Acad. Sci. . 113 , E4976–E4984 (2016). doi:10.1073/pnas.1600749113
31. Kodali, R., Wetzel, R.: Polymorphism in the intermediates and products of amyloid assembly. Curr. Opin. Struct. Biol. 17, 48–57 (2007). doi:10.1016/j.sbi.2007.01.007
32. Williams, A.D., Sega, M., Chen, M., Kheterpal, I., Geva, M., Berthelier, V., Kaleta, D.T., Cook, K.D., Wetzel, R.: Structural properties of Abeta protofibrils stabilized by a small molecule. Proc. Natl. Acad. Sci. 102, 7115–7120 (2005)
33. Goldsbury, C., Frey, P., Olivieri, V., Aebi, U., Müller, S.A.: Multiple Assembly Pathways Underlie Amyloid-β Fibril Polymorphisms. J. Mol. Biol. 352, 282–298 (2005). doi:10.1016/j.jmb.2005.07.029

34. Müller, S.A., Engel, A.: Structure and mass analysis by scanning transmission electron microscopy. Micron. 32, 21–31 (2001). doi:10.1016/S0968-4328(00)00022-6
35. Thomas, D., Schultz, P., Steven, A.C., Wall, J.S.: Mass analysis of biological macromolecular complexes by STEM. Biol. Cell. 80, 181–192 (1994). doi:10.1111/j.1768-322X.1994.tb00929.x
36. Sousa, A.A., Leapman, R.D.: Mass Mapping of Amyloid Fibrils in the Electron Microscope Using STEM Imaging. In: Sousa, A.A. and Kruhlak, M.J. (eds.) Nanoimaging: Methods and Protocols. pp. 195–207. Humana Press, Totowa, NJ (2013)
37. Schmidt, M., Sachse, C., Richter, W., Xu, C., Fändrich, M., Grigorieff, N.: Comparison of Alzheimer Aβ(1–40) and Aβ(1–42) amyloid fibrils reveals similar protofilament structures. Proc. Natl. Acad. Sci. . 106 , 19813–19818 (2009). doi:10.1073/pnas.0905007106
38. Sachse, C., Faendrich, M., Grigorieff, N.: Paired beta-sheet structure of an A beta(1-40) amyloid fibril revealed by electron microscopy. Proc. Natl. Acad. Sci. U.S.A. 105, 7462–7466 (2008). doi:10.1073/pnas.0712290105
39. Wälti, M.A., Ravotti, F., Arai, H., Glabe, C.G., Wall, J.S., Böckmann, A., Güntert, P., Meier, B.H., Riek, R.: Atomic-resolution structure of a disease-relevant Aβ(1–42) amyloid fibril. Proc. Natl. Acad. Sci. . 113 , E4976–E4984 (2016). doi:10.1073/pnas.1600749113
40. Schmidt, M., Sachse, C., Richter, W., Xu, C., Fändrich, M., Grigorieff, N.: Comparison of Alzheimer Aβ(1–40) and Aβ(1–42) amyloid fibrils reveals similar protofilament structures. Proc. Natl. Acad. Sci. . 106 , 19813–19818 (2009). doi:10.1073/pnas.0905007106
41. Sachse, C., Fändrich, M., Grigorieff, N.: Paired β-sheet structure of an Aβ(1-40) amyloid fibril revealed by electron microscopy. Proc. Natl. Acad. Sci. . 105 , 7462–7466 (2008). doi:10.1073/pnas.0712290105
42. Pedersen, J.S., Dikov, D., Flink, J.L., Hjuler, H.A., Christiansen, G., Otzen, D.E.: The Changing Face of Glucagon Fibrillation: Structural Polymorphism and Conformational Imprinting. J. Mol. Biol. 355, 501–523 (2006). doi:10.1016/j.jmb.2005.09.100
43. Toyama, B.H., Kelly, M.J.S., Gross, J.D., Weissman, J.S.: The structural basis of yeast prion strain variants. Nature. 449, 233–237 (2007)
44. Klement, K., Wieligmann, K., Meinhardt, J., Hortschansky, P., Richter, W., Fändrich, M.:

Effect of Different Salt Ions on the Propensity of Aggregation and on the Structure of Alzheimer's Aβ(1-40) Amyloid Fibrils. J. Mol. Biol. 373, 1321–1333 (2007). doi:10.1016/j.jmb.2007.08.068

45. Stine, W.B., Dahlgren, K.N., Krafft, G.A., LaDu, M.J.: In Vitro Characterization of Conditions for Amyloid-β Peptide Oligomerization and Fibrillogenesis . J. Biol. Chem. . 278 , 11612–11622 (2003). doi:10.1074/jbc.M210207200
46. Petkova, A.T., Leapman, R.D., Guo, Z., Yau, W.-M., Mattson, M.P., Tycko, R.: Self-Propagating, Molecular-Level Polymorphism in Alzheimers ß-Amyloid Fibrils. Science (80-.). 307, 262 LP – 265 (2005)
47. Sachse, C., Xu, C., Wieligmann, K., Diekmann, S., Grigorieff, N., Fändrich, M.: Quaternary Structure of a Mature Amyloid Fibril from Alzheimer's Aβ(1-40) Peptide. J. Mol. Biol. 362, 347–354 (2006). doi:10.1016/j.jmb.2006.07.011
48. Sachse, C., Xu, C., Wieligmann, K., Diekmann, S., Grigorieff, N., Fändrich, M.: Quaternary Structure of a Mature Amyloid Fibril from Alzheimer's Aβ(1-40) Peptide. J. Mol. Biol. 362, 347–354 (2006). doi:10.1016/j.jmb.2006.07.011
49. Meinhardt, J., Sachse, C., Hortschansky, P., Grigorieff, N., Fändrich, M.: Aβ(1-40) Fibril Polymorphism Implies Diverse Interaction Patterns in Amyloid Fibrils. J. Mol. Biol. 386, 869–877 (2009). doi:10.1016/j.jmb.2008.11.005
50. Andersen, C.B., Yagi, H., Manno, M., Martorana, V., Ban, T., Christiansen, G., Otzen, D.E., Goto, Y., Rischel, C.: Branching in Amyloid Fibril Growth. Biophys. J. 96, 1529–1536 (2017). doi:10.1016/j.bpj.2008.11.024
51. Milhiet, P.-E., Yamamoto, D., Berthoumieu, O., Dosset, P., Le Grimellec, C., Verdier, J.-M., Marchal, S., Ando, T.: Deciphering the Structure, Growth and Assembly of Amyloid-Like Fibrils Using High-Speed Atomic Force Microscopy. PLoS One. 5, e13240 (2010)
52. Baskakov, I. V: Branched chain mechanism of polymerization and ultrastructure of prion protein amyloid fibrils. FEBS J. 274, 3756–3765 (2007). doi:10.1111/j.1742-4658.2007.05916.x
53. Harper, J.D., Lieber, C.M., Lansbury, P.T.: Atomic force microscopic imaging of seeded fibril formation and fibril branching by the Alzheimer's disease amyloid-β protein. Chem. Biol. 4, 951–959 (1997). doi:10.1016/S1074-5521(97)90303-3
54. Pedersen, J.S., Andersen, C.B., Otzen, D.E.: Amyloid structure – one but not the same: the

many levels of fibrillar polymorphism. FEBS J. 277, 4591–4601 (2010). doi:10.1111/j.1742-4658.2010.07888.x

55. Conway, K.A., Harper, J.D., Lansbury, P.T.: Fibrils Formed in Vitro from α-Synuclein and Two Mutant Forms Linked to Parkinson's Disease are Typical Amyloid. Biochemistry. 39, 2552–2563 (2000). doi:10.1021/bi991447r
56. Jakes, R., Spillantini, M.G., Goedert, M.: Identification of two distinct synucleins from human brain. FEBS Lett. 345, 27–32 (1994). doi:10.1016/0014-5793(94)00395-5
57. Spillantini, M.G., Crowther, R.A., Jakes, R., Hasegawa, M., Goedert, M.: α-Synuclein in filamentous inclusions of Lewy bodies from Parkinson's disease and dementia with Lewy bodies. Proc. Natl. Acad. Sci. . 95 , 6469–6473 (1998)
58. Serpell, L.C., Berriman, J., Jakes, R., Goedert, M., Crowther, R.A.: Fiber diffraction of synthetic α-synuclein filaments shows amyloid-like cross-β conformation. Proc. Natl. Acad. Sci. . 97 , 4897–4902 (2000). doi:10.1073/pnas.97.9.4897
59. Prusiner, S.B.: A Unifying Role for Prions in Neurodegenerative Diseases. Science (80-.). 336, 1511–1513 (2012)
60. Brundin, P., Melki, R., Kopito, R.: Prion-like transmission of protein aggregates in neurodegenerative diseases. Nat Rev Mol Cell Biol. 11, 301–307 (2010)
61. Desplats, P., Lee, H.-J., Bae, E.-J., Patrick, C., Rockenstein, E., Crews, L., Spencer, B., Masliah, E., Lee, S.-J.: Inclusion formation and neuronal cell death through neuron-to-neuron transmission of α-synuclein. Proc. Natl. Acad. Sci. . 106 , 13010–13015 (2009). doi:10.1073/pnas.0903691106
62. Luk, K.C., Kehm, V., Carroll, J., Zhang, B., O'Brien, P., Trojanowski, J.Q., Lee, V.M.-Y.: Pathological α-Synuclein Transmission Initiates Parkinson-like Neurodegeneration in Nontransgenic Mice. Science (80-.). 338, 949 LP – 953 (2012). doi:10.1126/science.1227157
63. Dearborn, A.D., Wall, J.S., Cheng, N., Heymann, J.B., Kajava, A. V, Varkey, J., Langen, R., Steven, A.C.: α-Synuclein Amyloid Fibrils with Two Entwined, Asymmetrically Associated, Protofibrils. J. Biol. Chem. . (2015). doi:10.1074/jbc.M115.698787
64. Iljina, M., Garcia, G.A., Horrocks, M.H., Tosatto, L., Choi, M.L., Ganzinger, K.A., Abramov, A.Y., Gandhi, S., Wood, N.W., Cremades, N., Dobson, C.M., Knowles, T.P.J., Klenerman, D.: Kinetic model of the aggregation of alpha-synuclein provides insights into

prion-like spreading. Proc. Natl. Acad. Sci. . 113 , E1206–E1215 (2016). doi:10.1073/pnas.1524128113

65. Qin, Z., Hu, D., Han, S., Hong, D.-P., Fink, A.L.: Role of Different Regions of α-Synuclein in the Assembly of Fibrils. Biochemistry. 46, 13322–13330 (2007). doi:10.1021/bi7014053
66. van Raaij, M.E., Segers-Nolten, I.M.J., Subramaniam, V.: Quantitative Morphological Analysis Reveals Ultrastructural Diversity of Amyloid Fibrils from α-Synuclein Mutants. Biophys. J. 91, L96–L98 (2006). doi:10.1529/biophysj.106.090449
67. Bousset, L., Pieri, L., Ruiz-Arlandis, G., Gath, J., Jensen, P.H., Habenstein, B., Madiona, K., Olieric, V., Böckmann, A., Meier, B.H., Melki, R.: Structural and functional characterization of two alpha-synuclein strains. Nat. Commun. 4, 2575 (2013). doi:10.0.4.14/ncomms3575
68. Gath, J., Bousset, L., Habenstein, B., Melki, R., Böckmann, A., Meier, B.H.: Unlike Twins: An NMR Comparison of Two α-Synuclein Polymorphs Featuring Different Toxicity. PLoS One. 9, e90659 (2014). doi:10.1371/journal.pone.0090659
69. van Raaij, M.E., Segers-Nolten, I.M.J., Subramaniam, V.: Quantitative Morphological Analysis Reveals Ultrastructural Diversity of Amyloid Fibrils from α-Synuclein Mutants. Biophys. J. 91, L96–L98 (2006). doi:10.1529/biophysj.106.090449
70. Chamberlain, A.K., MacPhee, C.E., Zurdo, J., Morozova-Roche, L.A., Hill, H.A.O., Dobson, C.M., Davis, J.J.: Ultrastructural Organization of Amyloid Fibrils byAtomic Force Microscopy. Biophys. J. 79, 3282–3293 (2000). doi:10.1016/S0006-3495(00)76560-X
71. Hoyer, W., Antony, T., Cherny, D., Heim, G., Jovin, T.M., Subramaniam, V.: Dependence of α-Synuclein Aggregate Morphology on Solution Conditions. J. Mol. Biol. 322, 383–393 (2002). doi:10.1016/S0022-2836(02)00775-1
72. Dearborn, A.D., Wall, J.S., Cheng, N., Heymann, J.B., Kajava, A. V, Varkey, J., Langen, R., Steven, A.C.: α-Synuclein Amyloid Fibrils with Two Entwined, Asymmetrically Associated, Protofibrils. J. Biol. Chem. . (2015). doi:10.1074/jbc.M115.698787
73. Ballatore, C., Lee, V.M.-Y., Trojanowski, J.Q.: Tau-mediated neurodegeneration in Alzheimer’s disease and related disorders. Nat Rev Neurosci. 8, 663–672 (2007). doi:10.1038/nrn2194

74. Wegmann, S., Jung, Y.J., Chinnathambi, S., Mandelkow, E.-M., Mandelkow, E., Muller, D.J.: Human Tau Isoforms Assemble into Ribbon-like Fibrils That Display Polymorphic Structure and Stability. J. Biol. Chem. . 285 , 27302–27313 (2010). doi:10.1074/jbc.M110.145318
75. Wang, Y., Mandelkow, E.: Tau in physiology and pathology. Nat Rev Neurosci. 17, 22–35 (2016). doi:10.1038/nrn.2015.1
76. KIDD, M.: Paired Helical Filaments in Electron Microscopy of Alzheimer's Disease. Nature. 197, 192–193 (1963)
77. Crowther, R.A.: Straight and paired helical filaments in Alzheimer disease have a common structural unit. Proc. Natl. Acad. Sci. 88, 2288–2292 (1991)
78. Grundke-Iqbal, I., Iqbal, K., Tung, Y.C., Quinlan, M., Wisniewski, H.M., Binder, L.I.: Abnormal phosphorylation of the microtubule-associated protein tau (tau) in Alzheimer cytoskeletal pathology. Proc. Natl. Acad. Sci. . 83 , 4913–4917 (1986)
79. Barghorn, S., Mandelkow, E.: Toward a Unified Scheme for the Aggregation of Tau into Alzheimer Paired Helical Filaments. Biochemistry. 41, 14885–14896 (2002). doi:10.1021/bi026469j
80. Friedhoff, P., von Bergen, M., Mandelkow, E.-M., Davies, P., Mandelkow, E.: A nucleated assembly mechanism of Alzheimer paired helical filaments. Proc. Natl. Acad. Sci. . 95 , 15712–15717 (1998). doi:10.1073/pnas.95.26.15712
81. Ramachandran, G., Udgaonkar, J.B.: Understanding the Kinetic Roles of the Inducer Heparin and of Rod-like Protofibrils during Amyloid Fibril Formation by Tau Protein. J. Biol. Chem. . 286 , 38948–38959 (2011). doi:10.1074/jbc.M111.271874
82. Wegmann, S., Jung, Y.J., Chinnathambi, S., Mandelkow, E.-M., Mandelkow, E., Muller, D.J.: Human Tau Isoforms Assemble into Ribbon-like Fibrils That Display Polymorphic Structure and Stability. J. Biol. Chem. . 285 , 27302–27313 (2010). doi:10.1074/jbc.M110.145318
83. Goedert, M., Jakes, R., Spillantini, M.G., Hasegawa, M., Smith, M.J., Crowther, R.A.: Assembly of microtubule-associated protein tau into Alzheimer-like filaments induced by sulphated glycosaminoglycans. Nature. 383, 550–553 (1996). doi:10.1038/383550a0
84. Pérez, M., Valpuesta, J.M., Medina, M., de Garcini, E., Avila, J.: Polymerization of τ into Filaments in the Presence of Heparin: The Minimal Sequence Required for τ - τ

Interaction. J. Neurochem. 67, 1183–1190 (1996). doi:10.1046/j.1471-4159.1996.67031183.x

85. Xu, S., Brunden, K.R., Trojanowski, J.Q., Lee, V.M.-Y.: Characterization of tau fibrillization in vitro. Alzheimer’s Dement. J. Alzheimer's Assoc. 6, 110–117 (2017). doi:10.1016/j.jalz.2009.06.002
86. von Bergen, M., Friedhoff, P., Biernat, J., Heberle, J., Mandelkow, E.-M., Mandelkow, E.: Assembly of τ protein into Alzheimer paired helical filaments depends on a local sequence motif (306VQIVYK311) forming β structure. Proc. Natl. Acad. Sci. . 97 , 5129–5134 (2000). doi:10.1073/pnas.97.10.5129
87. Andronesi, O.C., Bergen, M. von, Biernat, J., Seidel, K., Griesinger, C., Mandelkow, E., Baldus, M.: Characterization of Alzheimer’s-like Paired Helical Filaments from the Core Domain of Tau Protein Using Solid-State NMR Spectroscopy. J. Am. Chem. Soc. 130, 5922–5928 (2008). doi:10.1021/ja7100517
88. Wegmann, S., Medalsy, I.D., Mandelkow, E., Müller, D.J.: The fuzzy coat of pathological human Tau fibrils is a two-layered polyelectrolyte brush. Proc. Natl. Acad. Sci. . 110 , E313–E321 (2013). doi:10.1073/pnas.1212100110
89. Rambaldi, D.C., Zattoni, A., Reschiglian, P., Colombo, R., De Lorenzi, E.: In vitro amyloid Aβ1-42 peptide aggregation monitoring by asymmetrical flow field-flow fractionation with multi-angle light scattering detection. Anal. Bioanal. Chem. 394, 2145–2149 (2009). doi:10.1007/s00216-009-2899-1

Chapter Seven:

Epilogue and Future Outlook

"Everything in the past is a particle; everything in the future is a wave."

– Lawrence Bragg

On a personal view of scientific discovery, Francis Crick wrote ‘If you want to understand function, study structure’. This statement is a source of my motivations combining light and mass spectrometry to study the structure of large (bio) molecules unveiling their functions. Small and large molecules adopt distinctive structures or shapes to perform diverse functions. The structure of the large molecules such as protein, polymer, DNA, RNA, aggregates and fibrils are multifaceted compared to small molecules. Also, the concept of multi-scale organization is interesting as compared to small molecules. Understanding the structures and functions of these molecules requires various tools to detect, identify, resolve, and characterize them. Dissociation is one of the fundamental processes to characterize these large molecules in terms of their identification, structures, modifications, interactions and networks. Dissociation of these molecules can be performed by introducing collision with gases, electrons and photons. By coupling laser with mass spectrometry, one can develop a new tool in photodissociation and offer an alternative option to collision induced and electron transfer dissociations for characterizing large biomolecules. Although the idea of coupling lasers with mass spectrometers was conceived three decades ago [1], most of the study focused on small molecule characterization. In recent years, considerable improvements (both in mass spectrometry and laser technology) have been made towards its applications for biomolecule characterization including peptides, proteins, nucleic acids, carbohydrates, and lipids [2–4]. In photodissociation mass spectrometry, the charged molecules are allowed to interact with photons in a so-called ‘trapping’ device so that molecules can absorb single or multiple photons, resulting in an accumulation of internal energy leading to fragmentation. A large palette of light source with pulsed and continuous modes can be used for lasers. Single high energy UV photon of ~2–10 eV or multiple low energy IR photons of ~0.1 eV can be employed for ion activations. Various mass spectrometers including linear-ion trap, Fourier transform ion cyclotron (FT-ICR), and Orbitrap can be coupled with laser sources *via* optical setting and windows to introduce photons in the collision cell of a mass spectrometer. Coupling electron transfer dissociation with infrared photodissociation [5], combining ultraviolet dissociation with electron transfer dissociation [6] and assimilating electron-driven technique with low or high collision activation methods [7, 8] have also been implemented recently. However, combining high and low energy photons with high resolution mass spectrometer, what we named HiLoPD as a new method, for characterizing biomolecules was not envisioned earlier.

In the first course of this thesis, we performed the implementation of 213 nm UVPD in a hybrid quadrupole-Orbitrap mass spectrometer in negative polarity for peptide anions characterization. This method provides distinctive C_α–C, N–C_α and C–N backbone fragmentations from the hydrogen-deficient radical anions. Radical-driven extensive side-chain loss is equally observed with this method. Moreover, series of hydrogen-deficient and hydrogen-rich fragments are detected. Due to radical-induced fragmentation, unprecedented numbers of fragment ions of 22 ion types are discovered. Due to the plethora of fragment ions, the data analysis remained challenging. After addressing the issue of complex data processing, this study can be used as 'ion-type' template to include, modify and improve the available commercial software and databases in top-down proteomics for acidic proteome. Once automatic data processing is available, this method will be suitable for larger proteins and protein-complexes characterization in negative polarity. This robust photodissociation method has a potential to make important contribution in non-targeted metabolomics (especially acidic metabolites) as an alternative to collision induced dissociation.

In the second phase of my work, we developed a new method (HiLoPD) in which two activation channels are combined by high (UV) and low (IR) photodissociation in a high-resolution mass spectrometer. We implemented this method in such a way that one can utilize these two channels consecutively and simultaneously in a single MS/MS experiment. For top-down characterization of ubiquitin, when UV and CO_2 laser irradiated simultaneously, the total number of fragment ions is improved considerably than IRMPD and UVPD alone. We noticed that while "peptide backbone" fragment ions decreased, nearly equal numbers of "side-chain loss" fragment ions emerged. The secondary fragment ions (d, v and w), which are generated from a/x and z ions, are also detected. These ions can ease the identification of isomeric residues such as leucine and isoleucine in a protein. In simultaneous irradiation, UV laser promotes the excited states dissociation whereas CO_2 laser stimulates the ground state dissociation, producing rich and well-balance fragmentation pattern of ubiquitin. We also studied the relation between regions of the ubiquitin that displayed high fragmentation yields and its conformational flexibility. The ability of high-low photon energy based photodissociation is a promising avenue for elucidating more rigid regions of proteins in the gas phase.

In HiLoPD, we only employed 213 nm to high energy photons; other wavelengths such as fourth harmonic at 266 nm can also be considered. In future, the combination of 266 nm UV lasers with a CO_2 laser will allow to conduct "activated-EPD" and to improve sequence coverage for large proteins in negative ionization mode. This coupling has not yet been implemented in Orbitrap MS instruments.

In terms of applications, HiLoPD can be applied for large soluble proteins, and integral membrane proteins (IMPs). IMPs are essential components of all cells and organelles as they maintain transport and interaction of molecules across the membrane. They perform diverse functions including signalling, immune response, transport, energy conversion, and drug transport [9]. Around 70% of all drug candidates target IMPs [10, 11]. 20-40% of the sequences encoded in the human genome are thought to be IMPs [12]. The most common problems associated with IMPs include their very hydrophobic nature, poor digestion efficiency, and the tendency to undergo rapid denaturation and aggregation after they are removed from the membrane environment [13, 14]. Therefore, a prime challenge in structural biology is not only to resolve new structures but improve the general understanding of IMPs folding, dynamics, and function. Top-down characterization of IMPs employing 213 nm UVPD and HiLoPD can yield profound insights that will have a major impact in the field of structural biology.

Mass spectrometry based methods made significant progress on characterizing post-translational modifications in peptides and protein; however, many issues remain on the fragmentation technique which can provide good sequence information, locate the PTMs sites, and retain the labile PTMs groups. To address these issues, we investigate 10.6 μm IRMPD, 213 nm UVPD and HiLoPD for phospho-, sulfo- and glycol-peptides' cation. Results reveal that 213 nm UVPD and HiLoPD methods can provide diverse backbone fragmentation with excellent sequence coverage, location of PTMs sites and reasonable retention efficiency for phospho- and glycol-peptides. For sulfopeptide, excellent sequence coverage is achieved and the position of the SO_3 group is identified, however, widespread SO_3 losses are detected irrespective to the methods used herein. Based on the overall performance, we believe that UVPD and HiLoPD can serve as alternative options to collision activation and electron transfer dissociations for phospho and glycoproteomics. However, large-scale investigations are prerequisite to establish these techniques as a workable tool for PTMs based proteomics.

A CO_2 laser was also coupled with charge-detection mass spectrometer to understand the fundamental aspect of unimolecular dissociation mechanism for megadalton polymer cation and anion. The experiment reveals several fragmentation pathways having distinct signatures at the single molecule level. Also, the analysis of single ion trajectories, after a heating period, allows one to measure stepwise changes in the charge and time-of-flight of the trapped ion. By conducting a statistical analysis of single ion trajectories, activation energies associated to dissociation of positive and negative polymer ions are measured. Results show that a cation requires more energy in comparison with negative ions to overcome the unimolecular barrier. The difference observed in activation energy values between positively and negatively charged ions may be due to different binding energy depending on the nature of the charge on the polymer. These results are also supported by density functional theory (DFT), which reveals that the non-bonding interaction plays an important role in stabilizing the polymer cation system. Further study can be directed on other large polymers associated to industrial applications and on more heterogeneous samples such as virus and nucleosome to understand the dissociation mechanism (thus their structural diversity) of large megadalton biological objects.

While native mass spectrometry can measure the mass of biological entities of few megadaltons and provide information of their structures, intricate topology and dynamics [15, 16], weighing the massive and giant assemblies, aggregates and fibrils over 20 MDa is simply not feasible as resolving charge states of such large object is nearly impossible. These large biological assemblies and complexes retain over hundreds to thousands of charges in electrospray ionization. The mass and high charges of megadalton assemblies can be detected individually through charge-detection device applying simple but robust image current concept. The charge-detection technique is perfectly suited for megadalton polymers and biological assembles such as DNA, RNA, and fibrils larger than those accessible with the native mass spectrometry.

Besides laser-MS coupling and characterization of small peptides and proteins, we report details study of charge-detection mass spectrometry for megadalton amyloid fibers of $A\beta_{1-42}$, α-synuclein and Tau involved in neurodegenerative diseases. Mass and charge distribution of the various fibril populations owing to their intrinsic polymorphism are measured for the first time. This study discloses that overall mass and charge distribution of short protofibrils, elongated protofilaments, isolated fibers, ribbon-like fibers, and paired helical filaments are greatly varied as their morphologies. While masses of the short protofibrils and mature protofilaments are significantly different, protofibrils retain relatively high charges compared to the mature protofilaments which may be a reason why short protofibrils strongly interact with lipid membrane and become more toxic than the mature protofilaments. This study could be a foundation for several future studies. Since these amyloid fibrils formation and heterogeneous structures are highly sensitive to sampling conditions including pH, temperature, incubation time, salt concentration, and buffer conditions; systematic studies combining TEM, AFM and CDMS can be performed to elicit how these conditions influence the overall aggregation and heterogeneity of these fibrils.

The structure and heterogeneity in the fibril formation process remain difficult to assess by any traditional MS-based methods. This first step will require a unique coupling between charge-detection mass spectrometry and separation techniques. The continuous flow separation using a dielectrophoretic field (DEF) for instance with charge detection mass spectrometry (DEF-CDMS) could be used to profile the time-dependent aggregation pattern, in order to pave the complicated phase diagram depending on protein concentration, solution pH, salt concentration and the excitation mode. In DEF, there is no stationary phase able to induce mechanical or shear stress on the protein molecules, and the mobile phase composition can be chosen to preserve the native state.

Bibliography

1. Bomse, D.S., Woodin, R.L., Beauchamp, J.L.: Molecular activation with low-intensity CW infrared laser radiation. Multiphoton dissociation of ions derived from diethyl ether. J. Am. Chem. Soc. 101, 5503–5512 (1979). doi:10.1021/ja00513a008
2. Brodbelt, J.S.: Photodissociation mass spectrometry: new tools for characterization of biological molecules. Chem. Soc. Rev. 43, 2757–83 (2014). doi:10.1039/c3cs60444f
3. Brodbelt, J.S.: Shedding Light on the Frontier of Photodissociation. J. Am Soc. Mass Spectrom. 22, 197–206 (2011). doi:10.1007/s13361-010-0023-6
4. Brodbelt, J.S., Wilson, J.J.: Infrared multiphoton dissociation in quadrupole ion traps. Mass Spectrom. Rev. 28, 390–424 (2009). doi:10.1002/mas.20216
5. Riley, N.M., Westphall, M.S., Coon, J.J.: Activated Ion Electron Transfer Dissociation for Improved Fragmentation of Intact Proteins. Anal. Chem. 87, 7109–7116 (2015). doi:10.1021/acs.analchem.5b00881
6. Cannon, J.R., Holden, D.D., Brodbelt, J.S.: Hybridizing Ultraviolet Photodissociation with Electron Transfer Dissociation for Intact Protein Characterization. Anal. Chem. 86, 10970–10977 (2014). doi:10.1021/ac5036082
7. Frese, C.K., Altelaar, A.F.M., van den Toorn, H., Nolting, D., Griep-Raming, J., Heck, A.J.R., Mohammed, S.: Toward Full Peptide Sequence Coverage by Dual Fragmentation Combining Electron-Transfer and Higher-Energy Collision Dissociation Tandem Mass Spectrometry. Anal. Chem. 84, 9668–9673 (2012). doi:10.1021/ac3025366
8. Swaney, D.L., McAlister, G.C., Wirtala, M., Schwartz, J.C., Syka, J.E.P., Coon, J.J.: Supplemental Activation Method for High-Efficiency Electron-Transfer Dissociation of Doubly Protonated Peptide Precursors. Anal. Chem. 79, 477–485 (2007). doi:10.1021/ac061457f
9. White, S.H.: Biophysical dissection of membrane proteins. Nature. 459, 344–346 (2009). doi:10.1038/nature08142
10. Whitelegge, J.P.: Integral Membrane Proteins and Bilayer Proteomics. Anal. Chem. 85, 2558–2568 (2013). doi:10.1021/ac303064a
11. Bowie, J.U.: Membrane Protein Twists and Turns. Science (80-.). 339, 398–399 (2013). doi:10.1126/science.1228655
12. Souda, P., Ryan, C.M., Cramer, W.A., Whitelegge, J.: Profiling of integral membrane proteins and their post translational modifications using high-resolution mass spectrometry. Methods. 55, 330–336 (2011). doi:10.1016/j.ymeth.2011.09.019
13. Rabilloud, T.: Membrane proteins and proteomics: love is possible, but so difficult. Electrophoresis. 30, S174–S180 (2009). doi:10.1002/elps.200900050

14. Santoni, V., Molloy, M., Rabilloud, T.: Membrane proteins and proteomics: Un amour impossible? Electrophoresis. 21, 1054–1070 (2000). doi:10.1002/(SICI)1522-2683(20000401)
15. Heck, A.J.R.: Native mass spectrometry: a bridge between interactomics and structural biology. Nat. Methods. 5, 927–933 (2008). doi:10.1038/nmeth.1265
16. Snijder, J., Heck, A.J.R.: Analytical Approaches for Size and Mass Analysis of Large Protein Assemblies. Annu. Rev. Anal. Chem. 7, 43–64 (2014). doi:10.1146/annurev-anchem-071213-020015

Appendix

Table A2.1 Exact masses and assignments of ions from backbone dissociation detected in the UVPD of doubly-deprotonated (*m/z* 597.8057) of YTIAALLSPYS $[M-2H]^{2-}$.

Experimental *m/z*	Theoretical *m/z*	Assignment	Chemical Composition	Mass Difference (ppm)
267.0977	267.0981	$(y_2)^-$	$C_{12}H_{15}N_2O_5$	-0.1721
294.0848	294.0852	$(x_2+1)^{-\cdot}$	$C_{13}H_{14}N_2O_6$	-0.1477
295.0924	295.0852	$(x_2+2)^-$	$C_{13}H_{15}N_2O_6$	2.9264
362.1348	362.1352	$(y_3-2)^-$	$C_{17}H_{20}N_3O_6$	-0.1696
364.1505	364.1509	$(y_3)^-$	$C_{17}H_{22}N_3O_6$	-0.1575
491.2612	491.2744	$(a_5+1)^{-\cdot}$	$C_{24}H_{37}N_5O_6$	-5.3107
591.2533	591.2540	$(x_5+1)^{-\cdot}$	$C_{27}H_{37}N_5O_{10}$	-0.2914
604.3579	604.3586	$(a_6+1)^{-\cdot}$	$C_{30}H_{48}N_6O_7$	-0.2089
676.3437	676.3432	$(y_6-1)^{-\cdot}$	$C_{32}H_{48}N_6O_{10}$	0.1889
677.3503	677.3510	$(y_6)^-$	$C_{32}H_{49}N_6O_{10}$	-0.2864
703.3294	703.3303	$(x_6)^-$	$C_{33}H_{47}N_6O_{11}$	-0.3636
704.3384	704.3381	$(x_6+1)^{-\cdot}$	$C_{33}H_{48}N_6O_{11}$	0.1069
717.4287	717.4425	$(a_7+1)^{-\cdot}$	$C_{36}H_{59}N_7O_8$	-5.5519
747.3786	747.3803	$(y_7-1)^{-\cdot}$	$C_{35}H_{54}N_7O_{11}$	-0.6880
748.3876	748.3881	$(y_7)^-$	$C_{35}H_{55}N_7O_{11}$	-0.2259
759.4406	759.4405	$(c_7-2)^-$	$C_{37}H_{59}N_8O_9$	0.0404
761.4556	761.4561	$(c_7)^-$	$C_{37}H_{61}N_8O_9$	-0.2059
773.3587	773.3596	$(x_7-1)^{-\cdot}$	$C_{36}H_{51}N_7O_{12}$	-0.3591
774.3659	774.3674	$(x_7)^-$	$C_{36}H_{52}N_7O_{12}$	-0.5911
775.3733	775.3752	$(x_7+1)^{-\cdot}$	$C_{36}H_{53}N_7O_{12}$	-0.7867
803.4658	803.4667	$(a_8)^-$	$C_{39}H_{63}N_8O_{10}$	-0.3571
804.4737	804.4745	$(a_8+1)^{-\cdot}$	$C_{39}H_{64}N_8O_{10}$	-0.3470
805.4815	805.4824	$(a_8+2)^-$	$C_{39}H_{65}N_8O_{10}$	-0.3612
817.4079	817.4096	$(y_8-2)^-$	$C_{38}H_{57}N_8O_{12}$	-0.6472
818.4158	818.4174	$(y_8-1)^{-\cdot}$	$C_{38}H_{58}N_8O_{12}$	-0.6331
819.4256	819.4252	$(y_8)^-$	$C_{38}H_{59}N_8O_{12}$	0.1435
833.4757	833.4773	$(b_8+2)^-$	$C_{40}H_{65}N_8O_{11}$	-0.6535
845.4032	845.4045	$(x_8)^-$	$C_{39}H_{57}N_8O_{13}$	-0.5119
846.4109	846.4123	$(x_8+1)^{-\cdot}$	$C_{39}H_{58}N_8O_{13}$	-0.5866
847.4204	847.4201	$(x_8+2)^-$	$C_{39}H_{59}N_8O_{13}$	0.1174
900.5049	900.5195	$(a_9)^-$	$C_{44}H_{70}N_9O_{11}$	-5.8453
901.5120	901.5273	$(a_9+1)^{-\cdot}$	$C_{44}H_{71}N_9O_{11}$	-6.1741
930.4916	930.4937	$(y_9-2)^-$	$C_{44}H_{69}N_9O_{13}$	-0.8223
944.5335	944.5331	$(c_9-1)^{-\cdot}$	$C_{45}H_{72}N_{10}O_{12}$	0.1744
945.5378	945.5409	$(c_9)^-$	$C_{45}H_{73}N_{10}O_{12}$	-1.2759

957.4795	957.4807	$(x_9\text{-}1)^{-\cdot}$	$C_{45}H_{67}N_9O_{14}$	-0.4833
958.4859	958.4886	$(x_9)^{-}$	$C_{45}H_{68}N_9O_{14}$	-1.0864
1032.5470	1032.5492	$(y_{10}\text{-}1)^{-\cdot}$	$C_{48}H_{76}N_{10}O_{15}$	-0.8721
1059.5334	1059.5440	$(x_{10})^{-}$	$C_{49}H_{75}N_{10}O_{16}$	-4.2870
1060.5395	1060.5440	$(x_{10}+1)^{-\cdot}$	$C_{49}H_{76}N_{10}O_{16}$	-1.8463
1106.5866	1106.5886	$(c_{10}\text{-}2)^{-}$	$C_{54}H_{80}N_{11}O_{14}$	-0.8114
1107.5938	1107.5964	$(c_{10}\text{-}1)^{-\cdot}$	$C_{54}H_{81}N_{11}O_{14}$	-1.0757

Table A2.2 Exact masses and assignments of neutral loss detected in the UVPD of doubly-deprotonated (*m/z* 597.8057) of YTIAALLSPYS $[M\text{-}2H]^{2-}$.

Experimental *m/z*	Theoretical *m/z*	Assignment	Chemical Composition	Mass Difference (ppm)
1195.6094	1195.6119	$[M\text{-}2H]^{-\bullet}$	$C_{57}H_{85}N_{11}O_{17}$	-1.0065
1180.5852	1180.5885	$[M\text{-}2H\text{-}CH_3]^{-}$	$C_{56}H_{82}N_{11}O_{17}$	-1.3313
1167.6147	1167.6170	$[M\text{-}2H\text{-}CO]^{-\bullet}$	$C_{56}H_{85}N_{11}O_{16}$	-0.9306
1166.6099	1166.5728	$[M\text{-}2H\text{-}CH_3CH_2]^{-}$	$C_{55}H_{80}N_{11}O_{17}$	14.9551
1165.6009	1165.6047	$[M\text{-}2H\text{-}CH_2O]^{-\bullet}$	$C_{56}H_{83}N_{11}O_{16}$	-1.5532
1164.5942	1164.5935	$[M\text{-}2H\text{-}CH_2OH]^{-}$	$C_{56}H_{82}N_{11}O_{16}$	0.2703
1151.5829	1151.6221	$[M\text{-}2H\text{-}C_2H_4O]^{-\bullet}$	$C_{55}H_{81}N_{11}O_{16}$	-15.7951
1150.5783	1150.6143	$[M\text{-}2H\text{-}COOH]^{-}$	$C_{56}H_{84}N_{11}O_{15}$	-14.5355
1139.5855	1139.5504	$[M\text{-}2H\text{-}C_4H_8]^{-\bullet}$	$C_{53}H_{78}N_{11}O_{17}$	14.1289
1133.6099	1133.6116	$[M\text{-}2H\text{-}(CO_2+H_2O)]^{-\bullet}$	$C_{56}H_{83}N_{11}O_{14}$	-0.6445
1123.5910	1123.5312	$[M\text{-}2H\text{-}C_4H_{11}N]^{-\bullet}$	$C_{53}H_{75}N_{10}O_{17}$	24.1551
1121.5759	1121.5513	$[M\text{-}2H\text{-}(C_3H_8ON)]^{-}$	$C_{54}H_{77}N_{10}O_{16}$	9.9354
1089.5688	1089.5712	$[M\text{-}2H\text{-}(OC_6H_4{=}CH_2)]^{-\bullet}$	$C_{50}H_{79}N_{11}O_{16}$	-0.9454
1088.5622	1088.5633	$[M\text{-}2H\text{-}(HOC_6H_4{=}CH_2)]^{-}$	$C_{51}H_{78}N_{11}O_{16}$	-0.4512
1045.5419	1045.5449	$[M\text{-}2H\text{-}(OC_6H_4{=}CH_2+C_2H_4O)]^{-\bullet}$	$C_{48}H_{75}N_{11}O_{15}$	-1.2420
1044.5346	1044.5371	$[M\text{-}2H\text{-}(HOC_6H_4{=}CH_2+C_2H_4O)\ ]^{-\bullet}$	$C_{48}H_{74}N_{11}O_{15}$	-1.0060
987.5129	987.5271	$[z_{10}\text{-}CHO]^{-\bullet}$	$C_{47}H_{73}N_9O_{14}$	-5.7445
986.5053	986.5193	$[z_{10}\text{-}1\text{-}CHO]^{-}$	$C_{47}H_{72}N_9O_{14}$	-5.6699
871.5031	871.5162	$[a_9\text{-}CH_3CH_2]^{-\ \bullet}$	$C_{43}H_{69}N_9O_{10}$	-5.2771
856.4917	856.5291	$[a_9\text{-}C_2H_4O]^{-}$	$C_{43}H_{70}N_9O_9$	-15.0806
789.4493	789.4869	$[b_8+2\text{-}C_2H_4O]^{-}$	$C_{39}H_{65}N_8O_9$	-15.1617
597.8057	597.8059	$[M\text{-}2H]^{2-}$	$C_{57}H_{85}N_{11}O_{17}$	-0.1139
575.7925	575.8111	$[M\text{-}2H\text{-}CO_2]^{2-}$	$C_{56}H_{85}N_{11}O_{15}$	-7.4861
205.0700	205.0972	$[y_2\text{-}CO_2+H_2O]^{-}$	$C_{11}H_{13}N_2O_2$	-10.9548

Table A2.3 Exact masses and assignments of ions from backbone dissociation detected in the UVPD of doubly-deprotonated (*m/z* 505.1906) of DYKDDDDK $[M\text{-}2H]^{2-}$.

Experimental *m/z*	Theoretical *m/z*	Assignment	Chemical Composition	Mass Difference (ppm)
113.0339	113.0113	$(b_1\text{-}1)^{-\cdot}$	$C_4H_3NO_3$	9.1566
114.0179	114.0191	$(b_1)^{-}$	$C_4H_4NO_3$	-0.4551
242.1134	242.0903	$(z_2\text{-}1)^{-\cdot}$	$C_{10}H_{14}N_2O_5$	9.3508
243.0975	243.0981	$(z_2)^{-}$	$C_{10}H_{15}N_2O_5$	-0.2527
249.0869	249.0875	$(a_2)^{-}$	$C_{12}H_{13}N_2O_4$	-0.2630
251.0926	251.1032	$(a_2\text{+}2)^{-}$	$C_{12}H_{14}N_2O_4$	-4.2771
286.1034	286.1039	$(x_2)^{-}$	$C_{11}H_{16}N_3O_6$	-0.2139
288.1197	288.1196	$(x_2\text{+}2)^{-}$	$C_{11}H_{18}N_3O_6$	0.0724
357.1405	357.1172	$(z_3\text{-}1)^{-\cdot}$	$C_{14}H_{19}N_3O_8$	9.3899
358.1252	358.1250	$(z_3)^{-}$	$C_{14}H_{18}N_3O_8$	0.0647
374.1324	374.1438	$(y_3\text{-}1)^{-\cdot}$	$C_{14}H_{22}N_4O_8$	-4.5965
375.1509	375.1516	$(y_3)^{-}$	$C_{14}H_{23}N_4O_8$	-0.2818
376.1976	376.1747	$(a_3\text{-}1)^{-\cdot}$	$C_{18}H_{24}N_4O_5$	9.2708
377.1818	377.1825	$(a_3)^{-}$	$C_{18}H_{25}N_4O_5$	-0.2723
401.1300	401.1309	$(x_3)^{-}$	$C_{15}H_{21}N_4O_9$	-0.3442
402.1380	402.1387	$(x_3\text{+}1)^{-\cdot}$	$C_{15}H_{22}N_4O_9$	-0.2656
404.1926	404.1696	$(b_3\text{-}1)^{-\cdot}$	$C_{19}H_{24}N_4O_6$	9.2932
471.1592	471.1363	$(z_4\text{-}2)^{-}$	$C_{18}H_{23}N_4O_{11}$	9.2294
472.1673	472.1442	$(z_4\text{-}1)^{-\cdot}$	$C_{18}H_{24}N_4O_{11}$	9.3202
490.1778	490.1785	$(y_4)^{-}$	$C_{18}H_{28}N_5O_{11}$	-0.3057
491.1933	491.1864	$(y_4\text{+}1)^{-\cdot}$	$C_{18}H_{29}N_5O_{11}$	2.7890
492.1965	492.2094	$(a_4)^{-}$	$C_{22}H_{30}N_5O_8$	-5.2316
493.2165	493.2173	$(a_4\text{+}1)^{-\cdot}$	$C_{22}H_{31}N_5O_8$	-0.3199
516.1568	516.1578	$(x_4)^{-}$	$C_{19}H_{26}N_5O_{12}$	-0.3898
519.2194	519.2043	$(b_4\text{-}1)^{-\cdot}$	$C_{23}H_{29}N_5O_9$	6.0706
536.2224	536.2231	$(c_4\text{-}1)^{-\cdot}$	$C_{23}H_{32}N_6O_9$	-0.2609
537.2301	537.2309	$(c_4)^{-}$	$C_{23}H_{33}N_6O_9$	-0.3274
587.1941	587.1711	$(z_5\text{-}1)^{-\cdot}$	$C_{22}H_{30}N_5O_{14}$	9.2746
605.2049	605.2055	$(y_5)^{-}$	$C_{22}H_{33}N_6O_{14}$	-0.2439
606.2282	606.2287	$(a_5\text{-}1)^{-\cdot}$	$C_{26}H_{34}N_6O_{11}$	-0.1597
607.2356	607.2364	$(a_5)^{-}$	$C_{26}H_{35}N_6O_{11}$	-0.3272
608.2435	608.2442	$(a_5\text{+}1)^{-\cdot}$	$C_{26}H_{36}N_6O_{11}$	-0.2848
631.1839	631.1847	$(x_5)^{-}$	$C_{23}H_{31}N_6O_{15}$	-0.3064
634.2464	634.2235	$(b_5\text{-}1)^{-\cdot}$	$C_{27}H_{34}N_6O_{12}$	9.2706
651.2492	651.2500	$(c_5\text{-}1)^{-\cdot}$	$C_{27}H_{37}N_7O_{12}$	-0.3387

652.2569	652.2578	$(c_5)^-$	$C_{27}H_{38}N_7O_{12}$	-0.3569
715.2885	715.2661	$(z_6-1)^{-\cdot}$	$C_{28}H_{41}N_7O_{15}$	9.0636
716.2965	716.2739	$(z_6)^-$	$C_{28}H_{42}N_7O_{15}$	9.1301
721.2544	721.2555	$(a_6-1)^{-\cdot}$	$C_{30}H_{39}N_7O_{14}$	-0.4393
722.2624	722.2633	$(a_6)^-$	$C_{30}H_{40}N_7O_{14}$	-0.3728
723.2722	723.2711	$(a_6+1)^{-\cdot}$	$C_{30}H_{41}N_7O_{14}$	0.4320
732.2915	732.2926	$(y_6-1)^{-\cdot}$	$C_{28}H_{44}N_8O_{15}$	-0.4529
733.29893	733.3004	$(y_6)^-$	$C_{28}H_{45}N_8O_{15}$	-0.6083
749.2729	749.2504	$(b_6-1)^{-\cdot}$	$C_{31}H_{39}N_7O_{15}$	9.0999
759.2785	759.2797	$(x_6)^-$	$C_{29}H_{43}N_8O_{16}$	-0.4891
760.2859	760.2875	$(x_6+1)^{-\cdot}$	$C_{29}H_{44}N_8O_{16}$	-0.6767
761.2953	761.2953	$(x_6+2)^-$	$C_{29}H_{45}N_8O_{16}$	-0.0009
766.2783	766.2769	$(c_6-1)^{-\cdot}$	$C_{31}H_{42}N_8O_{15}$	0.5476
767.2834	767.2848	$(c_6)^-$	$C_{31}H_{43}N_8O_{15}$	-0.5397
837.2890	837.2903	$(a_7)^-$	$C_{34}H_{45}N_8O_{17}$	-0.4950
838.2963	838.2980	$(a_7+1)^{-\cdot}$	$C_{34}H_{46}N_8O_{17}$	-0.7068
864.2765	864.2774	$(b_7-1)^{-\cdot}$	$C_{35}H_{44}N_8O_{18}$	-0.3536
865.2866	865.2852	$(b_7)^-$	$C_{35}H_{45}N_8O_{18}$	0.5561
878.3293	878.3294	$(z_7-1)^{-\cdot}$	$C_{37}H_{50}N_8O_{17}$	-0.0574
879.3587	879.3372	$(z_7)^-$	$C_{37}H_{51}N_8O_{17}$	8.6466
881.3027	881.3039	$(c_7-1)^{-\cdot}$	$C_{35}H_{49}N_9O_{18}$	-0.4783
882.3102	882.3117	$(c_7)^-$	$C_{35}H_{48}N_9O_{18}$	-0.6175
894.3471	894.3481	$(y_7-2)^-$	$C_{37}H_{54}N_9O_{17}$	-0.4140
895.3538	895.3559	$(y_7-1)^{-\cdot}$	$C_{37}H_{53}N_9O_{17}$	-0.8800
921.3364	921.3352	$(x_7-1)^{-\cdot}$	$C_{38}H_{51}N_9O_{18}$	0.4656
922.3421	922.3430	$(x_7)^-$	$C_{38}H_{52}N_9O_{18}$	-0.3594

Table A2.4 Exact masses and assignments of neutral loss detected in the UVPD of doubly-deprotonated (*m/z* 505.1906) of DYKDDDDK $[M-2H]^{2-}$.

Experimental *m/z*	Theoretical *m/z*	Assignment	Chemical Composition	Mass Difference (ppm)
1010.3812	1010.3829	$[M-2H]^{-\bullet}$	$C_{41}H_{58}N_{10}O_{20}$	-0.6656
992.3709	992.3718	$[M-2H-H_2O]^{-}$	$C_{41}H_{56}N_{10}O_{19}$	-0.3674
982.3857	982.3874	$[M-2H-CO]^{-\bullet}$	$C_{40}H_{58}N_{10}O_{19}$	-0.6780
966.3913	966.3925	$[M-2H-CO_2]^{-}$	$C_{40}H_{58}N_{10}O_{18}$	-0.4866
948.3803	948.3819	$[M-2H-(CO_2+H_2O)]^{-}$	$C_{40}H_{56}N_{10}O_{17}$	-0.6824
939.3099	939.3088	$[M-2H-C_4H_9N]^{-\bullet}$	$C_{37}H_{49}N_9O_{20}$	0.4453
938.3961	938.3612	$[M-2H-C_3H_4O_2]^{-}$	$C_{38}H_{54}N_{10}O_{18}$	14.0692
922.4019	922.4027	$[M-2H-2CO_2]^{-}$	$C_{39}H_{58}N_{10}O_{16}$	-0.3296
922.3441	922.3425	$[M-2H-C_3H_6O_2N]^{-}$	$C_{38}H_{52}N_9O_{18}$	0.6608
910.3076	910.2823	$[M-2H-C_5H_{12}N_2]^{-}$	$C_{36}H_{46}N_8O_{20}$	10.1959
878.4116	878.4128	$[M-2H-3CO_2]^{-}$	$C_{38}H_{58}N_{10}O_{14}$	-0.5074
904.3394	904.3405	$[M-2H-(OC_6H_4{=}CH_2)]^{-}$	$C_{34}H_{52}N_{10}O_{19}$	-0.4238
903.3321	903.3326	$[M-2H-(HOC_6H_4{=}CH_2)]^{-}$	$C_{34}H_{51}N_{10}O_{19}$	-0.2201
886.3281	886.3213	$[x_7-2H_2O]^{-}$	$C_{38}H_{48}N_9O_{16}$	2.7382
878.3516	878.3526	$[x_7-CO_2]^{-}$	$C_{37}H_{52}N_9O_{16}$	-0.4247
860.3502	860.3421	$[x_7-(H_2O+CO_2)]^{-}$	$C_{37}H_{50}N_9O_{15}$	3.2927
820.2853	820.2869	$[a_7+1-H_2O]^{-\bullet}$	$C_{34}H_{44}N_8O_{16}$	-0.6650
819.2776	819.2791	$[a_7-H_2O]^{-}$	$C_{34}H_{43}N_8O_{16}$	-0.6267
793.2991	793.2999	$[a_7-CO_2]^{-}$	$C_{33}H_{45}N_8O_{15}$	-0.3062
714.2574	714.2815	$[x_6-COOH]^{-\bullet}$	$C_{28}H_{42}N_8O_{14}$	-9.7102
563.2456	563.2460	$[y_5-COO]^{-}$	$C_{25}H_{35}N_6O_9$	-0.1707
559.1989	559.1994	$[y_5-1-COOH]^{-\bullet}$	$C_{21}H_{31}N_6O_{12}$	-0.1883
505.1908	505.1912	$[M-2H]^{2-}$	$C_{41}H_{58}N_{10}O_{20}$	-0.1402
496.1855	496.1859	$[M-2H-H_2O]^{2-}$	$C_{41}H_{56}N_{10}O_{19}$	-0.1555
491.1933	491.1937	$[M-2H-CO]^{2-\bullet}$	$C_{39}H_{58}N_{10}O_{17}$	-0.1776
487.1801	487.1814	$[M-2H-2H_2O]^{2-}$	$C_{41}H_{54}N_{10}O_{18}$	-0.5527
483.1955	483.1971	$[M-2H-CO_2]^{2-}$	$C_{40}H_{58}N_{10}O_{18}$	-0.6334
341.1216	341.0979	$[z_3-NH_3]^{-}$	$C_{14}H_{17}N_2O_8$	9.5572
340.1138	340.0901	$[z_3-1-NH_3]^{-\bullet}$	$C_{14}H_{16}N_2O_8$	9.5451
314.1347	314.1585	$[x_3+1-2CO_2]^{-\bullet}$	$C_{13}H_{22}N_4O_5$	-9.5739
225.0868	225.0869	$[z_2-H_2O]^{-}$	$C_{10}H_{13}N_2O_4$	-0.0780
199.1074	199.1077	$[z_2-CO_2]^{-}$	$C_9H_{15}N_2O_3$	-0.1447

181.0967	181.0971	$[z_2-(H_2O+CO_2)]^-$	$C_9H_{13}N_2O_2$	-0.1873

Table A2.5 Exact masses and assignments of ions from backbone dissociation detected in the UVPD of doubly-deprotonated (*m/z* 499.2393) of RGDSPASSKP $[M-2H]^{2-}$.

Experimental *m/z*	Theoretical *m/z*	Assignment	Chemical Composition	Mass Difference (ppm)
112.0390	112.0398	$(y_1-2)^-$	$C_5H_6NO_2$	-0.3443
114.0546	114.0555	$(y_1)^-$	$C_5H_8NO_2$	-0.3443
139.0499	139.0269	$(x_1-1)^{-\cdot}$	$C_6H_5NO_3$	9.2655
140.0339	140.0348	$(x_1)^-$	$C_6H_6NO_3$	-0.3421
141.0418	141.0426	$(x_1+1)^{-\cdot}$	$C_6H_7NO_3$	-0.3361
155.0813	155.0933	$(b_1)^-$	$C_6H_{11}N_4O$	-4.8315
172.1192	172.1198	$(c_1)^-$	$C_6H_{14}N_5O$	-0.2683
184.1080	184.1198	$(a_2)^-$	$C_7H_{14}N_5O$	-4.7625
185.1033	185.1277	$(a_2+1)^{-\cdot}$	$C_7H_{15}N_5O$	-9.8397
212.1144	212.1147	$(b_2)^-$	$C_8H_{14}N_5O_2$	-0.1572
214.1188	214.1304	$(b_2+2)^-$	$C_8H_{16}N_5O_2$	-4.6877
225.1237	225.1239	$(z_2)^-$	$C_{11}H_{17}N_2O_3$	-0.0958
226.1315	226.1317	$(z_2+1)^{-\cdot}$	$C_{11}H_{18}N_2O_3$	-0.0897
227.1253	227.1396	$(c_2-2)^-$	$C_8H_{16}N_6O_2$	-5.7478
229.1411	229.1413	$(c_2)^-$	$C_8H_{17}N_6O_2$	-0.0923
240.1347	240.1348	$(y_2-2)^-$	$C_{11}H_{18}N_3O_3$	-0.0591
241.1424	241.1426	$(y_2-1)^{-\cdot}$	$C_{11}H_{19}N_3O_3$	-0.0772
242.1504	242.1505	$(y_2)^-$	$C_{11}H_{20}N_3O_3$	-0.0389
268.1298	268.1297	$(x_2)^-$	$C_{12}H_{18}N_3O_4$	0.0278
269.1251	269.1376	$(x_2+1)^{-\cdot}$	$C_{12}H_{19}N_3O_4$	-5.0372
270.1455	270.1454	$(x_2+2)^-$	$C_{12}H_{20}N_3O_4$	0.0439
299.1468	299.1468	$(a_3)^-$	$C_{11}H_{19}N_6O_4$	0.0129
300.1546	300.1546	$(a_3+1)^{-\cdot}$	$C_{11}H_{20}N_6O_4$	0.0189
301.1625	301.1624	$(a_3+2)^-$	$C_{11}H_{21}N_6O_4$	0.0128
311.1483	311.1481	$(z_3-1)^{-\cdot}$	$C_{14}H_{21}N_3O_5$	0.0602
312.1561	312.1559	$(z_3)^-$	$C_{14}H_{22}N_3O_5$	0.0622
326.1466	326.1339	$(b_3-1)^{-\cdot}$	$C_{12}H_{18}N_6O_5$	5.1204
327.1418	327.1417	$(b_3)^-$	$C_{12}H_{19}N_6O_5$	0.0392
329.1826	329.1825	$(y_3)^-$	$C_{14}H_{25}N_4O_5$	0.0464
342.1527	342.1526	$(c_3-2)^-$	$C_{12}H_{20}N_7O_5$	0.0356
343.1605	343.1604	$(c_3-1)^{-\cdot}$	$C_{12}H_{21}N_7O_5$	0.0416
344.1683	344.1682	$(c_3)^-$	$C_{12}H_{22}N_7O_5$	0.0235
355.1618	355.1618	$(x_3)^-$	$C_{15}H_{23}N_4O_6$	0.0325
356.1694	356.1696	$(x_3+1)^{-\cdot}$	$C_{15}H_{24}N_4O_6$	-0.0825
357.1764	357.1774	$(x_3+2)^-$	$C_{15}H_{25}N_4O_6$	-0.4032
386.1791	386.1788	$(a_4)^-$	$C_{14}H_{24}N_7O_6$	0.1063

387.1868	387.1866	$(a_4+1)^{-\cdot}$	$C_{14}H_{25}N_7O_6$	0.0760
388.1947	388.1945	$(a_4+2)^{-}$	$C_{14}H_{26}N_7O_6$	0.0982
399.1880	399.1879	$(z_4)^{-}$	$C_{17}H_{27}N_4O_7$	0.0306
400.1959	400.1958	$(z_4+1)^{-\cdot}$	$C_{17}H_{28}N_4O_7$	0.0366
414.1739	414.1737	$(b_4)^{-}$	$C_{15}H_{24}N_7O_7$	0.0923
415.1818	415.1815	$(b_4+1)^{-\cdot}$	$C_{15}H_{25}N_7O_7$	0.0984
416.1896	416.1894	$(b_4+2)^{-}$	$C_{15}H_{26}N_7O_7$	0.1004
441.1861	441.1859	$(x_4-1)^{-\cdot}$	$C_{18}H_{27}N_5O_8$	0.0634
442.1940	442.1938	$(x_4)^{-}$	$C_{18}H_{28}N_5O_8$	0.0856
443.2018	443.2016	$(x_4+1)^{-\cdot}$	$C_{18}H_{29}N_5O_8$	0.0674
470.2251	470.2251	$(z_5)^{-}$	$C_{20}H_{32}N_5O_8$	-0.0073
471.2330	471.2329	$(z_5+1)^{-\cdot}$	$C_{20}H_{33}N_5O_8$	0.0391
483.2319	483.2316	$(a_5)^{-}$	$C_{19}H_{31}N_8O_7$	0.1209
484.2337	484.2394	$(a_5+1)^{-\cdot}$	$C_{19}H_{32}N_8O_7$	-2.2936
485.2429	485.2472	$(a_5+2)^{-}$	$C_{19}H_{32}N_8O_7$	-1.7511
486.2441	486.2438	$(y_5-1)^{-\cdot}$	$C_{20}H_{35}N_6O_8$	0.1202
487.2521	487.2516	$(y_5)^{-}$	$C_{20}H_{34}N_6O_8$	0.1746
511.2155	511.2265	$(b_5)^{-}$	$C_{20}H_{31}N_8O_8$	-4.4115
512.2232	512.2343	$(b_5+1)^{-\cdot}$	$C_{20}H_{32}N_8O_8$	-4.4982
513.2310	513.2309	$(x_5)^{-}$	$C_{21}H_{33}N_6O_9$	0.0558
528.2534	528.2530	$(c_5)^{-}$	$C_{20}H_{34}N_9O_8$	0.1476
529.2625	529.2609	$(c_5+1)^{-\cdot}$	$C_{20}H_{35}N_9O_8$	0.6619
553.2618	553.2607	$(a_6-1)^{-\cdot}$	$C_{22}H_{35}N_9O_8$	0.3675
554.2689	554.2687	$(a_6)^{-}$	$C_{22}H_{36}N_9O_8$	0.0871
555.2766	555.2765	$(a_6+1)^{-\cdot}$	$C_{22}H_{37}N_9O_8$	0.0407
567.2784	567.2778	$(z_6)^{-}$	$C_{25}H_{39}N_6O_9$	0.2213
568.2723	568.2857	$(z_6+1)^{-\cdot}$	$C_{25}H_{40}N_6O_9$	-5.4128
569.2802	569.2935	$(z_6+2)^{-}$	$C_{25}H_{41}N_6O_9$	-5.3623
582.2892	582.2887	$(y_6-2)^{-}$	$C_{25}H_{40}N_7O_9$	0.1973
583.2971	583.2966	$(y_6-1)^{-\cdot}$	$C_{25}H_{41}N_7O_9$	0.1993
584.3047	584.3044	$(y_6)^{-}$	$C_{25}H_{42}N_7O_9$	0.1247
597.2752	597.2745	$(c_6-2)^{-}$	$C_{23}H_{37}N_{10}O_9$	0.2712
598.2831	598.2823	$(c_6-1)^{-\cdot}$	$C_{23}H_{38}N_{10}O_9$	0.3014
599.2907	599.2901	$(c_6)^{-}$	$C_{23}H_{39}N_{10}O_9$	0.2348
610.2845	610.2837	$(x_6)^{-}$	$C_{26}H_{40}N_7O_{10}$	0.3367
611.2918	611.2915	$(x_6+1)^{-\cdot}$	$C_{26}H_{41}N_7O_{10}$	0.1087
612.2993	612.2993	$(x_6+2)^{-}$	$C_{26}H_{42}N_7O_{10}$	0.0098
641.3017	641.3007	$(a_7)^{-}$	$C_{25}H_{41}N_{10}O_{10}$	0.4064
642.3091	642.3085	$(a_7+1)^{-\cdot}$	$C_{25}H_{42}N_{10}O_{10}$	0.2309
643.3171	643.3164	$(a_7+2)^{-}$	$C_{25}H_{43}N_{10}O_{10}$	0.2813
653.3027	653.3021	$(z_7-1)^{-\cdot}$	$C_{28}H_{43}N_7O_{11}$	0.2682
654.3105	654.3099	$(z_7)^{-}$	$C_{28}H_{44}N_7O_{11}$	0.2419
655.3183	655.3177	$(z_7+1)^{-\cdot}$	$C_{28}H_{45}N_7O_{11}$	0.2318
656.3124	656.3255	$(z_7+2)^{-}$	$C_{28}H_{46}N_7O_{11}$	-5.2971
669.3214	669.3208	$(y_7-2)^{-}$	$C_{28}H_{45}N_8O_{11}$	0.2625
670.3293	670.3286	$(y_7-1)^{-\cdot}$	$C_{28}H_{46}N_8O_{11}$	0.2806

671.3371	671.3364	$(y_7)^-$	$C_{28}H_{47}N_8O_{11}$	0.2827
684.3073	684.3065	$(c_7-2)^-$	$C_{26}H_{42}N_{11}O_{11}$	0.2960
685.3149	685.3143	$(c_7-1)^{-\cdot}$	$C_{26}H_{43}N_{11}O_{11}$	0.2254
686.3226	686.3222	$(c_7)^-$	$C_{26}H_{44}N_{11}O_{11}$	0.1911
695.3001	695.3000	$(x_7-2)^-$	$C_{29}H_{43}N_8O_{12}$	0.0089
696.3084	696.3079	$(x_7-1)^{-\cdot}$	$C_{29}H_{44}N_8O_{12}$	0.2022
697.3161	697.3157	$(x_7)^-$	$C_{29}H_{45}N_8O_{12}$	0.1719
698.3236	698.3235	$(x_7+1)^{-\cdot}$	$C_{29}H_{46}N_8O_{12}$	0.0529
699.3314	699.3313	$(x_7+2)^-$	$C_{29}H_{47}N_8O_{12}$	0.0145
728.3337	728.3327	$(a_8)^-$	$C_{28}H_{46}N_{11}O_{12}$	0.3909
729.3417	729.3406	$(a_8+1)^{-\cdot}$	$C_{28}H_{47}N_{11}O_{12}$	0.4413
730.3494	730.3484	$(a_8+2)^-$	$C_{28}H_{48}N_{11}O_{12}$	0.3909
755.3087	755.3198	$(b_8-1)^{-\cdot}$	$C_{29}H_{45}N_{11}O_{13}$	-4.4984
756.3160	756.3277	$(b_8)^-$	$C_{29}H_{46}N_{11}O_{13}$	-4.6901
767.3457	767.3212	$(z_8-2)^-$	$C_{32}H_{47}N_8O_{14}$	9.8827
768.3531	768.3290	$(z_8-1)^{-\cdot}$	$C_{32}H_{48}N_8O_{14}$	9.7395
769.3361	769.3368	$(z_8)^-$	$C_{32}H_{49}N_8O_{14}$	-0.2837
771.3389	771.3385	$(c_8-2)^-$	$C_{29}H_{47}N_{12}O_{13}$	0.1272
772.3465	772.3464	$(c_8-1)^{-\cdot}$	$C_{29}H_{48}N_{12}O_{13}$	0.0647
773.3546	773.3542	$(c_8)^-$	$C_{29}H_{49}N_{12}O_{13}$	0.1514
784.3483	784.3477	$(y_8-2)^-$	$C_{32}H_{50}N_9O_{14}$	0.2452
785.3564	785.3555	$(y_8-1)^{-\cdot}$	$C_{32}H_{51}N_9O_{14}$	0.3359
786.3650	786.3634	$(y_8)^-$	$C_{32}H_{52}N_9O_{14}$	0.6647
811.3353	811.3348	$(x_8-1)^{-\cdot}$	$C_{33}H_{49}N_9O_{15}$	0.2049
812.3433	812.3426	$(x_8)^-$	$C_{33}H_{50}N_9O_{15}$	0.2796
825.3753	825.3505	$(z_9-1)^{-\cdot}$	$C_{34}H_{51}N_9O_{15}$	10.0083
826.3604	826.3583	$(z_9)^-$	$C_{34}H_{52}N_9O_{15}$	0.8524
827.3673	827.3661	$(z_9+1)^{-\cdot}$	$C_{34}H_{53}N_9O_{15}$	0.4672
841.3696	841.3692	$(y_9-2)^-$	$C_{34}H_{53}N_{10}O_{15}$	0.1791
842.3775	842.3770	$(y_9-1)^{-\cdot}$	$C_{34}H_{54}N_{10}O_{15}$	0.2053
843.3848	843.3848	$(y_9)^-$	$C_{34}H_{55}N_{10}O_{15}$	-0.0146
855.4221	855.4199	$(a_9-1)^{-\cdot}$	$C_{34}H_{57}N_{13}O_{13}$	0.8960
856.4281	856.4277	$(a_9)^-$	$C_{34}H_{58}N_{13}O_{13}$	0.1396
857.4357	857.4355	$(a_9+1)^{-\cdot}$	$C_{34}H_{59}N_{13}O_{13}$	0.0689
858.4437	858.4433	$(a_9+2)^-$	$C_{34}H_{60}N_{13}O_{13}$	0.1436
868.3570	868.3563	$(x_9-1)^{-\cdot}$	$C_{35}H_{52}N_{10}O_{16}$	0.3043
869.3647	869.3641	$(x_9)^-$	$C_{35}H_{53}N_{10}O_{16}$	0.2418
870.3723	870.3719	$(x_9+1)^{-\cdot}$	$C_{35}H_{54}N_{10}O_{16}$	0.1349
883.4153	883.4148	$(b_9-1)^{-\cdot}$	$C_{35}H_{57}N_{13}O_{14}$	0.2124
884.4231	884.4226	$(b_9)^-$	$C_{35}H_{58}N_{13}O_{14}$	0.1902
885.4307	885.4304	$(b_9+1)^{-\cdot}$	$C_{35}H_{59}N_{13}O_{14}$	0.1236
886.4387	886.4383	$(b_9+2)^-$	$C_{35}H_{60}N_{13}O_{14}$	0.1861
900.4183	900.4413	$(c_9-1)^{-\cdot}$	$C_{35}H_{60}N_{14}O_{14}$	-9.2759
901.4257	901.4492	$(c_9)^-$	$C_{35}H_{61}N_{14}O_{14}$	-9.4716
902.4337	902.4569	$(c_9+1)^{-\cdot}$	$C_{35}H_{62}N_{14}O_{14}$	-9.3808

Table A2.6 Exact masses and assignments of neutral loss detected in the UVPD of doubly-deprotonated (*m/z* 499.2393) of RGDSPASSKP $[M\text{-}2H]^{2-}$.

Experimental *m/z*	Theoretical *m/z*	Assignments	Chemical Composition	Mass Difference (ppm)
998.4767	998.4776	$[M\text{-}2H]^{-\bullet}$	$C_{40}H_{66}N_{14}O_{16}$	-0.3643
980.4673	980.4670	$[M\text{-}2H\text{-}H_2O]^{-}$	$C_{40}H_{64}N_{14}O_{15}$	0.1216
968.4672	968.4670	$[M\text{-}2H\text{-}CH_2O]^{-\bullet}$	$C_{39}H_{64}N_{14}O_{15}$	0.0611
954.4872	954.4877	$[M\text{-}2H\text{-}CO_2]^{-}$	$C_{39}H_{66}N_{14}O_{14}$	-0.2218
938.4227	938.4326	$[M\text{-}2H\text{-}C_2H_6ON]^{-}$	$C_{38}H_{60}N_{13}O_{15}$	-4.0060
912.4072	912.4057	$[M\text{-}2H\text{-}C_3H_8N_3]^{-}$	$C_{37}H_{57}N_{11}O_{16}$	0.5365
899.3982	899.3979	$[M\text{-}2H\text{-}C_4H_9N_3]^{-}$	$C_{36}H_{57}N_{11}O_{16}$	0.1210
910.4269	910.4377	$[M\text{-}2H\text{-}C_3H_6O_2N]^{-}$	$C_{37}H_{60}N_{13}O_{14}$	-4.3368

Table A3.1 Exact masses and assignments of ions detected by IRMPD of the +12 charge state precursor ion (*m/z*=714.7279) of ubiquitin.

Serial	Experimental *m/z*	Experimental Mass (Da)	Theoretical Mass (Da)	Assignment	Mass Difference (ppm)
1	619.3269	618.3196	618.3200	$(b_5)^+$	-0.1412
2	442.2950	882.5755	882.5763	$(y_8)^{2+}$	-0.3207
3	472.2755	942.5364	942.5366	$(b_8\text{-}H_2O)^{2+}$	-0.0943
4	961.5536	960.5464	960.5467	$(b_8)^+$	-0.1009
5	510.8247	1019.6348	1019.6352	$(y_9)^{2+}$	-0.1634
6	1062.6016	1061.5943	1061.5943	$(b_9)^+$	-0.0121
7	1119.6230	1118.6158	1118.6158	$(b_{10})^+$	0.0040
8	567.3669	1132.7192	1132.7193	$(y_{10})^{2+}$	-0.0262
9	1247.7173	1246.7100	1246.7108	$(b_{11})^+$	-0.3026
10	624.3626	1246.7107	1246.7108	$(b_{11})^{2+}$	-0.0202
11	652.4030	1302.7915	1302.7890	$(y_{12}\text{-}H_2O)^{2+}$	1.0252
12	441.2731	1320.7976	1320.7990	$(y_{12})^{3+}$	-0.5547
13	674.8868	1347.7591	1347.7584	$(b_{12})^{2+}$	0.2703
14	716.9240	1431.8334	1431.8315	$(y_{13}\text{-}H_2O)^{2+}$	0.7469
15	478.2837	1431.8292	1431.8315	$(y_{13}\text{-}H_2O)^{3+}$	-0.9475
16	722.4239	1442.8332	1442.8325	$(b_{13}\text{-}H_2O)^{2+}$	0.2930
17	481.9510	1442.8313	1442.8325	$(b_{13}\text{-}H_2O)^{3+}$	-0.4735
18	484.2872	1449.8398	1449.8416	$(y_{13})^{3+}$	-0.7121
19	731.4271	1460.8396	1460.8425	$(b_{13})^{2+}$	-1.1659
20	772.9465	1543.8785	1543.8802	$(b_{14}\text{-}H_2O)^{2+}$	-0.6672
21	780.9623	1559.9100	1559.9265	$(y_{14}\text{-}H_2O)^{2+}$	-6.6601
22	781.9514	1561.8882	1561.8902	$(b_{14})^{2+}$	-0.7948
23	526.9856	1577.9351	1577.9365	$(y_{14})^{3+}$	-0.5749
24	553.3282	1656.9626	1656.9642	$(b_{15}\text{-}H_2O)^{3+}$	-0.6510
25	829.4881	1656.9617	1656.9642	$(b_{15}\text{-}H_2O)^{2+}$	-1.0141
26	838.4936	1674.9727	1674.9742	$(b_{15})^{2+}$	-0.6172
27	845.4823	1688.9501	1688.9686	$(y_{15}\text{-}NH_3)^{2+}$	-7.4531
28	563.9960	1688.9663	1688.9686	$(y_{15}\text{-}NH_3)^{3+}$	-0.9175
29	596.3423	1786.0052	1786.0068	$(b_{16}\text{-}H_2O)^{3+}$	-0.6470
30	894.0103	1786.0061	1786.0068	$(b_{16}\text{-}H_2O)^{2+}$	-0.2839
31	602.3461	1804.0166	1804.0168	$(b_{16})^{3+}$	-0.0888
32	903.0156	1804.0167	1804.0168	$(b_{16})^{2+}$	-0.0484
33	607.3666	1819.0781	1819.0792	$(y_{16})^{3+}$	-0.4297
34	472.2755	1885.0727	1885.0752	$(b_{17}\text{-}H_2O)^{4+}$	-1.0141
35	943.5444	1885.0743	1885.0752	$(b_{17}\text{-}H_2O)^{2+}$	-0.3686
36	629.3654	1885.0743	1885.0752	$(b_{17}\text{-}H_2O)^{3+}$	-0.3686
37	952.5470	1903.0795	1903.0852	$(b_{17})^{2+}$	-2.3116
38	476.7772	1903.0799	1903.0852	$(b_{17})^{4+}$	-2.1503
39	635.3695	1903.0867	1903.0852	$(b_{17})^{3+}$	0.5930
40	672.3803	2014.1191	2014.1178	$(b_{18}\text{-}H_2O)^{3+}$	0.5230
41	1008.0658	2014.1171	2014.1178	$(b_{18}\text{-}H_2O)^{2+}$	-0.2839

42	509.0387	2032.1258	2032.1278	$(b_{18})^{4+}$	-0.8149
43	1017.0706	2032.1267	2032.1278	$(b_{18})^{2+}$	-0.4518
44	693.7323	2078.1752	2078.1754	$(y_{18}\text{-}H_2O)^{3+}$	-0.0842
45	694.0634	2079.1682	2079.1594	$(y_{18}\text{-}NH_3)^{3+}$	3.5404
46	520.8014	2079.1765	2079.1594	$(y_{18}\text{-}NH_3)^{4+}$	6.8888
47	525.0534	2096.1843	2096.1854	$(y_{18})^{4+}$	-0.4539
48	1049.1000	2096.1854	2096.1854	$(y_{18})^{2+}$	-0.0101
49	699.7359	2096.1859	2096.1854	$(y_{18})^{3+}$	0.1916
50	575.3171	2297.2394	2297.2366	$(y_{20}\text{-}1)^{4+}$	1.1417
51	668.1270	2668.4788	2668.4772	$(y_{23})^{4+}$	0.6273
52	542.5047	2707.4871	2707.4887	$(y_{24}\text{-}H_2O)^{5+}$	-0.6409
53	909.5066	2725.4981	2725.4987	$(y_{24})^{3+}$	-0.2441
54	546.1070	2725.4988	2725.4987	$(y_{24})^{5+}$	0.0383
55	682.3843	2725.5082	2725.4987	$(y_{24})^{4+}$	3.8306
56	565.5108	2822.5175	2822.5156	$(y_{25}\text{-}H_2O)^{5+}$	0.7549
57	569.1123	2840.5249	2840.5256	$(y_{25})^{5+}$	-0.3006
58	711.1390	2840.5270	2840.5256	$(y_{25})^{4+}$	0.5466
59	771.6700	3082.6509	3082.6523	$(y_{27})^{4+}$	-0.5628
60	639.5475	3192.7011	3192.7009	$(y_{28}\text{-}H_2O)^{5+}$	0.0973
61	533.1234	3192.6967	3192.7009	$(y_{28}\text{-}H_2O)^{6+}$	-1.6777
62	799.4320	3193.6989	3193.6849	$(y_{28}\text{-}NH_3)^{4+}$	5.6584
63	643.1498	3210.7128	3210.7109	$(y_{28})^{5+}$	0.7766
64	694.1793	3465.8612	3465.8566	$(y_{31}\text{-}1)^{5+}$	1.8639
65	723.5956	3612.9375	3612.9250	$(y_{32}\text{-}1)^{5+}$	5.0469
66	925.7614	3699.0166	3699.0168	$(b_{33})^{4+}$	-0.0767
67	1000.5507	3998.1737	3998.1649	$(b_{36})^{4+}$	3.5502
68	847.8688	4234.3078	4234.3092	$(y_{37}\text{-}H_2O)^{5+}$	-0.5602
69	706.7258	4234.3113	4234.3092	$(y_{37}\text{-}H_2O)^{6+}$	0.8518
70	605.9086	4234.3089	4234.3092	$(y_{37}\text{-}H_2O)^{7+}$	-0.1165
71	851.4708	4252.3176	4252.3192	$(y_{37})^{5+}$	-0.6475
72	608.4812	4252.3177	4252.3192	$(y_{37})^{7+}$	-0.6072
73	709.7283	4252.3262	4252.3192	$(y_{37})^{6+}$	2.8220
74	862.4674	4307.3006	4307.2974	$(b_{39})^{5+}$	1.3071
75	745.0730	4464.3945	4464.3989	$(y_{39})^{6+}$	-1.7771
76	913.2980	4561.4537	4561.4517	$(y_{40})^{5+}$	0.8210
77	652.6437	4561.4547	4561.4517	$(y_{40})^{7+}$	1.2244
78	571.1881	4561.4547	4561.4517	$(y_{40})^{8+}$	1.2244
79	789.6001	4731.5568	4731.5572	$(y_{42})^{6+}$	-0.1553
80	808.1062	4842.5936	4842.5898	$(y_{43}\text{-}H_2O)^{6+}$	1.5497
81	969.5244	4842.5856	4842.5898	$(y_{43}\text{-}H_2O)^{5+}$	-1.6777
82	692.8055	4842.5877	4842.5898	$(y_{43}\text{-}H_2O)^{7+}$	-0.8305
83	973.1268	4860.5978	4860.5998	$(y_{43})^{5+}$	-0.7968
84	811.1087	4860.6087	4860.5998	$(y_{43})^{6+}$	3.6006
85	990.1455	4945.6909	4945.6838	$(b_{44})^{5+}$	2.8845
86	832.4553	4988.6881	4988.6947	$(y_{44})^{6+}$	-2.6768
87	995.1429	4970.6780	4970.6847	$(y_{44}\text{-}H_2O)^{5+}$	-2.7105

88	713.6781	4988.6955	4988.6947	$(y_{44})^{7+}$	0.3086
89	998.7464	4988.6958	4988.6947	$(y_{44})^{5+}$	0.4297
90	624.5949	4988.7011	4988.6947	$(y_{44})^{8+}$	2.5678
91	1019.5578	5092.7542	5092.7522	$(b_{45})^{5+}$	0.8230
92	1033.7586	5163.7818	5163.7893	$(b_{46})^{5+}$	-3.0136
93	891.8188	5344.8673	5344.8643	$(y_{47})^{6+}$	1.2042
94	669.1164	5344.8692	5344.8643	$(y_{47})^{8+}$	1.9707
95	782.8556	5472.9547	5472.9593	$(y_{48})^{7+}$	-1.8457
96	694.0061	5543.9936	5543.9964	$(y_{49})^{8+}$	-1.1235
97	793.0071	5543.9990	5543.9964	$(y_{49})^{7+}$	1.0550
98	797.1548	5573.0319	5573.0219	$(b_{50}\text{-}NH_3)^{7+}$	4.0447
99	728.0168	5816.0763	5816.1078	$(b_{52}\text{-}H_2O)^{8+}$	-12.7256
100	834.4510	5834.1059	5834.1179	$(b_{52})^{7+}$	-4.8250
101	973.3599	5834.1156	5834.1179	$(b_{52})^{6+}$	-0.9117
102	734.4072	5867.1996	5867.1927	$(y_{52}\text{-}H_2O)^{8+}$	2.7963
103	841.7505	5885.2023	5885.2027	$(y_{52})^{7+}$	-0.1553
104	736.6576	5885.2029	5885.2027	$(y_{52})^{8+}$	0.0867
105	654.9188	5885.2041	5885.2027	$(y_{52})^{9+}$	0.5709
106	750.5386	5996.2509	5996.2353	$(y_{53}\text{-}H_2O)^{8+}$	6.3102
107	669.2568	6014.2439	6014.2453	$(y_{53})^{9+}$	-0.5547
108	752.7878	6014.2493	6014.2453	$(y_{53})^{8+}$	1.6238
109	860.1852	6014.2497	6014.2453	$(y_{53})^{7+}$	1.7852
110	888.2028	6210.3680	6210.3670	$(y_{55}\text{-}H_2O)^{7+}$	0.4040
111	777.3024	6210.3632	6210.3670	$(y_{55}\text{-}H_2O)^{8+}$	-1.5325
112	890.7747	6228.3719	6228.3770	$(y_{55})^{7+}$	-2.0635
113	779.5545	6228.3775	6228.3770	$(y_{55})^{8+}$	0.1957
114	693.0497	6228.3814	6228.3770	$(y_{55})^{9+}$	1.7690
115	791.6810	6325.3978	6325.3939	$(y_{56}\text{-}H_2O)^{8+}$	1.5578
116	793.9322	6343.3994	6343.4040	$(y_{56})^{8+}$	-1.8376
117	907.2074	6343.4006	6343.4040	$(y_{56})^{7+}$	-1.3535
118	705.8309	6343.4126	6343.4040	$(y_{56})^{9+}$	3.4876
119	642.2506	6412.4331	6412.4260	$(y_{57}\text{-}H_2O)^{10+}$	2.8770
120	715.5004	6430.4379	6430.4360	$(y_{57})^{9+}$	0.7726
121	804.8127	6430.4422	6430.4360	$(y_{57})^{8+}$	2.5073
122	930.9321	6509.4734	6509.4787	$(y_{58}\text{-}H_2O)^{7+}$	-2.1498
123	814.6934	6509.4887	6509.4787	$(y_{58}\text{-}H_2O)^{8+}$	4.0227
124	724.2860	6509.5082	6509.4787	$(y_{58}\text{-}H_2O)^{9+}$	11.8896
125	651.9559	6509.4864	6509.4787	$(y_{58}\text{-}H_2O)^{10+}$	3.0948
126	933.5059	6527.4907	6527.4887	$(y_{58})^{7+}$	0.7887
127	653.7569	6527.4959	6527.4887	$(y_{58})^{10+}$	2.8865
128	816.9452	6527.5037	6527.4887	$(y_{58})^{8+}$	6.0333
129	726.2875	6527.5220	6527.4887	$(y_{58})^{9+}$	13.4160
130	830.8218	6638.5165	6638.5209	$(y_{59}\text{-}H_2O)^{8+}$	-1.7584
131	738.6202	6638.5166	6638.5209	$(y_{59}\text{-}H_2O)^{9+}$	-1.7181
132	664.8598	6638.5248	6638.5209	$(y_{59}\text{-}H_2O)^{10+}$	1.5900
133	674.7674	6737.6043	6737.5897	$(y_{60}\text{-}H_2O)^{10+}$	5.8785

134	845.4571	6755.5813	6755.5997	$(y_{60})^{8+}$	-7.4412
135	751.6300	6755.6046	6755.5997	$(y_{60})^{9+}$	1.9586
136	676.5690	6755.6176	6755.5997	$(y_{60})^{10+}$	7.2032
137	687.6700	6866.6275	6866.6319	$(y_{61}\text{-}H_2O)^{10+}$	-1.7584
138	698.9793	6979.7201	6979.7160	$(y_{62}\text{-}H_2O)^{10+}$	1.6707
139	845.3499	7599.0656	7599.0699	$(y_{68})^{9+}$	-1.7408
140	712.8100	8541.6322	8541.6056	$M\text{-}H_2O)^{12+}$	10.7413
141	777.5168	8541.6059	8541.6056	$(M\text{-}H_2O)^{11+}$	0.1311

Table A3.2 Exact masses and assignments of ions detected by UVPD of the 13+ charge state precursor ion (*m/z*=659.8249) of ubiquitin.

Serial	Experimental *m/z*	Experimental Mass (Da)	Theoretical Mass (Da)	Assignment	Mass Difference (ppm)
1	585.3273	584.3200	584.3269	$(x_5+1)^+$	-11.7315
2	636.3491	635.3418	635.3463	$(c_5)^+$	-7.0041
3	730.3975	729.3902	729.3884	$(b_6-NH_3)^+$	0.7366
4	568.3179	1134.6212	1134.6339	$(c_{10}-1)^{2+}$	-11.2371
5	493.7830	1918.1069	1918.1107	$(z_{17}+1)^{4+}$	-1.5330
6	509.0394	2032.1286	2032.1278	$(b_{18})^{4+}$	0.3838
7	521.0490	2080.1671	2080.1667	$(z_{18})^{4+}$	0.2115
8	531.8007	2123.1737	2123.1725	$(x_{18}+1)^{4+}$	0.5581
9	550.0569	2196.1985	2196.2010	$(z_{19}+1)^{4+}$	1.0086
10	553.3015	2209.1768	2209.1962	$(y_{19}-2)^{4+}$	-8.7928
11	571.3097	2281.2098	2281.2179	$(y_{20}-NH_3)^{4+}$	-3.5393
12	582.3146	2325.2294	2325.2315	$(x_{20}+1)^{4+}$	-0.8967
13	603.5877	2410.3219	2410.3206	$(y_{21}-1)^{4+}$	0.5269
14	610.3356	2437.3132	2437.3077	$(x_{21})^{4+}$	2.2484
15	624.8459	2495.3543	2495.3496	$(y_{22}-NH_3)^{4+}$	1.8939
16	531.2975	2651.4512	2651.4512	$(y_{23}-NH_3)^{5+}$	-0.0166
17	534.5014	2667.4707	2667.4694	$(y_{23}-1)^{5+}$	0.4799
18	539.8996	2694.4614	2694.4565	$(x_{23})^{5+}$	1.8148
19	540.3007	2696.4672	2696.4722	$(x_{23}+2)^{5+}$	2.0010
20	542.7035	2708.4809	2708.4727	$(y_{24}-NH_3)^{5+}$	3.0261
21	545.9058	2724.4926	2724.4909	$(y_{24}-1)^{5+}$	0.6313
22	551.5049	2752.4881	2752.4858	$(x_{24}+1)^{5+}$	0.8374
23	565.9090	2824.5085	2824.5069	$(z_{25})^{5+}$	0.5736
24	568.9111	2839.5193	2839.5178	$(y_{25}-1)^{5+}$	0.5212
25	574.5104	2867.5155	2867.5127	$(x_{25}+1)^{5+}$	0.9642
26	591.7179	2953.5529	2953.5495	$(z_{26})^{5+}$	1.1613
27	594.7201	2968.5640	2968.5604	$(y_{26}-1)^{5+}$	1.2094
28	594.9207	2969.5674	2969.5682	$(y_{26})^{5+}$	-0.2812
29	747.9096	2987.6091	2987.6253	$(a_{27})^{4+}$	-5.4107
30	600.3184	2996.5558	2996.5553	$(x_{26}+1)^{5+}$	0.1585
31	759.1652	3032.6318	3032.6465	$(c_{27})^{4+}$	-4.8407
32	771.6674	3082.6406	3082.6523	$(y_{27})^{4+}$	-3.7938
33	638.5621	3187.7743	3187.7652	$(a_{29}+1)^{5+}$	2.8672
34	554.4684	3320.7665	3320.7958	$(y_{29}-H_2O)^{6+}$	-8.8289
35	557.3090	3337.8103	3337.7980	$(y_{29}-1)^{6+}$	3.6821
36	557.4670	3338.7582	3338.8058	$(y_{29})^{6+}$	-14.2671
37	564.3095	3379.8132	3379.8085	$(z_{30})^{6+}$	1.3817
38	566.8051	3394.7869	3394.8195	$(y_{30}-1)^{6+}$	-9.5940
39	571.4766	3422.8158	3422.8144	$(x_{30}+1)^{6+}$	0.4134
40	686.7889	3428.9079	3428.9078	$(a_{31}+1)^{5+}$	0.0292
41	575.8169	3448.8578	3448.8300	$(z_{31}-2)^{6+}$	8.0636

42	576.1492	3450.8516	3450.8456	$(z_{31})^{6+}$	1.7271
43	578.6503	3465.8583	3465.8566	$(y_{31}\text{-}1)^{6+}$	0.4963
44	583.3160	3493.8523	3493.8515	$(x_{31}+1)^{6+}$	0.2304
45	718.5945	3587.9360	3587.9481	$(c_{32})^{5+}$	-3.3808
46	600.6605	3597.9192	3597.9141	$(z_{32})^{6+}$	1.4314
47	607.8281	3640.9251	3640.9199	$(x_{32}+1)^{6+}$	1.4268
48	735.4093	3672.0102	3672.0297	$(a_{33}+1)^{5+}$	-5.3104
49	613.0128	3672.0330	3672.0297	$(a_{33}+1)^{6+}$	0.8987
50	619.5079	3711.0040	3710.9981	$(z_{33})^{6+}$	1.5872
51	622.0095	3726.0133	3726.0090	$(y_{33}\text{-}1)^{6+}$	1.1406
52	626.5074	3753.0005	3752.9961	$(x_{33})^{6+}$	1.1617
53	631.5133	3783.0361	3783.0385	$(a_{34}\text{-}NH_3)^{6+}$	-0.6249
54	634.5204	3801.0786	3801.0723	$(a_{34}+1)^{6+}$	1.6600
55	638.1894	3823.0927	3823.0749	$(y_{34}\text{-}NH_3)^{6+}$	4.6470
56	768.8249	3839.0884	3839.0931	$(y_{34}\text{-}1)^{5+}$	-1.2268
57	640.8580	3839.1045	3839.0931	$(y_{34}\text{-}1)^{6+}$	2.9669
58	772.6254	3858.0904	3858.0938	$(a_{35}+1)^{5+}$	-0.8683
59	644.0256	3858.1101	3858.0938	$(a_{35}+1)^{6+}$	4.2378
60	791.6423	3953.1750	3953.1440	$(a_{36}\text{-}NH_3)^{5+}$	7.8459
61	565.7450	3953.1638	3953.1440	$(a_{36}\text{-}NH_3)^{7+}$	5.0127
62	662.8653	3971.1479	3971.1778	$(a_{36}+1)^{6+}$	-7.5318
63	568.3179	3971.1743	3971.1778	$(a_{36}+1)^{7+}$	-0.8839
64	795.2429	3971.1780	3971.1778	$(a_{36}+1)^{5+}$	0.0478
65	796.8315	3979.1210	3979.1760	$(y_{35}\text{-}NH_3)^{5+}$	-13.8330
66	571.7492	3995.1934	3995.1942	$(y_{35}\text{-}1)^{7+}$	-0.2052
67	800.4369	3997.1479	3997.2099	$(y_{35}+1)^{5+}$	-15.5033
68	671.5456	4023.2328	4023.1891	$(x_{35}+1)^{6+}$	10.8533
69	579.6100	4050.2191	4050.1967	$(a_{37}\text{-}NH_3)^{7+}$	5.5197
70	582.1800	4068.2092	4068.2306	$(a_{37}+1)^{7+}$	-5.2529
71	814.6537	4068.2319	4068.2306	$(a_{37}+1)^{5+}$	0.3269
72	679.0460	4068.2324	4068.2306	$(a_{37}+1)^{6+}$	0.4498
73	587.8996	4108.2459	4108.2419	$(z_{36})^{7+}$	0.9834
74	590.0437	4123.2546	4123.2528	$(y_{36}\text{-}2)^{7+}$	0.4366
75	594.0438	4151.2554	4151.2477	$(x_{36}+2)^{7+}$	1.8512
76	693.0507	4152.2604	4152.2555	$(x_{36}+2)^{6+}$	1.1704
77	595.8994	4164.2445	4164.2755	$(a_{38})^{7+}$	-7.4455
78	834.0613	4165.2703	4165.2833	$(a_{38}+1)^{5+}$	-3.1282
79	695.2207	4165.2807	4165.2833	$(a_{38}+1)^{6+}$	-0.6314
80	699.5472	4191.2395	4191.2626	$(b_{38}\text{-}1)^{6+}$	-5.5103
81	599.8982	4192.2361	4192.2704	$(b_{38})^{7+}$	-8.1865
82	606.1942	4236.3086	4236.3004	$(z_{37})^{7+}$	1.9262
83	608.4799	4252.3087	4252.3192	$(y_{37})^{7+}$	-2.4704
84	612.3380	4279.3152	4279.3063	$(x_{37}+1)^{7+}$	2.0809
85	618.6285	4323.3482	4323.3156	$(c_{39}\text{-}1)^{7+}$	7.5289
86	618.9110	4325.3108	4325.3313	$(c_{39}+1)^{7+}$	-4.7395
87	871.2728	4351.3278	4351.3274	$(z_{38})^{5+}$	0.0965

88	726.2288	4351.3290	4351.3274	$(z_{38})^{6+}$	0.3723
89	622.6265	4351.3349	4351.3274	$(z_{38})^{7+}$	1.7282
90	624.7706	4366.3434	4366.3383	$(y_{38}\text{-}1)^{7+}$	1.1635
91	628.6260	4393.3314	4393.3254	$(x_{38})^{7+}$	1.3634
92	733.3950	4394.3263	4394.3332	$(x_{38}+1)^{6+}$	-1.5782
93	879.8741	4394.3316	4394.3332	$(x_{38}+1)^{5+}$	-0.3721
94	735.5684	4407.3665	4407.3610	$(a_{40})^{6+}$	1.2422
95	630.6328	4407.3786	4407.3610	$(a_{40})^{7+}$	3.9876
96	632.2061	4418.3920	4418.3295	$(b_{40}\text{-}NH_3)^{7+}$	14.1515
97	636.3491	4447.3929	4447.3725	$(y_{39}\text{-}NH_3)^{7+}$	4.5928
98	637.2086	4453.4091	4453.3898	$(c_{40}+1)^{7+}$	4.3338
99	638.4930	4462.4004	4462.3833	$(y_{39}\text{-}2)^{7+}$	3.8421
100	558.8069	4462.3967	4462.3833	$(y_{39}\text{-}2)^{8+}$	0.8292
101	558.9315	4463.3936	4463.3911	$(y_{39}\text{-}1)^{8+}$	0.5646
102	749.5713	4491.3844	4491.3860	$(x_{39}+1)^{6+}$	-0.3551
103	642.6362	4491.4027	4491.3860	$(x_{39}+1)^{7+}$	3.7193
104	758.5784	4545.4269	4545.4329	$(z_{40})^{6+}$	-1.3200
105	650.3622	4545.4843	4545.4329	$(z_{40})^{7+}$	11.3081
106	570.9363	4559.4323	4559.4360	$(y_{40}\text{-}2)^{8+}$	-0.8148
107	761.0810	4560.4424	4560.4438	$(y_{40}\text{-}1)^{6+}$	-0.3158
108	652.5053	4560.4863	4560.4438	$(y_{40}\text{-}1)^{7+}$	9.3105
109	765.5789	4587.4295	4587.4309	$(x_{40})^{6+}$	-0.3117
110	668.6520	4673.5129	4673.5279	$(y_{41}\text{-}1)^{7+}$	-3.2096
111	782.9268	4691.5173	4691.5207	$(a_{42})^{6+}$	-0.7279
112	671.3671	4692.5185	4692.5285	$(a_{42}+1)^{7+}$	-2.1396
113	676.6558	4729.5396	4729.5410	$(y_{42}\text{-}1)^{7+}$	-0.3013
114	687.5232	4805.6111	4805.6126	$(a_{43}+1)^{7+}$	-0.3121
115	692.8078	4842.6034	4842.5898	$(y_{43}\text{-}H_2O)^{7+}$	2.8169
116	695.2361	4859.6020	4859.5919	$(y_{43}\text{-}1)^{7+}$	2.0681
117	699.2347	4887.5920	4887.5869	$(x_{43}+1)^{7+}$	1.0506
118	613.5845	4900.6177	4900.6628	$(a_{44}\text{-}NH_3)^{8+}$	-9.2098
119	820.7886	4918.6880	4918.6967	$(a_{44}+1)^{6+}$	-1.7606
120	820.7886	4918.6880	4918.6967	$(a_{44}+1)^{6+}$	-1.7606
121	703.6797	4918.7071	4918.6967	$(a_{44}+1)^{7+}$	2.1225
122	622.4649	4971.6613	4971.6687	$(y_{44}\text{-}NH_3)^{8+}$	-1.4953
123	624.4691	4987.6949	4987.6869	$(y_{44}\text{-}1)^{8+}$	1.6020
124	627.9686	5015.6909	5015.6818	$(x_{44}+1)^{8+}$	1.8093
125	724.6871	5065.7591	5065.7651	$(a_{45}+1)^{7+}$	-1.1785
126	845.3011	5065.7632	5065.7651	$(a_{45}+1)^{6+}$	-0.3692
127	734.8352	5136.7989	5136.8022	$(a_{46}+1)^{7+}$	-0.6385
128	866.6444	5193.8238	5193.8236	$(a_{47}+1)^{6+}$	0.0308
129	742.9833	5193.8320	5193.8236	$(a_{47}+1)^{7+}$	1.6096
130	746.1148	5215.7530	5215.7615	$(z_{46})^{7+}$	-1.6278
131	752.1074	5257.7007	5257.7595	$(x_{46})^{7+}$	-11.1873
132	666.2430	5321.8857	5321.9186	$(a_{48}+2)^{8+}$	-6.1820
133	667.1089	5328.8130	5328.8456	$(z_{47})^{8+}$	-6.1083

134	609.0017	5471.9500	5471.9514	$(y_{48}-1)^{9+}$	-0.2650
135	696.3897	5563.0596	5563.0612	$(a_{50}+1)^{8+}$	-0.2948
136	620.0076	5570.9963	5570.9835	$(x_{49}+1)^{9+}$	2.3021
137	629.3496	5655.0809	5655.0649	$(y_{50}-NH_3)^{9+}$	2.8339
138	712.3961	5691.1104	5691.0960	$(a_{51})^{8+}$	2.5294
139	726.8979	5807.1230	5807.1308	$(a_{52}+1)^{8+}$	-1.3380
140	830.5964	5807.1311	5807.1308	$(a_{52}+1)^{7+}$	0.0568
141	733.9007	5863.1428	5863.1444	$(a_{53})^{8+}$	-0.2737
142	734.3986	5867.1308	5867.1923	$(y_{52}-H_2O)^{8+}$	-10.4750
143	753.4126	6019.2426	6019.2455	$(a_{54})^{8+}$	-0.4843
144	669.9224	6020.2361	6020.2533	$(a_{54}+1)^{9+}$	-2.8637
145	763.9152	6103.2635	6103.2668	$(a_{55}-NH_3)^{8+}$	-0.5364
146	691.1566	6211.3438	6211.3504	$(z_{55}-1)^{9+}$	-1.0666
147	622.2438	6212.3657	6212.3583	$(z_{55})^{10+}$	1.1992
148	623.8417	6228.3444	6228.3770	$(y_{55})^{10+}$	-5.2365
149	693.1599	6229.3736	6229.3848	$(y_{55}+1)^{9+}$	-1.8044
150	693.7168	6234.3857	6234.3851	$(a_{56}+1)^{9+}$	0.0994
151	626.5463	6255.3904	6255.3641	$(x_{55}+1)^{10+}$	4.2036
152	633.7473	6327.4001	6327.3852	$(z_{56})^{10+}$	2.3564
153	716.1649	6436.4183	6436.4441	$(a_{58}+1)^{9+}$	-4.0007
154	805.5633	6436.4481	6436.4441	$(a_{58}+1)^{8+}$	0.6292
155	718.3884	6456.4297	6456.4153	$(x_{57})^{9+}$	2.2381
156	594.2325	6525.4770	6525.4731	$(y_{58}-2)^{11+}$	0.5984
157	816.8168	6526.4760	6526.4809	$(y_{58}-1)^{8+}$	-0.7538
158	726.1717	6526.4795	6526.4809	$(y_{58}-1)^{9+}$	-0.2176
159	653.6608	6526.5347	6526.4809	$(y_{58}-1)^{10+}$	8.2403
160	734.1736	6598.4965	6598.4996	$(a_{59})^{9+}$	-0.4630
161	825.9476	6599.5224	6599.5074	$(a_{59}+1)^{8+}$	2.2759
162	664.9534	6639.4611	6639.5049	$(y_{59}-NH_3)^{10+}$	-6.5930
163	746.9571	6713.5481	6713.5503	$(a_{60}+1)^{9+}$	-0.3292
164	674.8693	6738.6197	6738.5733	$(y_{60}-NH_3)^{10+}$	6.8896
165	759.4141	6825.6614	6825.6265	$(a_{61})^{9+}$	5.1065
166	692.0735	6910.6622	6910.6216	$(x_{61})^{10+}$	5.8750
167	768.9650	6911.6196	6911.6294	$(x_{61}+1)^{9+}$	-1.4215
168	773.6386	6953.6951	6953.6851	$(a_{62})^{9+}$	1.4345
169	787.9817	7082.7695	7082.7879	$(a_{63}+1)^{9+}$	-2.5993
170	709.3884	7083.8108	7083.7957	$(a_{63}+2)^{10+}$	2.1267
171	792.7589	7125.7573	7125.7612	$(x_{63}+1)^{9+}$	-0.5424
172	720.4863	7194.7906	7194.8321	$(y_{64}-NH_3)^{10+}$	-5.7728
173	722.0888	7210.8151	7210.8227	$(a_{64})^{10+}$	-1.0505
174	722.0888	7210.8151	7210.8503	$(y_{64}-1)^{10+}$	-4.8829
175	811.7703	7296.8652	7296.8871	$(z_{65})^{9+}$	-2.9944
176	730.6955	7296.8818	7296.8871	$(z_{65})^{10+}$	-0.7195
177	739.1967	7381.8946	7381.8760	$(a_{66}-NH_3)^{10+}$	2.5232
178	752.2062	7511.9914	7511.9864	$(a_{67})^{10+}$	0.6596
179	835.7844	7512.9924	7512.9943	$(a_{67}+1)^{9+}$	0.2489

180	752.2064	7512.9924	7512.9943	$(a_{67}+1)^{10+}$	-0.2489
181	690.2807	7582.0080	7582.0435	$(y_{68}\text{-}NH_3)^{11+}$	-4.6787
182	766.0105	7650.0323	7650.0532	$(a_{68}+1)^{10+}$	-2.7294
183	696.4663	7650.0491	7650.0532	$(a_{68}+1)^{11+}$	-0.5333
184	700.5686	7695.1740	7695.1276	$(y_{69}\text{-}NH_3)^{11+}$	6.0332
185	777.3192	7763.1197	7763.1372	$(a_{69}+1)^{10+}$	-2.2594
186	706.8406	7764.1663	7764.1451	$(a_{69}+2)^{11+}$	2.7350
187	780.6230	7796.1574	7796.1753	$(y_{70}\text{-}NH_3)^{10+}$	-2.2927
188	787.1270	7861.2043	7861.1978	$(a_{70})^{10+}$	0.8237
189	721.4824	7925.2266	7925.2779	$(z_{71})^{11+}$	-6.4667
190	722.9445	7941.3094	7941.2966	$(y_{71})^{11+}$	1.6099
191	730.4907	8024.3181	8024.3463	$(z_{72})^{11+}$	-3.5093
192	673.2019	8066.3355	8066.3443	$(x_{72})^{12+}$	-1.0897
193	734.3206	8066.4464	8066.3443	$(x_{72})^{11+}$	12.6588
194	685.5384	8214.3730	8214.4205	$(x_{73}+1)^{12+}$	-5.7856
195	747.7728	8214.4299	8214.4205	$(x_{73}+1)^{11+}$	1.1413
196	747.7727	8214.4299	8214.4205	$(x_{73}+1)^{11+}$	1.1413
197	750.5136	8244.5693	8244.4749	$(a_{73}+1)^{11+}$	11.4525
198	691.3785	8284.4543	8284.4987	$(z_{74})^{12+}$	-5.3630
199	692.5549	8298.5712	8298.5014	$(y_{74}\text{-}2)^{12+}$	8.4081
200	699.5558	8382.5818	8382.5418	$(a_{74}\text{-}NH_3)^{12+}$	4.7749
201	702.0551	8412.5738	8412.5573	$(z_{75})^{12+}$	1.9602
202	703.2258	8426.6228	8426.5600	$(y_{75}\text{-}2)^{12+}$	7.4497
203	705.5567	8454.5929	8454.5553	$(x_{75})^{12+}$	4.4426
204	769.7864	8456.5706	8456.5896	$(a_{75})^{11+}$	-2.2497
205	651.5958	8457.6475	8457.5975	$(a_{75}+1)^{13+}$	5.9178
206	709.3884	8500.5730	8500.6030	$(c_{75}\text{-}1)^{12+}$	-3.5309
207	654.9071	8500.6976	8500.6030	$(c_{75}\text{-}1)^{13+}$	11.1269
208	773.8821	8501.6226	8501.6108	$(c_{75})^{11+}$	1.3833
209	712.8979	8542.6875	8542.5896	$(M\text{-}NH_3)^{12+}$	11.4632

Table A3.3 Exact masses and assignments of ions detected by IRMPD of the +13 charge state precursor ion (*m/z*=659.8249) of Ubiquitin.

Serial	Experimental *m/z*	Experimental Mass (Da)	Theoretical Mass (Da)	Assignment	Mass Difference (ppm)
1	619.3274	618.3201	618.3200	$(b_5)^+$	0.0002
2	415.7326	829.4507	829.4521	$(b_7\text{-}H_2O)^{2+}$	-1.6879
3	943.5440	942.5367	942.5366	$(b_8\text{-}H_2O)^+$	0.1061
4	472.2753	942.5361	942.5366	$(b_8\text{-}H_2O)^{2+}$	-0.5305
5	961.5532	960.5459	960.5467	$(b_8)^+$	-0.0008
6	340.8848	1019.6327	1019.6352	$(y_9)^{3+}$	-0.0025
7	510.8243	1019.6341	1019.6352	$(y_9)^{2+}$	-0.0011
8	531.8039	1061.5932	1061.5943	$(b_9)^{2+}$	-0.0011
9	410.5730	1228.6972	1228.7007	$(b_{11}\text{-}H_2O)^{3+}$	-2.8485
10	624.3631	1246.7116	1246.7108	$(b_{11})^{2+}$	0.0009
11	435.2698	1302.7876	1302.7890	$(y_{12}\text{-}H_2O)_{3+}$	0.6417
12	441.2731	1320.7975	1320.7990	$(y_{12})^{3+}$	-0.0015
13	674.8853	1347.7560	1347.7584	$(b_{12})^{2+}$	-0.0024
14	481.9509	1442.8308	1442.8325	$(b_{13}\text{-}H_2O)^{3+}$	-1.1782
15	487.2821	1458.8245	1458.8268	$(b_{13}\text{-}2)^{3+}$	-1.5766
16	731.4255	1460.8365	1460.8425	$(b_{13})^{2+}$	-0.0060
17	487.9538	1460.8396	1460.8425	$(b_{13})^{3+}$	-0.0029
18	772.9462	1543.8778	1543.8802	$(b_{14}\text{-}H_2O)^{2+}$	-1.5545
19	515.6334	1543.8782	1543.8802	$(b_{14}\text{-}H_2O)^{3+}$	-1.2954
20	521.2980	1560.8721	1560.8823	$(b_{14}\text{-}1)^{3+}$	-6.5348
21	781.9512	1561.8878	1561.8902	$(b_{14})^{2+}$	-0.0024
22	553.3281	1656.9625	1656.9642	$(b_{15}\text{-}H_2O)^{3+}$	-1.0260
23	559.3306	1674.9699	1674.9742	$(b_{15})^{3+}$	-0.0043
24	838.4937	1674.9729	1674.9742	$(b_{15})^{2+}$	-0.0013
25	894.0101	1786.0056	1786.0068	$(b_{16}\text{-}H_2O)^{2+}$	-0.6719
26	596.3424	1786.0054	1786.0068	$(b_{16}\text{-}H_2O)^{3+}$	-0.7839
27	903.0153	1804.0161	1804.0168	$(b_{16})^{2+}$	-0.0007
28	602.3460	1804.0163	1804.0168	$(b_{16})^{3+}$	-0.0005
29	629.3656	1885.0750	1885.0752	$(b_{17}\text{-}H_2O)^{3+}$	-0.1061
30	472.2753	1885.0722	1885.0752	$(b_{17}\text{-}H_2O)^{4+}$	-1.5914
31	476.7778	1903.0823	1903.0852	$(b_{17})^{4+}$	-0.0029
32	952.5491	1903.0836	1903.0852	$(b_{17})^{2+}$	-0.0016
33	635.3695	1903.0866	1903.0852	$(b_{17})^{3+}$	0.0014
34	484.2871	1933.1195	1933.1221	$(y_{17})^{4+}$	-0.0026
35	1008.0655	2014.1164	2014.1178	$(b_{18}\text{-}H_2O)^{2+}$	-0.6951
36	672.3783	2014.1132	2014.1178	$(b_{18}\text{-}H_2O)^{3+}$	-2.2839
37	504.5357	2014.1138	2014.1178	$(b_{18}\text{-}H_2O)^{4+}$	-1.9860
38	678.3822	2032.1247	2032.1278	$(b_{18})^{3+}$	-0.0031
39	509.0387	2032.1257	2032.1278	$(b_{18})^{4+}$	-0.0021
40	1017.0705	2032.1264	2032.1278	$(b_{18})^{2+}$	-0.0014
41	525.0535	2096.1847	2096.1854	$(y_{18})^{4+}$	-0.0007
42	699.7363	2096.1870	2096.1854	$(y_{18})^{3+}$	0.0016

43	550.5566	2198.1971	2198.2026	$(b_{20}-H_2O)^{4+}$	-2.5020
44	555.0599	2216.2104	2216.2126	$(b_{20})^{4+}$	-0.0022
45	832.4524	2494.3355	2494.3656	$(y_{22}-H_2O)^{3+}$	-12.0672
46	534.7019	2668.4731	2668.4772	$(y_{23})^{5+}$	-0.0041
47	542.5051	2707.4889	2707.4887	$(y_{24}-H_2O)^{3+}$	0.0739
48	909.5046	2725.4920	2725.4987	$(y_{24})^{3+}$	-0.0067
49	682.3818	2725.4980	2725.4987	$(y_{24})^{4+}$	-0.0007
50	546.1073	2725.5001	2725.4987	$(y_{24})^{5+}$	0.0014
51	569.1122	2840.5245	2840.5256	$(y_{25})^{5+}$	-0.0011
52	639.5476	3192.7016	3192.7009	$(y_{28}-H_2O)^{5+}$	0.2193
53	533.1232	3192.6957	3192.7009	$(y_{28}-H_2O)^{6+}$	-1.6287
54	536.1255	3210.7092	3210.7109	$(y_{28})^{6+}$	-0.0017
55	643.1511	3210.7193	3210.7109	$(y_{28})^{5+}$	0.0084
55	593.1574	3552.9009	3552.9114	$(b_{32}-H_2O)^{6+}$	-2.9553
57	603.3294	3613.9328	3613.9328	$(y_{32})^{6+}$	0.0000
58	614.5078	3681.0032	3681.0063	$(b_{33}-H_2O)^{6+}$	-0.8422
59	605.9086	4234.3095	4234.3092	$(y_{37}-H_2O)^{7+}$	0.0708
60	706.8913	4235.3043	4235.2932	$(y_{37}-NH_3)^{6+}$	2.6208
61	851.4706	4252.3167	4252.3192	$(y_{37})^{5+}$	-0.0025
62	608.4816	4252.3204	4252.3192	$(y_{37})^{7+}$	0.0012
63	709.7296	4252.3340	4252.3192	$(y_{37})^{6+}$	0.0148
64	862.4662	4307.2947	4307.2974	$(b_{39})^{5+}$	-0.0027
65	571.1881	4561.4464	4561.4517	$(y_{40})^{8+}$	-0.0053
66	652.7925	4562.4963	4562.4595	$(y_{40}+1)^{7+}$	8.0658
67	692.8042	4842.5784	4842.5898	$(y_{43}-H_2O)^{7+}$	-2.3541
68	811.1034	4860.5768	4860.5998	$(y_{43})^{6+}$	-0.0230
69	704.9617	4927.6809	4927.6733	$(b_{44}-H_2O)^{7+}$	1.5423
70	624.5940	4988.6939	4988.6947	$(y_{44})^{8+}$	-0.0008
71	849.7984	5092.7384	5092.7522	$(b_{45})^{6+}$	-0.0138
72	594.8814	5344.8578	5344.8643	$(y_{47})^{9+}$	-0.0065
73	797.1543	5573.0289	5573.0219	$(b_{50}-NH_3)^{7+}$	1.2561
74	727.8884	5815.0486	5815.1000	$(b_{52}-1-H_2O)^{8+}$	-8.8391
75	831.8774	5816.0908	5816.1078	$(b_{52}-H_2O)^{7+}$	-2.9229
76	730.1431	5833.0862	5833.1100	$(b_{52}-1)^{8+}$	-4.0802
77	834.4512	5834.1073	5834.1179	$(b_{52})^{7+}$	-0.0106
78	654.9139	5885.1596	5885.2027	$(y_{52})^{9+}$	-0.0431
79	667.2533	5996.2103	5996.2353	$(y_{53}-H_2O)^{9+}$	-4.1693
80	752.7841	6014.2144	6014.2453	$(y_{53})^{8+}$	-0.0309
81	669.2551	6014.2305	6014.2453	$(y_{53})^{9+}$	-0.0148
82	679.8181	6109.2971	6109.3193	$(y_{54}-H_2O)^{9+}$	-3.6338
83	766.9226	6127.3221	6127.3293	$(y_{54})^{8+}$	-0.0072
84	691.1673	6211.4402	6211.3510	$(y_{55}-NH_3)^{9+}$	14.3608
85	693.0501	6228.3856	6228.3770	$(y_{55})^{9+}$	0.0086
86	703.8285	6325.3906	6325.3939	$(y_{56}-H_2O)^{9+}$	-6.7314
87	793.9274	6343.3613	6343.4040	$(y_{56})^{8+}$	-0.0427
88	635.3490	6343.4132	6343.4040	$(y_{56})^{10+}$	0.0092
89	705.8314	6343.4171	6343.4040	$(y_{56})^{9+}$	0.0131
90	715.4990	6430.4251	6430.4360	$(y_{57})^{9+}$	-0.0109

91	804.8122	6430.4335	6430.4360	$(y_{57})^{8+}$	-0.0025
92	719.1677	6463.4441	6463.4311	$(b_{58})^{9+}$	0.0130
93	930.9317	6509.4693	6509.4787	$(y_{58}\text{-}H_2O)^{7+}$	-1.4440
94	814.6920	6509.4776	6509.4787	$(y_{58}\text{-}H_2O)^{8+}$	-0.1690
95	724.2892	6509.5369	6509.4787	$(y_{58}\text{-}H_2O)^{9+}$	8.9408
96	651.9622	6509.5496	6509.4787	$(y_{58}\text{-}H_2O)^{10+}$	10.8918
97	816.9435	6527.4895	6527.4887	$(y_{58})^{8+}$	0.0008
98	594.4158	6527.4932	6527.4887	$(y_{58})^{11+}$	0.0045
99	933.5091	6527.5127	6527.4887	$(y_{58})^{7+}$	0.0240
100	830.8221	6638.5189	6638.5213	$(y_{59}\text{-}H_2O)^{8+}$	-0.3615
101	738.6190	6638.5052	6638.5213	$(y_{59}\text{-}H_2O)^{9+}$	-2.4252
102	664.8559	6638.4862	6638.5213	$(y_{59}\text{-}H_2O)^{10+}$	-5.2873
103	666.5582	6655.5089	6655.5235	$(y_{59}\text{-}1)^{10+}$	-2.1937
104	740.6199	6656.5137	6656.5313	$(y_{59})^{9+}$	-0.0176
105	676.5669	6755.5958	6755.5997	$(y_{60})^{10+}$	-0.0039
106	763.9652	6866.6209	6866.6319	$(y_{61}\text{-}H_2O)^{9+}$	-1.6019
107	687.7706	6867.6329	6867.6159	$(y_{61}\text{-}NH_3)^{10+}$	2.4754
108	698.9792	6979.7344	6979.7160	$(y_{62}\text{-}H_2O)^{10+}$	-0.1776
109	751.6293	6755.5985	6755.5997	$(y_{60})^{9+}$	-0.0012
110	787.7582	7080.7621	7080.7637	$(y_{63}\text{-}H_2O)^{9+}$	-0.2260
111	709.0845	7080.7726	7080.7637	$(y_{63}\text{-}H_2O)^{10+}$	1.2569
112	690.1940	7581.0539	7581.0599	$(y_{68}\text{-}H_2O)^{11+}$	-0.7914
113	691.8304	7599.0547	7599.0699	$(y_{68})^{11+}$	-0.0152
114	691.2163	8282.5071	8282.5075	$(y_{74}\text{-}H_2O)^{12+}$	-0.0483
115	755.6021	8300.5426	8300.5175	$(y_{74})^{11+}$	0.0251
116	701.8797	8410.4692	8410.5367	$(b_{74}\text{-}NH_3)^{12+}$	-8.0256
117	777.5160	8541.5963	8541.6062	$(M\text{-}H_2O)^{11+}$	-1.1590
118	712.8113	8541.6481	8541.6062	$(M\text{-}H_2O)^{12+}$	4.9054
119	856.9684	8559.6109	8559.6162	$(M)^{10+}$	-0.6192
120	779.1539	8559.6131	8559.6162	$(M)^{11+}$	-0.3622
121	714.3111	8559.6454	-8561.6318	$(M)^{12+}$	3.4114

Table A3.4 Exact masses and assignments of ions detected by HiLoPD (scheme III) of the +13 charge state precursor ion (*m/z*=659.8249) of Ubiquitin.

Serial	Experimental m/z	Observed Mass	Theoretical Mass	Assignment	Mass Difference (ppm)
1	373.1900	372.1827	372.1831	$(b_3)^+$	-1.1553
2	556.3269	555.3196	555.3236	$(y_5\text{-}1)^+$	-7.2030
3	292.6662	583.3179	583.3190	$(x_5)^{2+}$	-1.9372
4	617.3121	616.3048	616.3043	$(b_5\text{-}2)^+$	0.8113
5	619.3278	618.3205	618.3200	$(b_5)^+$	0.8895
6	328.2094	654.4042	654.4051	$(z_6)^{2+}$	-1.3142
7	336.2185	670.4225	670.4238	$(y_6)^{2+}$	-1.9764
8	730.3982	729.3910	729.3889	$(b_6\text{-}NH_3)^+$	2.8791
9	747.4210	746.4137	746.4149	$(b_6)^+$	-1.6211
10	382.7276	763.4406	763.4412	$(c_6)^{2+}$	-0.7990
11	384.7450	767.4753	767.4760	$(y_7\text{-}2)^{2+}$	-0.9121
12	796.9503	795.4708	795.4715	$(x_7)^+$	-0.8800
13	398.7427	795.4708	795.4715	$(x_7)^{2+}$	-0.8800
14	434.2858	866.5570	866.5575	$(z_8)^{2+}$	-0.6116
15	442.2949	882.5751	882.5763	$(y_8)^{2+}$	-1.3540
16	943.5451	942.5379	942.5366	$(b_8\text{-}H_2O)^+$	1.3793
17	340.8853	960.5457	960.5467	$(b_8)^{3+}$	-0.9890
18	488.7859	975.5572	975.5573	$(c_8\text{-}2)^{2+}$	-0.1025
19	489.7937	977.5728	977.5730	$(c_8)^{2+}$	-0.1534
20	502.3115	1002.6084	1002.6086	$(z_9\text{-}1)^{2+}$	-0.1995
21	502.8147	1003.6149	1003.6164	$(z_9)^{2+}$	-1.5345
22	340.8853	1019.6341	1019.6352	$(y_9)^{3+}$	-1.0837
23	510.8250	1019.6354	1019.6352	$(y_9)^{2+}$	0.1912
24	522.7989	1043.5832	1043.5843	$(b_9\text{-}H_2O)^{2+}$	-1.0541
25	523.8144	1045.6142	1045.6145	$(x_9)^{2+}$	-0.2582
26	1062.6023	1061.5950	1061.5943	$(b_9)^+$	0.6311
27	567.3667	1132.7189	1132.7193	$(y_{10})^{2+}$	-0.3222
28	406.2543	1215.7410	1215.7325	$(z_{11}\text{-}2)^{3+}$	6.9917
29	406.9223	1217.7451	1217.7482	$(z_{11})^{3+}$	-2.5293
30	610.8695	1219.7244	1219.7237	$(a_{11}\text{+}1)^{2+}$	0.6067
31	412.2623	1233.7652	1233.7669	$(y_{11})^{3+}$	-1.4144
32	421.2584	1260.7533	1260.7540	$(x_{11}\text{+}1)^{3+}$	-0.5830
33	422.5866	1264.7380	1264.7446	$(c_{11}\text{+}1)^{3+}$	-5.2184
34	435.5977	1303.7713	1303.7730	$(y_{12}\text{-}NH_3)^{3+}$	-1.3039
35	441.2736	1320.7990	1320.7990	$(y_{12})^{3+}$	0.0189
36	661.4069	1320.7993	1320.7990	$(y_{12})^{2+}$	0.2461
37	450.2678	1347.7817	1347.7861	$(x_{12}\text{+}1)^{3+}$	-3.2387
38	481.9510	1442.8311	1442.8325	$(b_{13}\text{-}H_2O)^{3+}$	-0.9703
39	484.2873	1449.8402	1449.8416	$(y_{13})^{3+}$	-0.9415
40	725.9286	1449.8427	1449.8416	$(y_{13})^{2+}$	0.7828
41	726.9316	1451.8487	1451.8572	$(y_{13}\text{+}2)^{2+}$	-5.8546

42	731.4283	1460.8420	1460.8425	$(b_{13})^{2+}$	-0.3354
43	772.9470	1543.8794	1543.8802	$(b_{14}\text{-}H_2O)^{2+}$	-0.5182
44	390.9815	1559.8969	1559.8745	$(b_{14}\text{-}2)^{4+}$	14.3601
45	781.9516	1561.8886	1561.8902	$(b_{14})^{2+}$	-1.0052
46	395.4910	1577.9350	1577.9365	$(y_{14})^{4+}$	-0.9665
47	526.9861	1577.9365	1577.9365	$(y_{14})^{3+}$	-0.0158
48	789.9758	1577.9371	1577.9365	$(y_{14})^{2+}$	0.3644
49	829.4889	1656.9632	1656.9642	$(b_{15}\text{-}H_2O)^{2+}$	-0.6035
50	553.3281	1656.9625	1656.9642	$(b_{15}\text{-}H_2O)^{3+}$	-1.0260
51	838.4945	1674.9745	1674.9742	$(b_{15})^{2+}$	0.1612
52	423.2495	1688.9689	1688.9685	$(z_{15}\text{-}1)^{4+}$	0.2368
53	845.9903	1689.9661	1689.9763	$(z_{15})_{2+}$	-6.0593
54	563.9961	1689.9661	1689.9763	$(z_{15})^{3+}$	-6.0593
55	427.2536	1704.9854	1704.9873	$(y_{15}\text{-}1)^{4+}$	-1.1026
56	448.0163	1786.0063	1786.0068	$(b_{16}\text{-}H_2O)^{4+}$	-0.2800
57	596.3427	1786.0063	1786.0068	$(b_{16}\text{-}H_2O)^{3+}$	-0.2800
58	601.6911	1802.0515	1802.0526	$(z_{16}\text{-}1)^{3+}$	-0.6104
59	451.7720	1803.0591	1803.0604	$(z_{16})^{4+}$	-0.7210
60	602.0273	1803.0600	1803.0604	$(z_{16})^{3+}$	-0.2218
61	602.3464	1804.0175	1804.0168	$(b_{16})^{3+}$	0.3769
62	903.0161	1804.0176	1804.0168	$(b_{16})^{2+}$	0.4324
63	455.7768	1819.0779	1819.0792	$(y_{16})^{4+}$	-0.6954
64	607.3673	1819.0802	1819.0792	$(y_{16})^{3+}$	0.5690
65	911.0130	1820.0115	1820.0350	$(c_{16}\text{-}1)^{2+}$	-12.9118
66	462.5227	1846.0616	1846.0663	$(x_{16}+1)^{4+}$	-2.5216
67	616.3620	1846.0642	1846.0663	$(x_{16}+1)^{3+}$	-1.1132
68	943.5451	1885.0757	1885.0752	$(b_{17}\text{-}H_2O)^{2+}$	0.2652
69	629.3654	1885.0742	1885.0752	$(b_{17}\text{-}H_2O)^{3+}$	-0.5305
70	476.2750	1901.0707	1901.0696	$(b_{17}\text{-}2)^{4+}$	0.5786
71	476.7780	1903.0829	1903.0852	$(b_{17})^{4+}$	-1.2243
72	952.5499	1903.0853	1903.0852	$(b_{17})^{2+}$	0.0368
73	480.2829	1917.1024	1917.1033	$(z_{17})^{4+}$	-0.4851
74	640.3757	1918.1053	1918.1112	$(z_{17}+1)^{3+}$	-3.0759
75	484.2873	1933.1202	1933.1221	$(y_{17})_{4+}$	-0.9803
76	490.7824	1959.1004	1959.1014	$(x_{17})^{4+}$	-0.4900
77	1003.5765	2005.1384	2005.1407	$(a_{18}+1)^{2+}$	-1.1620
78	504.5361	2014.1155	2014.1178	$(b_{18}\text{-}H_2O)^{4+}$	-1.1419
79	672.3801	2014.1183	2014.1178	$(b_{18}\text{-}H_2O)^{3+}$	0.2482
80	1008.0663	2014.1181	2014.1178	$(b_{18}\text{-}H_2O)^{2+}$	0.1489
81	678.3826	2032.1261	2032.1278	$(b_{18})^{3+}$	-0.8464
82	509.0391	2032.1275	2032.1278	$(b_{18})^{4+}$	-0.1575
83	1017.0715	2032.1284	2032.1278	$(b_{18})^{2+}$	0.2854
84	521.0486	2080.1651	2080.1662	$(z_{18})^{4+}$	-0.5288
85	525.0538	2096.1862	2096.1854	$(y_{18})^{4+}$	0.3697
86	699.7362	2096.1868	2096.1854	$(y_{18})^{3+}$	0.6560
87	531.7999	2123.1707	2123.1725	$(x_{18}+1)^{4+}$	-0.8549

88	549.8058	2195.1943	2195.1936	$(z_{19})^{4+}$	0.3189
89	553.8093	2211.2082	2211.2124	$(y_{19})^{4+}$	-1.8836
90	575.5679	2298.2424	2298.2444	$(y_{20})^{4+}$	-0.8681
91	767.0886	2298.2440	2298.2444	$(y_{20})^{3+}$	-0.1719
92	582.3136	2325.2253	2325.2315	$(x_{20}+1)^{4+}$	-2.6600
93	603.5875	2410.3208	2410.3206	$(y_{21}-1)^{4+}$	0.0705
94	805.7750	2414.3033	2414.2772	$(b_{22}-H_2O)^{3+}$	10.8107
95	811.7741	2432.3006	2432.2872	$(b_{22})^{3+}$	5.4969
96	613.3351	2449.3114	2449.3135	$(c_{22})^{4+}$	-0.8696
97	817.4452	2449.3139	2449.3135	$(c_{22})^{3+}$	0.1511
98	624.8452	2495.3518	2495.3496	$(y_{22}-NH_3)^{4+}$	0.8816
99	832.7905	2495.3496	2495.3496	$(y_{22}-NH_3)^{3+}$	0.0000
100	513.4851	2562.3891	2562.3976	$(c_{23})^{5+}$	-3.3133
101	667.6242	2666.4676	2666.4616	$(y_{23}-2)^{4+}$	2.2502
102	534.5013	2667.4700	2667.4694	$(y_{23}-1)^{5+}$	0.2174
103	539.8986	2694.4568	2694.4565	$(x_{23})^{5+}$	0.1076
104	674.6220	2694.4589	2694.4565	$(x_{23})^{4+}$	0.8870
105	542.5051	2707.4893	2707.4887	$(y_{24}-H_2O)^{5+}$	0.2216
106	677.8803	2707.4920	2707.4887	$(y_{24}-H_2O)^{4+}$	1.2188
107	909.5072	2725.4999	2725.4987	$(y_{24})^{3+}$	0.4385
108	546.1073	2725.5000	2725.4987	$(y_{24})^{5+}$	0.4751
109	682.3824	2725.5005	2725.4987	$(y_{24})^{4+}$	0.6586
110	688.8863	2751.5160	2751.4780	$(x_{24})^{4+}$	13.8217
111	551.5038	2752.4825	2752.4858	$(x_{24}+1)^{5+}$	-1.1971
112	565.7105	2823.5163	2823.4996	$(y_{25}-NH_3)^{5+}$	5.9146
113	569.1124	2840.5257	2840.5256	$(y_{25})^{5+}$	0.0194
114	711.1394	2840.5287	2840.5256	$(y_{25})^{4+}$	1.0755
115	574.3076	2866.5018	2866.5049	$(x_{25})^{5+}$	-1.0849
116	591.3197	2951.5619	2951.5578	$(y_{26}-H_2O)^{5+}$	1.3891
117	738.8979	2951.5625	2951.5578	$(y_{26}-H_2O)^{4+}$	1.5924
118	600.3183	2996.5553	2996.5553	$(x_{26}+1)^{5+}$	-0.0084
119	771.6698	3082.6501	3082.6523	$(y_{27})^{4+}$	-0.7120
120	799.1825	3192.7009	3192.7004	$(y_{28}-H_2O)^{4+}$	0.1566
121	639.5475	3192.7012	3192.7004	$(y_{28}-H_2O)^{5+}$	0.2506
122	533.2913	3193.7042	3193.6844	$(y_{28}-NH_3)^{6+}$	6.1997
123	803.1870	3208.7188	3208.6947	$(y_{28}-2)^{4+}$	7.5108
124	810.1897	3236.7298	3236.6901	$(x_{28})^{4+}$	12.2533
125	825.9687	3299.8458	3299.8414	$(a_{30})^{4+}$	1.3349
126	554.9652	3323.7474	3323.7944	$(z_{29}+1)^{6+}$	-14.1405
127	557.4668	3338.7573	3338.8058	$(y_{29})^{6+}$	-14.5366
128	558.3084	3343.8069	3343.8545	$(c_{30}-1)^{6+}$	-14.2500
129	566.8041	3394.7807	3394.8195	$(y_{30}-1)^{6+}$	-11.4203
130	680.1742	3395.8346	3395.8273	$(y_{30})_{5+}$	2.1512
131	685.5697	3422.8124	3422.8144	$(x_{30}+1)^{5+}$	-0.5799
132	575.9809	3449.8419	3449.8384	$(y_{31}-NH_3)^{6+}$	1.0145
133	690.9771	3449.8489	3449.8384	$(y_{31}-NH_3)^{5+}$	3.0436

134	578.6497	3465.8548	3465.8566	$(y_{31}\text{-}1)^{6+}$	-0.5136
135	694.3801	3466.8643	3466.8644	$(y_{31})^{5+}$	-0.0303
136	867.7244	3466.8685	3466.8644	$(y_{31})^{4+}$	1.1812
137	583.1488	3492.8494	3492.8437	$(x_{31})^{6+}$	1.6405
138	699.5788	3492.8574	3492.8437	$(x_{31})^{5+}$	3.9309
139	588.6525	3525.8715	3525.9009	$(a_{32}\text{-}NH_3)^{6+}$	-8.3411
140	706.1854	3525.8907	3525.9009	$(a_{32}\text{-}NH3)^{5+}$	-2.8957
141	709.1883	3540.9054	3540.9113	$(a_{32}\text{-}2)^{5+}$	-1.6549
142	886.7391	3542.9274	3542.9269	$(a_{32})^{4+}$	0.1369
143	720.1917	3595.9220	3595.9228	$(y_{32}\text{-}H_2O)^{5+}$	-0.2225
144	600.4923	3596.9099	3596.9068	$(y_{32}\text{-}NH_3)^{6+}$	0.8591
145	603.3295	3613.9332	3613.9328	$(y_{32})^{6+}$	0.1065
146	904.4912	3613.9358	3613.9328	$(y_{32})^{4+}$	0.8260
147	723.7948	3613.9374	3613.9328	$(y_{32})^{5+}$	1.2687
148	607.6585	3639.9073	3639.9121	$(x_{32})^{6+}$	-1.3132
149	614.6692	3681.9718	3681.9903	$(b_{33}\text{-}NH_3)^{6+}$	-5.0163
150	619.3403	3710.0057	3709.9909	$(y_{33}\text{-}NH_3)^{6+}$	3.9973
151	619.3416	3710.9968	3710.9981	$(z_{33})^{6+}$	-0.3530
152	621.8474	3725.0408	3725.0012	$(y_{33}\text{-}2)^{6+}$	10.6255
153	746.4104	3727.0158	3727.0169	$(y_{33})^{5+}$	-0.2884
154	768.8246	3839.0864	3839.0931	$(y_{34}\text{-}1)^{5+}$	-1.7478
155	651.3563	3902.0939	3902.1071	$(c_{35})^{6+}$	-3.3930
156	794.8421	3969.1739	3969.1622	$(a_{36}\text{-}1)^{5+}$	2.9578
157	662.7018	3970.1670	3970.1700	$(a_{36})^{6+}$	-0.7519
158	993.5515	3970.1757	3970.1700	$(a_{36})^{4+}$	1.4395
159	795.2431	3971.1791	3971.1778	$(a_{36}+1)^{5+}$	0.3248
160	571.7485	3995.1888	3995.1942	$(y_{35}\text{-}1)^{7+}$	-1.3566
161	800.2412	3996.1695	3996.2020	$(y_{35})^{5+}$	-8.1440
162	667.0441	3996.2209	3996.2020	$(y_{35})^{6+}$	4.7182
163	1000.5490	3998.1668	3998.1649	$(b_{36})^{4+}$	0.4752
164	800.8404	3999.1657	3999.1727	$(b_{36}+1)^{5+}$	-1.7579
165	575.6056	4022.1880	4022.1813	$(x_{35})^{7+}$	1.6633
166	579.6089	4050.2111	4050.1967	$(a_{37}\text{-}NH_3)^{7+}$	3.5455
167	676.0432	4050.2154	4050.1967	$(a_{37}\text{-}NH_3)^{6+}$	4.6072
168	678.7180	4066.2641	4066.2149	$(a_{37}\text{-}1)^{6+}$	12.0948
169	678.8780	4067.2243	4067.2227	$(a_{37})^{6+}$	0.3823
170	814.6529	4068.2283	4068.2306	$(a_{37}+1)^{5+}$	-0.5580
171	685.5444	4107.2225	4107.2340	$(z_{36}\text{-}1)^{6+}$	-2.8072
172	587.8989	4108.2415	4108.2419	$(z_{36})^{7+}$	-0.0876
173	688.3842	4124.2613	4124.2606	$(y_{36})^{6+}$	0.1637
174	692.7163	4150.2515	4150.2399	$(x_{36})^{6+}$	2.7974
175	594.0427	4151.2477	4151.2477	$(x_{36}+1)^{7+}$	-0.0036
176	699.7144	4192.2429	4192.2704	$(b_{38})^{6+}$	-6.5645
177	702.3839	4208.2595	4208.2886	$(c_{38}\text{-}1)^{6+}$	-6.9268
178	706.7232	4234.2956	4234.3092	$(y_{37}\text{-}H_2O)^{6+}$	-3.2095
179	608.4803	4252.3111	4252.3192	$(y_{37})^{7+}$	-1.9060

180	851.4706	4252.3165	4252.3192	$(y_{37})^{5+}$	-0.6361
181	709.7279	4252.3237	4252.3192	$(y_{37})^{6+}$	1.0571
182	857.0696	4280.3107	4280.3103	$(a_{39}+1)^{5+}$	0.1005
183	612.6232	4281.3113	4281.3181	$(a_{39}+2)^{7+}$	-1.5883
184	715.8889	4289.2889	4289.2873	$(b_{39}\text{-}H_2O)^{6+}$	0.3730
185	858.8622	4289.2843	4289.2873	$(b_{39}\text{-}H_2O)^{5+}$	-0.6994
186	616.1971	4306.3287	4306.2895	$(b_{39}\text{-}1)^{7+}$	9.1030
187	862.4686	4307.3065	4307.2974	$(b_{39})^{5+}$	2.1220
188	871.2717	4351.3220	4351.3274	$(z_{38})^{5+}$	-1.2364
189	622.6268	4351.3365	4351.3274	$(z_{38})^{7+}$	2.0959
190	874.2712	4366.3369	4366.3383	$(y_{38}\text{-}2)^{5+}$	-0.3252
191	728.8984	4367.3465	4367.3461	$(y_{38})^{6+}$	0.0813
192	732.9024	4391.3706	4391.3098	$(x_{38}\text{-}2)^{6+}$	13.8455
193	733.2271	4393.3192	4393.3254	$(x_{38})^{6+}$	-1.4135
194	628.6250	4393.3242	4393.3254	$(x_{38})^{7+}$	-0.2754
195	879.6834	4393.3807	4393.3254	$(x_{38})^{5+}$	12.5850
196	735.7286	4408.3282	4408.3689	$(a_{40}+1)^{6+}$	-9.2211
197	740.2370	4435.3786	4435.3559	$(b_{40})^{6+}$	5.1089
198	636.2056	4446.3882	4446.3889	$(y_{39}\text{-}H_2O)^{7+}$	-0.1574
199	742.0705	4446.3794	4446.3889	$(y_{39}\text{-}H_2O)^{6+}$	-2.1366
200	743.2398	4453.3949	4453.3898	$(c_{40}+1)^{6+}$	1.1452
201	637.3511	4454.4065	4454.3976	$(c_{40}+2)^{7+}$	1.9980
202	638.4918	4462.3919	4462.3833	$(y_{39}\text{-}2)^{7+}$	1.9272
203	893.6841	4463.3840	4463.3911	$(y_{39}\text{-}2)^{5+}$	-1.5862
204	744.9057	4463.3908	4463.3911	$(y_{39}\text{-}1)^{6+}$	-0.0627
205	754.0786	4518.4277	4518.3926	$(a_{41}\text{-}NH_3)^{6+}$	7.7682
206	913.0968	4560.4477	4560.4438	$(y_{40}\text{-}1)^{5+}$	0.8464
207	652.5003	4560.4509	4560.4438	$(y_{40}\text{-}1)^{7+}$	1.5481
208	789.5994	4731.5530	4731.5572	$(y_{42})^{6+}$	-0.8845
209	798.9324	4787.5508	4787.5783	$(a_{43}\text{-}NH_3)^{6+}$	-5.7440
210	692.8077	4842.6029	4842.5898	$(y_{43}\text{-}H_2O)^{7+}$	2.7052
211	808.2729	4843.5938	4843.5738	$(y_{43}\text{-}NH_3)^{6+}$	4.1292
212	810.9403	4859.5947	4859.5919	$(y_{43}\text{-}1)^{6+}$	0.5659
213	811.2746	4861.6008	4861.6076	$(y_{43}+1)^{6+}$	-1.3987
214	820.7903	4918.6979	4918.6967	$(a_{44}+1)^{6+}$	0.2521
215	713.6782	4988.6962	4988.6947	$(y_{44})^{7+}$	0.2937
216	685.0026	5471.9627	5471.9514	$(y_{48}\text{-}1)^{8+}$	2.0559
217	696.3855	5563.0256	5563.0612	$(a_{50}+1)^{9+}$	-6.4066
218	736.6567	5885.1951	5885.2027	$(y_{52})^{8+}$	-1.2888
219	753.4139	6019.2526	6019.2455	$(a_{54})^{8+}$	1.1771
220	766.9225	6127.3202	6127.3293	$(y_{54})^{8+}$	-1.4909
221	686.1546	6166.3261	6166.3220	$(c_{55}+1)^{9+}$	0.6649
222	691.1579	6211.3559	6211.3510	$(y_{55}\text{-}NH_3)^{9+}$	0.7889
223	692.9365	6227.3631	6227.3692	$(y_{55}\text{-}1)^{9+}$	-0.9779
224	779.4281	6227.3663	6227.3692	$(y_{55}\text{-}1)^{8+}$	-0.4641
225	703.8272	6325.3794	6325.3939	$(y_{56}\text{-}H_2O)^{9+}$	-2.2923

226	704.4972	6331.4091	6331.3778	$(b_{57}-NH_3)^{9+}$	4.9436
227	793.8083	6342.4037	6342.3961	$(y_{56}-1)^{8+}$	1.1936
228	705.8305	6343.4091	6343.4040	$(y_{56})^{9+}$	0.8111
229	705.8305	6343.4091	6343.4040	$(y_{56})^{9+}$	0.8111
230	637.6519	6366.4117	6366.4381	$(c_{57}+1)^{10+}$	-4.1467
231	708.4972	6367.4097	6367.4459	$(c_{57}+2)^{9+}$	-5.6852
232	713.5014	6412.4470	6412.4260	$(y_{57}-H_2O)^{9+}$	3.2749
233	715.3919	6429.4614	6429.4282	$(y_{57}-1)9+$	5.1700
234	811.1894	6481.4573	6481.4651	$(c_{58}+1)^{8+}$	-1.2034
235	814.6917	6509.4754	6509.4543	$(z_{58}-2)^{8+}$	3.2414
236	651.9553	6509.4804	6509.4543	$(z_{58}-2)^{10+}$	4.0096
237	931.0763	6510.4799	6510.4622	$(z_{58}-1)^{7+}$	2.7187
238	724.5062	6511.4869	6511.4700	$(z_{58})^{9+}$	2.5985
239	933.4982	6527.4363	6527.4887	$(y_{58})_{9+}$	-8.0345
240	816.9437	6527.4918	6527.4887	$(y_{58})^{8+}$	0.4680
241	653.7569	6527.4964	6527.4887	$(y_{58})^{10+}$	1.1727
242	726.2849	6527.4982	6527.4887	$(y_{58})^{9+}$	1.4485
243	830.8229	6638.5270	6638.5209	$(y_{59}-H_2O)^{8+}$	0.9189
244	738.6210	6638.5232	6638.5209	$(y_{59}-H2O)^{9+}$	0.3465
245	664.8606	6638.5329	6638.5209	$(y_{59}-H_2O)^{10+}$	1.8076
246	751.4075	6753.6024	6753.5836	$(y_{60}-2)^{9+}$	2.7837
247	751.8513	6757.5961	6757.5637	$(c_{60})^{9+}$	4.7946
248	651.2827	8453.5810	8453.5475	$(x_{75}-1)^{13+}$	3.9628
249	705.5562	8454.5875	8454.5553	$(x_{75})^{12+}$	3.8039
250	772.3337	8484.5905	8484.5845	$(b_{75})^{11+}$	0.7025
251	777.5195	8541.6343	8541.6056	$(M-H_2O)^{11+}$	3.3630
252	712.8094	8541.6258	8541.6056	$(M-H_2O)^{12+}$	2.3678
253	658.0558	8541.6306	8541.6056	$(M-H_2O)^{13+}$	2.9298

Table A4.1 Theoretical and observed *m/z* value with fragment ions assignment detected in the IRMPD, UVPD and HiLoPD spectra of the +3 charge state precursor ion (*m/z*=533.9356) of RRLIEDAEY(H_2PO_4)AARG peptide.

Theoretical *m/z*	IRMPD Observed *m/z*	UVPD Observed *m/z*	HiLoPD Observed *m/z*	Assignment
215.1139	215.1131		215.1139	$(y_2\text{-}NH_3)^+$
216.1217		216.1218	216.1217	$(z_2)^+$
217.1295		217.1013	217.1012	$(z_2+1)^+$
230.1248		230.1248	230.1248	$(y_2\text{-}2)^+$
231.1326		231.1169	231.1326	$(y_2\text{-}1)^+$
232.1404	232.1396	232.1405	232.1404	$(y_2)^+$
233.1482	233.1430	233.1430		$(y_2+1)^+$
257.1119		257.1325	257.0961	$(x_2\text{-}1)^+$
258.1197		258.1198	258.1197	$(x_2)^+$
268.1880		268.2187	268.1880	$(a_2\text{-}NH_3)^+$
284.2068		284.2501	284.2501	$(a_2\text{-}1)^+$
285.2146		285.2147	285.2147	$(a_2)^+$
286.2225		286.2225	286.2225	$(a_2+1)^+$
286.1510	286.1501	286.1511	286.1510	$(y_3\text{-}NH_3)^+$
287.1588		287.1590	287.1588	$(z_3)^+$
288.1666		288.1510	288.1508	$(z_3+1)^+$
296.1829	296.1820	296.1831	296.1829	$(b_2\text{-}NH_3)^+$
301.1619	301.1366	301.1620	301.1619	$(y_3\text{-}2)^+$
303.1775	303.1765	303.1777	303.1777	$(y_3)^+$
304.1853	304.1798		304.1798	$(y_3+1)^+$
313.2095	313.2085	313.2096	313.2096	$(b_2)^+$
314.2173	314.2118		314.2132	$(b_2+1)^+$
329.1568		329.1570	329.1568	$(x_3)^+$
330.1646		330.1648		$(x_3+1)^+$
331.1725		331.1727		$(x_3+2)^+$
329.2282		329.2169	329.2170	$(c_2\text{-}1)^+$
330.2360		330.2361	330.2358	$(c_2)^+$
357.1881	357.1869	357.1883	357.1881	$(y_4\text{-}NH_3)^+$
358.1959		358.1961	358.1960	$(z_4)^+$
372.1990		372.1993	372.1991	$(y_4\text{-}2)^+$
374.2146	374.2135	374.2149	374.2146	$(y_4)^+$
381.2721		381.2977	381.2722	$(a_3\text{-}NH_3)^+$
398.2986		398.2989	398.2977	$(a_3)^+$
400.1939		400.1942	400.1935	$(x_4)^+$
401.2017		401.2022	401.1970	$(x_4+1)^+$
402.2096		402.2099	402.2095	$(x_4+2)^+$
409.2670		409.2673	409.2670	$(b_3\text{-}NH_3)^+$
426.2936		426.2939	426.2936	$(b_3)^+$
443.3201		443.3205	443.3204	$(c_3)^+$
494.3562		494.3568	494.3564	$(a_4\text{-}NH_3)^+$
510.3749		510.3755		$(a_4\text{-}1)^+$

511.3827		511.3836	511.3830	$(a_4)^+$
256.1950		256.1932	256.1938	$(a_4)^{2+}$
513.3984		513.3990		$(a_4+2)^+$
519.2680	519.2662		519.2672	$(y_5\text{-}H_3PO_4)^+$
521.2598		521.2576	522.2423	$(z_5\text{-}HPO_3)^+$
522.3511	522.3499	522.3515	523.3551	$(b_4\text{-}NH_3)^+$
537.2785		537.2704	537.2784	$(y_5\text{-}HPO_3)^+$
539.3776	539.3762	539.3782	539.3780	$(b_4)^+$
270.1925	270.1916		270.1925	$(b_4)^{2+}$
540.3854	540.3800			$(b_4+1)^+$
556.4042		556.4049		$(c_4)^+$
600.2188		600.2178		$(y_5\text{-}NH_3)^+$
601.2256		601.2265		$(z_5)^+$
615.2294		615.2294		$(y_5\text{-}2)^+$
617.2451	617.2428	617.2451	617.2416	$(y_5)^+$
623.3988		623.3996	623.3993	$(a_5\text{-}NH_3)^+$
640.4253		640.4263	640.4258	$(a_5)^+$
320.7163		320.7140	320.7149	$(a_5)^{2+}$
643.2236		643.2244	643.2326	$(x_5)^+$
645.2393		645.2401		$(x_5+2)^+$
648.3106	648.3085	648.3094	648.3104	$(y_6\text{-}H_3PO_4)^+$
650.4097	325.7074		325.7085	$(b_5\text{-}H_2O)^{2+}$
651.3937	651.3921	651.3948	651.3942	$(b_5\text{-}NH_3)^+$
652.4015	652.3956		652.3975	$(b_5+1\text{-}NH_3)^+$
666.3211		666.3179	666.3210	$(y_6\text{-}HPO_3)^+$
668.4202	668.4187	668.4210	668.4207	$(b_5)^+$
334.7137	334.7115	334.7116	334.7122	$(b_5)^{2+}$
669.4280			669.4244	$(b_5+1)^+$
685.4468		685.4417	685.4472	$(c_5)^+$
686.4501			686.4499	$(c_5+1)^+$
719.3477	719.3455	719.3467	719.3477	$(y_7\text{-}H_3PO_4)^+$
721.3395		721.3226	721.3363	$(z_7\text{-}HPO_3)^+$
728.2763		728.2776		$(y_6\text{-}H_2O)^+$
730.2682		730.2695		$(z_6)^+$
737.3582	737.3561	737.3540	737.3581	$(y_7\text{-}HPO_3)^+$
738.4257		738.3619		$(a_6\text{-}H_2O)^+$
744.2712		744.2726		$(y_6\text{-}2)^+$
746.2869	746.2829	746.2881	746.2836	$(y_6)^+$
755.4522		755.4534	755.4526	$(a_6)^+$
756.4600		756.4606	756.4552	$(a_6+1)^+$
757.4679		757.4690		$(a_6+2)^+$
765.4128	765.4349		765.4372	$(b_6\text{-}H_2O)^+$
383.2219	383.2209		383.2221	$(b_6\text{-}H_2O)^{2+}$
766.4206	766.4188	766.4216	766.4210	$(b_6\text{-}NH_3)^+$
767.4284	767.4219		767.4243	$(b_6+1\text{-}NH_3)^+$
772.2662		772.2674	772.2674	$(x_6)^+$

783.4472	783.4455	783.4485	783.4479	$(b_6)^+$
392.2272	392.2264	392.2269	392.2275	$(b_6)^{2+}$
784.4550	784.4488		784.4512	$(b_6+1)^+$
785.4629	392.2264		392.2275	$(b_6+2)^+$
815.3084		815.3096		$(y_7\text{-}2)^+$
816.3162			816.3639	$(y_7\text{-}1)^+$
817.3240	817.3221	817.3251	817.3480	$(y_7)^+$
818.3318	818.3253	818.3270		$(y_7+1)^+$
826.4894			826.4907	$(a_7)^+$
413.7483	413.7472	413.7482	413.7485	$(a_7)^{2+}$
834.3747	834.3722	834.3739	834.3743	$(y_8\text{-}H_3PO_4)^+$
836.4737	836.4717			$(b_7\text{-}H_2O)^+$
418.7405	418.7393		418.7406	$(b_7\text{-}H_2O)^{2+}$
837.4577	837.4554			$(b_7\text{-}NH_3)^+$
838.4655	838.4588		838.4617	$(b_7+1\text{-}NH_3)^+$
843.3033		843.3406		$(x_7)^+$
845.3190		845.3203	845.3756	$(x_7+2)^+$
852.3852	852.3826	852.3800	852.3847	$(y_8\text{-}HPO_3)^+$
854.4843	854.4823		854.4848	$(b_7)^+$
427.7458	427.7457	427.7446	427.7459	$(b_7)^{2+}$
855.4921	855.4853		855.4880	$(b_7+1)^+$
871.5108		871.5122		$(c_7)^+$
932.3510	932.3456	932.3525	932.3471	$(y_8)^+$
955.5320		955.5335		$(a_8)^+$
956.5398		956.5400		$(a_8+1)^+$
957.5477		957.5489		$(a_8+2)^+$
963.4172	963.4147	963.4162	963.4170	$(y_9\text{-}H_3PO_4)^+$
965.5163	483.2606			$(b_8\text{-}H_2O)^+$
483.2618	483.2606		483.2621	$(b_8\text{-}H_2O)^{2+}$
983.5269	983.5244	983.5283	983.5283	$(b_8)^+$
492.2671	492.2659		492.2674	$(b_8)^{2+}$
984.5347	984.5270		984.5311	$(b_8+1)^+$
1000.5534		1000.5551		$(c_8)^+$
564.7760	564.7921			$(b_9\text{-}H_3PO_4)^{2+}$
1199.5694		1199.5712		$(a_9)^+$
600.2946	600.3105			$(b_{10}\text{-}H_3PO_4)^{2+}$

Table A4.2 Theoretical and observed *m/z* value with fragment ions assignment detected in the IRMPD, UVPD and HiLoPD spectra of the +2 charge state precursor ion *(m/z*=626.7492) of RDY(SO$_3$)TGWLDF peptide.

Theoretical *m/z*	IRMPD Observed *m/z*	UVPD Observed *m/z*	HiLoPD Observed *m/z*	Assignment
227.1139		227.1139	227.1141	$(a_2\text{-NH3})^+$
229.1295		229.1159	229.1174	$(a_2\text{+2-NH}_3)^+$
244.1404		244.1405	244.1406	$(a_2)^+$
245.1482		245.1483	245.1484	$(a_2\text{+1})^+$
246.1561		246.1561		$(a_2\text{+2})^+$
254.1248			254.1234	$(b_2\text{-H}_2\text{O})^+$
255.1088	255.1083	255.1089	255.1170	$(b_2\text{-NH}_3)^+$
263.1026	263.1022		263.1029	$(y_2\text{-H}_2\text{O})^+$
264.1104			264.1063	$(y_2\text{+1-H}_2\text{O})^+$
265.0945			265.0932	$(z_2)^+$
272.1353	272.1349	272.1355	272.1356	$(b_2)^+$
279.0975		279.0977	279.0963	$(y_2\text{-2})^+$
281.1132	281.1128	281.1133	281.1135	$(y_2)^+$
282.1210	282.1161		282.1168	$(y_2\text{+1})^+$
288.1541		288.1523		$(c_2\text{-1})^+$
289.1619			289.1622	$(c_2)^+$
376.1867		376.1800	376.1870	$(y_3\text{-H}_2\text{O})^+$
394.1973	394.1967	394.1975	394.1977	$(y_3)^+$
395.2051	395.2000		395.2010	$(y_3\text{+1})^+$
407.2032		407.2041	407.2043	$(a_3\text{-SO}_3)^+$
418.1765		418.1724		$(x_3\text{-2})^+$
435.1981	435.1982	435.1991	435.1993	$(b_3\text{-SO}_3)^+$
452.2246		452.2257	452.2259	$(c_3\text{-SO}_3)^+$
487.1606		487.1613		$(a_3)^+$
508.2508		508.2521		$(a_4\text{-SO}_3)^+$
534.1932			534.2049	$(c_3\text{+2})^+$
536.2458	536.2459	536.2471	536.2474	$(b_4\text{-SO}_3)^+$
553.2723			553.2738	$(c_4\text{-SO}_3)^+$
562.2660	562.2417		562.2433	$(y_4\text{-H}_2\text{O})^+$
563.2738			563.2466	$(y_4\text{+1-H}_2\text{O})^+$
580.2762	580.2766	580.2754	580.2779	$(y_4)^+$
593.2672	593.2671	593.2686	593.2688	$(b_5\text{-SO}_3)^+$
610.2938		610.2951	610.2954	$(c_5\text{-SO}_3)^+$
637.2975	637.2980	637.2904	637.2952	$(y_5)^+$
690.2512		690.2520	690.2495	$(c_5)^+$
691.2590		691.2556	691.2519	$(c_5\text{+1})^+$
738.3457	738.3453	738.3466	738.3467	$(y_6)^+$
751.3516		751.3533	751.3533	$(a_6\text{-SO}_3)^+$
762.3250		762.3215	762.3207	$(x_6\text{-2})^+$
763.3172			763.3236	$(x_6\text{-1})^+$

764.3250			764.3256	$(x_6)^+$
779.3465	779.3466	779.3484	779.3485	$(b_6\text{-}SO_3)^+$
864.4357		864.4375	864.4374	$(a_7\text{-}SO_3)^+$
892.4306	892.4307	892.4324	892.4326	$(b_7\text{-}SO_3)^+$
446.7189	446.7170	446.7151	446.7178	$(b_7\text{-}SO_3)^{2+}$
901.4085		901.3979	901.4117	$(y_7\text{-}SO_3)^+$
999.4089		999.4183	999.4181	$(z_8\text{-}1\text{-}SO_3)^+$
1007.4575	1007.4574	1007.4597	1007.4596	$(b_8\text{-}SO_3)^+$
504.2324	504.2309	504.2281	504.2311	$(b_8\text{-}SO_3)^{2+}$
1042.4147		1042.4603	1042.4735	$(x_8\text{-}SO_3)^+$
541.2443		541.2400	541.2429	$(M+H\text{-}W)^{2+}$
562.2394		562.2380	562.2408	$(M+H\text{-}{}_{im}R)^{2+}$
577.76665	577.7676	577.7672	577.7671	$(M+H\text{-}SO_3+H_2O)^{2+}$
1172.5364	1172.5379	1172.5388	1172.5392	$(M+H\text{-}SO_3)^+$
617.7453		617.7399		$(M+H\text{-}H_2O)^{2+}$
1252.4957	1252.4939	1252.4957		$(M+H)^+$

Table A4.3 Theoretical and observed *m/z* values with assignments of ions detected in the IRMPD, UVPD and HiLoPD spectra of the +3 charge state precursor ion (*m/z*=556.9529) of EAISPPDAAS (GalNAc)AAPLR peptide.

Theoretical, *m/z*	IRMPD Observed *m/z*	UVPD Observed *m/z*	HiLoPD Observed *m/z*	Assignment
201.0870		201.0870	201.0872	$(b_2)^+$
217.1057		217.1010	217.1014	$(c_2\text{-}1)^+$
218.1135		218.1133	218.1092	$(c_2)^+$
219.1169		219.1167	219.1170	$(c_2+1)^+$
269.1609	269.1489		269.1691	$(y_2\text{-}2\text{-}NH_3)^+$
271.1765		271.1762	271.1767	$(y_2\text{-}NH_3)^+$
272.1843		272.1841	272.1845	$(z_2)^+$
286.1761		286.1759	286.1763	$(a_3)^+$
287.1952		287.1949	287.1840	$(a_3+1)^+$
288.2030	288.2032	288.2027	288.2032	$(y_2)^+$
296.1605		296.1602	296.1672	$(b_3\text{-}H_2O)^+$
314.1710	314.1703	314.1708	314.1713	$(b_3)^+$
315.1788			315.1903	$(b_3+1)^+$
331.1976		331.1973	331.1978	$(c_3)^+$
373.2082		373.2083	373.2085	$(a_4)^+$
375.2239		375.2239	375.2242	$(a_4+2)^+$
383.1925	383.1917	383.1928	383.1930	$(b_4\text{-}H_2O)^+$
383.2402		383.2402	383.2404	$(y_3\text{-}2)^+$
384.2480		384.2484	384.2435	$(y_3\text{-}1)^+$
385.2558	385.2549	385.2558	385.2560	$(y_3)^+$
399.1875			399.1878	$(b_4\text{-}2)^+$
401.2031	401.2022	401.2032	401.2035	$(b_4)^+$
402.2109		402.2024	402.2069	$(b_4+1)^+$
403.2188			403.2192	$(b_4+2)^+$
412.2428		412.2430	412.2431	$(x_3+1)^+$
439.2664			439.2668	$(z_4\text{-}1)^+$
440.2742		440.2744	440.2753	$(z_4)^+$
456.2929	456.2920	456.2931	456.2934	$(y_4)^+$
457.3007	457.2955		457.2968	$(y_4+1)^+$
470.2609		470.2612	470.2614	$(a_5)^+$
471.2687		471.2692	471.2690	$(a_5+1)^+$
472.2766		472.2769	472.2772	$(a_5+2)^+$
480.2453		480.2455	480.2461	$(b_5\text{-}H_2O)^+$
498.2558		498.2562	498.2566	$(b_5)^+$
500.2715		500.2718	500.2720	$(b_5+2)^+$
511.3113		511.3118	511.3120	$(z_5)^+$
525.3144		525.3148		$(y_5\text{-}2)^+$
526.3222		526.3227		$(y_5\text{-}1)^+$
527.3300	527.3293		527.3308	$(y_5)^+$
528.3378			528.3345	$(y_5+1)^+$

554.3171		554.3175	554.3175	$(x_5+1)^+$
567.3137		567.3142	567.3142	$(a_6)^+$
568.3215		568.3220		$(a_6+1)^+$
595.3086		595.3091		$(b_6)^+$
597.3243		597.3251		$(b_6+2)^+$
612.3352		612.3292		$(c_6)^+$
614.3509	614.3609		614.3629	$(c_6+2)^+$
615.3587	615.3644		615.3667	$(c_6+3)^+$
682.3406		682.3411	682.3407	$(a_7)^+$
684.3563		683.3491	683.3371	$(a_7+2)^+$
685.3992	685.3981	685.3991	685.4002	$(y_7-203)^+$
669.3805		669.3801		$(z_7-203)^+$
710.3355	710.3344	710.3366	710.3368	$(b_7)^+$
740.4176		740.4174		$(z_8-203)^+$
753.3777		753.3962		$(a_8)^+$
754.3855		754.3859		$(a_8+1)^+$
756.4363	756.4352	756.4361	756.4373	$(y_8-203)^+$
763.3621		763.3620	763.3631	$(b_8-H_2O)^+$
781.3732	781.3717	781.3732	781.3739	$(b_8)^+$
782.3810			782.3774	$(b_8+1)^+$
799.4026		799.4075		$(c_8+1)^+$
800.4254		800.3973		$(y_6-H_2O)^+$
817.4520	817.4403	817.4330	817.4428	$(y_6)^+$
834.3992	834.3981		834.4005	$(b_9-H_2O)^+$
852.4098	852.4084	852.4104	852.4110	$(b_9)^+$
853.4176	853.4115		853.4143	$(b_9+1)^+$
855.4445		855.4432		$(z_9-203)^+$
869.4363		869.4377		$(c_9)^+$
871.4626		871.4539	871.4644	$(z_7-1)^+$
872.4704		872.4617		$(z_7)^+$
888.4891		888.4782		$(y_7)^+$
897.4425		897.4421		$(x_9-203)^+$
921.4317	921.4298	921.4311	921.4326	$(b_{10}-221)^+$
939.4418	939.4405	939.4421	939.4436	$(b_{10}-203)^+$
943.5075		943.4983		$(z_8)^+$
959.5262		959.5160	959.5160	$(y_8)^+$
968.5160	968.5143	968.5158	968.5175	$(y_{10}-203)^+$
982.4840		982.4840		$(a_{11}-203)^+$
992.4689	992.4669	992.4687	992.4701	$(b_{11}-221)^+$
994.4926		995.5031		$(x_{10}-203)^+$
1010.4787	1010.4775	1010.4793	1010.4803	$(b_{11}-203)^+$
1027.5055		1027.5055	1027.5072	$(c_{11}-203)^+$
1053.5212		1053.5213		$(a_{12}-203)^+$
1058.5344		1058.5250	1058.5250	$(z_9)^+$
1063.5060	1063.5038	1063.5532	1063.5083	$(b_{12}-221)^+$
1065.5688	1065.5670	1065.5687	1065.5706	$(y_{11}-203)^+$

533.2880	533.2873	533.2841	533.2875	$(y_{11}-203)^{2+}$
1081.5161	1081.5141	1081.5160	1081.5179	$(b_{12}-203)^{+}$
1101.5402		1101.5306		$(x_{9}+1)^{+}$
1152.5875	1152.5986		1152.6032	$(y_{12}-2-NH_{3})^{+}$
1152.6008	1152.5987	1152.6010	1152.6032	$(y_{12}-203)^{+}$
1153.5953			1153.6063	$(y_{10}-H_{2}O)^{+}$
576.7976	576.8031	576.8041	576.8050	$(y_{10}-H_{2}O)^{2+}$
1154.6031			1154.6089	$(y_{10}-NH_{3})^{+}$
585.2987		585.2936	585.2926	$(y_{10}-1)^{2+}$
593.7947		593.7830	593.7882	$(a_{11}+2)^{2+}$
607.28835	607.2817	607.2764	607.2823	$(b_{10}+1)^{2+}$
629.3133		629.3078	629.3070	$(a_{12}+2)^{2+}$
634.8332	634.8267	634.8205	634.8270	$(y_{11}+1)^{2+}$
642.8069	642.8003	642.7947	642.8006	$(b_{13}+1)^{2+}$
1465.7646			1465.7668	$(MH-203)^{+}$
733.3795	733.3849	733.3861	733.3873	$(y_{13}-2)^{2+}$